A tumor invasion model for heterogeneous cancer cell populations: mathematical analysis and numerical methods

Dissertation

zur Erlangung des Grades eines
"Doktor rerum naturalium (Dr. rer. nat.)"

der Fachbereiche:

08 - Physik, Mathematik und Informatik,
09 - Chemie, Pharmazie und Geowissenschaften,
10 - Biologie,
Universitätsmedizin

der Johannes Gutenberg-Universität.

Niklas Kolbe

October 2017

Max Planck Graduate Center
mit der Johannes Gutenberg-Universität Mainz

JOHANNES GUTENBERG
UNIVERSITÄT MAINZ

JG|U

Datum der mündlichen Prüfung: 14.12.2017

D77 Mainzer Dissertationen

Abstract

Tumor invasion of tissue is the first step in cancer metastasis and thus a process that is co-responsible for most deaths in cancer patients. In this thesis we consider two macroscopic tumor invasion models from the literature and derive a third one that takes the presence of recently discovered stem-like cells within tumors into account. The modeling considers microscopic events on the cancer cell receptors and tissue remodeling by fibroblast cells. In addition to the model derivation, we prove global in time existence of classical solutions in two space dimensions for a slightly simplified version of the new model. We show in numerical experiments in one and two space dimensions that the new model can qualitatively reproduce the biomedical understanding of the invasion by the two considered types of cancer cells.

Since Keller-Segel type models of tumor invasion such as our new model are associated with very rich dynamics, their numerical simulation requires elaborate methods. These constitute another core theme of this thesis. Here we design and study, in particular, combined finite volumes/finite differences with implicit-explicit time discretization in the first place, adaptive mesh refinement methods in the second place and a new mass-transport scheme in the third place.

Zusammenfassung

Die Invasion von Tumor benachbartem Gewebe durch Krebszellen ist der erste Schritt bei der Entstehung von Metastasen. Somit ist dieser Prozess mitverantwortlich für die meisten Todesfälle unter Krebspatienten. In dieser Arbeit betrachten wir zwei makroskopische Modelle der Tumorinvasion aus der Literatur und wir leiten ein drittes her, welches insbesondere die erst kürzlich entdeckten Stammzellen-ähnlichen Zellen innerhalb von Tumoren miteinbezieht. Bei der Modellierung berücksichtigen wir die Remodellierung des Gewebes durch Fibroblasten und Prozesse an den Zellrezeptoren. Neben der Modellherleitung zeigen wir die globale Existenz und Eindeutigkeit von klassischen Lösungen in zwei Raumdimensionen in einem leicht vereinfachtem Modell. Wir demonstrieren darüber hinaus durch numerische Experimente in einer und zwei Raumdimensionen, dass das neue Modell die biomedizinische Auffassung des Invasionsprozesses durch die beiden betrachteten Krebszellentypen qualitativ reproduzieren kann.

Keller-Segel-artige Tumorinvasionsmodelle, zu denen auch unser neues Modell gehört, gehen mit einer komplexen Dynamik der zugehörigen Lösungen einher. Deshalb benötigt man für die numerische Approximation geeignete Verfahren, welche einen weiteren Schwerpunkt dieser Arbeit darstellen. Wir entwickeln und vergleichen hier im Speziellen kombinierte finite Volumen/finite Differenzen mit implizit-expliziter Zeitdiskretisierung, adaptive Gitterverfeinerungsverfahren und eine neue Massetransportmethode.

Acknowledgements

Foremost, I would like to thank both my supervisors from the math department of the University of Mainz. Without their support this work would not have been possible. I have greatly benefited from the guidance and help by my first thesis advisor and from the collaborations and conference visits that she made possible for me. Further, the advice and the enthusiasm of my third thesis advisor, with whom I was fortune enough to work closely together, enormously supported me throughout the PhD years. Also, I thank my second thesis advisor from the biophysics department of the University of Mainz, especially for her helpful remarks from a biological point of view.

Moreover, I am very thankful that I had the opportunity to collaborate with several experts from external institutions. Their knowledge and ideas led to various exciting projects related to this thesis. I thank all of them for the remarks and discussions from which I learned a lot.

I owe my deepest gratitude to my family, friends and colleagues for their support and understanding. In this respect, my girlfriend deserves special mention for her unceasing encouragement. I also wish to thank, in particular, those friends who assisted me in the proofreading.

Finally, I would like to thank the Max Planck Graduate Center. Its financial support made it possible for me to attend many interesting conferences and meetings, and its lecture cycle encouraged various helpful interdisciplinary discussions.

Contents

List of Figures

List of Tables

Acronyms

ADR	advection-diffusion-reaction
AMR	adaptive mesh refinement
CSC	cancer stem cell
DCC	differentated cancer cell
ECM	extracellular matrix
EGF	epidermal growth factor
EGFR	epidermal growth factor receptor
EMT	epithelial-mesenchymal transition
EOC	experimental order of convergence
FVFD	finite volume/finite difference
IMEX RK	Implicit-explicit Runge-Kutta
KS	Keller-Segel
MET	mesenchymal-epithelial transition
MMP	matrix metalloproteinase
MTFE	mass-transport finite element
ODE	ordinary differential equation
PAI-1	plasminogen activator inhibitor 1
PDE	partial differential equation
TGF-β	transcription growth factor β
uPA	urokinase plasminogen activator
uPAR	urokinase plasminogen activator receptor
VN	vitronectin

1 Introduction

Despite huge advancements in medication and therapy throughout the last decades, cancer still belongs to the most frequent causes of death in the world. In fact, roughly one person in six dies because of cancer [176]. The severity of this disease, or more precisely of this group of diseases, is not only due to the associated abnormal cell growth, but mostly due to the ability of many cancers to invade the adjacent tissue and to infest distant sites of the body through metastasis [67].

In view of its prevalence and danger, cancer is a very active research topic. Scientists from various disciplines aim to comprehend the mechanisms of cancer and to develop methods for its diagnosis and treatment. Important advances from the past include, for example, the development of chemo- and radiation therapy for cancer treatment and the identification of risk factors such as tobacco use and obesity [174]. Besides classical biomedical approaches that include clinical and experimental studies, mathematical modeling, analysis and simulation are considered as a further scientific pillar that aims to contribute to this field.

Originating rather from physical applications, mathematical models and simulations are recognized today as important tools for the investigation of real world phenomena. Mathematical models have also been widely used to address biological problems for more than a century with rising popularity. To name only a few popular examples, the models were applied to describe population growth in the Malthusian model, to analyze predator-prey animal populations in the Lotka-Volterra model or to understand the occurrence of pattern in nature with the morphogenesis approach by Turing [115, 116, 166, 170].

Good mathematical models are also sought to improve our understanding of cancer. Several important processes in cancer cannot be observed in a tumor patient, not only due to technical limitations but also due to moral issues. Ethical reasons prevent risky experiments with the cancer therapy in the living patient. Here suitable mathematical models along with *in vitro* studies might help to gain new insights. Moreover, a quantitatively accurate model of tumor growth might ultimately assist in the diagnosis by predicting the speed of the growth process.

There exists a plethora of mathematical models of cancer these days. The first of them were developed already in the 1950s [11, 128]. They cover a wide spectrum of cancer related biochemical processes and different types of cancer, see, e.g., [22, 29, 74, 139]. A broad class of these models makes a discrete approach describing the evolution and interaction of isolated cells and molecules, e.g., [23, 142, 167]. Other models, e.g., [155, 177], focus on the intracellular dynamics and protein signaling pathways. As opposed to these microscopic descriptions one can also take a continuum approach and model the temporal evolution of number concentrations of cells and molecules. This is the way of modeling on which we focus in this thesis. The resulting models are commonly based on the Keller-Segel model [90], which describes the collective migration of cells by a system of partial differential equations.

In this work we will solely address the modeling of the invasion of tissue by the cancer cells. Models of this process have been derived and analyzed in the mathematical literature

for approximately two decades. Since the tissue invasion is very complex and innumerable processes on various scales play a role [67], we will consider only a few aspects involved. We will particularly focus on the role of a sub-population of stem-like cells within tumors that was identified only recently and that is now known to play a pivotal role in cancer invasion and metastasis [118].

In addition to the derivation of the model and the conduction and interpretation of numerical experiments, we will deal with its mathematical analysis. Of high interest in this regard is the question of the existence and uniqueness of solutions. In the classical Keller-Segel model the existence of solutions global in time does not hold unconditionally since blowup in finite time occurs in certain situations [125]. Due to the close relation to the Keller-Segel model, the possibility of blowup in macroscopic cancer models should be investigated.

The development of a suitable numerical method is another particular challenge. Due to the characteristics of cancer, the solutions of the cancer invasion models develop heterogeneous spatio-temporal dynamics in the form of merging/emerging clusters of high cancer cell concentrations. Classical methods often fail to resolve these dynamics accurately, i.e. they require unfeasibly high mesh resolutions to obtain acceptable numerical results. If these methods are used together with lower mesh resolutions, the computed solutions will be highly dependent on the employed numerical mesh. We emphasize that the application of such an unsuitable method can render the modeling/simulation process useless since it can result in very inaccurate results for key quantities such as the invasion speed of the tumor, and it can lead to cases where interesting characteristics of the model are hidden behind numerical artifacts.

In this thesis we will consider three models of cancer invasion of Keller-Segel type and study them from a modeling, a numerical and an analytical point of view. The first model (I) was derived in [29] and is well known and accepted in the literature. This model will take the role as a reference for the development of the numerical methods in this work. The second model (II) is a new model which we derived to study the role of cancer stem cells in tumor invasion. In this model we also consider microscopic processes on the level of individual cells which is why the model can be referred to as a multiscale model. It will take the leading role of this work. The third model (III) from [156] takes also the heterogeneity in cancer cell populations into account. It moreover includes nonlinear diffusion and migration terms to account for the varying mobility of the cancer cells. We employ it as a reference for comparison with our new model and to demonstrate the flexibility of our numerical method that can be adapted to this model despite the nonlinearities in the system.

We will analyze the new model (II) analytically in terms of the existence, uniqueness and regularity of solutions. In more detail, we will prove global existence and uniqueness of classical solutions in a slightly simplified version of model (II).

The development of suitable numerical methods is the main part of this thesis. As a first step we will derive second order semi-discrete finite volumes/finite differences for all three considered cancer invasion models. We will discuss and test several strategies for the time discretization, particularly implicit-explicit splitting methods. Albeit these schemes were accurate and efficient in most cases, in certain situations, particularly with model (I), very fine mesh resolution were needed leading to an unsatisfying efficiency. For that reason we go one step further and develop suitable adaptive mesh refinement methods to improve the performance. For the case of a one-dimensional domain, we moreover develop another method, which makes use of a variable transformation. We will demonstrate the advantage of this new method over the implicit-explicit finite volumes/finite differences with and without

mesh adaptation in the case of model (I).

Finally, we will present and discuss numerical experiments in one and two space dimensions. We exhibit, in particular, that the model dynamics of the new model (II) qualitatively coincide with the current understanding of the considered biochemical processes. To gain detailed insight in the role of every model component we will also study the parameter sensitivities of model (II).

Parts of this thesis, which we will indicate, are based on the following journal publications and preprints:

[28] J. A. Carrillo, N. Kolbe and M. Lukácová-Medviďová. A hybrid mass transport finite element method for Keller-Segel type systems. Preprint, `https://arxiv.org/abs/1709.07394`, submitted, Sept. 2017.

[58] J. Giesselmann, N. Kolbe, M. Lukáčová-Medviďová and N. Sfakianakis. Existence and uniqueness of global classical solutions to a two species cancer invasion haptotaxis model. Preprint, `https://arxiv.org/abs/1704.08208`, submitted, Apr. 2017.

[70] N. Hellmann, N. Kolbe and N. Sfakianakis. A mathematical insight in the epithelial-mesenchymal-like transition in cancer cells and its effect in the invasion of the extracellular matrix. *Bull. Braz. Math. Soc.*, 47(1):397–412, 2016.

[96] N. Kolbe, J. Kat'uchová, N. Sfakianakis, N. Hellmann and M. Lukáčová-Medviďová. A study on time discretization and adaptive mesh refinement methods for the simulation of cancer invasion : The urokinase model. *Appl. Math. Comput.*, 273:353–376, 2016.

[98] N. Kolbe, M. Lukáčová-Medviďová, N. Sfakianakis and B. Wiebe. Numerical simulation of a contractivity based multiscale cancer invasion model. In A. Gerisch, R. Penta and J. Lang, editors, *Multiscale Models in Mechano and Tumor Biology: Modeling, Homogenization, and Applications*. Springer, to appear 2017.

[99] N. Kolbe and N. Sfakianakis. A flexible multidimensional rectangular mesh administration and refinement technique with application in cancer invasion models. Preprint, `https://arxiv.org/abs/1706.06191`, 2016.

[151] N. Sfakianakis, N. Kolbe, N. Hellmann and M. Lukáčová-Medviďová. A Multiscale Approach to the Migration of Cancer Stem Cells: Mathematical Modelling and Simulations. *Bull. Math. Biol.*, 79(1):209–235, 2017.

The thesis is organized as follows: Chapter 2 starts with an introduction about basics from cancer biology and elementary population and density modeling. The rest of the second chapter then describes the derivation of the three cancer invasion models, with a focus on the new model (II). Having set forth necessary mathematical prerequisites in Chapter 3, we review in Chapter 4 some analytical properties of the Keller-Segel model on the one hand and the previous literature on existence analysis in cancer invasion models on the other hand. Afterwards uniqueness and global existence of solutions for a two cancer species model similar to (II) is proven. The fifth chapter is devoted to the construction of finite volumes/finite differences for the considered models with suitable implicit-explicit time discretization. Here we also prove the positivity preserving property of the method in the case of model (II), we discuss additional techniques that we apply to deal with the nonlinearities in model (III) and we compare several time integration schemes in first numerical experiments with model (I). In Chapter 6 we motivate, construct and test adaptive mesh refinement methods for cancer invasion models in one and two space dimensions. Afterwards in Chapter 7 we introduce a new 1D method that operates on inverse cumulative distributions instead of using the

density representation. We will present not only generic numerical experiments with the Keller-Segel model but also experiments with model (I) and a comparison with the other numerical methods considered in this work. In Chapter 8 we exhibit numerical experiments and parameter studies with model (III) and, most prominently, with the new model (II). We conclude in Chapter 9 and provide technical details on the numerical experiments in Appendix A.

2 Modeling

In this chapter we introduce mathematical models of cancer invasion. We derive, in particular, a multiscale invasion model that incorporates the epithelial-mesenchymal transition in heterogeneous cancer cell populations. This model constitutes the chief subject of this thesis but we will also discuss further models of this kind. The study of these models both analytically and numerically will be addressed in the following chapters.

To start with we provide in Section 2.1 a short overview of some aspects of cancer that will play a role in the modeling. Afterwards, we introduce the common models for basic biological processes such as cell kinetic, chemical diffusion and taxis in Sections 2.2–2.4. In Section 2.5 we briefly review the common approaches in cancer invasion modeling. Then we dive into more detail in the modeling of cancer processes and focus on the particular role of the urokinase-type plasminogen activator system in Section 2.6, the epithelial-mesenchymal transition in cancer cells in Section 2.7–2.9 and cellular receptors and contractivity in Section 2.10. For clarity we will build up the models gradually and consider the crucial modeling steps one at a time.

The modeling techniques we consider in Sections 2.2–2.4 are well known and discussed in the textbooks [22, 122, 123] in more detail.

2.1 Tumors, invasion of the tissue and the epithelial-mesenchymal transition

In this section we introduce several fundamentals from cancer biology. Due to the complexity of the matter, we do not intend to give a comprehensive review but rather to provide an overview and selected information that will play a role in the model derivation in the later course of this chapter.

The term *tumor* refers to a cell population that got out of control [174]. The affected cells exhibit, among other characteristics, abnormal cell growth and resistance to programmed cell death (*apoptosis*) [67]. Tumors can be categorized as being either benign or malignant. *Benign* tumors have the potential to grow large, but they stay localized at the place where they emerged without intruding the adjacent tissue [2]. Often they are either harmless and do not require any treatment or they can be cured, mostly by surgical removal [30]. In some cases though they can evolve and become malignant, a process that is referred to as *tumor progression* [174]. *Malignant* or cancerous tumors, which interest us in this thesis, are by far more dangerous for the patient. They can invade the surrounding tissue and infiltrate remote sites of the body through metastasis. Malignant and particularly metastatic tumors cause roughly 90% of human cancer deaths [153].

Most malignant tumors in human arise from *epithelial* cells, which line bodily channels like, for example, blood vessels and form the outer cellular layer of organs [146]. These epithelial

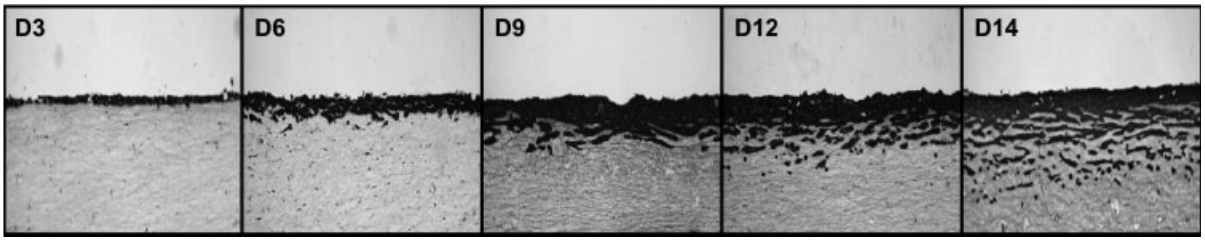

Figure 2.1: Temporal progression of cancer invasion *in vitro*: carcinoma cells invade a collagen gel containing human fibroblasts. The cultures were fixed after 3, 6, 9, 12 and 14 days and processed to paraffin blocks. Immunostaining for cytokeratins was used. Each image shows an excerpt of the culture of 2.4 mm width. From [129]. Copyright © 2005 by Pathological Society of Great Britain and Ireland. Reprinted by permission of John Wiley & Sons, Inc.

cancers are termed *carcinoma* and they will constitute the subject of our studies. Note that other tumors which originate for example from blood cells or from neural cells exhibit similar characteristics [174].

The invasion of the *extracellular matrix* (ECM) by the malignant cancer cells is considered the first step in tumor metastasis [67]. This process involves many bio-chemical processes such as paracrine and autocrine cell-cell signaling and the activation of proteolytic enzymes [160]. A crucial role is played by *chemokines* which are signaling proteins that, among others, trigger the migration of the cancer cells, a key factor in invasion and metastasis [145]. An example of a chemokine is CXCL12 which was found in cancerous, but not in normal, epithelial breast cells [178]. Cell migration along the directions of either extracellular adhesion sites (*haptotaxis*) or directions of chemical substances involved in the proteolysis process (*chemotaxis*) are believed to be of particular importance in the local invasion of the tumor [29]. Both chemo- and haptotaxis are associated with complex biochemical reactions inside the cell and a remodeling of the *cytoskeleton*, the skeleton of the cell [108]. See also [117] for a mathematical model of cell migration on the microscopic level.

The invasion in carcinoma starts with the breaching of the basement membrane between the cancerous epithelium and the *stroma* which consists of connective and structural tissue [174]. The basement membrane is invaded by degradation of its protein constituents (*proteolysis*) [146]. Also, proteolysis is an essential step for the migration of cancer cells since the intact ECM is a tight net, composed of various proteins, which offers only small pores for the cells to move through [96]. Some proteins that are involved in the proteolytic process belong to the family of *matrix metalloproteinase*s (MMPs), others include, e.g., the serine proteases [92]. The proteolytic proteins are activated either directly by the tumor cells or indirectly by tumor associated inflammatory cells via enzymatic pathways [92, 173, 174]. An example of such a pathway is the urokinase plasminogen activation system that we will investigate further in Section 2.6.

Not only the degradation of the ECM is enhanced in the microenvironment of invading and metastasizing tumors but also the ECM remodeling [39]. A pivotal role in this remodeling is played by *fibroblasts* which were found in increased numbers in the cellular environment of the tumor [16].

Figure 2.1 shows a study of tumor invasion in squamous carcinoma cells in an *in vitro* model from [129]. Apparently, the invasion of the tumor leads to a spatially heterogeneous distribution of cancer cells in the gel imitating the human tissue. In more detail, the cancer cells form clusters that gradually invade and spread over the gel. A similar phenomenon can be seen in Figure 2.2 which shows a melanoma in a tissue sample of a patient. *Melanomas* are

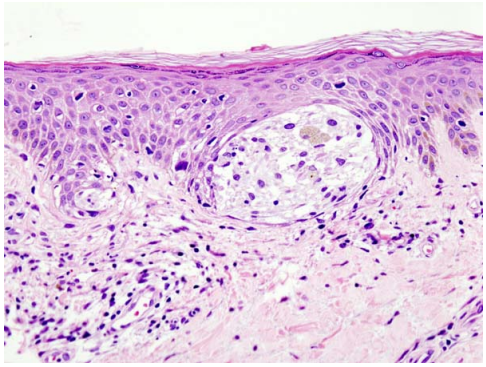

Figure 2.2: H & E stain of a patient tissue sample showing a malignant melanoma. From librepathology.org, licensed under the Creative Commons BY-SA 3.0 license (creativecommons.org/licenses/by-sa/3.0/).

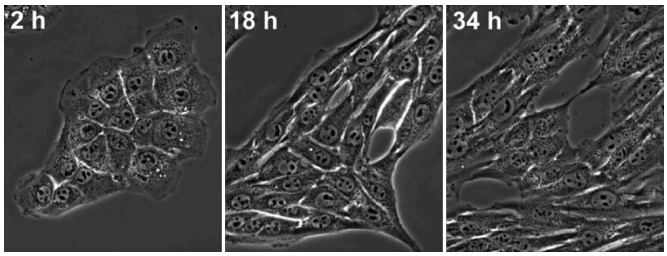

Figure 2.3: EMT in mammary epithelial mouse cells induced by TGF-β *in vitro*. The images were obtained by phase contrast time-lapse microscopy. The changes in the cell morphology are shown after 2, 18 and 34 hours. The cells elongate and loose the cell-cell contact to their neighbors. Modified from [69], licensed under the Creative Commons BY-NC-SA 3.0 license (creativecommons.org/licenses/by-nc-sa/3.0/).

tumors that arise from melanocyte cells which are mostly located in the skin. The *hematoxylin and eosin* (H & E) stain that was used here identifies tumor cells by dark blueish points while dead cells are stained in pink [62]. In this sample the main tumor forms "fingers" that penetrate the extracellular space and isolated clusters of tumor cells invade the tissue.

As the invading cancer cells have reached the vascular system the cells may initiate *metastasis* and afflict secondary sites of the body through *intra-* and *extravasation*, i.e. entering and escaping from a blood vessel [146]. Only few tumor cells survive the transport through the bloodstream, but once a tumor cell extravasates successfully it continues to proliferate and possibly engenders a secondary tumor [174].

There is only a small subpopulation within the tumor, consisting of so-called *cancer stem cell*s (CSCs), which possesses the ability to metastasize [65, 143]. These CSCs have further properties that are similar to the traits of *mesenchymal stem cells* and include the capability for cell differentiation, lower proliferation and higher motility [87, 143]. These properties distinct the CSCs from the more common *differentated cancer cell*s (DCCs) which make up the bulk of the tumor [86].

The CSCs were found in human acute myeloid leukemia and tumors in, e.g., breast, brain and skin [48]. The cell differentiation of the CSCs is moreover related to the presence of fibroblasts in the tumor microenvironment [89].

Current literature supports that the CSCs emanate from the DCCs after the activation of a de-differentiation program known as the *epithelial-mesenchymal transition* (EMT) [65, 87]. This program is also known to be active in wound healing and embryogenesis [118]. The stromal micro-environment of the tumor cells is responsible for the activation of the EMT in the DCCs [141]. Of particular importance seem to be growth factor enzymes such as the *epidermal growth factor* (EGF) or the *transcription growth factor* β (TGF-β), as current evidence suggests [69, 152, 171].

The protein EGF, for example, binds to *epidermal growth factor receptor* (EGFR) on the cancer cell and triggers a signal cascade that promotes unregulated cell growth and eventually alterations in the cancer cell genome associated with the EMT [14, 107, 148]. The role of EGFR in tumors was also studied in [54] where its over-expression was connected to a bad prognosis

in breast cancer due to associated stronger proliferation and migration capabilities of the tumor cells. The considered growth factors are further involved in the inverse program to the EMT, i.e. the *mesenchymal-epithelial transition* (MET), that is active once a CSC has completed the metastatic cycle and established a new colony of cancer cells [89, 174].

Figure 2.3 shows the changes in the cell morphology caused by the EMT in an *in vitro* model from [69]. The authors induced the EMT in epithelial mice cell using TGF-β. While the epithelial cells are initially arranged in adherent tiers, the cell-cell adhesion break as the cells acquire the mesenchymal gene expression by the EMT. Moreover, the cytoskeleton of the cells reorganizes and the cells elongate. It is evident that these changes in the cells have enhanced their motility.

2.2 A macroscopic modeling approach

In the continuum approach that we discuss in this section we describe the temporal evolution of a *state variable* w. To this end we consider a domain $\Omega \subset \mathbb{R}^d$ with smooth boundary and *space dimension* $d \in \{1, 2, 3\}$. We assume that the variable $w(x, t)$ maps a point $x \in \Omega$ and an instance in time $t \geqslant 0$ to the *number concentration* of a substance or cell of interest. More specifically, we let w denote a measure of *particles per volume*. The term "particles" refers here to either molecules or cells. By volume on the other hand we denote the Lebesgue Measure or d-volume in Ω.

The number of microscopic particles can be comfortably measured in *mole*,

$$1\,\mathrm{mol} = N_A \approx 6.022 \times 10^{23},$$

where N_A is known as Avogadro's number [82]. In this case, w technically becomes a *molar concentration*. If we endow the concentration measure in $\Omega \subset \mathbb{R}^3$ with the unit dm^3, we can measure the state variable in the common unit *molar*, where

$$[w] = \mathrm{molar} = \mathrm{mol}\,\mathrm{dm}^{-3}.$$

For our purposes though we do not restrict ourselves to molar concentrations in space dimension $d = 3$ but instead consider a general domain Ω of any dimension $d \in \{1, 2, 3\}$ and a (number) concentration w given on this domain. For simplicity we follow the common mathematical convention and use the terms concentration and *density* indistinguishably.

In what follows we describe the general macroscopic modeling approach that we adapt in this thesis. Let V be an arbitrary and time independent volume in Ω enclosed by its boundary ∂V. The principle of conservation of matter dictates that the amount of particles in V after a time period Δt changes only due to creation and decay of particles inside V and due to particles that enter or leave the volume V. This results in the equation

$$\int_V w(x, t+\Delta t)\,dx - \int_V w(x, t)\,dx = \underbrace{-\int_t^{t+\Delta t}\int_{\partial V} \nu(x)\cdot \mathbf{J}(w, x, t)\,dx\,dt}_{\text{Entering particles} - \text{leaving particles}} + \underbrace{\int_t^{t+\Delta t}\int_V S(w, x, t)\,dx\,dt}_{\text{Created particles} - \text{destroyed paricles}}. \tag{2.1}$$

In the above formula we have used the *source term* $S(w, x, t)$ that we define to be the net rate of created particles per unit volume and unit time. The vector valued function $\mathbf{J}(w, x, t)$ denotes the *flux* which is the rate of crossing particles per surface and time unit. It can be defined as follows: for $\Delta S, \Delta\tau > 0$ let $T_i^{\Delta S, \Delta\tau}(w, x, t)$ be the net amount of particles corresponding to w that cross a small surface element

$$\bigtimes_{j=1}^{d} [x_j, x_j + (1 - \delta_{ij})\Delta S] \ni x$$

of dimension $d - 1$ perpendicular in positive x_i direction during $[t, t + \Delta\tau]$. Here δ_{ij} is either 1 if $i = j$ or 0 otherwise. The components of the flux function are given as the limit

$$[\mathbf{J}(w, x, t)]_i = \lim_{\Delta S, \Delta\tau \to 0} \frac{T_i^{\Delta S, \Delta\tau}(w, x, t)}{\Delta t\, \Delta S^{d-1}}, \quad i = 1, \ldots, d. \tag{2.2}$$

For the further derivation we assume that both source term S and flux $\mathbf{J}$ are sufficiently smooth.

By dividing (2.1) by Δt and using the mean value theorem on the right hand side, a Taylor expansion in t on both sides and finally taking the limit as $\Delta t \to 0$, we get

$$\int_V \partial_t w \, dx = -\int_{\partial V} \nu \cdot \mathbf{J}(w, x, t) \, dx + \int_V S(w, x, t) \, dx.$$

In the next step we apply the divergence theorem and obtain

$$\int_V \partial_t w + \nabla \cdot \mathbf{J}(w, x, t) - S(w, x, t) \, dx = 0, \tag{2.3}$$

where the *divergence operator* is given by

$$\nabla \cdot \mathbf{f} = \sum_{i=1}^{d} \frac{\partial f_i}{\partial x_i}, \quad \mathbf{f} = (f_1, \ldots, f_d)^T \in C^1(\Omega, \mathbb{R}^d).$$

By the continuity of the integrand in (2.3) and the arbitrary choice of $V \subseteq \Omega$ we can drop the integral. Thus, we end up with a so-called *balance law* of the form

$$\partial_t w + \nabla \cdot \mathbf{J} = S, \quad x \in \Omega. \tag{2.4}$$

These types of *partial differential equation*s (PDEs) constitute the general form of macroscopic models we consider in this thesis. The above discussion can be extended to a vector valued state variable

$$\mathbf{w} = (w_1, \ldots, w_n)^T$$

by following the derivation for each biological or chemical *species* w_i where $i = 1, \ldots, n$. In this process we end up with the following *system of balance laws*

$$\partial_t w_i + \nabla \cdot \mathbf{J}_i(\mathbf{w}, x, t) = S_i(\mathbf{w}, x, t), \quad i = 1, \ldots, n, \quad x \in \Omega. \tag{2.5}$$

Note that here the flux and the source term $\mathbf{J}_i$, S_i of a species w_i might depend on other species w_j. We will deal mostly with *autonomous* systems, i.e. we use flux and source terms that are time and space invariant, i.e.

$$\partial_t w_i = S_i(\mathbf{w}) - \nabla \cdot \mathbf{J}_i(\mathbf{w}), \quad i = 1, \ldots, n, \quad x \in \Omega. \tag{2.6}$$

We will moreover focus on the *deterministic* case of system (2.5) that does neither allow for random deviations in the parameters included nor does it allow for any other stochastic terms.

For some discussions that follow we need to introduce the terms steady state and linear stability and clarify their meaning.

Definition 2.1 A state $\mathbf{w} : \Omega^d \to \mathbb{R}^n$ of system (2.6) is called *steady state* if and only if

$$\nabla \cdot \mathbf{J}_i(\mathbf{w}(x)) = S_i(\mathbf{w}(x)) \quad i = 1, \dots, n, \quad x \in \Omega.$$

Definition 2.2 Consider a steady state $\mathbf{w}$ of system (2.6). The state is called *linearly stable*, if for a linearization of (2.6) of the form

$$\partial_t \tilde{\mathbf{w}} = L(\mathbf{w})\tilde{\mathbf{w}} + \mathcal{O}(\tilde{\mathbf{w}}), \tag{2.7}$$

where $\mathbf{w} = \hat{\mathbf{w}} + \tilde{\mathbf{w}}$ denotes a perturbed state the *Jacobian matrix* $L(\mathbf{w})$ is negative definite.

A linearly stable steady state $\mathbf{w}$ is also called *attractive*. This is because one can show that for a neighborhood U around $\mathbf{w}$, system (2.6) converges to the steady state $\mathbf{w}$ for any initial datum $\mathbf{w}(\cdot, 0) = \mathbf{w}_0 \in U$ and $t \to \infty$ [35].

2.3 Interactions of cells and chemical substances

In this section we take a closer look to the source term in (2.4). Let us therefore assume that no translocation of particles occurs, i.e. $\mathbf{J} \equiv 0$. Thus, we can neglect the space dependence in (2.5) and it suffices to consider a single point in space. The conservation of matter used in (2.1) leads here to an *ordinary differential equation* (ODE) or to a system of ODEs in the case of multiple species. Due to the independence on the spatial domain we will discuss populations (0D concentrations) in this section. All models and their properties transfer to general concentrations in higher space dimensions.

Cell population models

Let $w(t)$ be the population size of a cell species at time t and $w(0) = w_0 > 0$ the population size at time instance $t = 0$. The population dynamic can be modeled very easily by the *Malthusian* model

$$\partial_t w = bw - dw \tag{2.8}$$

with given birth and death rates $b,\ d \geqslant 0$ [116]. After solving the differential equation, we obtain

$$w(t) = w_0 e^{(b-d)t}$$

and the model predictions become evident: if the birth rate is dominant, i.e. $b > d$, the cell population grows exponentially without a limit. If on the other hand $d > b$ then the population dies out. This is a useful approach as long as w does not exceed an amount, where the environment (e.g., limited resources such as nutrients or space) interferes with the population growth.

The *logistic growth* model by Verhulst [169] takes the limitations by the environment into account and reads

$$\partial_t w = \mu w \left(1 - \frac{w}{w_c}\right). \tag{2.9}$$

We assume here a given *proliferation rate* $\mu > 0$. The second degree of freedom in (2.9) is the *carrying capacity* $w_c > 0$, which is an attracting steady-state of the system. In fact, the solution of (2.9) can be computed by separation of variables and yields the *logistic function*

$$w(t) = \frac{w_c\, w_0 e^{\mu t}}{w_0[e^{\mu t} - 1] + w_c}. \tag{2.10}$$

We can see that $\lim_{t\to\infty} w(t) = w_c$ and the system describes a monotonic growth up to the carrying capacity for $w_0 < w_c$. In the converse case $w_0 > w_c$ the state variable (2.9) decreases monotonically.

Note that in certain modeling applications such as cancer cell proliferation this decrease is not wanted. This is because it implies cell *apoptosis* (programmed cell death) that does not occur in the (immortal) cancer cells. Here one can instead use the *positive logistic growth model*

$$\partial_t w = \mu w \left(1 - \frac{w}{w_c}\right)^+, \tag{2.11}$$

where $f^+ = \max\{0, f\}$. In this model the limited amount of resources make the growth of the population stagnate but does not lead to a reduction of the population.

Often the carrying capacity of a species is used for the rescaling of the system. In more detail, let us consider $\tilde{w} = w/w_c$, which is unit-less. By dividing (2.9) by w_c, we obtain

$$\partial_t \tilde{w} = \mu \tilde{w}(1 - \tilde{w}). \tag{2.12}$$

We will discuss the rescaling thoroughly in an example in Section 2.9.

We emphasize that the carrying capacity, as we use it in this thesis, should be understood as the maximal concentration up to which a species is able to reproduce itself. It should not be seen as a maximal concentration or a fixed point of the system. This is especially true since we employ the (positive) logistic growth as only one of the components of a complex model.

Competition between species We consider $\mathbf{w}(t)$ to be a vector of populations of n cell species at time t and $\mathbf{w}(0) = \mathbf{w}_0 \geqslant 0$. A classical model for the population dynamics of n species is the *Lotka-Volterra model* given by

$$\partial_t w_i = \alpha_i w_i - w_i \sum_{i=1}^{n} \beta_{ij} w_j, \quad i = 1, \ldots, n, \tag{2.13}$$

where α_i is the growth rate of the species i and β_{ij} is a coefficient that takes the competition between the species i and j into account [115, 170]. These models were derived 1925/1926 and they have their major application in describing predator-prey animal populations [22]. For our purposes though, the direct competition between two cell species is hard to describe. This is particularly the case since we do not consider cells attacking each other, which would happen, e.g., in the immune system. We consider the competition between the cells only due to limited resources.

Similar to (2.9) we model this process by

$$\partial_t w_i = \mu_i w_i \left(1 - \sum_{j=1}^{n} \frac{w_j}{w_j^c}\right) \tag{2.14}$$

using again proliferation rates $\mu_i > 0$ and carrying capacities $w_j^c \geqslant 1$ for $1 \leqslant i \leqslant n$. The quantity

$$R(\mathbf{w}) = 1 - \sum_{j=1}^{n} \frac{w_j}{w_j^c} \tag{2.15}$$

accounts for the remaining available resources necessary for reproduction. Here we make the assumption that w_j^c cells of species j require roughly the same amount of resources as w_k^c cells of species k for $1 \leqslant j, k \leqslant n$. In the growth model (2.14) each state of the hyperplane

$$\left\{ \mathbf{v} \in \mathbb{R}^n_+, \quad \sum_{i=1}^{n} \frac{v_i}{w_j^c} = 1 \right\} \ni \mathbf{w}$$

is an attracting steady state since for all $0 \neq \mathbf{v} \in \mathbb{R}^n$ and the Jacobian J of (2.14) we have

$$v^T J v = -\left(\sum_{i=1}^{n} \frac{\mu_i w_i v_i}{w_i^c}\right)\left(\sum_{i=1}^{n} \frac{v_i}{w_i^c}\right) < -\min_{1 \leqslant i \leqslant n} \mu_i w_i \, |v|^2 \leqslant 0.$$

Note that this approach can also take the restriction of resources due to extracellular space into account by introducing a variable w_j to system (2.14) (with $\mu_j = 0$) that accounts for the density of the extracellular matrix.

Analog to the single cell case, we can also consider positive logistic growth for multiple species by

$$\partial_t w_i = \mu_i w_i \left(1 - \sum_{j=1}^{n} \frac{w_j}{w_j^c}\right)^+. \tag{2.16}$$

When applying this approach to cancer cells, apoptosis is excluded from the model to account for the immortality of cancer cells as in (2.11).

One can further generalize the resource functions by considering the case of species that favor different resources. This can be reflected by considering weighted resource functions of the type

$$R_i(\mathbf{w}) = 1 - \sum_{j=1}^{n} \eta_{ij} \frac{w_j}{w_j^c}, \quad i = 1, \ldots, n, \tag{2.17}$$

which is to be combined either with the logistic model (2.14) or the positive logistic model (2.16).

Mass action kinetics *Biochemical kinetics* describe the temporal evolution of chemical substances by interactions with each other. These kinetics play a crucial role in biological systems where chemical reactions in proteins and receptors are considered. Of particular importance is the process of *catalysis* in which a catalytic enzyme increases the rate of a chemical reaction significantly without being consumed in the reaction process.

In this work we will apply the *law of mass action* which states that the reaction

$$S_1 + S_2 \xrightarrow{k} S_3,$$

where the substances S_1 and S_2 react with each other to produce substance S_3 with *rate constant* $k > 0$, results in the ODE system

$$\partial_t S_1 = -kS_1 S_2, \quad \partial_t S_2 = -kS_1 S_2, \quad \partial_t S_3 = kS_1 S_2.$$

Here, by abuse of notation, S_1, S_2 and S_3 also denote the concentrations of the chemical substances S_1, S_2 and S_3. Multiple reactions add up in the ODE equations. For example, the two coupled reactions

$$S_1 + S_2 \xrightarrow{k_1} S_3 \xrightarrow{k_2} S_1 + S_4$$

result in the system

$$\begin{cases} \partial_t S_1 = -k_1 S_1 S_2 + k_2 S_3, & \partial_t S_2 = -k_1 S_1 S_2, \\ \partial_t S_3 = k_1 S_1 S_2 - k_2 S_1 S_4, & \partial_t S_4 = k_2 S_3. \end{cases} \tag{2.18}$$

Note that there can be significant differences in reaction time scales when considering large biological systems that include many chemical reactions. For that reason only the equilibrium state of a system like (2.18) is considered in some cases of fast reactions.

Production rates In many biochemical systems the production of chemical substances by cells as well as the interaction of cells with these substances play important roles. Cells can, e.g., emit proteins which regulate cell-cell communication. Moreover, certain proteins can provoke reactions inside cells that promote cell proliferation. Such reactions are triggered by the attachment of the protein to a cell receptor that initiates a cascade of reactions inside the cell. To exhibit the modeling of these dynamics we consider as example the toy system

$$\partial_t c_1 = \mu c_1 s, \quad \partial_t c_2 = 0, \quad \partial_t s = \alpha c_2 - \beta c_1 s \tag{2.19}$$

with constant rates $\mu, \alpha, \beta > 0$. In (2.19) the cell species with concentration c_2, whose density does not change in time, produces a protein with concentration denoted by s with production rate α. This protein attaches to receptors on the cells of another species with density c_1. The protein-receptor compound triggers a proliferation-promoting reaction in c_1, and the compound is evacuated from the cell and does not play a further role in the dynamics. Altogether the coefficient μ includes here the number of relevant receptors per cell c_1, the probability of the binding of a protein molecule with a cell receptor and the effect of the reaction.

2.4 Movement of cells and chemical substances

In this section we examine several types of particle movement. To this end we consider the general balance law (2.4) on a domain of space dimension $d \in \{1, 2, 3\}$ without production or destruction of particles, i.e. $S \equiv 0$. We assume sufficient smoothness of the function w and augment (2.4) with the *initial condition*

$$w(x, 0) = w_0(x), \quad x \in \Omega. \tag{2.20}$$

Advection Firstly, we consider the *advection flux*, which is given by

$$\mathbf{J} = \mathbf{a}w. \tag{2.21}$$

The corresponding PDE (2.4) together with (2.21) is the common model for bulk motion of the particles with density denoted by w. In this model the *velocity vector* $\mathbf{a}$ points to the direction of the movement. Further, the rate (per time and surface element) of particles crossing a test surface perpendicular to $\mathbf{a}$ is equal to $|\mathbf{a}|$. The case of a constant velocity turns (2.4) into

$$\partial_t w + \mathbf{a}\nabla w = 0, \tag{2.22}$$

which is known as the *linear transport equation*.

Random motion To a certain extent, all cells and molecules move randomly. The phenomenon that one observes, when individual random movement of many particles on the microscopic level results in a macroscopic structured motion is characterized as *diffusion*. For that reason the diffusion flux that describes this process in a continuum model can be derived from a random walk of particles on a latter in discrete time, see, e.g., [123]. The corresponding flux description is known as *Fick's Law of diffusion* and reads

$$\mathbf{J} = -D\nabla w, \tag{2.23}$$

where $D > 0$ is called the *diffusion coefficient*. In the case of *linear diffusion* this coefficient depends only on the constant probability with which an individual particle jumps to an adjacent position. The isolated linear diffusion of a single concentration w results, for instance, in the *heat equation* $\partial_t w = D\Delta w$ where the *Laplace operator* Δ is defined as

$$\Delta w = \sum_{i=1}^{d} \frac{\partial^2 w}{\partial x_i^2}.$$

In this work we will also consider *nonlinear diffusion* where the coefficient D in (2.23) depends on time, space or the state w. We can understand these generalized coefficients as a dependence of the jump probabilities on the medium or on other localized influences.

Taxis In large part the movement of cells is determined by stimuli in their environment. Having sensed its surroundings, a cell might respond by moving towards an external signal or in the opposite direction. In this work we focus in this regard on chemotaxis that refers to migration triggered by a chemical substance and on haptotaxis in which an adhesive side promotes the movement.

Consider a two equation system of type (2.6) and a state vector $\mathbf{w} = (c, a)^T$ that includes the concentration of cells c and the concentration of an attracting species a. Then the taxis flux is defined as an advection flux with the velocity vector given proportional to the gradient of the density of the attracting species. Hence, the movement of the cells is towards (or against) higher densities of the attracting species and the velocity increases with the magnitude of the gradient. The corresponding flux description reads

$$\mathbf{J} = \chi\, c\, \nabla a, \tag{2.24}$$

where we note that the *tactic sensitivity* χ can be positive or negative, depending on the attracting species being attractive or repulsive. Furthermore, the sensitivity χ can be space,

time and state dependent. Similarly to the case of cellular diffusion, biased cell movement, where the flux consists of a sum of taxis (2.24) and cellular diffusion (2.23), can be derived from the microscopic level by considering biased random walks of individual cells, see [154].

A well known application that makes use of this approach is the *Keller-Segel model* [90]. Here c models the concentration of the single cell slime mold *Dictyostelium discoideum* that produces the chemo-attracting substance cyclic adenosine monophosphate (cAMP) a by the PDE system

$$\begin{cases} \partial_t c = \nabla \cdot (D_c \nabla c - \chi c \nabla a), \\ \partial_t a = D_a \Delta a + \alpha c - \beta a \end{cases} \tag{2.25}$$

with positive parameters $D_c,\ D_a,\ \chi,\ \alpha,\ \beta > 0$. System (2.25) and similar models have been of high mathematical interest since their derivation. We will investigate the reason for this in Chapter 4.

Boundary conditions To close system (2.4) in the case of a bounded domain $\Omega \subset \mathbb{R}^d$ and make it thus suitable for further analysis and numerical simulations, we require *boundary conditions*. In this work we employ *homogeneous Neumann* conditions

$$\partial_\nu w_i = \nu(x) \cdot \nabla w_i = 0, \quad x \in \partial\Omega, \quad i = 1, \dots, n, \tag{2.26}$$

where $\nu(x)$ denotes the outer normal vector of Ω in $x \in \partial\Omega$. In the systems that we consider in this work condition (2.26) implies

$$\nu(x) \cdot \mathbf{J}_i(\cdot, x, \cdot) = 0, \quad x \in \partial\Omega. \tag{2.27}$$

Thus, condition (2.26) does not let any particles move out of the domain, from a modeling perspective. In simulations that reproduce *in vitro* experiments the boundaries of the domain can be understood as margins of a petri dish. In reproductions of *in vivo* tumors the domain boundaries can be associated with bone or hard tissue.

2.5 Classical models of cancer invasion

Chemo- and haptotaxis systems of *Keller-Segel* (KS) type such as (2.25) were applied in a wide range of biological phenomena spanning from bacterial aggregations to wound healing. A particular application is the modeling of cancer growth and the invasion of the ECM. The latter subject has been of high interest in mathematical modeling for the last two decades, see, e.g., [8, 9, 51, 57, 133, 136, 137, 159, 167].

In what follows we will describe the common modeling in cancer invasion by following the approach in [8]. Let us consider the concentrations of cancer cells, of the ECM and of an MMP enzyme that we denote by c, v, and m, respectively. The ECM consists of macro-molecules such as, e.g., collagen, fibronectin and vitronectin. The protein vitronectin, in particular, is responsible for the attachment of the cells to the ECM and binds to the transmembrane proteins (*integrins*) that sense for cell adhesions with the substrate and transduce signals from the outside to the inside of the cell [40]. From a macroscopic point of view, we assume the ECM to be a static biochemically homogeneous compound of all of its constituents and consider v to be the corresponding concentration.

The first invasion model we consider describes the interactions between the tumor cells, the ECM and the MMPs and is given by

$$\begin{cases} \partial_t c = \nabla \cdot (D_c \nabla c - \chi c \nabla a), \\ \partial_t v = -\delta v m, \\ \partial_t m = D_m \Delta m + \alpha c - \beta m \end{cases} \tag{2.28}$$

for constant parameters $D_c,\ \chi,\ \delta,\ D_m,\ \mu,\ \beta > 0$. In this model the tumor cells move randomly and follow the haptotactic gradient of the ECM. The second equation describes the evolution of the ECM. It is degraded upon contact with the MMPS. Although the matrix degradation is a complicated biophysical process, we model it in simplification as a chemical reaction between MMPs and tissue molecules and follow formal mass action kinetics corresponding to the reaction equation

$$V + M \to M.$$

Here V and M denote tissue and MMP proteins. The MMPs, with temporal evolution modeled in the third equation of (2.28), undergo molecular diffusion. We assume that they are produced by the tumor cells with rate α and that they decay with rate β.

In the original paper [8] numerical simulations of model (2.28) in 1- and 2D already withstood a qualitative comparison with medical images. This haptotaxis model was subjected to various modeling extensions.

In further modeling approaches, for example, in [9, 136] the authors assume that the chemotaxis of the tumor cells has another impact on the invasion of the tumor. Let us exemplarily consider the model from [30] reading

$$\begin{cases} \partial_t c = \nabla \cdot (D_c \nabla c - \chi_v c \nabla v - \chi_m c \nabla m) + \mu_1\, c(1 - c - v), \\ \partial_t v = -\delta m v + \mu_2 v(1 - c - v), \\ \partial_t m = D_m \Delta m + \alpha c - \beta m \end{cases} \tag{2.29}$$

with motility parameters $D_c,\ \chi_v,\ \chi_m\ D_m > 0$ and growth/decay rates $\mu_1, \mu_2, \delta,\ \alpha,\ \beta > 0$. In comparison to model (2.28), the present system models an additional chemotactic movement of the tumor cells towards the MMPs. Moreover, logistic growth terms that account for the competition of resources between the cancer cells and the extracellular material as in (2.14) are added to the evolution equations of the tumor cell concentration and the vitronectin concentration. These terms model cell proliferation and tissue remodeling. Note that due to the possible negativity of the growth rate $(1 - c - v)$, death of cancer cell as well as ECM degradation due to resource limitation is included in model (2.29).

Simulations with (2.29) in [30] revealed rich spatio-temporal dynamics that involve the formation and movement of tumor cell clusters which are characteristic in the invasion process.

2.6 The urokinase system

A further cancer invasion model that we consider in this section was first proposed in [29] and further studied in [7, 30, 56, 57, 97, 159]. In addition to chemotactically and haptotactically driven motility and diffusion, it takes the urokinase plasminogen activation system into account. This enzymatic system is crucial in angiogenesis, ECM protein synthesis, as well as in tissue invasion. It gives rise to supplementary enzyme interactions complementing the modeling of cancer invasion as done in Section 2.5. This section is based on the modeling part of our paper [96].

The uPA system The protein *urokinase plasminogen activator* (uPA) and its inhibitors are important chemokines in tumor progression and metastasis. The uPA, in particular, is an extracellular serine protease which is responsible for the activation of plasminogen, the inactive form of the protease plasmin (P) which is produced by the liver and which is omnipresent in the extracellular space. UPAs precurser pro-uPA in turn is activated by plasmin.

The activation of plasminogen to plasmin occurs mainly if uPA is bound to *urokinase plasminogen activator receptor*s (uPARs) on the cell membrane. The receptor bound uPA moreover enhances the affinity of uPAR to the ECM constituent *vitronectin* (VN) [173] and integrins. Hence, the uPA/uPAR-complex indirectly regulates the vitronectin-integrin interactions. Both proteases plasmin and uPA catalyze the degradation of vitronectin, collagens and other ECM components and therefore degrade the tissue.

Plasminogen activator inhibitors are produced by the cells. They control and limit the activation of plasminogen to prevent tissue damage and to maintain homeostasis. We consider, in particular, the *plasminogen activator inhibitor 1* (PAI-1), which is the fastest operating inhibitor in the system [10]. It inhibits the proteolytic function of uPA upon binding on both the soluble and the membrane-bound form. After binding the full complex uPAR/uPA/PAI-1 is removed from the cell surface by endocytosis. PAI-1 also binds to vitronectin, which impedes cell-signaling and the formation cell-ECM contacts [149].

The model The considered model from [29] employs the following components: the cancer cells with density c, the ECM component vitronectin with concentration v and uPA, PAI-1 and plasmin with densities denoted by u, p and m, respectively. The model does not distinguish between uPA and pro-uPA and the concentration of uPARs is assumed proportional to the cancer cell concentration c.

The uPA system extends the cancer invasion models (2.28) and (2.29) and includes roughly the reactions

$$\text{uPA} + \text{PAI-1} \to \text{VN}, \tag{2.30a}$$

$$\text{VN} + \text{PAI-1} \to \text{P}, \tag{2.30b}$$

$$\text{uPA} + \text{uPAR} \to \text{uPAR} + \text{P}. \tag{2.30c}$$

The formation of uPA/PAI-1 compounds in (2.30a) diminishes the binding of vitronectin to PAI-1 and promotes in this way VN self production. This in turn enhances VN-integrin contact. Binding between VN and the inhibitor PAI-1 in (2.30b) moreover promotes indirectly the activation of plasmin by preventing uPA inhibition by PAI-1. Lastly, uPA/uPAR compounds activate plasmin in (2.30c). Due to the large amount of uPAR receptors per cell, we neglect the consumption of uPAR molecules in this reaction.

In what follows we sketch the model dynamics, see [7, 29] for more detail. The evolution of the tumor cell density c is determined by cellular diffusion, hapto- and chemotaxis due to ECM, uPA and PAI-1 and logistic proliferation. Thus, we have

$$\partial_t c = \nabla \cdot (D_c \nabla c - \chi_v c \nabla v - \chi_u c \nabla u - \chi_p c \nabla p) + \mu_1 c \left(1 - \frac{c}{c_0}\right).$$

For the component VN with concentration v, no transport terms are included since the ECM does not translocate. A constant logistic reconstruction, degradation by plasmin (as in (2.28)) and mass action kinetics due to the reactions (2.30a), (2.30b) are assumed though. We obtain consequently

$$\partial_t v = -\delta v m + \phi_{2,1}\, up - \phi_{2,2}\, vp + \mu_2 v \left(1 - \frac{v}{v_0}\right).$$

Next, for the protease density u we assume linear diffusion, production by the cancer cells and mass action kinetics due to reactions (2.30a) and (2.30c). Thus, we obtain

$$\partial_t u = D_u \Delta u - \phi_{31}\, up - \phi_{33}\, cu + \alpha_3 c.$$

The inhibitor PAI-1 with densitiy p is produced by plasmin, it diffuses and it is affected by mass action kinetics due to reactions (2.30a) and (2.30b). The corresponding model reads

$$\partial_t p = D_p \Delta p - \phi_{41}\, up - \phi_{42}\, vp + \alpha_4 m.$$

Lastly, we make the assumption that, apart from mass action kinetics due to (2.30b), (2.30c), diffusion and natural decay affect the plasmin density m. This results in

$$\partial_t m = D_m \Delta m + \phi_{52}\, vp + \phi_{53}\, uc - \alpha_5 m.$$

For a better comparability of numerical solutions the model was nondimensionalised in [29]. To this end it was scaled with a reference length $L = 0.1$ cm, a reference diffusion coefficient $D = 10^{-6}$ cm^{2}s^{-1}, a rescaled time parameter $t = L^2 D^{-1}$ and reference concentrations c_0, v_0, u_0, p_0, m_0 for the model components. In the case of the tumor cells and the vitronectin, the reference concentrations coincide with the carrying capacities. We will consider a full nondimensionalization in the following section. In the case of the current model we refer to [7, 29] for further details.

By keeping the former notations in the unit free variables, the rescaled systems is an autonomous five component system of type (2.6) and it reads in its full form

$$\begin{cases} \partial_t c = \nabla \cdot (D_c \nabla c\ - \chi_u c \nabla u - \chi_p c \nabla p - \chi_v c \nabla v) + \mu_1 c(1-c), \\ \partial_t v = -\delta v m + \phi_{21} up - \phi_{22} vp + \mu_2 v(1-v), \\ \partial_t u = D_u \Delta u - \phi_{31} up - \phi_{33} cu + \alpha_3 c, \\ \partial_t p = D_p \Delta p - \phi_{41} up - \phi_{42} vp + \alpha_4 m, \\ \partial_t m = D_m \Delta m + \phi_{52} vp + \phi_{53} cu - \alpha_5 m. \end{cases} \tag{I}$$

2.7 Modeling of the EMT

In what follows in the next three sections we derive a cancer invasion model that involves two cell species. To this end we expand on the modeling sections from our papers [70] and [151].

Our aim is to include the EMT discussed in Section 2.1 in the framework of cancer invasion systems. For this purpose we consider two cancer cell types the DCCs and the CSCs and also the transition between them. This transition is triggered by the interaction of the DCCs with the EGF molecules and the cellular EGF receptors (EGFR). In the modeling process we combine the macroscopic dynamics of the ECM invasion with the microscopic dynamics of the EGF attachment/detachment to EGFRs. Since the dynamics take place on time scales of different magnitudes, we take a temporal limit in the microscopic system. The availability of free EGF molecules and the number of free EGFRs on the surfaces of the cells play crucial roles in the modeling.

Note that the EGF acts as a black box component in the model since we do not require any traits that are unique to EGF except for its capability to trigger the EMT. Thus, EGF and EGFR in the model can easily be replaced by other EMT inducing proteins and corresponding receptors. Another choice would be TGF-β and its receptor [89].

Other tissue invasion systems that consider two cancer cell populations as well as the transition between them, were studied, e.g., in [7, 44, 156]. However, these works do not cover an investigation of the EMT triggering mechanism but assume that EMT takes place with a constant rate.

A two cancer type invasion system We take the haptotaxis approach (2.28) as basis for our model and thus include concentrations for tumor cells, vitronectin and MMPs. Unlike the aforementioned models, the one developed here is endowed with two types of cancer cells, the DCCs and the CSCs. Thus, the common model approach for tumor cell concentrations applies with an additional coupling term, which accounts for the EMT transition. We therefore have

$$\begin{cases} \partial_t c^D = \text{diffusion} + \text{haptotaxis} - \mu_{EMT}\, c^D + \text{proliferation}, \\ \partial_t c^S = \text{diffusion} + \text{haptotaxis} + \mu_{EMT}\, c^D + \text{proliferation}, \end{cases} \tag{2.31}$$

where c^S and c^D denote the concentrations of CSCs and DCCs, respectively. The coefficient μ_{EMT} refers to the number of DCCs that undergo the EMT per time unit.

We assume that the EMT is induced by EGF. In particular, we assume that the amount of EGF bound DCC-specific EGFRs controls the EMT rate. The interactions that we consider in the modeling of the EMT are sketched in the cartoon in Figure 2.4. We model the rate μ_{EMT} to be a monotonically increasing function approaching asymptotically a maximum value μ_0 as

$$\mu_{EMT} = \mu_0 \frac{g_b^D}{\mu_{1/2} + g_b^D}\,. \tag{2.32}$$

Here g_b^D denotes the concentration of the EGF molecules that are bound onto the EGFRs on the membrane of the DCCs and $\mu_{1/2}$ is a parameter that accounts for the critical amount of bound EGF needed to generate half maximal EMT. This general modeling approach is common in mathematical biology and was motivated by the ODE models for the EMT in [46, 177]. Although (2.32) is a relatively simple modeling choice, it exhibits the importance of considering a nontrivial EGF-driven EMT rate. In what follows we consider the binding dynamics of the EGF to obtain a closed formula for the number of EGFs bound to EGFRs on the DCCs denoted by g_b^D.

We introduce g_b, g_f, g_0 referring to the concentrations of bound (to DCCs or CSCs), free (unbound) and total EGF molecules in the extracellular environment. Moreover, we let r_0, r_b and r_f denote the total, occupied and free receptor concentrations on the surface of both types of considered cancer cells. Since we assume the EGF to be either free or bound to EGFRs, it holds at each point in space

$$g_0 = g_f + g_b, \tag{2.33}$$

$$r_0 = r_f + r_b. \tag{2.34}$$

Binding dynamics For given constant rates k_+ and k_- we assume that free EGF molecules bind onto free EGFR receptors with rate k_+ while bound EGF molecules detach with rate k_-. In terms of a reaction equation this can be modeled as

$$\mathrm{EGFR} + \mathrm{EGF} \underset{k_-}{\overset{k_+}{\rightleftarrows}} \mathrm{EGFR/EGF}, \tag{2.35}$$

where EGFR/EGF denotes the compound of EGF and EGFR, whose concentration coincides with g_b. We consider binding to both types of cancer cells DCCs and CSCs and thus use the

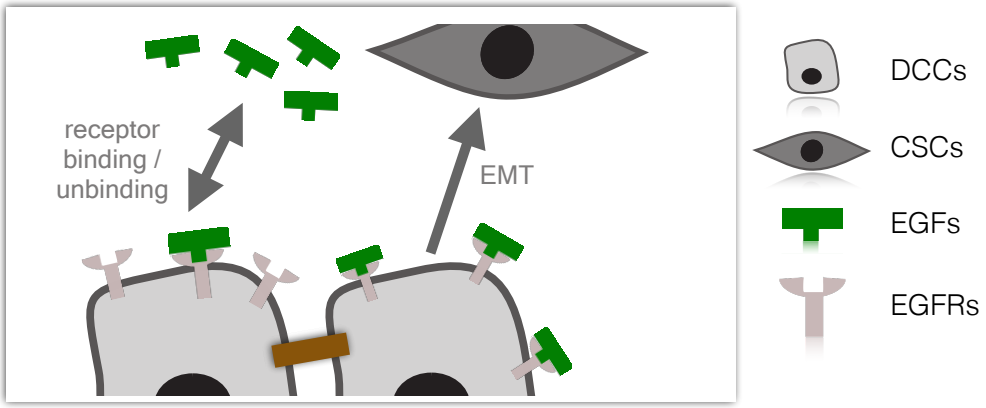

Figure 2.4: The binding of EGF to EGFR on the cancer cells promotes the EMT.

same binding rates for both cancer types. Further, we assume molecular diffusion of the free EGF in the extracellular space. The temporal evolution of both the free and the bound EGF molecules is consequently given by the PDE model

$$\begin{cases} \dfrac{\partial g_b}{\partial \bar{t}} = & k_+ g_f r_f - k_- g_b, \\ \dfrac{\partial g_b}{\partial \bar{t}} = D_f \Delta g_f - & k_+ g_f r_f + k_- g_b. \end{cases} \tag{2.36}$$

Here $\bar{t}$ is a time variable in the temporal magnitude in which the reaction takes place.

Assuming that only EGF can occupy EGFRs implies $r_b = g_b$. Together with (2.34) we therefore obtain

$$r_f = r_0 - r_b = \lambda^S c^S + \lambda^D c^D - g_b, \tag{2.37}$$

where λ^S and λ^D represent the amount of EGFR receptors per cell for both DCCs and CSCs. Furthermore, we apply the principle of stoichiometry saying that the ratio between EGF bound to DCCs denoted by g_b^D and total bound EGF satisfies

$$\frac{\lambda^D c^D}{r_0} = \frac{g_b^D}{g_b}. \tag{2.38}$$

Time scaling The EGF attachment/detachment onto EGFRs take place in a much faster time when compared to the dynamics of cell movement and invasion in (2.31). We can relate the time variable used to describe the invasion (t) to the time variable used to model the EGF binding ($\tilde{t}$) by

$$\bar{t} = \frac{t}{\varepsilon}, \quad 0 < \varepsilon << 1. \tag{2.39}$$

We introduce the vector valued concentration function $\mathbf{w} = (g_b(x, t(\bar{t})),\ g_f(x, t(\bar{t})))^T$ and, taking the derivative with respect to the time variable t, we obtain

$$\varepsilon \partial_t \mathbf{w} = \begin{pmatrix} 0 \\ D_f \Delta g_f \end{pmatrix} + \begin{pmatrix} 1 \\ -1 \end{pmatrix} (k_+ g_f r_f - k_- g_b) \tag{2.40}$$

since it yields that $\frac{\partial \tilde{t}(t)}{\partial t} = \frac{1}{\varepsilon}$ and $\frac{\partial x}{\partial t} = 0$. Due to the significant difference in time scales corresponding to the time variables t and $\tilde{t}$, we consider now the limit case $\varepsilon \to 0$ in (2.40) and deduce hence using (2.37) the algebraic-elliptic system

$$\begin{cases} 0 = k_D^{-1} g_f(\lambda^S c^S + \lambda^D c^D - g_b) - g_b, \\ 0 = \Delta g_f. \end{cases} \tag{2.41}$$

The rate $k_D = k_-/k_+$ in (2.41) denotes the attachment/detachment ratio of the EGFs onto the EGFRs. Although there is no time derivative in (2.41), both concentrations g_b and g_f depend on time t through the cancer cell densities c^S and c^D. We consider system (2.41) closed with the boundary conditions (2.26). Hence, the free EGF satisfies

$$\partial_\nu g_f(x) = \nu(x) \cdot \nabla g_f(x) = 0, \quad x \in \partial\Omega. \tag{2.42}$$

Remark 2.3 System (2.41) considered with boundary conditions (2.42) and no further restrictions does not have a unique solution. To see that we consider $g_b = K(\lambda^S c^S + \lambda^D c^D)$ for $K \in (0,1)$. For this choice the spatially uniform concentration

$$g_f = k_D \frac{K}{1-K}$$

together with g_b satisfy the algebraic equation of (2.41), the boundary condition (2.42) and $\Delta g_f = 0$. Consequently, there is a solution of (2.41), (2.42) for every $K \in (0,1)$.

We can recover the uniqueness in (2.41), (2.42) by taking (2.33) into account. Indeed, if we consider the mass evolution of the total EGF employing (2.36), we can see that

$$\frac{d}{d\tilde{t}} \int_\Omega (g_b + g_f)\, dx = \int_\Omega \frac{dg_b}{d\tilde{t}} - \frac{dg_b}{d\tilde{t}} + D_f \Delta g_f \, dx = 0.$$

As a result, the average concentration of the total EGF on the domain Ω denoted by

$$\Gamma = |\Omega|^{-1} \int_\Omega g_0(t,x)\, dx = |\Omega|^{-1} \left(\int_\Omega g_b(0,x)\, dx + \int_\Omega g_f(0,x)\, dx \right) \tag{2.43}$$

stays constant in time. This also implies that the initial data of g_f and g_b determine Γ.

Remark 2.4 When considering (2.43), the solution of algebraic-elliptic system (2.41) can be understood as the solution of the parabolic system for $\tilde{t} \to \infty$. Indeed, numerically computed EGF concentrations with (2.41) converge to the concentrations determined by (2.36) relatively quickly for reasonable parameter choices (see below). This justifies taking the limit $t/\tilde{t} \to 0$ in the model. See also Figure 2.5.

Solution of the elliptic system with boundary conditions and EGF mass conservation The concentration of free EGF is subject to the second equation in system (2.41), which is the Laplace equation under homogeneous Neumann conditions. Thus, we can deduce that its gradient ∇g_f is unique and equal to zero, cf. [47]. Hence, the concentration g_f is constant on Ω. Consequently, the first equation of system (2.41) implies

$$g_b = \frac{g_f}{k_D + g_f} \left(\lambda^S c^S + \lambda^D c^D \right). \tag{2.44}$$

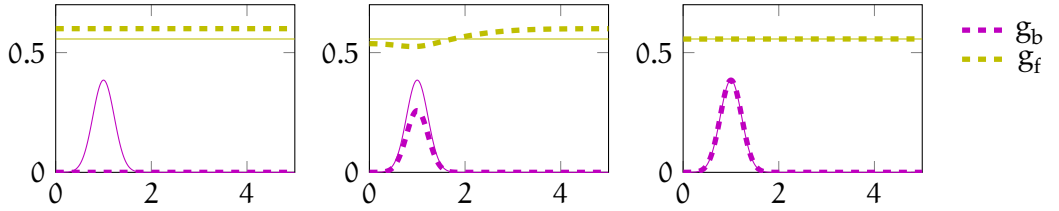

Figure 2.5: Experimental convergence in time of a solution of parabolic system (2.36) (dahed lines) to the solution of the corresponding algebraic-elliptic system, i.e. system (2.41) (solid lines). We show numerically computed spatial concentrations in 1D at the time instances $\tilde{t} = 0, 2, 40$.

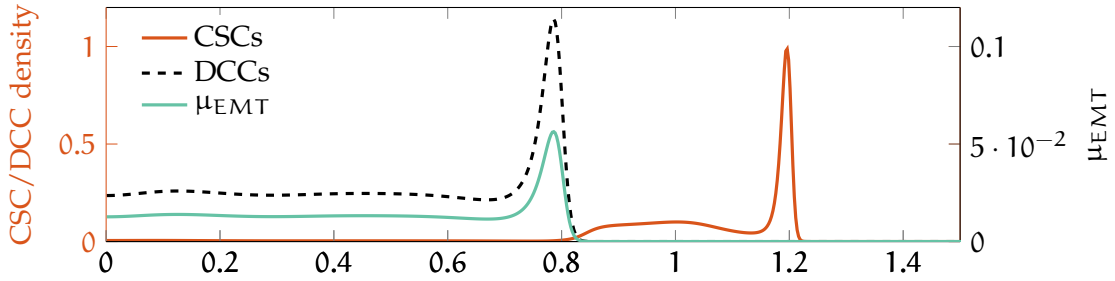

Figure 2.6: Plot of the μ_{EMT} coefficient (2.49) in space for system (II) at a fixed time instance in a 1D simulation. It varies in space and has the same support as the DCC density.

Accordingly, by (2.38) we can write the concentration of DCC-bound EGFs as

$$g_b^D = \frac{g_f}{k_D + g_f} \lambda^D c^D. \tag{2.45}$$

In addition, the spatially constant free EGF satisfies

$$0 = g_f^2 + \left(k_D + \frac{1}{|\Omega|} \int_\Omega \lambda^S c^S + \lambda^D c^D dx - \Gamma \right) g_f - k_D \Gamma . \tag{2.46}$$

We obtain (2.46) due to (2.43) and after integration of the first equation of (2.41) over Ω. Equation (2.46) is quadratic in g_f. It has a single positive root in g_f due to the nonnegativity of its discriminant

$$d = \left(k_D + \frac{1}{|\Omega|} \int_\Omega \lambda^S c^S + \lambda^D c^D dx - \Gamma \right)^2 + 4 k_D \Gamma \geqslant 0 \tag{2.47}$$

and because of the negativity of the last term in (2.46). Consequently, we end up with the following formula for the free EGF density

$$g_f = \frac{\Gamma + \sqrt{d} - k_D}{2} - \frac{1}{2|\Omega|} \int_\Omega \lambda^S c^S + \lambda^D c^D dx. \tag{2.48}$$

Note that g_f is not constant in time since the integral term $\int_\Omega \lambda^S c^S + \lambda^D c^D dx$ is subject to changes in the cancer cell concentrations, which are not mass conservative. Eventually we get by (2.32) and (2.45) that

$$\mu_{EMT} = \mu_0 \frac{\lambda^D c^D}{\mu_{1/2} (k_D g_f^{-1} + 1) + \lambda^D c^D}, \tag{2.49}$$

which is nonuniform in space through the DCC density c^D as illustrated in Figure 2.6.

2.8 Fibroblasts and matrix remodeling

Commonly, models of tissue invasion such as (2.29) and (I) consider *self-remodeling* of the extracellular matrix. This means that new tissue material sprouts in the ECM without contribution of other components of the system. In such cases the reconstruction of the tissue is modeled in the same manner as the proliferation of cells by a (possibly positive) logistic growth term, see (2.9), (2.11). In other approaches, e.g., [44], *spontaneous remodeling* with a rate proportional to the remaining amount of resources is assumed, i.e.

$$\partial_t v = \text{proteolysis} + \mu R(\mathbf{w})^+, \quad \mu > 0.$$

In this thesis, we promote a more detailed and biologically more realistic model: the ECM is remodeled by fibroblasts.

We use two subsystems to explain our approach. In the first, we present the transition/transdifferentiation of the CSCs to fibroblasts. In the second system we model the reconstruction of the ECM by the fibroblasts.

The transdifferentiation subsystem In the tumor environment both fibroblast cells and *cancer associated fibroblast cells*, which originate from differentiation of CSCs, are present [89]. We do not distinct between these two types and thus neglect the differences in their biochemical and mechanical properties.

As observed in wound healing [40], we assume that the fibroblasts are directed towards damaged regions of the ECM that require reconstruction. We account for this in the model by adding haptotactic movement towards lower concentration of ECM particles. This is opposing to the haptotactic motion of the cancer cells which is oriented reverse, i.e. towards higher ECM densities.

For the proliferation of the fibroblasts we employ the positive logistic growth model (2.11) to account for the competition for resources. The fibroblast cells, as opposed to the cancer cells, undergo apoptosis. Hence, we add a death term with a constant rate. Further, we account for the transdifferentiation from CSCs to fibroblasts in the model. To this end we complement the system with linear transition terms from the CSC density to the fibroblast concentration. Accordingly, the transdifferentiation subsystem reads

$$\begin{cases} \partial_t c^S = \text{diffusion} - \chi_S \nabla \cdot \left(c^S \nabla v\right) - \mu_T \, c^S + \text{proliferation}, \\ \partial_t c^F = \text{diffusion} + \chi_F \nabla \cdot \left(c^F \nabla v\right) + \mu_T \, c^S + \text{proliferation} - \beta_F \, c^F, \end{cases} \tag{2.50}$$

where c^F denotes the concentration of fibroblast cells, χ_F their haptotactic sensitivity, μ_T their *transdifferentiation rate* and μ_F and β_F the rates of their proliferation and apoptosis.

The matrix remodeling subsystem The fibroblast-driven ECM-remodeling that we propose is modeled by

$$\begin{cases} \partial_t c^F = \text{diffusion} + \text{haptotaxis} + \text{transdiff.} + \text{proliferation}, \\ \partial_t v = \text{proteolysis} + \mu_F \, c^F \, R(\mathbf{w})^+, \end{cases} \tag{2.51}$$

where the ECM reproduction is proportional to the positive-part of the remaining resources. In this way, degradation due to fibroblasts is precluded. Consequently, only the proteolytic MMP proteins degrade the matrix. We will compare this modeling approach to the self remodeling in Section 8.3.

2.9 The haptotaxis EMT/invasion model

In this section we combine the models developed in the previous sections to derive the full haptotaxis EMT/invasion model. Moreover, we consider the nondimensionalization and scaling of the model in detail.

The complete ECM invasion model results from piecing together subsystems (2.29), (2.31), (2.50) and (2.51). It takes into account the invasion of tissue, the EMT and the ECM reconstruction by fibroblasts. Consequently, it reads

$$\begin{cases} \partial_t c^D = \nabla \cdot \left(D_D \nabla c^D - \chi_D c^D \nabla v\right) - \mu_{EMT}\, c^D + \mu_D\, c^D\, R^+, \\ \partial_t c^S = \nabla \cdot \left(D_S \nabla c^S - \chi_S c^S \nabla v\right) - \mu_T\, c^S + \mu_{EMT}\, c^D + \mu_S\, c^S\, R^+, \\ \partial_t c^F = \nabla \cdot \left(D_F \nabla c^F + \chi_F c^F \nabla v\right) + \mu_T\, c^S - \beta_F\, c^F + \mu_F\, c^F\, R^+, \\ \partial_t v = -\delta_v\, m v + \mu_v\, c^F\, R^+, \\ \partial_t m = D_m \Delta m + \alpha_D\, c^D + \alpha_S\, c^S - \beta_m\, m, \end{cases} \tag{II}$$

where the resources depend on the densities of both types of cancer cells, the fibroblasts and the ECM via $R = 1 - c^D - c^S - c^F - v$. We point out that we employ the positive logistic growth model (2.11) for the cell proliferation. In the rest of this work, we will refer to this model as the *haptotaxis EMT/invasion model*.

Scaling and parameters

In the previous sections we considered the models in their *nondimensional* form. Therefore, parameters and concentrations are not given in measurable physical units but rather in relation to reference densities. This allows for a simplification of the systems and better comparability when looking into simulation results. We also presented model (II) in this form.

In this subsection we justify the dimensionless formulations by presenting, in particular, for model (II) the nondimensionalisation process in detail. Consequently, we also consider the model in its original variables which allows us to discuss the model parameters. We therefore highlight the state variables in original units with the $\tilde{\cdot}$-notation and bio-relevant parameters using the superscript $\cdot^{bio}$.

Deriving the unit free macroscopic system The derivation of (II), as discussed above, leads in the first place to the following system in original variables

$$\begin{cases} \partial_t \tilde{c}^D = \nabla_{\tilde{x}} \cdot \left(D_D^{bio} \nabla_{\tilde{x}} \tilde{c}^D - \chi_D^{bio} \tilde{c}^D \nabla_{\tilde{x}} v\right) - \mu_{EMT}^{bio}\, \tilde{c}^D + \mu_D^{bio}\, \tilde{c}^D\, R^{bio}(\tilde{\mathbf{w}})^+, \\ \partial_t \tilde{c}^S = \nabla_{\tilde{x}} \cdot \left(D_S^{bio} \nabla_{\tilde{x}} \tilde{c}^S - \chi_S^{bio} \tilde{c}^S \nabla_{\tilde{x}} v\right) + \mu_{EMT}^{bio}\, \tilde{c}^D - \mu_T^{bio}\, \tilde{c}^S + \mu_S^{bio}\, \tilde{c}^S\, R^{bio}(\tilde{\mathbf{w}})^+, \\ \partial_t \tilde{c}^F = \nabla_{\tilde{x}} \cdot \left(D_F^{bio} \nabla_{\tilde{x}} \tilde{c}^F + \chi_F^{bio} \tilde{c}^F \nabla_{\tilde{x}} v\right) + \mu_T^{bio}\, \tilde{c}^S - \beta_F^{bio}\, \tilde{c}^F + \mu_F^{bio}\, \tilde{c}^F\, R^{bio}(\tilde{\mathbf{w}})^+, \\ \partial_t \tilde{v} = -\delta_v^{bio}\, m v + \mu_v^{bio}\, \tilde{c}^F\, R^{bio}(\tilde{\mathbf{w}})^+, \\ \partial_t \tilde{m} = D_m^{bio} \Delta_{\tilde{x}} \tilde{m} - \beta_m^{bio}\, \tilde{m} + \alpha_D^{bio}\, \tilde{c}^D + \alpha_S^{bio}\, \tilde{c}^S, \end{cases} \tag{2.52}$$

The free resources in the system are given by

$$R^{bio}(\tilde{\mathbf{w}}) = 1 - \frac{\tilde{c}^D}{c_0^D} - \frac{\tilde{c}^S}{c_0^S} - \frac{\tilde{c}^F}{c_0^F} - \frac{\tilde{v}}{v_0}$$

	parameter	bio. relevant value	rescaled value	reference
D_D	diffusion coeff. of DCCs	$3.5 \times 10^{-10}\,cm^2s^{-1}$	3.5×10^{-4}	[8, 20, 29]
D_S	diffusion coeff. of CSCs	$3.8 \times 10^{-11}\,cm^2s^{-1}$	3.8×10^{-5}	[7, 20], our choice
D_F	diffusion coeff. of fibroblasts	$3.5 \times 10^{-10}\,cm^2s^{-1}$	3.5×10^{-4}	[93], our choice
D_m	diffusion coeff. of MMPs	$2.5 \times 10^{-9}\,cm^2s^{-1}$	2.5×10^{-3}	[29, 144, 158]
χ_D	haptotaxis coeff. of DCCs	$1.3\,cm^{d+2}mol^{-1}s^{-1}$	8×10^{-3}	[29, 158]
χ_S	haptotaxis coeff. of CSCs	$62.5\,cm^{d+2}mol^{-1}s^{-1}$	4×10^{-1}	[7, 158], our choice
χ_f	haptotaxis coeff. of fibroblasts	$1.3\,cm^{d+2}mol^{-1}s^{-1}$	8×10^{-3}	[158], our choice
λ^D	EGF receptors per DCC	1.9×10^7	1	[81, 95, 132], our choice
λ^S	EGF receptors per CSC	2.7×10^7	1.4	[81, 95, 132], our choice
k_D	EGF unbinding/binding	$3.2 \times 10^{-12}\,cm^{-d}mol$	2	[132], estimated
Γ	average of total EGF	$8 \times 10^{-14}\,cm^{-d}mol$	0.05	estimated
μ_0	EMT factor	$5.5 \times 10^{-6}\,s^{-1}$	0.055	estimated
$\mu_{1/2}$	critical EGF density	$3.2 \times 10^{-12}\,cm^{-d}mol$	2	estimated
μ_D	proliferation rate of DCCs	$2 \times 10^{-5}\,s^{-1}$	0.2	[29, 157]
μ_S	proliferation rate of CSCs	$10^{-5}\,s^{-1}$	0.1	our choice
μ_F	proliferation rate of fibroblasts	$10^{-5}\,s^{-1}$	0.1	our choice
μ_v	ECM remodeling rate	$1.9 \times 10^8\,s^{-1}$	25	our choice
β_F	apoptosis rate of fibroblasts	$3 \times 10^{-7}\,s^{-1}$	3×10^{-3}	[93]
β_m	decay rate of MMPs	$10^{-4}\,s^{-1}$	1	[8]
α_D	MMP production rate of DCCs	$2.3\,s^{-1}$	0.1	[8, 29]
α_S	MMP production rate of CSCs	$22.9\,s^{-1}$	1	our choice
δ_v	ECM degradation rate	$5.3 \times 10^9\,cm^d mol^{-1}s^{-1}$	1	[8, 29]
μ_T	transdifferentiation rate	$10^{-6}\,s^{-1}$	0.01	estimated
c^{ref}	reference cell density	$8.3 \times 10^{-20}\,cm^{-d}mol$	-	[93]
v^{ref}	reference ECM density	$6.4 \times 10^{-9}\,cm^{-d}mol$	-	[93]
m^{ref}	reference MMP density	$1.9 \times 10^{-14}\,cm^{-d}mol$	-	[93]
g^{ref}	reference EGF density	$1.6 \times 10^{-12}\,cm^{-d}mol$	-	[85, 93]
D	diffusion scaling coeff.	$10^{-6}\,cm^2s^{-1}$	-	[20, 29]
t_{sc}	time scaling coeff.	$10^4\,s$	-	[8, 29]

Table 2.1: Parameter values in their derived biological units and in a rescaled formulation, which we used in our simulations. For the nondimensionalization the reference densities and the scaling coefficients in the lower part of the table were used. The integer $d \in \{1, 2\}$ denotes the space dimension. Parameter values referenced by "our choice" were chosen according to our biological understanding of the processes while we decided on "estimated" parameter values after numerical experimentation [151]

for carrying capacities c_0^D, c_0^S, c_0^F, v_0. The vector of state variables depends on the time instance $\tilde{t} \in (0, \infty)$ and the point in space $\tilde{x} \in \tilde{\Omega}$. In system (2.52) the variables and parameters have the units

$$
\begin{aligned}
[\tilde{t}] = s, [\tilde{x}] = cm, \qquad & [\tilde{c}^D] = [\tilde{c}^S] = [\tilde{c}^F] = \frac{mol}{cm^d},\\
[D_D^{bio}] = [D_S^{bio}] = [D_F^{bio}] = [D_M^{bio}] = \frac{cm^2}{s}, \qquad & [\tilde{v}] = [\tilde{m}] = \frac{mol}{cm^d},\\
[\chi_D^{bio}] = [\chi_S^{bio}] = [\chi_f^{bio}] = \frac{cm^{d+2}}{mol \cdot s}, \qquad & [\mu_D^{bio}] = [\mu_D^{bio}] = [\mu_F^{bio}] = \frac{1}{s},\\
[\alpha_D^{bio}] = [\alpha_S^{bio}] = [\delta_v] = \frac{1}{s}, \qquad & [\mu_{EMT}^{bio}] = [\mu_T^{bio}] = [\beta^{bio}] = \frac{1}{s},\\
[c_0^D] = [c_0^S] = [c_0^F] = [v_0] = \frac{mol}{cm^d}. &
\end{aligned}
$$

We assume that Ω is such that $\mathrm{diam}\{\Omega\}$ is in the range of $L = 0.1cm$, which is the size of the part of the tissue we are interested in.

For the rescaling of the system we define the scaling constants $D = \frac{cm^2}{10^6 \cdot s}, t_{sc} = \frac{L^2}{D}$ and consider a reference MMP density m_0. For the other components of system (2.52) we take the

corresponding carrying capacities as reference densities. We employ $t = \tilde{t}/t_{sc}$ and $x = \tilde{x}/L$ as dimensionless time and space variables and note that

$$\frac{\partial u}{\partial t} = t_s c \frac{\partial u}{\partial \tilde{t}}, \quad \nabla u = L \nabla_{\tilde{x}} u$$

for $u \in \{c^D, c^S, c^F, \nu, m\}$ and where ∇ denotes the gradient with respect to the dimensionless space variable x. By defining now the dimensionless concentrations

$$c^D = \frac{\tilde{c}^D}{c_0}, \quad c^S = \frac{\tilde{c}^S}{c_0}, \quad c^F = \frac{\tilde{c^F}}{c_0}, \quad \nu = \frac{\tilde{\nu}}{\nu_0}, \quad m = \frac{\tilde{m}}{m_0}$$

and dividing each equation in (2.52) by the product of its corresponding reference density and the time scaling variable t_{sc}, we end up with system (II). The dimensionless parameters and variables relate to the bio-relevant numbers as

$$\begin{gathered} D_D = \frac{D_D^{bio}}{D}, \quad D_S = \frac{\tilde{D}_S^{bio}}{D}, \quad D_F = \frac{D_F^{bio}}{D}, \quad D_m = \frac{D_m^{bio}}{D}, \\ \chi_D = \chi_D^{bio} \frac{\nu_0}{D}, \quad \chi_S = \chi_S^{bio} \frac{\nu_0}{D}, \quad \chi_F = \chi_F^{bio} \frac{\nu_0}{D}, \\ \mu_D = \frac{\mu_D^{bio}}{t_{sc}}, \quad \mu_S = \frac{\mu_D^{bio}}{t_{sc}}, \quad \mu_F = \frac{\mu_F^{bio}}{t_{sc}}, \quad \mu_{EMT} = \frac{\mu_{EMT}^{bio}}{t_{sc}}, \\ \mu_T = \frac{\mu_T^{bio}}{t_{sc}}, \quad \beta = \frac{\beta^{bio}}{t_{sc}}, \alpha_D = \frac{\alpha_D c_0}{m_0 t_{sc}}, \quad \alpha_S = \frac{\alpha_D c_0}{m_0 t_{sc}}, \quad \delta = \frac{\delta^{bio} m_0}{t_{sc}}. \end{gathered}$$

Parameter scaling in the EMT subsystem In the same manner as above, we also rescale the EMT subsystem derived in Section 2.7. The original derivation leads to the EMT coefficient

$$\mu_{EMT}^{bio} = \mu_0^{bio} \frac{\tilde{g_b}^D}{\mu_{1/2}^{bio} + \tilde{g_b}^D} \tag{2.53}$$

and to the bio-relevant parabolic system analog to (2.36), which reads

$$\begin{cases} \dfrac{\partial \tilde{g_b}}{\partial \tilde{t}} = k_+^{bio} \tilde{g_f} (\lambda_D^{bio} \tilde{c}^D + \lambda_S^{bio} \tilde{\tilde{c}}^S - \tilde{g}_b) - k_-^{bio} \tilde{g_b}, \\ \dfrac{\partial \tilde{g_b}}{\partial \tilde{t}} = D_f^{bio} \Delta \tilde{g_f} - k_+^{bio} + \tilde{g_f} (\lambda_D^{bio} \tilde{c}^D + \lambda_S^{bio} \tilde{\tilde{c}}^S - \tilde{g}_b) + k_-^{bio} - \tilde{g_b}. \end{cases} \tag{2.54}$$

In this system we deal with the units

$$\begin{gathered} [\mu_0^{bio}] = \frac{1}{s}, \quad [\mu_{1/2}^{bio}] = [g_b] = [g_f] = \frac{mol}{cm^d}, \quad [D_f^{bio}] = \frac{cm^2}{s}, \\ [k_+^{bio}] = \frac{cm^d}{mol \cdot s}, \quad [k_-^{bio}] = \frac{1}{s}, \quad [\lambda_D] = [\lambda_S] = 1. \end{gathered}$$

Another parameter that is left to consider is the relative binding rate k_D^{bio} given in mol/cm^d. It appears in the elliptic system

$$\begin{cases} 0 = \dfrac{1}{k_D^{bio}} \tilde{g}_f (\lambda_D^{bio} \tilde{c}^D + \lambda_S^{bio} \tilde{c}^S - \tilde{g}_b) - \tilde{g}_b, \\ 0 = \Delta \tilde{g}_f \end{cases} \tag{2.55}$$

that originates from (2.54) after the time scaling $\tilde{t}/\bar{t} \to 0$ (see above). We scale the submodel by using the reference EGF density g_r and define

$$g_f = \frac{\tilde{g}_f}{g_r}, \quad g_b = \frac{\tilde{g}_b}{g_r}, \quad \lambda_D = \lambda_D^{bio}\frac{c_0^D}{g_r}, \quad \lambda_S = \lambda_S^{bio}\frac{c_0^D}{g_r}, \quad k_D = \frac{k_D^{bio}}{g_r}.$$

Dividing both equations by g_r we eventually obtain nondimensional system (2.41) and nondimensional EMT coefficient (2.32) where $\mu_0 = \mu_0^{bio}/t_{sc}$ and $\mu_{1/2} = \mu_{1/2}^{bio}/g_r$.

Parameter choice We employ parameters from the biological and modeling literature for model (II). A full overview on the chosen parameter values and references where they were found are given in Table 2.1. In many cases, only the order of magnitude could be found since these numbers are hard to measure experimentally. Some parameters were estimated by us or found via numerical experimentation.

We present the parameters in their original values, i.e. for the nondimensionalized model (II), as well as in their rescaled form in which they are used in numerical experiments. Along with them we exhibit the values of the scaling constants for replicability of the derivation of the simulation parameters.

2.10 A multiscale contractivity model

Besides the haptotaxis EMT/invasion model which constitutes the primary model considered in this thesis, there are other models in the literature that also consider heterogeneity in the tumor, see, e.g., [7, 44, 57]. The last model we address in this chapter was derived in [156] and examines this setting as well. It takes into account integrin binding on the macroscopic level and cell *contractivity*, a measure of the migration ability of the cancer cells. The rest of this chapter is based on the modeling part of our paper [98].

The macroscopic model As in model (II) we consider two types of cancer cells. We assume that the bulk of the tumor consists of *proliferative* cancer cells that do not migrate or otherwise translocate. The migration is taken upon by stem-like *migratory* cancer cells. There exist a bidirectional transition between the two families of cancer cells, modeling the parallel action of EMT and MET, see Section 2.1. We assume both transitions to take place with constant rates. In addition, we assume proliferation of the cancer cells and self remodeling of the matrix both modeled by logistic terms.

On the macroscopic level the model reads

$$\begin{cases} \partial_t c^p = \mu_p c^p(1 - (c^p + c^m) - \eta_p\, v) + \gamma c^m - \lambda c^p, \\ \partial_t c^m = \nabla \cdot (\phi_D\, \nabla c^m - \phi_M\, c^m \nabla v) + \lambda c^p - \gamma c^m, \\ \partial_t v = -\delta_v (c^p + c^m)\, v + \mu_v v(1 - \eta_v\, (c^p + c^m) - v), \end{cases} \tag{2.56}$$

where λ and γ denote EMT and MET rates. Using model (2.17), η_p and η_v account for different compositions of resources affecting cell proliferation and remodeling. Cellular diffusion and haptotaxis of the migratory cells are moreover weighted by non constant functions ϕ_D and ϕ_M to be determined by microscopic dynamics of the integrins. We consider system (2.56) only in its nondimensional form.

Microscopic binding and contractivity On the microscopic level we consider integrins located on the membranes of the migrating cells. Let $y(t,x)$ denote the amount of integrins bound to the tissue per cell. We assume that each cell has a fixed number of $R_0 > 0$ integrins. The number of free integrin receptors per cell is consequently $R = R_0 - y$. Locally, we assume reversible integrin binding to the tissue by the reaction equation

$$v + R \underset{k_-}{\overset{k_+}{\rightleftharpoons}} Rv, \tag{2.57}$$

where Rv denotes the complexes of integrins and tissue molecules. Assuming mass action kinetics we end up with the ODE

$$\frac{\partial y}{\partial \vartheta} = k_+ v(R_0 - y) - k_- y. \tag{2.58}$$

By θ in the above equation we refer to a time variable suitable to describe these dynamics that are assumed to be very fast in comparison to the cancer cell migration. We assume moreover that the binding (2.57), which affects only a tiny fraction of the ECM molecules, does not influence the macroscopic density v.

The binding of the considered integrins increases the contractivity of the cells. This measure quantifies the microscopic influence on the cells ability to deform. An increased contractivity is associated with a heightened motility of the migratory cells. Contractivity is initiated by integrin binding and the result of a cascade of subsequent biochemical processes such as actin polimerization, polarization and protrusion formation [121]. The model for the contractivity assumes a delay between the initial binding and the resulting improved deformation competence of the cell. By denoting the time and space dependent contractivity by κ, we thus derive the *delay differential equation*

$$\frac{\partial \kappa}{\partial \vartheta} = -q\kappa + M\, y(\vartheta - \tau) \tag{2.59}$$

with decay rate q, constant time delay τ and growth proportional to the amount of bound integrins at time $\theta - \tau$ with rate M.

We model the influence of the contractivity on the cancer cell migration by

$$\phi_D = \frac{D_d\, \kappa}{1 + (c^p + c^m)\, v}, \quad \phi_M = \frac{D_h\, \kappa v}{1 + v} \tag{2.60}$$

for constant rates D_d and D_h. Thus, cell tissue contact extenuates the random cell movement while the density of the ECM strengthens the haptotaxis in a saturating manner.

Scaling of the full model Combining the microscopic integrin and contractivity model with macroscopic system (2.56) we obtain

$$\begin{cases} \partial_t c^p = \mu_p c^p (1 - (c^p + c^m) - \eta_p\, v) + \gamma c^m - \lambda c^p, \\ \partial_t c^m = \nabla \cdot \left(\dfrac{D_d\, \kappa}{1 + (c^p + c^m)\, v} \nabla c^m - \dfrac{D_h\, \kappa v}{1 + v}\, c^m \nabla v \right) + \lambda c^p - \gamma c^m, \\ \partial_t v = -\delta_v (c^p + c^m)\, v + \mu_v v (1 - \eta_v\, (c^p + c^m) - v), \\ \dfrac{\partial y}{\partial \vartheta} = k_+\, v(1 - y) - k_-\, y, \\ \dfrac{\partial \kappa}{\partial \vartheta} = -q\kappa + M\, y(\theta - \tau). \end{cases} \tag{2.61}$$

To simplify the model we have scaled here the integrin concentration and the binding and unbinding rates k_+, k_- with respect to R_0 but kept the former notations. For a further facilitation we unify now both time variables in system (2.61). To this end we assume that both considered time scales are related via

$$\vartheta = \frac{t}{\varepsilon}, \tag{2.62}$$

where the factor $0 < \vartheta < 1$ is a fixed constant. Hence, we obtain by rescaling the system

$$\begin{cases} \partial_t c^p = \mu_p c^p (1 - (c^p + c^m) - \eta_p\, \nu) + \gamma c^m - \lambda c^p, \\ \partial_t c^m = \nabla \cdot \left(\dfrac{D_d\, \kappa}{1 + (c^p + c^m)\, \nu} \nabla c^m - \dfrac{D_h\, \kappa \nu}{1 + \nu}\, c^m \nabla \nu \right) + \lambda c^p - \gamma c^m, \\ \partial_t \nu = -\delta_\nu (c^p + c^m)\, \nu + \mu_\nu \nu (1 - \eta_\nu\, (c^p + c^m) - \nu), \\ \partial_t y = \varepsilon^{-1}\, k_+\, \nu (1 - y) - \varepsilon^{-1}\, k_-\, y, \\ \partial_t \kappa = -\varepsilon^{-1}\, q \kappa + \varepsilon^{-1}\, M\, y(t - \varepsilon\tau), \end{cases} \tag{III}$$

which depends only on the time variable t. In this formulation it is evident that the dynamics of both integrins and contractivity become faster as ε decreases.

3 Mathematical prerequisites

In this chapter we provide the mathematical prerequisites that we will employ in the following chapters. In more detail, we clarify the notation that we use, introduce the function spaces in which we operate and gather useful mathematical tools such as commonly used inequalities and results from the solution theory of parabolic PDEs. We used some elementary notations that we explain here already in Chapter 2.

3.1 Basic notations

In this work we operate either on bounded domains of the form $\Omega \subset \mathbb{R}^d$ or on the full real space $\mathbb{R}^d$. The integer $d \in \{1, 2, 3\}$ refers to the space dimension. To clarify our notation we take the point $x = (x_1, \dots, x_d) \in \Omega$, the scalar real function $u : \Omega \to \mathbb{R}$ and two vector valued functions

$$\mathbf{v} = (v_1, \dots, v_d), \quad \mathbf{w} = (w_1, \dots, w_d) : \Omega \to \mathbb{R}^d.$$

By these definitions we can introduce the notations for the *Euclidean norm*, the *Euclidean product* and several differential operators

$$|\mathbf{v}| = \left(\sum_{i=1}^{d} v_i \right)^{1/2}, \qquad \mathbf{v} \cdot \mathbf{w} = \sum_{i=1}^{d} v_i w_i,$$

$$\partial_{x_i} u = \frac{\partial u}{\partial x_i}, \qquad \nabla u = \left(\partial_{x_1} u, \dots, \partial_{x_d} u \right),$$

$$\Delta u = \sum_{i=1}^{d} \partial_{x_i}^2 u, \qquad \nabla \cdot v = \sum_{i=1}^{d} \partial_{x_i} v_i.$$

Here we have assumed sufficient smoothness of the functions u, $\mathbf{v}$ and $\mathbf{w}$, such that the derivatives are well defined. For points at the boundary $x \in \partial\Omega$ we use the notation $\partial_\nu u = \nabla u \cdot \nu(x)$, where $\nu(x)$ is the outer normal vector of Ω in x. For a sufficiently smooth function u we denote the α-th *partial derivative* by

$$\partial^\alpha u = \frac{\partial^{|\alpha|} u}{\partial x_1^{\alpha_1}, \dots, \partial x_d^{\alpha_d}}, \quad |\alpha| \geqslant 1, \quad \partial^0 u = u,$$

where $\alpha = (\alpha_1, \dots, \alpha_d) \in \mathbb{N}_0^d$ is a *multiindex* and $|\alpha| = \sum_{i=0}^{d} \alpha_i$. If u is also time dependent, we denote the time derivative by $\partial_t u = \frac{\partial u}{\partial t}$.

For real vectors or vector valued functions $\mathbf{v} = (v_1, \dots, v_d)$ we will use the notation $v > 0$, if and only if $v_i > 0$ for all $i = 1, \dots, d$. If moreover $X(\Omega)$ is a Banach space of scalar functions on Ω and $\mathbf{v}$ is a vector valued function, then the notation $\mathbf{v} \in X(\Omega)$ means $v_i \in X(\Omega)$ for all $1 \leqslant i \leqslant d$.

3.2 Function spaces

For the following definitions we consider a domain Ω and the corresponding space-time cylinder $Q_T = \Omega \times (0, T)$ for $0 < T < \infty$. The function spaces that we introduce here are well known and their definitions can be found in great detail in the textbooks [1, 47, 106, 113].

Continuous functions Let Ω be a bounded domain. For $k \in \mathbb{N}_0$ we denote by $C^k(\bar{\Omega})$ the space of all k times continuously differentiable functions $u : \bar{\Omega} \to \mathbb{R}$. The corresponding norm is given by

$$\|u\|_{C^k(\bar{\Omega})} = \sum_{|\alpha| \leqslant k} \max_{x \in \bar{\Omega}} |\partial^\alpha u(x)|.$$

Similarly, $C^{k,l}(\bar{Q}_T)$ denotes for $k, l \in \mathbb{N}_0$ the set of all functions $u : \bar{Q}_T \to \mathbb{R}$ that are k times continuously differentiable in space and l times continuously differentiable in time. We will use the norm in $C^{k,0}(\bar{Q}_T)$ which is defined as

$$\|u\|_{C^{k,0}(\bar{Q}_T)} = \sum_{|\alpha| \leqslant k} \max_{(x,t) \in \bar{Q}_T} |\partial^\alpha u(x,t)|.$$

Lebesgue spaces Let $L^0(\Omega)$ denote the set of all measurable functions $u : \Omega \to \mathbb{R}$. For $p \geqslant 1$ we define the L^p norm as

$$\|u\|_{L^p(\Omega)} = \begin{cases} \left(\int_\Omega |u|^p \, dx\right)^{1/p}, & 1 \leqslant p < \infty, \\ \operatorname{ess\,sup}_\Omega |u|, & p = \infty \end{cases} \tag{3.1}$$

with the *essential supremum* given by

$$\operatorname{ess\,sup}_\Omega |u| = \inf\{C \geqslant 0 : \ |u(x)| \leqslant C \text{ for almost every } x \in \Omega\}.$$

The *Lebesgue space* $L^p(\Omega)$ is defined as the space of measurable functions in $L^0(\Omega)$ that have finite norm $\|\cdot\|_{L^p(\Omega)}$.

In the case of functions on the whole domain $\mathbb{R}^d$ we moreover define $L^1(\mathbb{R}^d, f(x))$ as the space of all measurable functions u for which $\int_{\mathbb{R}^d} |u(x)| \cdot |f(x)| \, dx < \infty$.

Bochner spaces For functions $u : Q_T \to \mathbb{R}$ we use the notation $u(t) = u(\cdot, t) : \Omega \to \mathbb{R}$ to denote the corresponding space dependent functions at the fixed time instance t. More generally, let $X(\Omega)$ be a Banach space, then we define the corresponding *Bochner space*

$$L^p(0, T; X(\Omega)) = \left\{u : u(t) : (0, T) \to X(\Omega), \ \|u\|_{L^p(0,T;X(\Omega))} < \infty\right\}$$

for all $p \geqslant 1$ with corresponding norm

$$\|u\|_{L^p(0,T;X(\Omega))} = \begin{cases} \left(\int_0^T \|u\|_{X(\Omega)}^p \, dx\right)^{1/p}, & 1 \leqslant p < \infty, \\ \operatorname{ess\,sup}_{(0,T)} \|u\|_{X(\Omega)}, & p = \infty. \end{cases}$$

In this thesis we mostly consider the particular Bochner space

$$L^p(Q_T) = L^p(0, T; L^p(\Omega)).$$

Sobolev spaces For nonnegative integers k, $p \geqslant 1$ we define the *Sobolev space*

$$W_p^k(\Omega) = \{u \in L^0(\Omega) : \quad \partial^\alpha u \in L^p(\Omega) \quad \text{for all } |\alpha| \leqslant k\},$$

where the partial derivatives $D^\alpha u$ are understood in the weak sense, see, e.g., [47]. The corresponding norm is defined as

$$\|u\|_{W_p^k(\Omega)} = \begin{cases} \left(\sum_{|\alpha|\leqslant k} \int_\Omega |\partial^\alpha u|^p \, dx\right)^{1/p}, & 1 \leqslant p < \infty, \\ \sum_{|\alpha|\leqslant k} \operatorname{ess\,sup}_\Omega |\partial^\alpha u| \, dx, & p = \infty. \end{cases}$$

Similarly, we define the useful Sobolev space

$$W_p^{2,1}(Q_T) = \{u : \quad u,\ \partial^\alpha u,\ \partial_t u \in L^p(Q_T), \quad |\alpha| \leqslant 2\},$$

where the corresponding norm is given by

$$\|u\|_{W_p^{2,1}(Q_T)} = \|u\|_{L^p(Q_T)} + \|\partial_t u\|_{L^p(Q_T)} + \sum_{|\alpha|\leqslant 2} \|\partial^\alpha u\|_{L^p(Q_T)}.$$

Hölder spaces Let Ω be a bounded domain. For $0 < \lambda, \gamma < 1$ we define the *Hölder seminorms*

$$< u >_{x,\bar{Q}_T}^{\lambda} = \max_{(x_1,t),(x_2,t)\in\bar{Q}_T} \frac{|u(x_1,t) - u(x_2,t)|}{|x_1 - x_2|^\lambda},$$

$$< u >_{t,\bar{Q}_T}^{\gamma} = \max_{(x,t_1),(x,t_2)\in\bar{Q}_T} \frac{|u(x,t_1) - u(x,t_2)|}{|t_1 - t_2|^\gamma}.$$

These seminorms allow us to introduce for any nonnegative integer k the *Hölder space* $C^{k+\lambda,\gamma}(\bar{Q}_T)$. It contains all functions with finite norm

$$\|u\|_{C^{k+\lambda,\gamma}(\bar{Q}_T)} = \sum_{|\alpha|\leqslant k} \left(\|\partial^\alpha u\|_{C^{0,0}(\bar{Q}_T)} + < \partial^\alpha u >_{x,\bar{Q}_T}^{\lambda} + < \partial^\alpha u >_{t,\bar{Q}_T}^{\gamma}\right).$$

Another Hölder space that we will employ is $C^{2+\lambda,1+\gamma}(\bar{Q}_T)$ with its norm

$$\|u\|_{C^{2+\lambda,1+\gamma}(\bar{Q}_T)} = \|u\|_{C^{2+\lambda,\gamma}(\bar{Q}_T)} + \|\partial_t u\|_{C^{\lambda,\gamma}(\bar{Q}_T)}.$$

Decaying functions We say that the function $u \in C^1(\mathbb{R}^d)$ has sufficient decay at infinity if there is a sufficiently large $k \in \mathbb{N}$ with

$$\lim_{|x|\to\infty} u(x), \quad \lim_{|x|\to\infty} \nabla u(x) = o(|x|^{-k}),$$

such that for any $v, \mathbf{w} \in C^1(\Omega)$ needed we have

$$\lim_{r\to\infty} \int_{\partial B_r(0)} u\, v \, dx = 0, \quad \lim_{r\to\infty} \int_{\partial B_r(0)} \nabla u \cdot \mathbf{w} \, dx = 0.$$

This allows for integration by parts on the whole space $\mathbb{R}^d$.

3.3 Parabolic PDEs and Sobolev embeddings

In this thesis we will consider PDEs of first and second order. We follow [61] and call solutions to these equations *strong solutions* provided they are regular enough that all derivatives appearing are weak and the solution belongs to the corresponding Sobolev space. Thus, a strong solution would belong to the space $W_p^{2,1}(Q_T)$ in the case of a second order PDE. We refer to solutions of PDEs as *classical solutions* if all terms are pointwise well-defined.

Parabolic theory We will use some results on the existence, uniqueness and regularity of solutions to parabolic equations. Let us therefore consider the general problem

$$\partial_t u - D\Delta u + \sum_{i=1}^{d} a_i \frac{\partial u}{\partial x_i} + au = f \text{ in } Q_T, \tag{3.2}$$

$$\partial_\nu u = 0 \text{ in } \partial\Omega \times (0,T), \tag{3.3}$$

$$u(\cdot,0) = u_0 \text{ in } \Omega, \tag{3.4}$$

where $D > 0$ is constant and a, a_i and f are real valued functions defined in Q_T. For the initial condition we assume for a fixed $\lambda \in (0,1)$ that

$$u_0(x) \geqslant 0, \quad u_0 \in C^{2+\lambda}(\bar{\Omega}). \tag{3.5}$$

Moreover, we assume that the compatibility condition

$$\partial_\nu u_0 = 0, \quad x \in \partial\Omega \tag{3.6}$$

holds. Again, let Ω be a bounded domain. For finite T we will consider solutions of the above problem on the cylinder Q_T.

The first result that we will employ follows from [106, Chapter IV, Theorem 9.1, p. 341]. It establishes a unique strong solution if the coefficients of the problem belong to sufficiently regular Bochner spaces.

Theorem 3.1 *Let* (3.5) *and* (3.6) *hold and let the coefficients of the parabolic problem* (3.2) *satisfy*

$$a\,, a_i \in L^{d+2}(Q_T), \quad f \in L^p(Q_T), \quad 1 \leqslant i \leqslant d, \quad \partial\Omega \in C^2$$

for $d + 2 < p$ *and further*

$$\lim_{\tau\to 0} \|a\|_{L^p(\Omega\times(t,t+\tau))} = \lim_{\tau\to 0} \|a_i\|_{L^p(\Omega\times(t,t+\tau))} = 0.$$

Then the problem (3.2)– (3.4) *has the unique solution*

$$u \in W_p^{2,1}(Q_T),$$

which can be bounded by

$$\|u\|_{W_p^{2,1}(Q_T)} \leqslant C\left(\|f\|_{L^p(Q_T)} + \|u_0\|^{2-2/p}_{L^p(\Omega)}\right).$$

A second statement that we will use to raise the regularity of functions in parabolic equations follows from [106, Chapter IV, Theorem 5.3 p. 320]. It establishes a classical solution of the parabolic problem in the case of sufficiently smooth coefficients.

Theorem 3.2 *Assume that* (3.5) *and* (3.6) *are satisfied and*

$$a\,, a_i,\ f \in C^{\lambda,\lambda/2}(\bar{Q}_T), \quad 1 \leqslant i \leqslant d, \quad 0 < T < 1, \quad \partial\Omega \in C^{2+\lambda}.$$

Then the problem (3.2)–(3.4) *has the unique solution*

$$u \in C^{2+\lambda,1+\lambda/2}(\bar{Q}_T).$$

Maximum principle The following result on the positivity of PDE solutions follows from the parabolic maximum principle. See [52, p. 41] for further details. Let u satisfy the differential inequality

$$\partial_t u - D\Delta u + \mathbf{v} \cdot \nabla u + cu \geqslant 0 \tag{3.7}$$

pointwise in Q_T together with homogeneous Neumann boundary conditions and initial condition $C^2(\Omega) \ni u(\cdot, 0) = u_0 \geqslant 0$. Further, assume continuous and bounded real functions $\mathbf{v}$ and c defined in Q_T and let $D > 0$. Then it holds that $u \geqslant 0$ in Q_T.

Sobolev embeddings For two normed function spaces X and Y we use the notation

$$X \hookrightarrow Y$$

if X is a vector subspace of Y and the embedding operator mapping X to Y is continuous. The latter condition means that for $u \in X$ the inequality

$$\|u\|_Y \leqslant C\|u\|_X$$

is true and the embedding constant C depends only on the spaces X and Y.

We consider here for Lipschitz domains Ω the general Sobolev embedding

$$W_p^k(\Omega) \hookrightarrow L^q(\Omega), \tag{3.8}$$

which is true provided

$$k < \frac{d}{p}, \quad \frac{1}{q} \leqslant \frac{1}{p} - \frac{k}{d}. \tag{3.9}$$

The embedding constant in this case depends only on the numbers k, p, $d \geqslant 1$ and on the domain Ω [1]. In the case $k = 1$, in particular, this embedding yields

$$W_p^1(\Omega) \hookrightarrow L^q(\Omega), \quad p < d, \quad q \leqslant \frac{dp}{d-p}. \tag{3.10}$$

In addition to Sobolev embeddings for Lebesgue spaces, we will employ two embeddings for Bochner spaces which follow from [106, Chapter II, Lemma 3.3, p. 80]. The first one embeds Bochner spaces into Hölder spaces and reads

$$W_p^{2,1}(Q_T) \hookrightarrow C^{1+\lambda,(1+\lambda)/2}(\bar{Q}_T), \quad d \in \{1, 2, 3\}, \quad p > 5, \quad \lambda = 1 - \frac{5}{p}. \tag{3.11}$$

The second one embeds functions of higher regularity into higher Lebesgue spaces in the following way

$$W_p^{2,1}(Q_T) \hookrightarrow W_q^{1,0}(Q_T), \quad d = 2, \quad p \geqslant 4, \quad q \geqslant p. \tag{3.12}$$

3.4 Inequalities and Gronwall's Lemma

In this section we gather some common inequalities that we will use later on. And we consider two useful statements to resolve differential inequalities.

Young's inequality For nonnegative x, $y \in \mathbb{R}$ and p, $q > 1$ such that $\frac{1}{p} + \frac{1}{q} = 1$ *Young's inequality* holds and reads

$$xy \leqslant \frac{x^p}{p} + \frac{y^q}{q}. \tag{3.13}$$

The inequality is often used in the scaled form

$$xy \leqslant \varepsilon x^p + \frac{(p\varepsilon)^{1-q}}{q} y^q \tag{3.14}$$

for $\varepsilon > 0$. This yields, in particular, in the case $p = q = 2$ that

$$xy \leqslant \varepsilon x^2 + \frac{1}{4\varepsilon} y^2 \leqslant \frac{1}{2}(\varepsilon x^2 + \varepsilon^{-1} y^2), \tag{3.15}$$

which is also true for negative values of x and y. See [113].

Hölder's inequality See, e.g., [47]. Assume again $p, q > 1$ such that $\frac{1}{p} + \frac{1}{q} = 1$, then it holds for measurable functions u and v that

$$\|uv\|_{L^1(\Omega)} \leqslant \|u\|_{L^p(\Omega)} \|v\|_{L^q(\Omega)}. \tag{3.16}$$

Gagliardo-Nirenberg inequality In some places in this thesis we will make use of the *Gagliardo-Nirenberg interpolation inequality*. We consider, in particular, the form from [42, 79] which states that for any $u \in W^1_q(\Omega)$ the estimate

$$\|u\|_{L^p(\Omega)} \leqslant C\|u\|^{\alpha}_{W^1_q(\Omega)} \|u\|^{(1-\alpha)}_{L^r(\Omega)} \tag{3.17}$$

is true provided $1 \leqslant p, q, r$ and $0 < \alpha < 1$ where

$$\alpha\left(1 - \frac{d}{q} + \frac{d}{r}\right) = \frac{d}{r} - \frac{d}{p}. \tag{3.18}$$

Another version we will use has been proposed in [106, Chapter II, Theorem 2.2, p. 62]. It states

$$\left\| u - \frac{1}{|\Omega|} \int_\Omega u \, dx \right\|_{L^2(\Omega)} \leqslant C\|\nabla u\|^{2a}_{L^2(\Omega)} \|u\|^{2(1-a)}_{L^1(\Omega)}, \tag{3.19}$$

for $\alpha = d/(d+2)$ and any $u \in W^1_2(\Omega)$.

Gronwall Lemma The following version of the *Gronwall Lemma* will be useful. It follows from the usual integral form, see, e.g., [5].

Lemma 3.3 (Gronwall) *Let f, α and β be real valued continuous functions defined in $I \subset \mathbb{R}$ with $(0, T) \subseteq I$. Further, let f be differentiable and α, β be nonnegative for all $t \in (0, T)$ and assume*

$$\partial_t f(t) \leqslant \alpha(t) + \beta(t) f(t).$$

Then for all $t \in (0, T)$ it holds that

$$f(t) \leqslant \left[\int_0^t \alpha(s)\, ds + f(0)\right] \exp\left(\int_0^t \beta(s)\, ds\right).$$

We moreover need the following elementary lemma for differential inequalities.

Lemma 3.4 *Let f be a real valued continuously differentiable function defined in the real interval I that includes $(0,T)$ and assume*

$$\partial_t f(t) \leqslant -\beta f(t) + K, \quad t \in (0,T)$$

holds for $\beta, K \in \mathbb{R}_+$. Then for all $t \in (0,T)$ the following inequality is fulfilled

$$f(t) \leqslant f(0) + \frac{K}{\beta}.$$

Proof. After multiplying both sides of the differential inequality with $e^{\beta t}$ and integrating over $(0,t)$ we get

$$f(t)e^{\beta t} - f(0) - \int_0^t \beta e^{\beta s} f(s)\,ds \leqslant \frac{K}{\beta} e^{\beta t} - \int_0^t \beta e^{\beta s} f(s)\,ds.$$

This implies the statement of the lemma after adding the integral on both sides and dividing by $e^{\beta t}$. □

4 Analytical study

In this chapter we investigate several topics in the mathematical analysis of cancer invasion models. Since this class of models is built upon the Keller-Segel model, we will start by discussing some of its characteristics such as the possible blowup in finite time. We will elaborate on the literature of this model in Section 4.1 and on the prevention of the mentioned blowup in Section 4.2. Subsequently, we will proceed to cancer invasion models and give a short summary of the existing literature in Section 4.3. The main goal of this chapter is to prove the global existence of a unique classical solution to a slightly simplified version of model (II). This proof is provided in Sections 4.5–4.8. We will also comment on a possible extension of the result to the case of the full model (II) in Section 4.9.

4.1 The Keller-Segel model

In Section 2.4 we introduced the Keller-Segel model as a popular mathematical model for the collective movement of cells. This system of two equations, modeling the migration of cells to an chemo-attractant that is emitted by the cells themselves, exhibits interesting dynamics that gave rise to an enormous interest of mathematicians over the last forty years.

Due to the remarkable dynamics of the solution, the model is capable of modeling various biological phenomena such as the swarming of Escherichia coli bacteria [21] and the aggregation of the slime mold Dictyostelium. The latter phenomenon is associated with *blowup* of the cell density, i.e. with a solution that becomes a Dirac mass in finite time [84].

In this section we outline some results from the existence theory of the general Keller-Segel model

$$\begin{cases} \partial_t c = \nabla \cdot (D_c \nabla c - \chi c \nabla a), \\ \varepsilon\, \partial_t a = D_a \Delta a + \alpha c - \beta a, \end{cases} \tag{KS}$$

for which we assume nonnegative and smooth initial data $c_0 = c(\cdot, 0)$, $a_0 = a(\cdot, 0) \in C^2(\Omega)$ for both the cell and the chemo-attractant densities. Moreover, we assume positive diffusion rates D_c, D_a, chemotactic sensitivity χ and production and decay rates α and β. The parameter $\varepsilon \in \{0, 1\}$ allows to deal either with the *parabolic-elliptic* case ($\varepsilon = 0$) or with the *parabolic-parabolic* case ($\varepsilon = 1$). The parabolic-elliptic model assumes that the chemical with density a admits the steady state of the parabolic equation due to the diffusion and reaction of the chemo-attractant being significantly faster than the cell migration. The parabolic-parabolic case of (KS) is mathematically more difficult to handle.

If not stated otherwise, we consider (KS) on the domain Ω of the class C^2 and assume homogeneous Neumann boundary conditions (2.26) for both the cell and the chemo-attractant concentration. In this case it is clear from the divergence theorem that the mass of the cells is

preserved, i.e.

$$\frac{d}{dt}\int_\Omega c(t,x)\,dx = 0. \tag{4.1}$$

Some results from the literature also consider the whole space $\Omega = \mathbb{R}^d$. Here the weak solutions of (KS) are constructed such that mass conservation (4.1) is still satisfied.

We will see in Theorem 4.1 that in space dimension $d = 2$ the *initial mass* of the cells

$$M_0 = \int_\Omega c_0(t,x)\,dx \tag{4.2}$$

constitutes a crucial quantity in the existence theory.

Blowup in a simplified case To give a mathematical insight in blowup in dimension $d = 2$ and its relation to the initial mass M_0 we follow the argument from [124, 135]. Therefore, we consider (KS) in the simple case $D_c = D_a = \alpha = 1,\ \varepsilon = \beta = 0$ that reads

$$\begin{cases} \partial_t c = \nabla\cdot(\nabla c - \chi c\nabla a), \\ \quad 0 = \Delta a + c. \end{cases} \tag{4.3}$$

We assume that both concentration functions $c(x,t)$ and $a(x,t)$ are defined on the whole space, i.e. $x \in \mathbb{R}^2$. If there was a solution (c,a) satisfying (4.3) in the classical sense, it could not exist globally in time as the following argument shows.

Theorem 4.1 *Let* (c,a) *be a classical solution to* (4.3) *with sufficient decay at infinity and initial mass* $M_0 > 8\pi/\chi$. *Then* (c,a) *can only exist up to a finite time, i.e. for* $t \in (0,T^*)$ *where* $T^* < \infty$.

Proof. Due to the ellipticity of the second equation in (4.3), we can use the Poisson kernel to rewrite the density of the chemo-attractant as

$$a(x,t) = -\frac{1}{2\pi}\int_{\mathbb{R}^2} \log|x-y|\,c(y,t)\,dy, \tag{4.4}$$

and thus its gradient recasts into

$$\nabla a(x,t) = -\frac{1}{2\pi}\int_{\mathbb{R}^2} \frac{x-y}{|x-y|^2}\,c(y,t)\,dy. \tag{4.5}$$

Now we consider the second moment of the cell concentration c given by

$$M^2(t) = \frac{1}{2}\int_{\mathbb{R}^2} |x|^2\,c(x,t)\,dx. \tag{4.6}$$

We can compute its time derivative employing (4.3), integration by parts, (4.5) and an inter-

change of variables. We obtain

$$\begin{aligned}
\frac{d}{dt}M^2(t) &= \frac{1}{2}\int_{\mathbb{R}^2} |x|^2\, \partial_t c\, dx \\
&= \frac{1}{2}\int_{\mathbb{R}^2} |x|^2\, \left(\Delta c - \nabla\cdot[\chi c \nabla a]\right)\, dx \\
&= \int_{\mathbb{R}^2} 2\,c + \chi c\, x\cdot\nabla a\, dx \\
&= 2\,M_0 - \frac{\chi}{2\pi}\int_{\mathbb{R}^2}\int_{\mathbb{R}^2} c(x,t)c(y,t)\frac{x\cdot(x-y)}{|x-y|^2}\, dx\, dy \\
&= 2\,M_0 - \frac{\chi}{4\pi}\int_{\mathbb{R}^2}\int_{\mathbb{R}^2} c(x,t)c(y,t)\frac{x\cdot(x-y)}{|x-y|^2}\, dx\, dy \\
&\qquad - \frac{\chi}{4\pi}\int_{\mathbb{R}^2}\int_{\mathbb{R}^2} c(y,t)c(x,t)\frac{-y\cdot(x-y)}{|x-y|^2}\, dx\, dy \\
&= 2\,M_0\left(1 - \frac{\chi}{8\pi}M_0\right). \qquad (4.7)
\end{aligned}$$

The boundary terms at infinity have been dropped due to the assumed decay in the functions c and a. For $M_0 > 8\pi/\chi$ the identity (4.7) implies a decay with a constant rate. Consequently, the second moment $M^2(t)$ becomes negative in finite time. However, in the case of a classical solution, the second moment (4.6) must be nonnegative by the nonnegativity of c that follows from the parabolic maximum principle, see Section 3.3. Therefore, the classical solution can only exist in a bounded time interval. □

The result above was extended to the case of weak solutions in $L^\infty(\mathbb{R}_+, L^1(\Omega))$. Hence, the solution to model (4.3) does not even stay in $L^1(\Omega)$ after a finite time for a sufficiently large initial mass [124]. Indeed, the density blows up, i.e. it concentrates to a Dirac mass. This was shown for radially symmetric initial data in [71] and it was numerically observed, e.g., in [31]. In generalized form, the solutions of model (KS) were extended to times after blowup in [43].

Free energy and analytical results from the literature In what follows we gather some analytical results about system (KS) from the literature. We distinguish here the case of an elliptic chemo-attractant from the case of a parabolic chemo-attractant. The latter is mathematically more challenging but more relevant for the study of cancer invasion systems.

While the global existence of classical solutions was unconditionally verified in dimension $d = 1$, the mass of the cell density determines if a global weak solution can be found in dimension $d = 2$. More generally, the existence of a global weak solution in dimension $d > 1$ depends on a bound on the quantity $\|c_0\|_{L^{d/2}(\Omega)}$.

Note that we do not present all known properties of the existing solutions. Neither do we give definitions of the weak solutions since they were adjusted to each particular case. For more details we refer to the references given in both theorems.

Theorem 4.2 (The parabolic-elliptic Keller-Segel model) *We consider* (KS) *in the parabolic-elliptic case, i.e.* $\varepsilon = 1$.

1. *(1D [124]) For dimension* $d = 1$ *system* (KS) *admits a global classical solution that is uniformly bounded for all* $t \geqslant 0$.

2. *(2D, global existence [124]) Assume* $d = 2$ *and*

$$M_0 < \frac{4\pi D_c D_a}{\alpha\chi}.$$

Then there exists a global classical solution to (KS) *with a uniform time independent bound.*

3. *(2D, blowup [126]) Let* $d = 2,\ q \in \Omega$ *and assume that* $\int_\Omega c_0(x)|x-q|^2\,dx$ *is sufficiently small. If further*

$$M_0 > \frac{8\pi D_c D_a}{\alpha\chi},$$

then the solution blows up in finite time. The same is true for $\Omega = \mathbb{R}^2$ *[125].*

4. *(Higher dimensions [36]) For dimension* $d \geqslant 2$, $\Omega = \mathbb{R}^d$ *and* $c_0 \in L^1_+(\mathbb{R}^d)$ *there exists a constant* K *depending on* d *and the parameters in* (KS)*, such that if*

$$\|c_0\|_{L^{d/2}(\mathbb{R}^d)} \leqslant K,$$

then there exists a global weak solution (c, a)*. This solution satisfies for all* $t > 0$ *the bounds*

$$\|c(t)\|_{L^p(\mathbb{R}^d)} \leqslant \|c_0\|_{L^p(\mathbb{R}^d)}, \qquad \max\left\{1,\ \frac{d}{2}-1\right\} \leqslant p \leqslant \frac{d}{2},$$

$$\|c(t)\|_{L^p(\mathbb{R}^d)} \leqslant C(t,\ K,\ \|c_0\|_{L^p(\mathbb{R}^d)}), \qquad \frac{d}{2} < p \leqslant \infty.$$

The mathematical literature on the parabolic-elliptic model is very extensive. In the 2D case there are further results on conditions for blowup and global existence of weak solutions [126]. There also exists a theory about blowup in the case $d \geqslant 3$. For more details we refer to the review [77, 78].

Theorem 4.3 (The parabolic-parabolic Keller-Segel model) *We consider* (KS) *in the parabolic-parabolic case, i.e.* $\varepsilon = 1$.

1. *(1D [131]) In dimension* $d = 1$ *there exists a classical global solution if the interval* Ω *is bounded.*

2. *(2D [24]) Assume* $d = 2$ *and* $\Omega = \mathbb{R}^2$*. Let the nonnegative initial data* (c_0, a_0) *satisfy*

$$c_0 \in L^1(\mathbb{R}^2) \cap L^1(\mathbb{R}^2, \log(1+|x|^2)), \qquad c_0 \log c_0 \in L^1(\mathbb{R}^2),$$
$$a_0 \in H^1(\mathbb{R}^2), \qquad c_0\, a_0 \in L^1(\mathbb{R}^2),$$

and let the initial mass be bounded by

$$M_0 < \frac{8\pi D_c D_a}{\alpha\chi}. \tag{4.8}$$

Then there exists a global weak nonnegative solution (c, a) *of* (KS) *for which it holds that*

$$c \in L^\infty((0,\infty); L^1(\mathbb{R}^2)) \cap L^\infty_{loc}((0,\infty); L^1(\mathbb{R}^2, \log(1+|x|^2)),$$
$$c \log c \in L^\infty_{loc}((0,\infty); L^1(\mathbb{R}^2)), \quad a \in L^\infty_{loc}((0,\infty); H^1(\mathbb{R}^2)).$$

3. *(higher dimensions [37]) Let* $d \geqslant 3$, $c_0 \in L^1(\mathbb{R}^d) \cap L^a(\mathbb{R}^d)$ *for* $d/2 < a \leqslant d$ *and* $\nabla a_0 \in L^d(\mathbb{R}^d)$. *Then there is a constant* $K(d, a)$, *such that if*

$$\|c_0\|_{L^a(\mathbb{R}^d)} + \|\nabla a_0\|_{L^{ad}(\mathbb{R}^d)} \leqslant K,$$

then there exists a weak global solution to (KS).

To our knowledge there is no proof that the weak solution in the parabolic-parabolic case exists only up to a finite time above a critical initial mass M_0. However, numerical experiments indicate that the same blowup phenomenon of the cell concentration occurs similarly to the parabolic-elliptic case [31, 103].

In the existence analysis of system (KS) the *free energy* functional played a central role, see the references in Theorems 4.2 and 4.2. In the case of the parabolic-parabolic system ($\varepsilon = 1$) this functional is given by

$$\mathcal{E}(t) = \frac{D_c}{\chi} \int_\Omega c \log c \, dx - \int_\Omega c\, a \, dx + \frac{D_a}{2\alpha} \int_\Omega |\nabla a|^2 \, dx + \frac{\beta}{2\alpha} \int_\Omega a^2 \, dx. \tag{4.9}$$

This time dependent quantity is a *Lyaponov* functional of system (KS), which means that it decreases monotonically in time for any solution (c, a) of (KS). Following [24], we can prove this property for (4.9) in the case of a smooth domain Ω and homogeneous Neumann boundary conditions.

Lemma 4.4 (The free energy principle) *Let* $(c,\ a)$ *be a classical solution to* (KS) *in the parabolic-parabolic case* ($\varepsilon = 1$) *with homogeneous Neumann boundary conditions in* $\Omega \times (0, T)$. *Then the free energy* $\mathcal{E}$ *given by* (4.9) *satisfies*

$$\frac{d}{dt}\mathcal{E}(t) = -\frac{1}{\chi} \int_\Omega c|\nabla(D_c \log c - \chi a)|^2 - \frac{1}{\alpha} \int_\Omega |\partial_t a|^2 \, dx < 0 \tag{4.10}$$

for $0 < t < T$ *and is thus monotonically decreasing.*

Proof. We proceed in two steps and firstly compute

$$\begin{aligned}
D_c \frac{d}{dt} \int_\Omega c \log c - \chi \int_\Omega \partial_t c a \, dx & \\
&= D_c \int_\Omega \partial_t c \log c \, dx + D_c \frac{d}{dt} \int_\Omega c \, dx - \chi \int_\Omega \partial_t c a \, dx \\
&= \int_\Omega \partial_t c \left(D_c \log c - \chi a\right) \, dx \\
&= \int_\Omega \nabla \cdot (c \nabla (D_c \log c - \chi a)) \left(D_c \log c - \chi a\right) \, dx \\
&= -\int_\Omega c \, |\nabla (D_c \log c - \chi a)|^2 \, dx,
\end{aligned} \tag{4.11}$$

where we have applied the mass conservation in c, integration by parts and the homogeneous Neumann boundary condition. Moreover, we have used that the evolution equation for the cells in (KS) can be rewritten as

$$\partial_t c = \nabla \cdot (c \nabla (D_c \log c - \chi a)) .$$

In the second step we multiply the equation for the chemo-attractant in (KS) by $\partial_t a$ and integrate. We obtain by the product rule, integration by parts, the homogeneous Neumann boundary conditions in c and Schwarz's theorem that

$$\begin{aligned}\int_\Omega |\partial_t a|\,dx &= D_a \int_\Omega \Delta a \partial_t a\,dx + \alpha \int_\Omega c\,\partial_t a\,dx - \beta \int_\Omega a\,\partial_t a\,dx \\ &= -D_a \int_\Omega \nabla a \cdot \nabla(\partial_t a)\,dx + \alpha \int_\Omega c\,\partial_t a\,dx - \frac{\beta}{2}\frac{d}{dt}\int_\Omega a^2\,dx \\ &= -\frac{D_a}{2}\frac{d}{dt}\int_\Omega |\nabla a|^2\,dx + \alpha \int_\Omega c\,\partial_t a\,dx - \frac{\beta}{2}\frac{d}{dt}\int_\Omega a^2\,dx. \end{aligned} \tag{4.12}$$

We end up with the free energy dissipation (4.10) by taking the difference of (4.11) and (4.12) divided by χ and α, respectively. □

Note that the same result can be obtained for (KS) on the whole space $\mathbb{R}^d$ when assuming sufficient decay at infinity. In the parabolic-elliptic case or in the case of vanishing parameters, system (KS) admits different free energy functionals.

Remark 4.5 For the parabolic-elliptic system ($\varepsilon = 0$) the free energy principle is still valid for adjusted functionals. For instance, for the parameters $\varepsilon = 0$, $D_c = D_a = \alpha = 1$ the free energy is given by

$$\mathcal{E}(t) = \int_\Omega c\,\log c\,dx - \frac{\chi}{2}\int_\Omega c\,a\,dx, \tag{4.13}$$

see also [135].

The free energy will play a key role in the derivation of the numerical method in Chapter 7.

4.2 Preventing blowup

Blowup of the cancer cell concentration in the Keller-Segel model is often problematic. This is not only because of numerical complications. Also in many modeling cases blowup is undesirable. While it is a reasonable feature of the model in the aggregation of Dictyostelium, in applications such as the modeling of swarming phenomena or cancer, a concentration to a single point is not expected.

In literature different strategies were proposed to prevent blowup by modifying the Keller-Segel model. In [27, 76] cross diffusion terms were added to establish global bounds. Moreover, in [75] the authors could also prevent blowup by replacing the chemical gradient in the cell evolution equation by a nonlocal term. Here we consider an explicit saturation of the flux term proposed in [33, 103] to overcome blowup. We will exhibit that this modification introduces a possibility to show *a priori* estimates of the solutions even in more complex generalizations of (KS).

To this end we consider the modified parabolic-parabolic model

$$\begin{cases} \partial_t c = \nabla \cdot (D_c \nabla c - c\,Q(\chi \nabla a)) + \mu c(1-c), \\ \partial_t a = D_a \Delta a + \alpha c - \beta a, \end{cases} \tag{4.14}$$

where we have added logistic growth according to (2.9) to model resource restricted cell proliferation. Also, we included the continuous saturation function Q given by

$$Q(\chi\nabla a) = \begin{cases} \chi\nabla a, & \text{if } \chi|\nabla a| \leqslant S, \\ \left(\dfrac{\chi|\nabla a| - S}{\sqrt{1 + (\chi|\nabla a| - S)^2}} + S \right) \dfrac{\nabla a}{|\nabla a|}, & \text{otherwise} \end{cases} \tag{4.15}$$

for a positive S. The function Q admits a bound on the advection velocity by

$$|Q(\chi\nabla a)| < S + 1 = C_1. \tag{4.16}$$

Global existence of weak solutions in the above system for the case $\mu = 0$ was shown in [33]. In what follows we provide explicit L^∞ bounds for the more general system (4.14). The following theorem improves our recent result in [96].

Theorem 4.6 *Consider* (4.14) *on* $\Omega \times (0, T)$ *for* $0 < T < \infty$, *a bounded* C^2 *domain* $\Omega \subset \mathbb{R}^d$ *and homogeneous Neumann boundary conditions*

$$\frac{\partial c}{\partial \nu} = \frac{\partial a}{\partial \nu} = 0, \quad x \in \partial\Omega, \quad t > 0. \tag{4.17}$$

Let (c, a) *be a positive classical solution with bounded nonnegative initial data. Then the estimates*

$$c(x,t) \leqslant C_2 \max\left\{ \|c_0\|_{L^\infty(\Omega)}, \ \|c_0\|_{L^1(\Omega)}, \ |\Omega| \right\},$$
$$a(x,t) \leqslant \|a_0\|_{L^\infty(\Omega)} + \frac{C_2\alpha}{\beta} \max\left\{ \|c_0\|_{L^\infty(\Omega)}, \ \|c_0\|_{L^1(\Omega)}, \ |\Omega| \right\}$$

hold for all $x \in \bar{\Omega}$ *and* $t \in [0, T]$ *where*

$$C_2 = C_3 \left(1 + \frac{2D_c\mu}{C_1^2} \right)^2 \left(1 + \frac{\sqrt{C_1^2 + 2\mu D_c}}{D_c} \right)^{2d},$$

and C_3 *depends on* Ω *only.*

Proof. We follow [103] and use the iteration technique by Moser–Alikakos [4]. To start with we multiply the first equation of (4.14) by c^{s-1} for $s \geqslant 2$. Integration by parts, the identity

$$\nabla(c^{s/2}) = \frac{s}{2} \nabla c \, c^{s/2-1},$$

the nonnegativity of c, the bound on Q and Young's inequality (3.15) yield

$$\begin{aligned}
\frac{1}{s}\frac{d}{dt}\int_\Omega c^s\,dx &= -D_c\int_\Omega \nabla c\cdot\nabla(c^{s-1})\,dx + \mu\int_\Omega c^s(1-c)\,dx \\
&\quad + \int_\Omega cQ(\chi\nabla a)\cdot\nabla(c^{s-1})\,dx \\
&\leqslant -\frac{4D_c(s-1)}{s^2}\int_\Omega |\nabla(c^{s/2})|^2\,dx + \mu\int_\Omega c^s\,dx \\
&\quad + \frac{2C_1(s-1)}{s}\int_\Omega c^{s/2}|\nabla(c^{s/2})|\,dx \\
&\leqslant -\frac{4D_c(s-1)}{s^2}\|\nabla(c^{s/2})\|^2_{L^2(\Omega)} + \mu\int_\Omega c^s\,dx \\
&\quad + \frac{2C_1(1-s)}{s}\int_\Omega \frac{1}{2}\left(\frac{2D_c}{C_1 s}|\nabla(c^{s/2})| + \frac{C_1 s}{2D_c}c^s\right)dx \\
&\leqslant -\frac{2D_c(s-1)}{s^2}\|\nabla(c^{s/2})\|^2_{L^2(\Omega)} + \frac{C_1^2(s-1)+2D_c\mu}{2D_c}\|c^s\|_{L^1(\Omega)}.
\end{aligned}$$

We can further estimate this expression using the inequality

$$\|\omega\|^2_{L^2(\Omega)} \leqslant \varepsilon\|\nabla\omega\|^2_{L^2(\Omega)} + C_4(1+\varepsilon^{-d/2})\|\omega\|^2_{L^1(\Omega)} \tag{4.18}$$

that follows from the Gagliardo-Nirenberg interpolation formula (3.19) and Young's inequality. The constant C_4 depends only on the domain Ω and a chosen ε. We choose ε, such that

$$\frac{C_1^2(s-1)+2D_c\mu}{2D_c} = \frac{2D_c(s-1)}{s^2\varepsilon} - \frac{C_1^2(s-1)+2D_c\mu}{2D_c} \tag{4.19}$$

and get

$$\varepsilon = \frac{2D_c^2(s-1)}{C_1^2 s^2(s-1)+2D_c\mu s^2} > 0.$$

By (4.19) we can now write

$$\begin{aligned}
\left(\frac{2D_c(s-1)}{s^2\varepsilon} - \frac{C_1^2(s-1)+2D_c\mu}{2D_c}\right)\int_\Omega c^s\,dx & \\
\leqslant \frac{2D_c(s-1)}{s^2}\|\nabla(c^{s/2})\|^2_{L^2(\Omega)} + \frac{2D_c(s-1)C_4(1+\varepsilon^{-\frac{d}{2}})}{s^2\varepsilon}\|c^{s/2}\|^2_{L^1(\Omega)} & \\
- \frac{C_1^2(s-1)+2D_c\mu}{2D_c}\int_\Omega c^s\,dx. &
\end{aligned} \tag{4.20}$$

Thus, the dependence on $\nabla(c^{s/2})$ in the above estimate vanishes. Using then the estimate $\varepsilon^{-1/2} \leqslant s\sqrt{C^2+2\mu D_c}/D_c$ we obtain

$$\begin{aligned}
\frac{d}{dt}\int_\Omega c^s\,dx &\leqslant -\frac{sC_1^2(s-1)+2sD_c\mu}{2D_c}\int_\Omega c^s\,dx \\
&\quad + D_c^{-1}C_4 s\left(1+\left(\frac{s\sqrt{C_1^2+2\mu D_c}}{D_c}\right)^d\right)(C_1^2(s-1)+2D_c\mu)\|c^{s/2}\|^2_{L^2(\Omega)}.
\end{aligned}$$

Here we estimate the second term from above by its maximum over time and apply the Gronwall Lemma (see Lemma3.4 for $\beta = (sC_1^2(s-1) + 2sD_c\mu)/2D_c$) to get

$$\int_\Omega c^s(x,t)\,dx \leqslant \int_\Omega c_0^s\,dx + 2C_4\left(1+\frac{2D_c\mu}{C_1^2(s-1)}\right)\left(1+\frac{s\sqrt{C_1^2+2\mu D_c}}{D_c}\right)^d \sup_{0\leqslant t\leqslant T}\|c^{s/2}\|^2_{L^2(\Omega)}.$$

Hence, the s-dependent quantity

$$M(s) = \max\left\{\|c_0\|_{L^\infty(\Omega)}, \sup_{0\leqslant t\leqslant T}\left(\int_\Omega c^s\,dx\right)^{\frac{1}{s}}\right\}$$

satisfies the recursive inequality

$$M(s) \leqslant \left(C_5\left(1+\frac{2D_c\mu}{C^2(s-1)}\right)\left(1+\frac{s\sqrt{C_1^2+2\mu D_c}}{D_c}\right)^d\right)^{\frac{1}{s}} M\left(\frac{s}{2}\right).$$

We define the sequence $s = 2^k$ for $k \in \mathbb{N}$ and note that the following estimate holds

$$\prod_{k=1}^{\infty}\left(1+2^kC_6\right)^{\frac{d}{2^k}} \leqslant (2+2C_7)^{2d},$$

since the sum $\sum_{i=1}^{\infty}\frac{k}{2^k}$ is finite. Thus, we obtain for all $k \in \mathbb{N}$ that

$$M(2^k) \leqslant C_8\left(1+\frac{2D_c\mu}{C_1^2}\right)^2\left(1+\frac{\sqrt{C_1^2+2\mu D_c}}{D_c}\right)^{2d} M(1),$$

where C_8 depends only on Ω. In the limit as $k\to\infty$ we get

$$\|c(t)\|_{L^\infty(\Omega)} \leqslant C_8\left(1+\frac{2D_c\mu}{C_1^2}\right)^2\left(1+\frac{\sqrt{C_1^2+2\mu D_c}}{D_c}\right)^{2d} M(1). \tag{4.21}$$

Next, we consider the mass of the cell density c and integrate the first equation of (4.14). After applying the divergence theorem and using the Hölder inequality ($u=1,\ v=c^2,\ p=q=2$) we obtain

$$\frac{d}{dt}\|c\|_{L^1(\Omega)} = \mu\|c\|_{L^1(\Omega)} - \mu\|c\|^2_{L^2(\Omega)} \leqslant \mu\|c\|_{L^1(\Omega)} - \frac{\mu}{|\Omega|}\|c\|^2_{L^1(\Omega)}.$$

Here the right hand side is nonnegative only for $\|c\|_{L^1(\Omega)} \in [0,|\Omega|]$. Therefore, we have by comparison

$$M(1) = \max\left\{\|c_0\|_{L^\infty(\Omega)},\ \|c_0\|_{L^1(\Omega)},\ |\Omega|\right\}.$$

Together with (4.21) the estimate for the cell density c follows.

By the maximum principle for the heat equation the solution of the initial value problem

$$\begin{cases} \partial_t \omega = -\beta\omega + \alpha C_2 M(1), \\ \omega(0) = \|a_0\|_{L^\infty(\Omega)} \end{cases}$$

is an upper bound for the chemo-attractant concentration a. Thus, we can estimate

$$\begin{aligned} 0 \leqslant a(x,t) \leqslant \omega(t) &= e^{-\beta t}\|a_0\|_{L^\infty(\Omega)} + (1 - e^{-\beta t})\frac{\alpha C_2}{\beta} M(1) \\ &\leqslant e^{-\beta t}\|a_0\|_{L^\infty(\Omega)} + \frac{\alpha C_2}{\beta} M(1), \end{aligned}$$

which proves the L^∞ bound on the chemo-attractant density a. □

By combining these *a priori* estimates with the local existence result and further techniques used in [33], one can establish the global existence of weak solutions in model (4.14). We do not exhibit these steps in detail but refer to Section 4.5 for a strategy to derive local existence in a model of this kind.

For model (4.14) global existence in dimension $d = 2$ was shown for $\mu > 0$ in the case without saturation, i.e. $S = \infty$ [130]. Thus, a saturation function such as (4.15) is not necessary for blowup prevention in the case of logistic proliferation. Yet, the latter Theorem 4.6 delivers explicit and time independent upper bounds for any time and dimension and gives a nice insight in the theory of *a priori* estimates in KS-type systems.

For many cancer invasion models it turned out that global existence of weak or even classical solutions can be established without any explicit modifications of the model for blowup prevention. In the course of this chapter we will exhibit this for a two species cancer invasion model.

4.3 Existence analysis for cancer invasion models, *a priori* results

Due to the complex dynamics that solutions of cancer invasion models exhibit (see, e.g., our numerical experiments in Section 5.11), the question of their existence and regularity is of mathematical interest. This is, in particular, the case because of their close relation to the Keller-Segel model that might blowup in finite time as we saw in Section 4.1.

Several works in the past decade addressed this subject. We mention here indicatively some relevant results. In [172] global existence of model (2.28), one of the pioneering macroscopic descriptions of cancer invasion, was shown. Model (2.29) has been more difficult to handle since it also involves chemotaxis, cell proliferation and tissue remodeling. Thus, it has raised further analytical challenges. We can write it in a general form as

$$\begin{cases} \partial_t c = \nabla \cdot (\nabla c - \chi c \nabla v - \xi c \nabla m) + \mu_c\, c(1 - c - v), \\ \partial_t v = -\delta m v + \mu_v\, v(1 - c - v), \\ \varepsilon \partial_t m = \Delta m + c - m, \end{cases} \tag{4.22}$$

see also Section 2.5 for the model derivation.

In [119] the haptotaxis case without tissue remodeling of (4.22) was studied. In this work global existence of weak solutions was proven. Additionally, it was shown that the solutions are uniformly bounded. In [162] the author considered the case of additional self-remodeling

model restriction	dimension	result	reference
$\xi = \mu_v = 0$	$d \leqslant 3$	global weak solutions	[119]
$\xi = 0$, $\mu_c \geqslant \chi\mu_v$	$d = 2$	global unique classical solution	[162]
$\varepsilon = 0$	$d = 2$	global unique classical solution	[164]
$\mu_v = 0$	$d \leqslant 2$	global unique classical solution	[161, 163]

Table 4.1: Results on the solvability of system (4.22). We assume positive model parameters if not otherwise stated in the restrictions.

of the ECM with sufficiently large proliferation rate of the tumor cells. The global existence of classical solutions followed from using the contraction mapping theorem to provide a local solution followed by *a priori* estimates and a boot-strapping argument. A similar strategy was used in [161] where the authors proved global existence of classical solutions for the chemotaxis-haptotaxis case of (4.22) without ECM remodeling. The case of chemotaxis, haptotaxis and tissue remodeling was adressed in [164] under the equilibrium hypothesis for the MMPs ($\varepsilon = 0$). The *a priori* estimates, which were derived here to prove global existence of the unique solution, used an energy dissipation principle similar to the one we studied in Lemma 4.4. To our knowledge, the question of solvability of model (4.22) is still open in the case when all parameters are positive. We also refer to Table 4.1 for a summary on the discussed analytical results for model (4.22). Further bounds and global existence results in similar models were moreover derived, e.g., in [36, 74, 79].

In what follows we will introduce some techniques that were used in the above mentioned works. We will exhibit them in a general way such that their application is not restricted to a particular model but is rather possible for the general class of haptotaxis cancer invasion models. We will employ these techniques to prove global existence of classical solutions in the particular case of a two species invasion model. The general form allows for a discussion on how to adapt the proof to model (II) being slightly more detailed than the model we address analytically.

A maximum principle for the tissue density

In what follows we derive upper and lower bounds on the ECM concentration v in various modeling cases. As pointed out in Chapter 2, the ECM is not subject to transport phenomena and its evolution equation is given as an ODE.

For the derivation of the bounds we focus on *initial value problems* for systems of ODEs of the form

$$\frac{d}{dt}\mathbf{w} = \mathbf{F}(t, \mathbf{w}), \quad t > 0, \quad \mathbf{w}(0) = \mathbf{w}_0. \tag{4.23}$$

Here we have used a continuous mapping $F : (0, \infty) \times \mathbb{R}^d \to \mathbb{R}^d$. We recall that by the Picard-Lindelöf theorem there is a time interval $[0, T]$ in which a unique solution to (4.23) exists, if the mapping F satisfies the Lipschitz condition

$$|F(t, \mathbf{v}_1) - F(t, \mathbf{v}_2)| \leqslant L|\mathbf{v}_1 - \mathbf{v}_2|, \quad t \in [0, T], \quad v_1, v_2 \in B_R(\mathbf{w}_0) \tag{4.24}$$

for a time independent constant $L > 0$ and a fixed ball $B_R(\mathbf{w}_0)$ in $\mathbb{R}^d$ around $\mathbf{w}_0$.

The models that we consider in this work such as (4.23) yield number concentration of molecules and cells as their solutions. We expect from our physical interpretation that the

number concentrations do not become negative. In order to verify that the same is also true for the model solution, we introduce the concept of positive ODE systems.

Definition 4.7 We call system (4.23) *positive* if from $\mathbf{w}(0) \geqslant 0$ follows $\mathbf{w}(t) \geqslant 0$ for any $t > 0$ in the existence interval of the solution to the ODE system.

Suppose that the mapping F satisfies condition (4.24), one can show that (4.23) is positive if F satisfies $F(t, 0) \geqslant 0$. We present here a general formulation of this sufficient condition to establish the positivity of ODE systems.

Theorem 4.8 *[35, 80] Let the mapping $F = (F_1, \dots, F_d)$ satisfy Lipschitz condition* (4.24)*. Moreover, assume that any $\mathbf{v} = (v_1, \dots, v_d) \in \mathbb{R}^d$, which vanishes in component i and which is nonnegative in all components, i.e.*

$$\mathbf{v} \geqslant 0, \quad v_i = 0,$$

fulfills $F_i(t, \mathbf{v}) \geqslant 0$ for all t in the existence interval of the solution. Then system (4.23) *is positive.*

Note that Theorem 4.8 does not hold without the Lipschitz condition (4.24) as it was demonstrated in counterexamples, see [80].

With this theorem in mind, we can proceed to prove the bounds on the ECM concentration. We consider models that include proteolysis and tissue remodeling. The following lemma is valid for different remodeling approaches such as self remodeling, spontaneous remodeling and remodeling by a different species like fibroblast cells. For more details on these models we refer to Section 2.8.

Lemma 4.9 *Assume the nonnegative functions u, m, $c \in C^0(\mathbb{R}_+)$ and the constants δ, $\mu > 0$. We consider the function v with initial data $0 \leqslant v(0) = v_0 \leqslant 1$ determined by one of the ODEs*

$$\partial_t v = -\delta v m + \mu v(1 - v - u), \tag{4.25a}$$
$$\partial_t v = -\delta v m + \mu v(1 - v - u)^+, \tag{4.25b}$$
$$\partial_t v = -\delta v m + \mu (1 - v - u)^+, \tag{4.25c}$$
$$\partial_t v = -\delta v m + \mu_v c(1 - v - u)^+. \tag{4.25d}$$

Then in all four cases v is bounded from above and below for any $t > 0$ by

$$0 \leqslant v(t) \leqslant 1. \tag{4.26}$$

Proof. By case analysis one can easily see that the function $x \mapsto x^+$ is Lipschitz continuous. The right hand sides of (4.25b)–(4.25d) satisfy (4.24) since compositions of Lipschitz continuous functions are Lipschitz continuous. The positivity of all four ODEs (4.25a)–(4.25d) follows from the nonnegativity of u, m and c and Theorem 4.8.

The upper bound is obtained by noting that for (4.25a)–(4.25b) the function v satisfies

$$\partial_t(1 - v) \geqslant -\mu_v v(1 - v),$$

and in the cases of (4.25c) and (4.25d) we have

$$\partial_t(1 - v) \geqslant -\mu_v(1 - v), \quad \partial_t(1 - v) \geqslant -\mu_v c(1 - v),$$

respectively. We apply again Theorem 4.8 and get the nonnegativity of $1 - v$, which proves the statement of the lemma. □

We note that the case of tissue reproduction by a secondary species does not imply the above positivity principle when we allow for tissue degradation by resource restriction. This corresponds to the modeling approach

$$\partial_t v = -\delta v m + \mu_v c(1 - v - u).$$

In this model we cannot apply Theorem 4.8 and v can indeed become negative.

A variable transformation for haptotaxis systems

A crucial role in the analysis of invasion models is played by the hapto-attracting ECM density v. The existence of a classical solution for systems like (I) and (II) would require a bounded second derivative of the attracting species. In the case of a chemo-attractant one can employ parabolic theory, e.g., Theorem 3.2, to obtain bounds for these higher order derivatives of the density of the diffusing species. In the case of haptotaxis though this is not possible and thus the situation is more challenging.

To facilitate these circumstances, a variable transformation was proposed in [162, 164]. For an elucidation of this process we consider the haptotaxis system

$$\begin{cases} \partial_t c = \nabla \cdot (\nabla c - \chi c \nabla v) + L_c\, c + R_c, \\ \partial_t v = R_v. \end{cases} \tag{4.27}$$

It models a cell species with concentration c that conducts cellular diffusion and is haptotactically attracted by the ECM with density v. We have further considered a reaction term of the form $L_c\, c + R_c$ for the cell species and a further source term R_v for the ECM concentration. We allow for the terms L_c and R_v being nonlinearly dependent on the concentrations. One can think of (4.27) as a subsystem of a more complex model. The following proposition introduces the change of variables for this system.

Proposition 4.10 *The abstract haptotaxis system* (4.27) *recasts after the change of variables* $a = ce^{-\chi v}$ *into*

$$\begin{cases} \partial_t a = e^{-\chi v} \nabla \cdot (e^{\chi v} \nabla a) - \chi a\, R_v + L_c\, a + e^{-\chi v} R_c, \\ \partial_t v = R_v. \end{cases} \tag{4.28}$$

Proof. The computation is straightforward. We have by the product rule

$$\partial_t a = e^{-\chi v} (\partial_t c - \chi c \partial_t v) = e^{-\chi v} \partial_t c - \chi a \partial_t v$$

and further

$$\nabla \cdot (\nabla c) = \nabla \cdot (e^{\chi v} \nabla a + a \chi e^{\chi v} \nabla v), \qquad \nabla \cdot (c \nabla v) = \nabla \cdot (a e^{\chi v} \nabla v).$$

When put together we obtain the evolution equation for the new variable a in (4.28) after replacing the cell density c by the term $e^{\chi v} a$. □

After the change of variables system (4.28) includes only a first order derivative of the ECM concentration. Thus, a classical solution of the system needs v to belong only to $C^{1,1}(\bar{Q}_T)$. If the evolution equation for v is such that we can apply Lemma 4.9 and yield $0 \leqslant v \leqslant 1$ we see due to $1 \leqslant e^{\chi v} \leqslant e^{\chi}$ that bounds on the new variable a are equivalent to bounds on the cell concentration c.

Estimates for the proteolytic enzymes

In the majority of models in this thesis generic MMPs take the role of the proteolytic enzymes that degrade the ECM. For their temporal evolution we have used a model of the form

$$\partial_t m = \Delta m + \alpha c - \beta m \tag{4.29}$$

in most cases, e.g., in (2.28) and (II). Equation (4.29) models the MMP evolution by a diffusion process, molecular decay and production by a cell species with density c. When distinguishing between two types of cancer cells, as done in model (II), the cancer cell density c in (4.29) can be replaced by a weighted sum of the densities of both cancer types.

We can use general analytical results that were found for equation (4.29). The following helpful Lemma was shown in [101] using the theory of analytical semigroups.

Lemma 4.11 *Assume $m_0 \in W^1_\infty(\Omega)$ and let c and m satisfy equation (4.29) together with $\partial_\nu m = 0$ for $x \in \partial\Omega$. We further assume that $\|c(t)\|_{L^p(\Omega)} \leqslant C$ for $p \geqslant 1$ and $t \in (0,T)$. Then for $\rho < d$ and $t \in (0,T)$ it holds*

$$\|m(t)\|_{W^1_q(\Omega)} \leqslant C(q) \tag{4.30}$$

if we have

$$q < \frac{d\rho}{d-\rho}. \tag{4.31}$$

Moreover, if $\rho = d$ then (4.30) is valid for $q < +\infty$ and if $\rho > d$ then (4.30) is valid for $q = +\infty$.

In [162] this lemma was combined with the Sobolev embedding to obtain a uniform bound for the MMP density m in higher Lebesgue spaces.

Lemma 4.12 *Assume $m_0 \in W^1_\infty(\Omega)$ and let c and m satisfy (4.29) together with homogeneous Neumann boundary conditions. Moreover, we assume that $\|c\|_{L^p(\Omega)} \leqslant C$ for $1 \leqslant \rho < \infty$ and all $t \in (0,T)$. Then*

$$\|m(t)\|_{L_r(\Omega)} \leqslant C(q) \tag{4.32}$$

is true for $t \in (0,T)$ and any $r > \rho$ that satisfies

$$\frac{1}{r} + \frac{2}{d} > \frac{1}{\rho}. \tag{4.33}$$

Proof (see also [58]). We use Sobolev embedding (3.10) and obtain $W^1_q(\Omega) \hookrightarrow L^{r'}(\Omega)$ for $r' < \frac{dq}{d-q}$. Since $q < \frac{d\rho}{d-\rho}$ by Lemma 4.11, it holds that $dr' < (d+r')q < (d+r')\frac{d\rho}{d-\rho}$. Consequently, we obtain $\left(d - \frac{d\rho}{d-\rho}\right) r' < \frac{d^2\rho}{d-\rho}$ from which follows that $\left(1 - \frac{\rho}{d-\rho}\right) r' < \frac{d\rho}{d-\rho}$ and hence $(d-2\rho)r' < d\rho$. This implies (4.33) and the statement of the lemma. □

4.4 A simplified EMT/invasion model

In the following four sections we will prove the existence and uniqueness of classical solutions for a two cancer species model. This part of the chapter is based on our preprint [58]. In this section we introduce the model and present the assumptions.

For our analytical study we consider a simplified form of model (II). In contrast to this more detailed model the simplification employs self remodeling of the ECM instead of fibroblasts driven matrix remodeling. We assume moreover the case of logistic growth dynamics not restricted to the positive part, which can lead to cell death and ECM degradation. The full model we are going to study reads

$$\begin{cases} \partial_t c^D = \nabla \cdot \left(\nabla c^D - \chi_D c^D \nabla v\right) - \mu_{EMT}\, c^D + \mu_D\, c^D R \ , \\ \partial_t c^S = \nabla \cdot \left(\nabla c^S - \chi_S c^S \nabla v\right) + \mu_{EMT}\, c^D + \mu_S\, c^S R \ , \\ \partial_t v = -m v + \mu_v\, v R, \\ \partial_t m = \Delta m + c^S + c^D - m, \end{cases} \tag{IV}$$

where χ_D, χ_S, μ_S, μ_D, $\mu_v > 0$ are fixed parameters and the resources are given by

$$R = 1 - c^S - c^D - v.$$

The EMT rate μ_{EMT} is a given function with properties that we specify below. We complement (IV) with homogeneous Neumann boundary conditions

$$\partial_\nu c^D = \partial_\nu c^S = \partial_\nu m = 0 \tag{4.34}$$

at the boundary $\partial\Omega \times (0,T)$. Further we prescribe compatible initial data

$$c^D(0) = c_0^D,\ c^S(0) = c_0^S,\ v(0) = v_0,\ m(0) = m_0 \quad \text{in } \Omega, \tag{4.35}$$

which are nonnegative and sufficiently regular in the sense

$$c_0^D, c_0^S, m_0 \geqslant 0, \quad 0 \leqslant v_0 \leqslant 1, \quad c_0^D, c_0^S, m_0, v_0 \in C^{2+l}(\bar\Omega) \tag{4.36}$$

for a given $0 < l < 1$. We assume that the boundary of the domain $\Omega \subset \mathbb{R}^2$ satisfies

$$\partial\Omega \in C^{2+l}. \tag{4.37}$$

For any finite $T > 0$ we moreover define the cylinder

$$Q_T = \Omega \times (0,T) \tag{4.38}$$

on which we study the solutions of the above PDE system.

The coefficients for diffusion and the decay and production rates for the evolution of the MMPs do not affect the analytical arguments that follow. For notational convenience we have reduced them to 1 in model (IV). For the remaining parameters in the model we make the assumptions

$$\mu_D \geqslant \chi_D \mu_v, \quad \mu_S \geqslant \chi_S \mu_v. \tag{4.39}$$

This condition is crucial for the derivation of *a priori* estimates for the cancer concentrations. Employing biologically relevant parameters the condition (4.39) does not cause a problem due to the low magnitude of reasonable haptotactic sensitivity parameters compared to the larger proliferation rate, cf., e.g., Table 2.1. Yet, we mention that it is not clear whether solutions to (IV) blow up if (4.39) does not hold.

We assume that the EMT rate is a mapping $\mu_{EMT} : \mathbb{R}^4 \to \mathbb{R}$ satisfying for any (c_1^D, c_1^S, v_1, m_1), $(c_2^D, c_2^S, v_2, m_2) \in C^{1,0}(\bar Q_T)^4$ the condition

$$\begin{aligned} &\|\mu_{EMT}(c_1^D, c_1^S, v_1, m_1) - \mu_{EMT}(c_2^D, c_2^S, v_2, m_2)\|_{C^{0,0}(\bar Q_T)} \\ &\quad \leqslant L \Big(\|c_1^D - c_2^D\|_{C^{1,0}(Q_T)} + \|c_1^S - c_2^S\|_{C^{1,0}(\bar Q_T)} \\ &\qquad + \|v_1 - v_2\|_{C^{1,0}(\bar Q_T)} + \|m_1 - m_2\|_{C^{1,0}(\bar Q_T)} \Big), \end{aligned} \tag{4.40a}$$

where the Lipschitz constant L might depend on (c_1^D, c_1^S, v_1, m_1), (c_2^D, c_2^S, v_2, m_2) and the corresponding first spatial derivatives. Moreover, we assume the EMT rate to be bounded

$$0 \leqslant \mu_{EMT} \leqslant \mu_M. \tag{4.40b}$$

Remark 4.13 In the case that μ_{EMT} is given by (2.49) according to the EGF model considered in Section 2.7 both assumed properties are fulfilled. We indeed have by (2.49) that $0 \leqslant \mu_{EMT} \leqslant \mu_0$ and thus (4.40b) is satisfied. The remaining property (4.40a) can be verified by rewriting the EMT rate (2.49) for fixed (x,t) as a function of $c^D(x,t)$, $c^S(x,t)$, $\|c^D(t)\|_{L^1(\Omega)}$ and $\|c^S(t)\|_{L^1(\Omega)}$ and applying the mean value theorem.

System (IV) is not restricted to our proposed EMT rate. In particular, any mapping that is Lipschitz continuous and has Lipschitz continuous first derivatives satisfies the condition (4.40a) for a constant L that can be written as

$$L = C\,\|(c_1^D, c_1^S, v_1, m_1)\|_{C^{1,0}(\bar{Q}_T)}.$$

In the following sections we will prove the existence and uniqueness of global classical solutions to system (IV) in 2D. To this end we firstly derive a local existence result for classical solutions in Section 4.5. Then we derive necessary *a priori* estimates, which allow us to extend the local solutions for large times. The derivation of bounds for the cancer cell densities, in particular, constitutes the major challenge. In the course of the proof we will also apply the results from Section 4.3.

Throughout the process we follow the techniques employed in [162]. We will see that the two coupled cancer species in model (IV) introduce new challenges requiring, e.g., a parallel iterative lift to higher Lebesgue spaces to prove *a priori* bounds for the tumor cell densities. Also, we note that for the L^4 bounds of ∇v in (4.142) and the final increase of regularity in Lemma 4.22, the strategies that we will use differ from those used in [162]. We will consider instead techniques from [164].

To our knowledge this is one of the first studies of the solvability for a two cancer type invasion system. A similar result was established in [156] where the authors proved the existence of a weak solution to model (III). Compared to our results they could not show uniqueness of the solution since the model they addressed featured further difficulties such as nonlinear diffusion and haptotaxis terms.

We refer to Chapter 3 for classical results concerning Hölder spaces, Sobolev embeddings and solution theory of parabolic equations that we require in the following considerations.

Variable transformation In the first step we conduct the variable transformation introduced in Proposition 4.10. To this end we define

$$a^D = c^D e^{-\chi_D v}, \quad a^S = c^S e^{-\chi_S v}. \tag{4.41}$$

Consequently, system (IV) recasts as

$$\begin{cases} \partial_t a^D = e^{-\chi_D v}\nabla\cdot\left(e^{\chi_D v}\nabla a^D\right) + \chi_D\, a^D v m - \mu_{EMT}\, a^D + (\mu_D - \chi_D\,\mu_v\, v) a^D\, R, \\ \partial_t a^S = e^{-\chi_S v}\nabla\cdot\left(e^{\chi_S v}\nabla a^S\right) + \chi_S\, a^S v m + \mu_{EMT}\, e^{\chi_D v - \chi_S v}\, a^D + (\mu_S - \chi_S \mu_v\, v) a^S\, R, \\ \partial_t m = \Delta m + e^{\chi_S v} a^S + e^{\chi_D v} a^D - m, \\ \partial_t v = -mv + \mu_v\, v R \end{cases} \tag{IV'}$$

with the resource function rewritten as

$$R = 1 - e^{\chi_S \nu} a^S - e^{\chi_D \nu} a^D - \nu. \tag{4.42}$$

The posed boundary and initial conditions (4.34) and (4.35) imply after the change of variables

$$\begin{cases} \partial_\nu a^D = \partial_\nu a^S = \partial_\nu m = 0 \quad \text{in } \partial\Omega \times (0,T), \\ a^D(0) = a_0^D,\ a^S(0) = a_0^S,\ \nu(0) = \nu_0,\ m(0) = m_0 \quad \text{in } \Omega, \end{cases} \tag{4.43}$$

for which (4.36) yields

$$a_0^D, a_0^S, m_0 \geqslant 0, \quad 0 \leqslant \nu_0 \leqslant 1, \quad a_0^D, a_0^S, m_0, \nu_0 \in C^{2+l}(\bar{\Omega}). \tag{4.44}$$

We will base the proof in the next sections on system (IV'). As discussed in the generalized example in Proposition 4.10 the transformed system is easier to handle, because it only features the first order derivatives of the tissue density. In the following section we will also derive upper and lower bounds for the tissue density ν, which make boundedness of the tumor cell concentrations c^D and c^S equivalent to boundedness of the transformed quantities a^D and a^S.

4.5 Local existence of classical and unique solutions

In this section we will prove the existence of strong solutions to model (IV) in a small time interval. Therefore, we will proceed in two major steps and first construct strong solutions using a fixed point argument. In the second step we will show that the obtained solution indeed satisfies the PDE system in a classical sense.

In more detail, we will make use of Banach's contraction mapping theorem for the local existence proof. In order to show that we operate in a Banach space we present a basic result from functional analysis.

Lemma 4.14 *The space $C^1(\bar{\Omega})$ is a Banach space when equipped with the norm*

$$\|u\|_{C^1(\bar{\Omega})} = \max_{x\in\bar{\Omega}} |u| + \sum_{i=1}^{d} \max_{x\in\bar{\Omega}} \left| \frac{\partial u}{\partial x_i} \right|.$$

Proof. Without loss of generality, assume $d = 1$. There is a Cauchy series in $C^1(\bar{\Omega})$, such that for a given $\varepsilon > 0$ and an arbitrary $x \in \bar{\Omega}$ we have

$$|u_n(x) - u_m(x)| + |u_n'(x) - u_m'(x)| \leqslant \|u_n - u_m\|_{C^1(\Omega)} < \varepsilon$$

for any $n, m \geqslant N_0$. Hence, both series $(u_n)_{n\in\mathbb{N}}$ and $(u_n')_{n\in\mathbb{N}}$ are Cauchy series with respect to the maximum norm and thus converge uniformly to continuous functions u and v. The function v is in this case differentiable with $v' = u$, cf. [147].

For $\tilde{\varepsilon} > 0$ we therefore find an integer N_1 such that for any $n > N_1$ both inequalities

$$\max_{x\in\bar{\Omega}} |u_n - u| \leqslant \frac{\tilde{\varepsilon}}{2}, \quad \max_{x\in\bar{\Omega}} |u_n' - v| \leqslant \frac{\tilde{\varepsilon}}{2}$$

hold and thus $\|u_n - u\|_{C^1(\bar{\Omega})} < \tilde{\varepsilon}$, which shows the completeness of $C^1(\bar{\Omega})$. □

The following theorem establishes a small time interval in which a strong solution to (IV') exists.

Theorem 4.15 (Local existence and uniqueness) *Let* (4.44) *and* (4.37) *be satisfied. Then system* (IV′) *with boundary conditions* (4.43) *and initial conditions* (4.44) *has the unique strong solution*

$$(a^D, a^S, v, m) \in W_p^{2,1}(Q_{T_0}) \times W_p^{2,1}(Q_{T_0}) \times C^{1,1}(\bar{Q}_{T_0}) \times W_p^{2,1}(Q_{T_0}), \quad p > 5.$$

It exists in the cylinder Q_{T_0} *with* $T_0 > 0$ *depending on*

$$M = 3\|a_0^D\|_{C^2(\bar{\Omega})} + 3\|a_0^S\|_{C^2(\bar{\Omega})} + 9\|v_0\|_{C^1(\bar{\Omega})} + \|m_0\|_{C^2(\bar{\Omega})} + 3.$$

Moreover, the components of the solution satisfy

$$a^D, a^S, m \geqslant 0, \quad 0 \leqslant v \leqslant 1. \tag{4.45}$$

Proof. We will prove the local existence by Banach's contraction mapping theorem. We assume throughout the proof that $0 < T < 1$.

Spaces Let X be the space of functions (a^D, a^S, v) with the finite norm

$$\|(a^D, a^S, v)\|_X = \|a^D\|_{C^{1,0}(\bar{Q}_T)} + \|a^S\|_{C^{1,0}(\bar{Q}_T)} + \|v\|_{C^{1,0}(\bar{Q}_T)},$$

which is a Banach space (cf. Lemma 4.14). We moreover define the subspace

$$X_M := \big\{(a^D, a^S, v) \in (C^{1,0}(\bar{Q}_T))^3 : a^D, a^S, v \text{ satisfy (4.43)}, \\ a^D, a^S, v \geqslant 0, \text{ and } \|(a^D, a^S, v)\|_X \leqslant M\big\}.$$

Fixed point iteration For any $(a^D, a^S, v) \in X_M$ we define $(a_*^D, a_*^S, v_*) = F(a^D, a^S, v)$ such that

$$\partial_t m - \Delta m + m = a^D e^{\chi_D v} + a^S e^{\chi_S v} \quad \text{in } Q_T, \tag{4.46a}$$
$$\partial_\nu m = 0 \text{ in } \partial\Omega \times (0,T), \quad m(\cdot,0) = m_0 \text{ in } \Omega, \tag{4.46b}$$
$$\partial_t v_* = -m v_* + \mu_v v_* R \quad \text{in } Q_T, \tag{4.46c}$$
$$v_*(\cdot,0) = v_0, \tag{4.46d}$$
$$\partial_t a_*^D - \Delta a_*^D - \chi_D \nabla v_* \cdot \nabla a_*^D + [\mu_{EMT} - (\mu_D - \chi_D \mu_v v)R] a_*^D = \chi_D a^D v m, \tag{4.46e}$$
$$\partial_\nu a_*^D = 0 \text{ in } \partial\Omega \times (0,T), \quad a_*^D(\cdot,0) = a_0^D \text{ in } \Omega, \tag{4.46f}$$
$$\partial_t a_*^S - \Delta a_*^S - \chi_S \nabla v_* \cdot \nabla a_*^S - (\mu_S - \chi_S \mu_v v) R a_*^S = \chi_S a^S v m + \mu_{EMT} e^{\chi_D v - \chi_S v} a_*^D, \tag{4.46g}$$
$$\partial_\nu a_*^S = 0 \text{ in } \partial\Omega \times (0,T), \quad a_*^S(\cdot,0) = a_0^S \text{ in } \Omega, \tag{4.46h}$$

where the resources R are given by $R = 1 - a^S e^{\chi_S v} - a^D e^{\chi_D v} - v$. For the proof we fix $p > 5$ and set $\lambda = 1 - \frac{5}{p}$.

F is well-defined and $F(X_M) \subset X_M$ We start with the MMP density m and consider equations (4.46a)–(4.46b). Since $(a^D, a^S, v) \in X_M$, this linear parabolic problem has a unique solution by Theorem 3.1 satisfying

$$\|m\|_{W_p^{2,1}(Q_T)} \leqslant C_1(M). \tag{4.47}$$

Here we can apply the Sobolev embedding (3.11) and get

$$\|m\|_{C^{1,0}(\bar{Q}_T)} \leqslant C_2(M). \tag{4.48}$$

Moreover, the parabolic maximum principle (see Section 3.3) yields

$$m \geqslant 0. \tag{4.49}$$

The initial value problem (4.46c), (4.46d) can be written as

$$v_{*t} = h_1 v_*, \quad v_*(\cdot, 0) = v_0, \tag{4.50}$$

where

$$\|h_1\|_{C^{1,0}(\bar{Q}_T)} = \| - m + \mu_v R\|_{C^{1,0}(\bar{Q}_T)} \leqslant C_3(M) \tag{4.51}$$

due to (4.48) and $(a^S, a^D, v) \in X_M$. The ODE system has the solution

$$v_* = v_0(x) \exp\left(\int_0^t h_1(x,s)ds\right) \geqslant 0 \tag{4.52}$$

with the gradient

$$\nabla v_* = \nabla v_0(x) \exp\left(\int_0^t h_1(x,s)ds\right) + v_0(x) \exp\left(\int_0^t h_1(x,s)ds\right) \int_0^t \nabla h_1(x,s)ds.$$

For $T \leqslant \frac{1}{2C_3(M)} < \log(2)/C_3(M)$ we obtain the estimates

$$\|v_*\|_{C(\bar{Q}_T)} \leqslant \|v_0\|_{C(\bar{\Omega})} e^{C_3(M)T} \leqslant 2\|v_0\|_{C(\bar{\Omega})}, \tag{4.53}$$

$$\begin{aligned}\|\nabla v_*\|_{C(\bar{Q}_T)} &\leqslant \|\nabla v_0(x)\|_{C(\bar{\Omega})} \exp(C_3(M)T) \\ &\quad + \|v_0(x)\|_{C(\bar{\Omega})} \exp(C_3(M)T) T C_3(M) \\ &\leqslant 2\|\nabla v_0\|_{C(\bar{\Omega})} + \|v_0\|_{C(\bar{\Omega})}\end{aligned} \tag{4.54}$$

and thus

$$\begin{aligned}\|v_*\|_{C^{1,0}(\bar{Q}_T)} &= \|v_*\|_{C(\bar{Q}_T)} + \|\nabla v_*\|_{C(\bar{Q}_T)} \\ &\leqslant 3\|v_0\|_{C(\bar{\Omega})} + 2\|\nabla v_0\|_{C(\bar{\Omega})} \\ &\leqslant 3\|v_0\|_{C^1(\bar{\Omega})} \leqslant M/3.\end{aligned} \tag{4.55}$$

Next, we deal with the parabolic problem (4.46e), (4.46f) that can be written as

$$\partial_t a_* - \Delta a_* - \chi \nabla v_* \cdot \nabla a_* - h_2 a_* = h_3 \tag{4.56}$$

with boundary and initial conditions given by (4.46f) and $a_* = a_*^D$, $\chi = \chi_D$. We have

$$\begin{cases} \|\nabla v_*\|_{L^\infty(Q_T)} \leqslant M, & \|h_2\|_{L^\infty(Q_T)} \leqslant C_4(M), \\ & \|h_3\|_{L^\infty(Q_T)} \leqslant C_5(M) \end{cases} \tag{4.57}$$

because of $(a^D, a^S, v) \in X_M$, (4.48) and (4.40b). Applying the maximal parabolic regularity result (Theorem 3.1), there is a unique solution a_* that satisfies for all $p > 1$ the inequality

$$\|a_*\|_{W_p^{2,1}(\bar{Q}_T)} \leqslant C_6(M). \tag{4.58}$$

Further the Sobolev embedding (3.11) gives us

$$\|a_*\|_{C^{1+\lambda,(1+\lambda)/2}(\bar{Q}_T)} \leqslant C_7(M).$$

If $T \leqslant C_7(M)^{\frac{-2}{1+\lambda}}$ we get

$$\begin{aligned}
\|a_*\|_{C^{0,0}(\bar{Q}_T)} &= \|a_*\|_{C^{0,0}(\bar{Q}_T)} + \|\nabla a_*\|_{C^{0,0}(\bar{Q}_T)} \\
&\leqslant \|a_* - a_0\|_{C^{0,0}(\bar{Q}_T)} + \|a_0\|_{C^0(\bar{\Omega})} + \|\nabla a_* - \nabla a_0\|_{C^{0,0}(\bar{Q}_T)} + \|\nabla a_0\|_{C^0(\bar{\Omega})} \\
&\leqslant T^{(1+\lambda)/2}\|a_*\|_{C^{1,(1+\lambda)/2}(\bar{Q}_T)} + \|a_0\|_{C^1(\bar{\Omega})} \\
&\leqslant T^{(1+\lambda)/2}C_7(M) + \|a_0\|_{C^1(\bar{\Omega})} \\
&\leqslant 1 + \|a_0\|_{C^1(\bar{\Omega})} \\
&\leqslant M/3, \qquad (4.59)
\end{aligned}$$

where we have used the definition of the Hölder norm in the second inequality. Moreover, we have

$$a_* \geqslant 0 \qquad (4.60)$$

by the parabolic maximum principle, as the right hand side of (4.46e) is non negative (see Section 3.3). Since we have shown that $a_*^D \in X_M$, the assertion (4.57) is also true for $a = a^S$ in the problem (4.56). Hence, (4.59), (4.60) for $a_* = a_*^S$ follow by the same arguments.

F is a contraction We take (a_1^D, a_1^S, ν_1), $(a_2^D, a_2^S, \nu_2) \in X_M$ and consider $(a_{1*}^D, a_{1*}^S, \nu_{1*}) = F(a_1^D, a_1^S, \nu_1)$ and $(a_{2*}^D, a_{2*}^S, \nu_{2*}) = F(a_2^D, a_2^S, \nu_2)$. As shown before, one can find two functions m_1 and m_2 with

$$\|m_1\|_{C^{1,0}(\bar{Q}_T)}, \|m_2\|_{C^{1,0}(\bar{Q}_T)} \leqslant C_8(M)$$

that satisfy equations (4.46a) and (4.46b) when we substitute the tuple (a^D, a^S, m, ν) by either $(a_1^D, a_1^S, m_1, \nu_1)$ or $(a_2^D, a_2^S, m_2, \nu_2)$. Moreover, we have

$$\begin{aligned}
&\partial_t(m_1 - m_2) - \Delta(m_1 - m_2) + (m_1 - m_2) \\
&\qquad = a_1^D e^{\chi_D \nu_1} + a_1^S e^{\chi_S \nu_1} - a_2^D e^{\chi_D \nu_2} - a_2^S e^{\chi_S \nu_2} \quad \text{in } Q_T, \qquad (4.61) \\
&\partial_\nu(m_1 - m_2) = 0 \text{ in } \partial\Omega \times (0,T), \qquad (4.62) \\
&(m_1 - m_2)(\cdot, 0) = 0 \text{ in } \Omega, \qquad (4.63)
\end{aligned}$$

where

$$\begin{aligned}
&\|a_1^D e^{\chi_D \nu_1} + a_1^S e^{\chi_S \nu_1} - a_2^D e^{\chi_D \nu_2} - a_2^S e^{\chi_S \nu_2}\|_{L^\infty(Q_T)} \\
&\quad \leqslant \|e^{\chi_D \nu_1}(a_1^D - a_2^D)\|_{L^\infty(Q_T)} + \|e^{\chi_S \nu_1}(a_1^S - a_2^S)\|_{L^\infty(Q_T)} \\
&\qquad + \|(e^{\chi_D \nu_1} - e^{\chi_D \nu_2})(a_2^D)\|_{L^\infty(Q_T)} + \|(e^{\chi_S \nu_1} - e^{\chi_S \nu_2})(a_2^S)\|_{L^\infty(Q_T)} \\
&\quad \leqslant C_9(M)(\|a_1^D - a_2^D\|_{L^\infty(Q_T)} + \|a_1^S - a_2^S\|_{L^\infty(Q_T)} \\
&\qquad + \|\nu_1 - \nu_2\|_{L^\infty(Q_T)}). \qquad (4.64)
\end{aligned}$$

Hence, thanks to Theorem 3.1, there is a solution to (4.61)–(4.63) satisfying

$$\|m_1 - m_2\|_{W_p^{2,1}(Q_T)} \leqslant C_{10}(M)(\|a_1^D - a_2^D\|_{L^\infty(Q_T)} + \|a_1^S - a_2^S\|_{L^\infty(Q_T)} + \|\nu_1 - \nu_2\|_{L^\infty(Q_T)})$$

for all $p \geqslant 1$. The Sobolev embedding (3.11) again yields

$$\begin{aligned}
\|m_1 - m_2\|_{C^{1,0}(\bar{Q}_T)} &\leqslant C_{11}(M)(\|a_1^D - a_2^D\|_{L^\infty(Q_T)} \\
&\qquad + \|a_1^S - a_2^S\|_{L^\infty(Q_T)} + \|\nu_1 - \nu_2\|_{L^\infty(Q_T)}). \qquad (4.65)
\end{aligned}$$

We get from (4.46c) and (4.46d) that

$$\begin{cases} \partial_t(v_{1*} - v_{2*}) = h_4(v_{1*} - v_{2*}) + h_5, \\ (v_{1*} - v_{2*})(\cdot, 0) = 0, \end{cases} \tag{4.66}$$

where

$$h_4 = -m_1 + \mu_v R_1, \quad h_5 = (m_2 - m_1)v_{2*} - \mu_v v_{2*}(R_2 - R_1).$$

Here we have used the notations

$$R_1 = 1 - e^{\chi_S v_1} a_1^S - e^{\chi_D v_1} a_1^D - v_1, \quad R_2 = 1 - e^{\chi_S v_2} a_2^S - e^{\chi_D v_2} a_2^D - v_2.$$

Since $(a_i^D, a_i^S, v_i) \in X_M$ for $i = 1, 2$ and due to (4.65), we obtain the estimates

$$\|h_4\|_{C^{1,0}(\bar{Q}_T)} \leqslant C_{12}(M), \tag{4.67}$$

$$\begin{aligned} \|h_5\|_{C^{1,0}(\bar{Q}_T)} \leqslant C_{13}(M)(&\|a_1^D - a_2^D\|_{C^{1,0}(\bar{Q}_T)} \\ &+ \|a_1^S - a_2^S\|_{C^{1,0}(\bar{Q}_T)} + \|v_1 - v_2\|_{C^{1,0}(\bar{Q}_T)}). \end{aligned} \tag{4.68}$$

The solution of the ODE (4.66) is given by

$$v_{1*} - v_{2*} = \int_0^t \exp\left(\int_\tau^t h_4(x, s)ds\right) h_5(x, \tau)d\tau,$$

and thus it holds that

$$\begin{aligned} \nabla(v_{1*} - v_{2*}) = &\int_0^t \exp\left(\int_\tau^t h_4(x, s)ds\right) \nabla_x h_5(x, \tau)d\tau \\ &+ \int_0^t \exp\left(\int_\tau^t h_4(x, s)ds\right) h_5(x, \tau) \int_\tau^t \nabla_x h_4(x, s)ds\, d\tau. \end{aligned}$$

Finally, we obtain by using the bounds (4.67), (4.68) that

$$\begin{aligned} \|v_{1*} - v_{2*}\|_{C^{1,0}(\bar{Q}_T)} &\leqslant TC_{14}(M)\|h_5\|_{C^{1,0}(\bar{Q}_T)} \\ &\leqslant TC_{15}(M)(\|a_1^D - a_2^D\|_{C^{1,0}(\bar{Q}_T)} \\ &\quad + \|a_1^S - a_2^S\|_{C^{1,0}(\bar{Q}_T)} + \|v_1 - v_2\|_{C^{1,0}(\bar{Q}_T)}). \end{aligned} \tag{4.69}$$

Next, we derive the parabolic problem for $a \in \{a^D, a^S\}$ with coefficients $(\chi, h_6, h_7) \in \{(\chi_D, h_6^D, h_7^D), (\chi_S, h_6^S, h_7^S)\}$ by (4.46e)–(4.46h). We get

$$\begin{aligned} \partial_t(a_{1*} - a_{2*}) - \Delta(a_{1*} - a_{2*}) - \chi\nabla v_{1*} \cdot \nabla(a_{1*} - a_{2*}) \\ + h_6(a_{1*} - a_{2*}) = h_7 \text{ in } Q_T, \end{aligned} \tag{4.70}$$

$$\partial_\nu(a_{1*} - a_{2*}) = 0 \text{ in } \partial\Omega, \quad (a_{1*} - a_{2*})(\cdot, 0) = 0 \text{ in } \Omega, \tag{4.71}$$

where

$$\begin{aligned} h_6^D &= \mu_{EMT,1} - (\mu_D - \chi_D \mu_v v_1)R_1, \\ h_6^S &= -(\mu_S - \chi_S \mu_v v_1)R_1, \\ h_7^D &= \chi_D(a_1^D m_1 v_1 - a_2^D m_2 v_2) + \chi_D \nabla(v_{1*} - v_{2*}) \cdot \nabla a_{2*}^D + a_{2*}^D[(\mu_D - \chi_D \mu_v v_1)R_1 \\ &\quad - (\mu_D - \chi_D \mu_v v_2)R_2 - (\mu_{EMT,1} - \mu_{EMT,2})], \\ h_7^S &= \chi_S(a_1^S m_1 v_1 - a_2^S m_2 v_2) + \chi_S \nabla(v_{1*} - v_{2*}) \cdot \nabla a_{2*}^S + a_{2*}^S[(\mu_S - \chi_S \mu_v v_1)R_1 \\ &\quad - (\mu_S - \chi_S \mu_v v_2)R_2] - (\mu_{EMT,1}\, e^{\chi_D v_1 - \chi_s v_1}\, a_{1*}^D - \mu_{EMT,2}\, e^{\chi_D v_2 - \chi_s v_2}\, a_{2*}^D). \end{aligned}$$

We have used above the notations

$$\mu_{EMT,1} = \mu_{EMT}(c_1^D, c_1^S, \nu_1, m_1), \quad \mu_{EMT,2} = \mu_{EMT}(c_2^D, c_2^S, \nu_2, m_2).$$

Due to $(a_i^D, a_i^S, \nu_i) \in X_M$, (4.55), (4.59), (4.65), (4.69) and (4.40a) we can estimate

$$\|\chi_D \nabla \nu_{1*}\|_{L^\infty(Q_T)}, \|\chi_S \nabla \nu_{1*}\|_{L^\infty(Q_T)} \leqslant C_{16}(M), \tag{4.72}$$

$$\|h_6^D\|_{L^\infty(Q_T)}, \|h_6^S\|_{L^\infty(Q_T)} \leqslant C_{17}(M), \tag{4.73}$$

$$\begin{aligned}\|h_7^D\|_{L^\infty(Q_T)}, \|h_7^S\|_{L^\infty(Q_T)} \leqslant C_{18}(M)(&\|a_1^D - a_2^D\|_{C^{1,0}(\bar{Q}_T)} + \|a_1^S - a_2^S\|_{C^{1,0}(\bar{Q}_T)} \\ &+ \|\nu_1 - \nu_2\|_{C^{1,0}(\bar{Q}_T)}).\end{aligned} \tag{4.74}$$

Thanks to Theorem 3.1, there is a solution of the initial value problem (4.70), (4.71). This solution satisfies

$$\begin{aligned}\|a_{1*} - a_{2*}\|_{W_p^{2,1}(Q_T)} &\leqslant C_{19}(M)\|h_7\|_{L^p(Q_T)} \\ &\leqslant C_{20}(M)(\|a_1^D - a_2^D\|_{C^{1,0}(\bar{Q}_T)} + \|a_1^S - a_2^S\|_{C^{1,0}(\bar{Q}_T)} \\ &\quad + \|\nu_1 - \nu_2\|_{C^{1,0}(\bar{Q}_T)}).\end{aligned}$$

Thus, the bound can be extended using the Sobolev embedding (3.11) and we get

$$\begin{aligned}\|a_{1*} - a_{2*}\|_{C^{1+\lambda,(1+\lambda)/2}(\bar{Q}_T)} \leqslant C_{21}(M)(&\|a_1^D - a_2^D\|_{C^{1,0}(\bar{Q}_T)} \\ &+ \|a_1^S - a_2^S\|_{C^{1,0}(\bar{Q}_T)} + \|\nu_1 - \nu_2\|_{C^{1,0}(\bar{Q}_T)}).\end{aligned}$$

Then follows

$$\begin{aligned}\|a_{1*} - a_{2*}\|_{C^{1,0}(\bar{Q}_T)} &= \|(a_{1*} - a_{2*})(x,t) - (a_{1*} - a_{2*})(x,0)\|_{C^{1,0}(\bar{Q}_T)} \\ &\leqslant T^{(1+\lambda)/2}\|a_{1*} - a_{2*}\|_{C^{1,(1+\lambda/2)}(\bar{Q}_T)} \\ &\leqslant T^{(1+\lambda)/2} C_{21}(M) \Big(\|a_1^D - a_2^D\|_{C^{1,0}(\bar{Q}_T)} \\ &\quad + \|a_1^S - a_2^S\|_{C^{1,0}(\bar{Q}_T)} + \|\nu_1 - \nu_2\|_{C^{1,0}(\bar{Q}_T)}\Big).\end{aligned} \tag{4.75}$$

If we take $T_0 = T$ such that

$$\max\{T C_{15}(M),\ T^{(1+\lambda)/2} C_{21}(M)\} < \frac{1}{3}$$

we see by (4.69) and (4.75) that F is a contraction in X_M.

Conclusion and regularity According to Banach's contraction mapping theorem F has a unique fixed point (a^D, a^S, ν), which together with m from (4.47) is the unique solution of (IV'), (4.43). By (4.47) and (4.58) we have that

$$m, a^D, a^S \in W_p^{2,1}(Q_T).$$

Due to (4.50), (4.51) and (4.55) we further get

$$\nu \in C^{1,1}(\bar{Q}_T).$$

By (4.60), (4.52) and (4.49) we get the nonnegativity of the solution

$$a^D, a^S, \nu, m \geqslant 0.$$

Moreover, we can deduce from the nonnegativity and Lemma 4.9 the upper bound $\nu \leqslant 1$. □

The local solutions that we have just obtained are in fact solution in the classical sense, as we will show in the next theorem.

Theorem 4.16 (Regularity) *Under the initial and boundary conditions* (4.43) *and* (4.44) *the solution in Theorem 4.15 satisfies*

$$(a^S, a^D, \nu, m) \in (C^{2+l,1+l/2}(\bar{Q}_{T_0}))^4.$$

Proof. We use Theorem 4.15 and the Sobolev embedding (3.11) and obtain for a sufficiently large $p > 5$ that

$$a^D, a^S, m \in C^{1+l,(1+l)/2}(\bar{Q}_T). \tag{4.76}$$

We further derive from (IV′) that

$$\partial_t(\partial_{x_i}\nu) = h_1\partial_{x_i}\nu - h_2, \tag{4.77}$$

where

$$h_1 = -m + \mu_\nu R - \mu_\nu\nu(1 + \chi_S e^{\chi_S\nu}a^S + \chi_D e^{\chi_D\nu}a^D), \tag{4.78}$$
$$h_2 = \nu\partial_{x_i}m + \mu_\nu\nu(e^{\chi_S\nu}\partial_{x_i}a^S + e^{\chi_D\nu}\partial_{x_i}a^D). \tag{4.79}$$

Because of (4.76) and $\nu \in C^{1,1}(\bar{Q}_T)$ we get

$$h_1, h_2 \in C^{l,l/2}(\bar{Q}_T). \tag{4.80}$$

The solution of (4.77) is given by

$$\partial_{x_i}\nu = \partial_{x_i}\nu_0(x)e^{\int_0^t h_1(x,s)\,ds} - \int_0^t h_2(x,\tau)e^{\int_\tau^t h_1(x,s)\,ds}\,d\tau, \tag{4.81}$$

and hence we obtain due to (4.80) that

$$\partial_{x_i}\nu \in C^{l,l/2}(\bar{Q}_T). \tag{4.82}$$

The equation for a^D in (IV′) can be written as

$$\partial_t a^D - \Delta a^D - \chi_D\nabla\nu\cdot\nabla a^D - h_3 a^D = h_4, \tag{4.83}$$

where

$$h_3 = (\mu_D - \chi_D\mu_\nu\nu)R \in C^{l,l/2}(\bar{Q}_T), \quad h_4 = \chi_D a^D\nu m - \mu_{EMT}a^D \in C^{l,l/2}(\bar{Q}_T)$$

by (4.76), (4.82) and (4.40a). Thus, we can apply Theorem 3.2 and get together with (4.82) that the solution of (4.83) satisfies

$$a^D \in C^{2+l,1+l/2}(\bar{Q}_T). \tag{4.84}$$

Similarly, the equation for a^S in (IV′) can be rewritten as

$$\partial_t a^S - \Delta a^S - \chi_S\nabla\nu\cdot\nabla a^S - h_5 a^S = h_6, \tag{4.85}$$
$$h_5 = (\mu_S - \chi_S\mu_\nu\nu)R \in C^{l,l/2}(\bar{Q}_T), \tag{4.86}$$
$$h_6 = \chi_S a^S\nu m + \mu_{EMT}a^D\, e^{\chi_D\nu - \chi_s\nu} \in C^{l,l/2}(\bar{Q}_T). \tag{4.87}$$

Applying Theorem 3.2 we obtain

$$a^S \in C^{2+l,1+l/2}(\bar{Q}_T). \tag{4.88}$$

Furthermore, (4.76), $\nu \in C^{1,1}(\bar{Q}_T)$, (4.46a) and (4.46b) yield

$$m \in C^{2+l,1+l/2}(\bar{Q}_T). \tag{4.89}$$

By using (4.82) together with (4.84), (4.88) and (4.89) and repeating the proof of (4.82) for $\partial^2_{x_i,x_j}\nu$ we get

$$\partial^2_{x_i,x_j}\nu \in C^{l,l/2}(\bar{Q}_T). \tag{4.90}$$

The equation for ν in (IV′) implies moreover that

$$\partial_t \nu = -m\nu + \mu_\nu \nu R \in C^{2+l,l/2}(\bar{Q}_T),$$

which yields together with $\nu \in C^{1,1}(\bar{Q}_T)$ and (4.90) that

$$\nu \in C^{2+l,1+l/2}(\bar{Q}_T). \qquad \square$$

4.6 A priori estimates for the densities of the cancer cells

To extend the existence interval of the local classical solutions established in the previous section we will derive *a priori* estimates. For the bootstrapping argument we need bounds for a^D, a^S and m in $C^2(\bar{Q}_T)$ and for ν in $C^1(\bar{Q}_T)$. The derivation of these *a priori* bounds is delicate and we proceed in multiple steps, firstly deriving bounds in Lebesgue and Bochner spaces.

For this process we assume that $(a^D, a^S, \nu, m) \in \left(C^{2,1}(\bar{Q}_T)\right)^4$ is a classical solution of (IV′) in $[0,T]$ for any $T > 0$. The estimates in the following statements are then supposed to be understood as *a priori* estimates, i.e. they are independent of the solution. The present section addresses, in particular, *a priori* estimates for the transformed cancer cell densities. At first we derive bounds in $L^1(\Omega)$.

Lemma 4.17 *Let* $(a^D, a^S, \nu, m) \in \left(C^{2,1}(\bar{Q}_T)\right)^4$ *be a solution of* (IV′)*, then for all* $t \in (0,T)$ *the following estimates are satisfied*

$$\|a^D(t)\|_{L^1(\Omega)} \leqslant \|c^D(t)\|_{L^1(\Omega)} \leqslant C, \tag{4.91a}$$

$$\|a^S(t)\|_{L^1(\Omega)} \leqslant \|c^S(t)\|_{L^1(\Omega)} \leqslant C, \tag{4.91b}$$

$$\|m(t)\|_{L^1(\Omega)} \leqslant C. \tag{4.91c}$$

Proof. The first inequality in both equations (4.91a) and (4.91b) follows from the variable transformations (4.41) and (4.45) and $0 \leqslant \nu \leqslant 1$. To prove the second inequality in (4.91a) we integrate the evolution equation for c^D in (IV) over Ω and obtain by the homogeneous Neumann boundaries and the positivity of the functions c^D, c^S and ν that

$$\frac{d}{dt}\int_\Omega c^D \, dx \leqslant \mu_D \int_\Omega c^D \, dx - \mu_D \int_\Omega (c^D)^2 \, dx.$$

When we proceed here as in the end of the proof of Theorem 4.6 we get

$$\|c^D\|_{L^1(\Omega)} \leqslant \max\left\{\|c_0^D\|_{L^1(\Omega)}, |\Omega|\right\} \leqslant C_1.$$

The same strategy applied to the evolution equation of c^S in (IV) brings us to the inequality

$$\begin{aligned}\frac{d}{dt}\|c^S\|_{L^1(\Omega)} &\leqslant \mu_M\|c^D\|_{L^1(\Omega)} + \mu_S\|c^S\|_{L^1(\Omega)} - \frac{\mu_S}{|\Omega|}\|c^S\|^2_{L^1(\Omega)} \\ &\leqslant C_2 + \mu_S\|c^S\|_{L^1(\Omega)} - \frac{\mu_S}{|\Omega|}\|c^S\|^2_{L^1(\Omega)}, \end{aligned} \tag{4.92}$$

where we have used the previously derived bound on $\|c^D\|_{L^1(\Omega)}$. The right-hand side in (4.92) is a quadratic function in $\|c^S\|_{L^1(\Omega)}$, which is nonnegative only for $\|c^S\|_{L^1(\Omega)} \in [-C_3, C_4]$. This implies

$$\|c^S\|_{L^1(\Omega)} \leqslant \max\left\{\|c_0^S\|_{L^1(\Omega)}, C_4\right\} \leqslant C_5.$$

The bound (4.91c) follows directly from the bounds on $\|c^D\|_{L^1(\Omega)}$ and $\|c^S\|_{L^1(\Omega)}$. □

Next, we present the main result of this section. It builds on Theorem 4.17 and establishes *a priori* L^∞ bounds for the cancer cell densities. The proof employs Lemmas 4.11 and 4.12 in order to obtain the necessary bounds for the MMP concentration.

Theorem 4.18 *Let* $(a^D, a^S, v, m) \in \left(C^{2,1}(\bar{Q}_T)\right)^4$ *be a solution of system* (IV′) *and let* (4.39) *hold. Then for all* $t \in (0, T)$ *we have*

$$\|a^D(t)\|_{L^\infty(\Omega)}, \|a^S(t)\|_{L^\infty(\Omega)} \leqslant C. \tag{4.93}$$

Proof. The proof is divided into 4 steps. We first derive a basic estimate in step 1, prove L^p bounds for all p in steps 2 and 3 and finally prove the L^∞ estimate in step 4.

Step 1: First L^p estimates We set $\gamma = 0$ if $p \leqslant 2$ and $\gamma \in (0, 1)$ otherwise. Then we define $a_\gamma = a + \gamma \geqslant \gamma \geqslant 0$, such that for all $p \geqslant 1$ it holds that

$$\begin{cases} \nabla\left((a_\gamma^D)^{p/2}\right) = \dfrac{p}{2}(a_\gamma^D)^{p/2-1}\nabla a_\gamma^D, \\ \nabla\left((a_\gamma^S)^{p/2}\right) = \dfrac{p}{2}(a_\gamma^S)^{p/2-1}\nabla a_\gamma^S. \end{cases} \tag{4.94}$$

Due to $0 \leqslant v \leqslant 1$ we can consider the integrals $\int_\Omega e^{\chi_D v}(a_\gamma^D)^p\,dx$, $\int_\Omega e^{\chi_S v}(a_\gamma^S)^p\,dx$ instead of $\int_\Omega (a_\gamma^D)^p\,dx$, $\int_\Omega (a_\gamma^S)^p\,dx$ and further get

$$0 \leqslant \mu_D - \chi_D\mu_v \leqslant \mu_D, \quad 0 \leqslant \mu_S - \chi_S\mu_v \leqslant \mu_S \tag{4.95}$$

employing the above assumption. Using moreover (IV'), (4.95), integration by parts, (4.94), (4.40b) and the fact that $0 \leqslant \nu \leqslant 1$, we obtain

$$\begin{aligned}
\frac{d}{dt}\int_\Omega e^{\chi_D \nu}(a_\gamma^D)^p\,dx &= \int_\Omega \chi_D e^{\chi_D \nu}\partial_t \nu (a_\gamma^D)^p\,dx + \int_\Omega e^{\chi_D \nu} p (a_\gamma^D)^{p-1}\partial_t a^D\,dx \\
&= -\chi_D \int_\Omega e^{\chi_D \nu} m \nu (a_\gamma^D)^p\,dx + \chi_D\,\mu_\nu \int_\Omega e^{\chi_D \nu}(a_\gamma^D)^p \nu R\,dx \\
&\quad + \int_\Omega p (a_\gamma^D)^{p-1}\nabla\cdot(e^{\chi_D \nu}\nabla a_\gamma^D)\,dx \quad + \chi_D \int_\Omega e^{\chi_D \nu} p (a_\gamma^D)^{p-1} a_\gamma^D \nu m\,dx \\
&\quad + \int_\Omega e^{\chi_D \nu} p (a_\gamma^D)^{p-1}(\mu_D - \chi_D\,\mu_\nu\,\nu) a_\gamma^D R\,dx \quad - \int_\Omega \mu_{EMT}\,a^D e^{\chi_D \nu} p (a_\gamma^D)^{p-1}\,dx \\
&\leqslant (\mu_D\,p + \chi_D\,\mu_\nu)\int_\Omega e^{\chi_D \nu}(a_\gamma^D)^p\,dx + \chi_D\,p \int_\Omega e^{\chi_D \nu}(a_\gamma^D)^p m\,dx \\
&\quad - \int_\Omega p(p-1)(a_\gamma^D)^{p-2}|\nabla a_\gamma^D|^2 e^{\chi_D \nu}\,dx \\
&\leqslant -\frac{4(p-1)}{p}\int_\Omega |\nabla (a_\gamma^D)^{p/2}|^2\,dx + (\mu_D\,p + \chi_D\,\mu_\nu) e^{\chi_D}\int_\Omega (a_\gamma^D)^p\,dx \\
&\quad + \chi_D\,p e^{\chi_D}\int_\Omega m (a_\gamma^D)^p\,dx. \qquad (4.96)
\end{aligned}$$

Similarly, we get

$$\begin{aligned}
\frac{d}{dt}\int_\Omega e^{\chi_S \nu}(a_\gamma^S)^p\,dx &= \int_\Omega \chi_S e^{\chi_S \nu}\partial_t \nu (a_\gamma^S)^p\,dx + \int_\Omega e^{\chi_S \nu} p (a_\gamma^S)^{p-1}\partial_t a^S\,dx \\
&\leqslant -\frac{4(p-1)}{p}\int_\Omega |\nabla (a_\gamma^S)^{p/2}|^2\,dx + (\mu_S\,p + \chi_S\,\mu_\nu) e^{\chi_S}\int_\Omega (a_\gamma^S)^p\,dx \\
&\quad + \chi_S\,p e^{\chi_S}\int_\Omega m (a_\gamma^S)^p\,dx + \mu_M\,p e^{\chi_D}\int_\Omega a^D (a_\gamma^S)^{p-1}\,dx. \qquad (4.97)
\end{aligned}$$

Step 2: Increase of p We assume that for a $q \geqslant 1$ both transformed densities satisfy $\|a_\gamma^D(t)\|_{L^q(\Omega)}, \|a_\gamma^S(t)\|_{L^q(\Omega)} \leqslant C_1$ and show that

$$\|a_\gamma^D(t)\|_{L^p(\Omega)}, \|a_\gamma^S(t)\|_{L^p(\Omega)} \leqslant C_2,$$

where $p = 4q/3$. Since we have assumed the space dimension $d = 2$, the inequality

$$\frac{dp}{dp+2q} < 1 + \frac{2}{d} - \frac{1}{q}$$

holds and allows us to find an $r > 1$, such that

$$\frac{dp}{dp+2q} < \frac{1}{r} < 1 + \frac{2}{d} - \frac{1}{q}. \qquad (4.98)$$

The first inequality of (4.98) implies $2/r - 2 > 2q/p$. This yields together with the Gagliardo-Nirenberg inequality (estimate (3.17)) that

$$\|\cdot\|_{L^{2r}}^{2r} \leqslant C_3 \|\cdot\|_{L^{2/r+2}}^{2(r-1)} \|\cdot\|_{W_2^1}^2 \leqslant C_4 \|\cdot\|_{L^{2q/p}}^{2(r-1)} \|\cdot\|_{W_2^1}^2. \qquad (4.99)$$

By the second inequality of (4.98) there is a dual exponent r' of r that satisfies the conditions of Lemma 4.12. We take $a \in \{a_\gamma^D, a_\gamma^S\}$. Applying Young's inequality, (4.99), Lemma 4.12 and assumption $\|a(\cdot,t)\|_{L^q(\Omega)} \leqslant C_1$, we get for any $\varepsilon > 0$ that

$$\begin{aligned}\int_\Omega m a^p \,dx &\leqslant C_5(\varepsilon)\int_\Omega m^{r'}\,dx + \varepsilon\int_\Omega a^{pr}\,dx\\ &\leqslant C_6(\varepsilon) + \varepsilon\|a^{p/2}\|^{2r}_{L^{2r}(\Omega)}\\ &\leqslant C_6(\varepsilon) + \varepsilon C_7\|a\|^{p(r-1)}_{L^q}\|a^{p/2}\|^2_{W_2^1(\Omega)}\\ &\leqslant C_6(\varepsilon) + \varepsilon C_8\int_\Omega a^p\,dx + \varepsilon C_8\int_\Omega |\nabla a^{p/2}|^2\,dx. \end{aligned} \tag{4.100}$$

Since we are in space dimension $d = 2$, the Gagliardo-Nirenberg interpolation inequality (follows from (3.17)) yields

$$\|\cdot\|_{L^2(\Omega)} \leqslant C\|\cdot\|^{1/4}_{W_2^1(\Omega)}\|\cdot\|^{3/4}_{L^{3/2}(\Omega)}. \tag{4.101}$$

We can moreover estimate $\int_\Omega a^p\,dx$ by employing (4.101), Young's inequality and the estimate $\|a(\cdot,t)\|_{L^q(\Omega)} \leqslant C_1$ to get

$$\begin{aligned}(C_9+\beta)\int_\Omega a^p\,dx &= (C_9+\beta)\int_\Omega (a^{p/2})^2\,dx\\ &= (C_9+\beta)\|a^{p/2}\|^2_{L^2}\\ &\leqslant C_{10}(C_9+\beta)\|a^{p/2}\|^{1/2}_{W_2^1(\Omega)}\|a^{p/2}\|^{3/2}_{L^{3/2}(\Omega)}\\ &\leqslant \frac{\beta}{2}\|a^{p/2}\|^2_{W_2^1(\Omega)} + C_{11}\|a^{p/2}\|^2_{L^{3/2}(\Omega)}\\ &= \frac{\beta}{2}\|a^{p/2}\|^2_{W_2^1(\Omega)} + C_{11}\|a\|^p_{L^{3p/4}(\Omega)}\\ &\leqslant \frac{\beta}{2}\|a^{p/2}\|^2_{W_2^1(\Omega)} + C_{12}, \end{aligned} \tag{4.102}$$

where C_9 and β are arbitrary positive numbers. In order to prove the L^p bound for a^D we insert (4.100), where $a = a^D$, into (4.96) and fix ε such that $\varepsilon\chi_D p e^{\chi_D} C_8 < 2(p-1)/p$. Thus, we obtain

$$\frac{d}{dt}\int_\Omega e^{\chi_D\nu}(a_\gamma^D)^p\,dx \leqslant -\frac{2(p-1)}{p}\int_\Omega |\nabla(a_\gamma^D)^{p/2}|^2\,dx + C_{13}\int_\Omega (a_\gamma^D)^p\,dx + C_{14}. \tag{4.103}$$

By adding $\beta\int_\Omega (a_\gamma^D)^p\,dx$ to both sides of (4.103) we get

$$\begin{aligned}\frac{d}{dt}\int_\Omega e^{\chi_D\nu}(a_\gamma^D)^p\,dx + \beta\int_\Omega (a_\gamma^D)^p\,dx &\leqslant -\frac{2(p-1)}{p}\int_\Omega |\nabla(a_\gamma^D)^{p/2}|^2\,dx\\ &\quad + (C_{13}+\beta)\int_\Omega (a_\gamma^D)^p\,dx + C_{14}. \end{aligned} \tag{4.104}$$

We can now insert (4.102), where $a = a^D$ and $\beta = 2(p-1)/p$, into (4.104) and get

$$\frac{d}{dt}\int_\Omega e^{\chi_D\nu}(a_\gamma^D)^p\,dx + \frac{p-1}{p}\int_\Omega (a_\gamma^D)^p\,dx \leqslant C_{15}, \tag{4.105}$$

which implies

$$\frac{d}{dt}\int_\Omega e^{\chi_D \nu}(a_\gamma^D)^p\,dx + \frac{p-1}{p\,e^{\chi_D}}\int_\Omega e^{\chi_D \nu}(a_\gamma^D)^p\,dx \leqslant C_{15}. \tag{4.106}$$

Thus, with Lemma 3.4 we obtain

$$\int_\Omega e^{\chi_D \nu}(a_\gamma^D)^p\,dx \leqslant C_{16}. \tag{4.107}$$

Consequently, we have shown that

$$\|a^D(\cdot,t)\|_{L^p(\Omega)} \leqslant C_{17}. \tag{4.108}$$

Applying Young's inequality and (4.108) leads to

$$\begin{aligned}\int_\Omega a^D(a_\gamma^S)^{p-1}\,dx &\leqslant \frac{p-1}{p}\int_\Omega (a_\gamma^S)^p\,dx + \frac{1}{p}\int_\Omega (a^D)^p\,dx \\ &\leqslant C_{18}\int_\Omega (a_\gamma^S)^p\,dx + C_{19}.\end{aligned} \tag{4.109}$$

Inserting (4.109) into (4.97) then yields

$$\begin{aligned}\frac{d}{dt}\int_\Omega e^{\chi_S \nu}(a_\gamma^S)^p dx \leqslant -\frac{4(p-1)}{p}\int_\Omega |\nabla (a_\gamma^S)^{p/2}|^2\,dx \\ + C_{20}\int_\Omega (a_\gamma^S)^p\,dx + C_{21}\int_\Omega m(a_\gamma^S)^p\,dx + C_{22}.\end{aligned} \tag{4.110}$$

Since (4.100) and (4.102) are also valid for $a = a^S$, we can repeat the steps in (4.103)–(4.107) for (4.110) to get

$$\|a^S(\cdot,t)\|_{L^p(\Omega)} \leqslant C_{23}. \tag{4.111}$$

Step 3: L^p bounds for all $p \geqslant 1$ From Lemma 4.17 and the previous step the estimates

$$\|a^D(\cdot,t)\|_{L^{(4/3)^n}(\Omega)},\ \|a^S(\cdot,t)\|_{L^{(4/3)^n}(\Omega)} \leqslant C_{24}(n) < \infty$$

follow by induction on $n \in \mathbb{N}$. Hence, we have for all $1 \leqslant p < \infty$ that

$$\|a^D(\cdot,t)\|_{L^p(\Omega)},\ \|a^S(\cdot,t)\|_{L^p(\Omega)} \leqslant C_{25}(p) < \infty. \tag{4.112}$$

Step 4: L^∞ bounds For this step we employ the technique from [4], which was applied before to a Keller-Segel model in [36]. We are in space dimension $d = 2$ and we know from Step 3 that there is a $\rho > d = 2$ such that $\|c^D + c^S\|_{L^\rho(\Omega)} \leqslant C_{20}$. Therefore, we get by Lemma 4.11 (where $c = c^D + c^S$) that

$$\|m\|_{L^\infty(Q_T)} \leqslant C_{26}. \tag{4.113}$$

Inserting (4.113) back into (4.96) we get for all $p \geqslant \rho$ that

$$\frac{d}{dt}\int_\Omega e^{\chi_D \nu}(a^D)^p\,dx + \frac{4(p-1)}{p}\int_\Omega |\nabla (a^D)^{p/2}|^2\,dx \leqslant C_{27}\,p\int_\Omega (a^D)^p\,dx. \tag{4.114}$$

We define the sequence $p_k = 2^k$ for $k \in \mathbb{N}$ and obtain from (3.17) the Gagliardo-Nirenberg inequality

$$\|\cdot\|_{L^2} \leqslant C_{28}\|\cdot\|_{W_2^1}^{1/2}\|\cdot\|_{L^1}^{1/2}. \tag{4.115}$$

Thus, we get for $a \in \{a^D,\ a^S\}$ by (4.115) and Young's inequality the estimate

$$\begin{aligned}\int_\Omega a^{p_k}\,dx = \|a^{p_{k-1}}\|_{L^2(\Omega)}^2 &\leqslant C_{29}\|a^{p_{k-1}}\|_{W_2^1(\Omega)}\|a^{p_{k-1}}\|_{L^1(\Omega)}\\ &\leqslant C_{29}\left(\frac{1}{\varepsilon_k}\|a^{p_{k-1}}\|_{L^1(\Omega)}^2 + \varepsilon_k\|a^{p_{k-1}}\|_{W_2^1(\Omega)}^2\right),\end{aligned} \tag{4.116}$$

which implies for sufficiently small ε_k that

$$\int_\Omega a^{p_k}\,dx \leqslant C_{29}\left(\frac{1}{\varepsilon_k}\|a^{p_{k-1}}\|_{L^1(\Omega)}^2 + \varepsilon_k\|\nabla a^{p_{k-1}}\|_{L^2(\Omega)}^2\right). \tag{4.117}$$

Next, we substitute $p = p_k$. Adding then $\varepsilon_k e^{\chi_D}\int_\Omega (a^D)^{p_k}\,dx$ to both sides of (4.114), choosing ε_k in (4.117) such that

$$(C_{27}\,p_k + \varepsilon_k e^{\chi_D})C_{29}\,\varepsilon_k \leqslant 4(p_k-1)/p_k < 4 \tag{4.118}$$

for $a = a^D$ and inserting in (4.114) yield for $k \geqslant 2$ the inequality

$$\begin{aligned}&\frac{d}{dt}\int_\Omega e^{\chi_D\nu}(a^D)^{p_k}\,dx + \varepsilon_k e^{\chi_D}\int_\Omega (a^D)^{p_k}\,dx\\ &\qquad\leqslant \frac{(C_{27}\,p_k + \varepsilon_k e^{\chi_D})C_{29}}{\varepsilon_k}\left(\int_\Omega (a^D)^{p_{k-1}}\,dx\right)^2.\end{aligned} \tag{4.119}$$

The latter implies that

$$\frac{d}{dt}\int_\Omega e^{\chi_D\nu}(a^D)^{p_k}\,dx \leqslant -\varepsilon_k\int_\Omega e^{\chi_D\nu}(a^D)^{p_k}\,dx + \frac{(C_{27}\,p_k + \varepsilon_k e^{\chi_D})C_{29}}{\varepsilon_k}M_{k-1}^2, \tag{4.120}$$

where

$$M_k = \max\left\{1,\ \sup_{0<t<T}\int_\Omega e^{\chi_D\nu}(a^D)^{p_k}\,dx\right\}. \tag{4.121}$$

By Gronwall's lemma we get from (4.120) that for $k \geqslant 2$ it holds

$$\int_\Omega e^{\chi_D\nu}(a^D)^{p_k}\,dx \leqslant \max\left\{\int_\Omega e^{\chi_D\nu_0}(a_0^D)^{p_k}\,dx,\ \frac{(C_{27}\,p_k + \varepsilon_k e^{\chi_D})C_{29}}{\varepsilon_k^2}M_{k-1}^2\right\}. \tag{4.122}$$

Hence, we have that

$$M_k \leqslant \max\left\{1,\ |\Omega|e^{\chi_D}\|(a_0^D)\|_{L^\infty(\Omega)}^{p_k},\ \delta_k M_{k-1}^2\right\} \quad \text{for } k \geqslant 2, \tag{4.123}$$

where $\delta_k = \max\{1,\ (C_{27}\,p_k + \varepsilon_k e^{\chi_D})C_{29}/\varepsilon_k^2\}$. Note that by (4.44) and (4.112) we can find a constant C_{30} such that

$$M_1 + 1 \leqslant C_{30}, \quad |\Omega|e^{\chi_D}\|(a_0^D)\|_{L^\infty(\Omega)}^{p_k} \leqslant C_{30}^{p_k} \text{ for } k \geqslant 1. \tag{4.124}$$

From (4.123), (4.124) and $\delta_k \geqslant 1$ we get

$$M_k \leqslant \delta_k \, \delta_{k-1}^{p_1} \, \delta_{k-2}^{p_2} \cdots \delta_2^{p_{k-2}} \, \delta_1^{p_{k-1}} C_{30}^{p_k}. \tag{4.125}$$

In addition, we get from (4.118) that ε_k can be chosen as $\varepsilon_k = C_{31}/p_k$ where the constant C_{31} is independent of k. This yields

$$\delta_k \leqslant C_{32} p_k^3,$$

and hence we obtain

$$M_k^{1/p_k} \leqslant C_{32}^{\sum_{i=0}^{k-1} 2^{i-k}} \, 2^{3 \sum_{i=0}^{k-1} 2^{i-k}(k-i)} C_{30} \leqslant C_{32}^{1-\frac{1}{p_k}} 2^{3 \sum_{i=1}^{k} \frac{i}{2^i}} C_{30}. \tag{4.126}$$

For $0 < t < T$ we note that $\max\{1, \ \|a^D(\cdot,t)\|_{L^{p_k}(\Omega)}\} \leqslant M_k^{1/p_k}$ by $0 \leqslant \nu \leqslant 1$. Letting $k \to \infty$ in (4.126) we get

$$\|a^D(\cdot,t)\|_{L^\infty(\Omega)} \leqslant C_{33}. \tag{4.127}$$

Then using the bounds (4.113), (4.127) as well as the sequence $p_k = 2^k$ for $k \in \mathbb{N}$ in (4.97) yield for $k \geqslant 2$ the inequality

$$\begin{aligned} \frac{d}{dt} \int_\Omega e^{\chi_S \nu} (a^S)^{p_k} \, dx + \frac{4(p_k - 1)}{p_k} \int_\Omega |\nabla (a^S)^{p_{k-1}}|^2 \, dx \\ \leqslant C_{34} \, p_k \int_\Omega (a^S)^{p_k} \, dx + C_{35} \, p_k \int_\Omega (a^S)^{p_k - 1} \, dx. \end{aligned} \tag{4.128}$$

By Hölder's inequality we estimate

$$\int_\Omega (a^S)^{p_k - 1} \, dx \leqslant |\Omega|^{1/p_k} \left(\int_\Omega (a^S)^{p_k} \, dx \right)^{(p_k-1)/p_k} \leqslant C_{36} \left(\int_\Omega (a^S)^{p_k} \, dx + 1 \right),$$

and obtain in this way

$$\begin{aligned} \frac{d}{dt} \int_\Omega e^{\chi_S \nu} (a^S)^{p_k} \, dx + \frac{4(p_k - 1)}{p_k} \int_\Omega |\nabla (a^S)^{p_{k-1}}|^2 \, dx \\ \leqslant C_{37} \, p_k \left(\int_\Omega (a^S)^{p_k} \, dx + 1 \right). \end{aligned} \tag{4.129}$$

We add again $\varepsilon_k e^{\chi_S} \int_\Omega (a^S)^{p_k} \, dx$ to both sides of (4.129) and choose ε_k such that

$$(C_{37} \, p_k + \varepsilon_k e^{\chi_S}) C_{29} \, \varepsilon_k \leqslant 4(p_k - 1)/p_k < 4, \tag{4.130}$$

where C_{29} and ε_k are chosen such that (4.117) is true for $a = a^S$. By setting $\varepsilon_k = C_{38}/p_k$ we find a constant $C_{39} > C_{29}$ such that

$$\frac{(C_{37} \, p_k + \varepsilon_k e^{\chi_S}) C_{39}}{\varepsilon_k} \geqslant C_{37} p_k. \tag{4.131}$$

Inserting now (4.131) into (4.129) yields

$$\frac{d}{dt} \int_\Omega e^{\chi_S \nu} (a^S)^{p_k} \, dx \leqslant -\varepsilon_k \int_\Omega e^{\chi_S \nu} (a^S)^{p_k} \, dx + \frac{2(C_{37} \, p_k + \varepsilon_k e^{\chi_S}) C_{39}}{\varepsilon_k} M_{k-1}^2, \tag{4.132}$$

where

$$M_k = \max \left\{ 1, \ \sup_{0<t<T} \int_\Omega e^{\chi_S \nu} (a^S)^{p_k} \right\}.$$

Using the same argumentation as in (4.122)–(4.127) it follows for $0 < t < T$ that it also holds

$$\|a^S(\cdot,t)\|_{L^\infty(\Omega)} \leqslant C_{40}, \tag{4.133}$$

which completes the proof of the theorem. □

4.7 An estimate for the gradient of the tissue density

In this section we show an *a priori* bound for ∇v in $L^4(\Omega)$. This bound is crucial for the expansion of the existence interval of the solution. We skip a rather technical part of the proof and refer to our work [58] for further details.

In the first step we derive a relation between bounds on the gradient of the tissue density and the gradient of the transformed cancer cell concentrations, i.e. between $\|\nabla v(t)\|_{L^p(\Omega)}$, $\|\nabla a^D\|_{L^p(Q_T)}$ and $\|\nabla a^S(t)\|_{L^p(Q_T)}$.

Lemma 4.19 *Assume that* $(a^D, a^S, v, m) \in (C^{2,1}(\bar{Q}_T))^4$ *is a solution of* (IV'). *Then for any* $p \geqslant 1$ *the following inequality holds*

$$\|\nabla v(t)\|^p_{L^p(\Omega)} \leqslant C(T,p)\left(\|\nabla a^D\|^p_{L^p(Q_T)} + \|\nabla a^S\|^p_{L^p(Q_T)} + 1\right). \tag{4.134}$$

Proof. We use the chain rule in (IV') to obtain

$$\nabla(\partial_t v) = h_1 \nabla v - \left(v\nabla m + \mu_v v e^{\chi_S v}\nabla a^S + \mu_v v e^{\chi_D v}\nabla a^D\right). \tag{4.135}$$

Here we have used the term

$$h_1 = -m + \mu_v R - \mu_v v e^{\chi_S v}\chi_S a^S - \mu_v v e^{\chi_D v}\chi_D a^D - 1, \tag{4.136}$$

for which we note that $h_1 \leqslant \mu_v$. Next, we take equation (4.135) and multiply it by $p\nabla v|\nabla v|^{p-2}$. Employing $0 \leqslant v \leqslant 1$, the bound $\|m(t)\|_{W^1_\infty(\Omega)} \leqslant C$ (from (4.93) and Lemma 4.11) and Young's inequality (3.13) (with exponents p and $p/(p-1)$) we obtain

$$\begin{aligned}
\partial_t(|\nabla v|^p) &= h_1\, p|\nabla v|^p - \Big(pv\nabla v\cdot\nabla m|\nabla v|^{p-2} \\
&\quad + p\mu_v v e^{\chi_S v}\nabla a^S\cdot\nabla v|\nabla v|^{p-2} + p\mu_v v e^{\chi_D v}\nabla a^D\cdot\nabla v|\nabla v|^{p-2}\Big) \\
&\leqslant \mu_v p|\nabla v|^p + p\|\nabla m\|_{L^\infty(\Omega)}|\nabla v|^{p-1} + p\mu_v e^{\chi_D}|\nabla a^D|\,|\nabla v|^{p-1} \\
&\quad + p\mu_v e^{\chi_S}|\nabla a^S||\nabla v|^{p-1} \\
&\leqslant C_1|\nabla v|^p + C_2|\nabla a^D|^p + C_3|\nabla a^S|^p + C_4.
\end{aligned} \tag{4.137}$$

By integrating over Ω we get

$$\frac{d}{dt}\|\nabla v\|^p_{L^p(\Omega)} \leqslant C_5\left(\|\nabla v\|^p_{L^p(\Omega)} + \|\nabla a^D\|^p_{L^p(\Omega)} + \|\nabla a^S\|^p_{L^p(\Omega)} + 1\right).$$

The estimate (4.134) follows by the Gronwall Lemma. □

The next Lemma provides *a priori* estimates for the transformed cancer cell densities in Bochner spaces. They will allow us to make use of the relation in Lemma 4.19.

Lemma 4.20 *Assume that* $(a^D, a^S, v, m) \in (C^{2,1}(\bar{Q}_T))^4$ *is a solution of system* (IV'). *Then the following inequalities hold*

$$\|\nabla a^D\|^4_{L^4(Q_T)} \leqslant C(T), \quad \|\nabla a^S\|^4_{L^4(Q_T)} \leqslant C(T). \tag{4.138}$$

Proof. The estimates (4.138) are obtained in several steps. In the first step we derive estimates for the spatial and temporal derivatives of the transformed cancer cell densities of the form

$$\|\nabla a^D(t)\|_{L^2(\Omega)} \leqslant Ce^{\chi_D \mu_v t}, \qquad \|\partial_t a^D\|_{L^2(Q_t)} \leqslant Ct + \tilde{C}e^{\chi_D \mu_v t},$$
$$\|\nabla a^S(t)\|_{L^2(\Omega)} \leqslant Ce^{\chi_S \mu_v t}, \qquad \|\partial_t a^S\|_{L^2(Q_t)} \leqslant Ct + \tilde{C}e^{\chi_S \mu_v t}. \tag{4.139}$$

These are obtained by multiplying the equation for a^D in (IV') by $e^{\chi_D v}\partial_t a^D$, integrating over Ω, a series of basic estimates and a similar treatment for the evolution equation of the transformed CSCs density a^S.

In the second step we apply (4.139), a rewritten formulation of the transformed cancer cell density evolution equation, a series of basic estimates and a time iteration process to derive

$$\|\Delta a^D(t)\|^2_{L^2(Q_T)} \leqslant C(T), \quad \|\Delta a^S(t)\|^2_{L^2(Q_T)} \leqslant C(T). \tag{4.140}$$

In the next step, we apply the Gagliardo-Nirenberg inequality (3.17) and obtain for any $0 \leqslant t \leqslant T$ the inequality

$$\int_0^t \|\nabla a^I\|^4_{L^4(\Omega)}\, ds \leqslant C_6 T e^{4\chi_D \mu_v T} + C_7 e^{2\chi_D \mu_v T} \int_0^t \|\Delta a^I\|^2_{L^2(\Omega)}\, ds. \tag{4.141}$$

By combining (4.141) and (4.140) in the final step the statement of the lemma follows. For the technical details we refer to [58]. □

The main result of this section is a direct consequence of estimates (4.138) and (4.134).

Corollary 4.21 *Assume that* $(a^D, a^S, v, m) \in (C^{2,1}(\bar{Q}_T))^4$ *is a solution of* (IV'). *Then we have*

$$\|\nabla v(t)\|_{L^4(\Omega)} \leqslant C_8(T)\,. \tag{4.142}$$

4.8 Global and unique classical solutions of an EMT cancer invasion system

In this section we combine the results from the previous sections and show existence and uniqueness of classical solutions of (IV'). For this purpose we firstly derive the final *a priori* estimates, which are needed to extend the local solution in time.

Lemma 4.22 *Let* $(a^D, a^S, v, m) \in \left(C^{2,1}(\bar{Q}_T)\right)^4$ *be a solution of system* (IV') *and let* (4.39) *hold. Then for all* $t \in (0, T)$ *we have*

$$\|a^D(t)\|_{C^2(\bar{\Omega})}, \|a^S(t)\|_{C^2(\bar{\Omega})}, \|v(t)\|_{C^1(\bar{\Omega})}, \|m(t)\|_{C^2(\bar{\Omega})} \leqslant C(T). \tag{4.143}$$

Proof. We obtain from estimates (4.39) and (4.93) and Lemma 4.11 that

$$\|a^D(t)\|_{L^\infty(\Omega)},\ \|a^S(t)\|_{L^\infty(\Omega)}, \|m(t)\|_{W^1_\infty(\Omega)} \leqslant C. \tag{4.144}$$

Now, using (IV'), we can rewrite the equations for the transformed cancer cell densities a^D and a^S as

$$\partial_t a^D = \Delta a^D + \chi_D \nabla v \cdot \nabla a^D + h_1 a^D \quad \text{in } \Omega \times (0, T), \tag{4.145}$$
$$\partial_t a^S = \Delta a^S + \chi_S \nabla v \cdot \nabla a^S + h_2 a^S + \mu_{EMT}\, e^{\chi_D v - \chi_S v}\, a^D \quad \text{in } \Omega \times (0, T), \tag{4.146}$$

where

$$h_1 = -\mu_{EMT} + (\mu_D - \chi_D \mu_\nu \nu)R + \chi_D \nu m, \tag{4.147}$$

$$h_2 = (\mu_S - \chi_S \mu_\nu \nu)R + \chi_S \nu m. \tag{4.148}$$

By employing (4.142), $0 \leqslant \nu \leqslant 1$, (4.144) and (4.40b) we have

$$\|\nabla v(t)\|_{L^4(\Omega)},\ \|h_1(t)\|_{L^\infty(\Omega)}, \|h_2(t)\|_{L^\infty(\Omega)},\ \|\mu_{EMT}\, e^{\chi_D \nu - \chi_S \nu}\, a^D(t)\|_{L^\infty(\Omega)} \leqslant C_1(T). \tag{4.149}$$

This allows us to use the maximal parabolic regularity result in L^p ([106, Chapter IV, Theorem 9.1, p. 341]) for both equations (4.145) and (4.146). We obtain for $1 \leqslant p < 4$ the inequality

$$\|a^D\|_{W_p^{2,1}(Q_T)}, \|a^S\|_{W_p^{2,1}(Q_T)} \leqslant C_2(p, T). \tag{4.150}$$

Thanks to this estimate and the Sobolev embedding ([106, Chapter II, Lemma 3.3, p. 80]) we have that

$$\|\nabla a^D\|_{L^p(Q_T)}, \|\nabla a^S\|_{L^p(Q_T)} \leqslant C_3(p, T) \quad \text{for all } p \geqslant 1 \tag{4.151}$$

and thus by (4.134) also

$$\|\nabla v(t)\|_{L^p(\Omega)} \leqslant C_4(p, T) \quad \text{for all } p \geqslant 1. \tag{4.152}$$

Due to Theorem 3.1, (4.149) and (4.152) estimate (4.150) is true for all $p \geqslant 1$.

Moreover, applying Theorem 3.1 once again in the evolution equation for m in (IV′) yields

$$\|m\|_{W_p^{2,1}(Q_T)} \leqslant C_5(p) \quad \text{for all } p \geqslant 1. \tag{4.153}$$

Then we apply the Sobolev embedding (3.11) to (4.150) and (4.153) for a fixed $p > 5$ to get for $\lambda = 1 - 5/p$ that

$$\|a^D\|_{C^{1+\lambda,(1+\lambda)/2}(\bar{Q}_T)},\ \|a^S\|_{C^{1+\lambda,(1+\lambda)/2}(\bar{Q}_T)}, \|m\|_{C^{1+\lambda,(1+\lambda)/2}(\bar{Q}_T)} \leqslant C_6(T). \tag{4.154}$$

By considering $0 \leqslant \nu \leqslant 1$, the evolution equation for a^S in (IV′) and the estimates (4.81), (4.78) and (4.79) together with (4.154) we obtain

$$\|v\|_{C^{1,1}(\bar{Q}_T)} \leqslant C_7(T). \tag{4.155}$$

Using now the same arguments as in the proof of Theorem 4.16 we see that

$$\|a^D\|_{C^{2+\lambda,1+\lambda/2}(\bar{Q}_T)}, \|a^S\|_{C^{2+\lambda,1+\lambda/2}(\bar{Q}_T)}, \|m\|_{C^{2+\lambda,1+\lambda/2}(\bar{Q}_T)} \leqslant C_8(T). \tag{4.156}$$

The estimate (4.143) follows from (4.156) and (4.155). □

Finally, we are ready to show existence and uniqueness of global classical solutions.

Theorem 4.23 (Global existence) *Let* (4.39) *be satisfied and let* $T > 0$ *be given. Then there exists a unique solution* $(c^D, c^S, \nu, m) \in (C^{2+l,1+l/2}(\bar{Q}_T))^4$ *of system* (IV). *For this solution it holds* $c^D, c^S, m \geqslant 0$ *and* $0 \leqslant \nu \leqslant 1$.

Proof. This statement results from Theorems 4.15 and 4.16, Lemma 4.22, and the equivalence of systems (IV) and (IV').

Assume the solution of (IV') existed up to a finite maximal point in time, i.e. assume there was a $T^* < \infty$, such that the solution existed only for $t \in [0, T^*)$. By Lemma 4.22 we would find a constant $C(T^*)$ that would satisfy for all $0 \leqslant t < T^*$ that

$$\|a^D(t)\|_{C^2(\bar{\Omega})}, \|a^S(t)\|_{C^2(\bar{\Omega})}, \|v(t)\|_{C^1(\bar{\Omega})}, \|m(t)\|_{C^2(\bar{\Omega})} \leqslant C(T^*).$$

By the local existence result of Theorem 4.15 and Theorem 4.16 we could find $M(T^*)$ as well as $T_0 = T_0(M(T^*))$ by which we could extend the classical solution in time from an arbitrary starting point $t \in [0, T^*)$. In particular, for $0 < \varepsilon < T_0$ we could extend the solution up to $T^* - \varepsilon + T_0 > T^*$, which in turn would contradict the assumption. This shows that there cannot be a finite maximal time of existence. □

4.9 Discussion

The proof of global existence and uniqueness of solutions to model (IV') gives rise to the question, if one can obtain similar results for the full model (II). In comparison to (IV') the haptotaxis EMT/invasion system introduces two additional challenges. These are the tissue remodeling by a third species of cells (fibroblasts) and positive logistic terms.

The case of fibroblast remodeling without positive resource terms does not imply the nonnegativity of the ECM density, see Section 4.3. Since this nonnegativity is used in many places throughout the proof, we believe that a direct adaptation of the presented techniques to this case is not possible and therefore the positive logistic terms are needed.

A positive resource term might in fact assist in the derivation of *a priori* estimates. One can see in (4.96) that in the case of $R > 0$ the condition (4.39) on the proliferation rate is not necessary in the derivation of *a priori* bounds for the transformed densities a^D and a^S. On the other hand one gets difficulties by the nondifferentiability of the positive part term, e.g., in the proof of Theorem 4.16. Thus, one could instead study a smooth positive function for R in the first place, for instance, a mollifier of R^+.

Due to the variable transformation (Proposition 4.10) tissue remodeling by fibroblasts introduces an additional coupling between the fibroblast density and the cancer cell concentrations. However, these additional terms do not cause problems in the proof of *a priori* bounds for the transformed densities a^D and a^S. This is because the arising term $(\mu - \chi\mu_f c^F)R$ can be easily estimated by the nonnegativity and boundedness of R and the nonnegativity of c^F. We also believe that using the variable transformation *a priori* bounds for the fibroblast density c^F can be derived with the techniques from the proof of Theorem 4.18.

In summary, we conjecture that global existence and uniqueness of solutions to system (II) can be obtained by an adaptation of the techniques presented in this chapter provided R is positive and smooth and $0 \leqslant v \leqslant 1$.

5 Implicit-explicit finite volume methods for cancer invasion models

In this chapter we develop finite volume/finite difference methods for the numerical simulation of systems (I), (II) and (III). To this end we introduce an adapted central upwind scheme. We describe the derivation of the scheme in Sections 5.1 and 5.2 and address the adjustment to nonuniform grids in 1D and to quadrilateral grids in 2D in Sections 5.3 and 5.4.

The scheme admits a semi-discrete form that we will provide for the three introduced cancer invasion systems in Section 5.5. These discretizations allow us to employ efficient time discretization methods. In particular, we consider splitting schemes that decouple the stiff diffusion terms and treat them implicitly. This increases the efficiency by making larger time steps possible. The time integration and particular methods are discussed in Sections 5.6–5.8.

We moreover show in Section 5.9 that for model (II) the nonnegativity of numerical solutions can be preserved throughout the simulation time when employing the proposed scheme. In Section 5.10 we discuss particular adjustments to the time discretization method when dealing with the contractivity model (III). We close this chapter with numerical experiments and a comparison of various time integration methods in the case of the uPA model (I) in Section 5.11.

5.1 Finite volume methods for scalar conservation laws

The numerical scheme that we propose employs a finite volume approach for the cancer cell equations. To introduce the idea we will briefly present the framework of finite volumes for nonlinear hyperbolic equations. For our purpose it suffices to restrict ourselves to scalar nonlinear *conservation laws* in 1D that read

$$\partial_t u + \partial_x f(u) = 0, \quad x \in \Omega = (a, b), \quad t > 0, \tag{5.1}$$

where u is a state variable depending on space and time. We complement (5.1) with homogeneous Neumann boundary conditions

$$\partial_x u(a, t) = \partial_x u(b, t) = 0, \quad t > 0$$

and smooth initial data

$$u(x, 0) = u_0(x) \geqslant 0, \quad x \in \Omega.$$

The solutions of (5.1) can develop discontinuities in finite time despite given smooth initial data. This makes the numerical approximation delicate. Nevertheless, the scalar case (5.1) was

extensively studied in the past and is now well understood from an analytical and a numerical point of view. Note though that there are still many open problems in more general cases, e.g., for systems of hyperbolic conservation laws [110].

To study suitable numerical schemes we firstly introduce a discrete mesh.

Definition 5.1 For the one-dimensional domain $\Omega = (a, b)$ a *finite volume mesh* of cardinality $N \in \mathbb{N}$ is given by the *grid cells*

$$C_i = (x_{i-1/2}, x_{i+1/2}), \quad i = 1, \dots, N$$

that cover the domain Ω in the sense $\bigcup_{i=1}^{N} \bar{C}_i = \bar{\Omega}$. The corresponding *cell midpoints* and *cell interfaces* are defined as

$$\begin{aligned} x_i &= a + \sum_{j=1}^{i-1} h_j + \frac{h_i}{2}, && i = 1, \dots, N, \\ x_{i\pm1/2} &= x_i \pm \frac{h_i}{2}, && i = 1, \dots, N, \end{aligned}$$

where $h_i = |C_i| > 0$ refers to the size of a particular grid cell. We denote the maximal grid cell size by $h = \max\{h_1, \dots, h_N\}$. In the case $h_i = h$ for $i = 1, \dots, N$ the mesh is called *uniform*.

We derive the general finite volume formulation by integrating (5.1) over a grid cell C_i in space and over an interval (t^n, t^{n+1}) in time. In this process we obtain by the divergence theorem

$$\begin{aligned} 0 &= \frac{1}{h_i} \int_{t^n}^{t^{n+1}} \int_{C_i} \partial_t u(x,t)\, dx\, dt + \frac{1}{h_i} \int_{t^n}^{t^{n+1}} \int_{C_i} \partial_x f(u)\, dx\, dt \\ &= \frac{1}{h_i} \int_{C_i} u(x, t^{n+1}) - u(x, t^n)\, dx + \frac{1}{h_i} \int_{t^n}^{t^{n+1}} \int_{\partial C_i} f(u)\, dx\, dt \\ &= u_i^{n+1} - u_i^n + \frac{1}{h_i} \int_{t^n}^{t^{n+1}} f(u(x_{i+1/2}, t)) - f(u(x_{i-1/2}, t))\, dt. \end{aligned} \tag{5.2}$$

Here we have assumed that both the state variable u and the function f are sufficiently smooth and we have used the notation $u_i^n = |C_i|^{-1} \int_{C_i} u(x, t^n)\, dx$ to refer to the cell average in mesh cell C_i at time instance t^n. In the following discussion we use the same notation u_i^n also for approximate cell averages and we denote the vector containing the numerical solution at time t^n over the full finite volume mesh by $u_h(t^n) = (u_i^n)_{i=1}^N$.

The major challenge in the construction of a suitable approximation method for (5.1) remains the reasonable approximation of the *fluxes* $\int_{t^n}^{t^{n+1}} f(u(x_{i+1/2}, t))$. The main reason for this is the possible discontinuity of the function u in $x_{i+1/2}$. For this purpose one considers the *numerical fluxes*

$$\mathcal{H}_{i+1/2}^n \approx \frac{1}{t^{n+1} - t^n} \int_{t^n}^{t^{n+1}} f(u(x_{i+1/2}, t))\, dt, \tag{5.3}$$

that are usually obtained by a *numerical flux function* that approximates the flux based on the adjacent cell averages

$$\mathcal{H}_{i+1/2}^n = \mathcal{H}(u_i^n, u_{i+1}^n). \tag{5.4}$$

The numerical fluxes yield together with (5.2) the *finite volume scheme*

$$u_i^{n+1} = u_i^n - \frac{\tau}{h_i}\left(\mathcal{H}_{i+1/2}^n - \mathcal{H}_{i-1/2}^n\right), \quad i = 1, \dots, N, \tag{5.5}$$

where $\tau = t^{n+1} - t^n$. For consistency with the homogeneous Neumann boundary conditions the numerical fluxes satisfy $\mathcal{H}_{0-1/2}^n = \mathcal{H}_{N+1/2}^n = 0$. In what follows we will consider a single step in time and drop the superscript n for brevity.

Most numerical flux functions are related to *Godunov's method* which makes use of the analytical structure of the problem. It is known that the solution of the conservation law (5.1) remains constant along the so-called *characteristic lines* or characteristics in the time-space phase. Intersections of these characteristic lines lead to discontinuous shock waves in the solution. Characteristics that spread apart result in rarefaction waves. Consider the conservation law (5.1) on the real line with initial data

$$u(x, 0) = \begin{cases} U_l, & x < 0, \\ U_r, & x > 0. \end{cases}$$

This is the so-called *Riemann problem* which has a solution that is either a shock or a rarefaction wave. Thus, the *Riemann solution* $u(0, t) = U^{RP}(U_l, U_r)$ is particularly constant for any $t > 0$. The *Godunov flux* is now defined as

$$\mathcal{H}^G(u_i, u_{i+1}) = f(U^{RP}(u_i, u_{i+1})) \tag{5.6}$$

and the corresponding finite volume scheme solves the Riemann problem at each cell interface. If we assume that the function f is continuously differentiable and if

$$f'(u_i) \leqslant 0 \leqslant f'(u_{i+1}) \tag{5.7}$$

is excluded, then the flux function (5.6) can be rewritten as

$$\mathcal{H}^G(u_i, u_{i+1}) = \begin{cases} f(u_i), & s > 0, \\ f(u_{i+1}), & s < 0. \end{cases} \tag{5.8}$$

Here the *shock speed* s is given by the *Rankine-Hugoniot condition*

$$s = \frac{f(u_{i+1}) - f(u_i)}{u_{i+1} - u_i}. \tag{5.9}$$

In the particular case (5.7) the numerical scheme (5.5) with flux function (5.8) does not approximate a physical *entropy solution* of (5.1). For this reason the flux (5.8) is usually modified with the so-called *entropy fix*. Here however, we do not consider the case (5.7) and refer to [110] for more information on how the entropy-consistent fluxes are constructed.

A simple scalar conservation law is the *linear transport equation*, which is given by (5.1) for $f(u) = au$ and a constant velocity $a > 0$. In the case of this equation the Godunov flux function reduces to the *upwind flux*

$$\mathcal{H}^U(u_i, u_{i+1}) = f(u_i). \tag{5.10}$$

Central schemes and linear reconstructions

Further popular numerical flux functions originate from the class of *central schemes*. These have the advantage of being easily applicable to systems of conservations laws without being dependent on the structures of eigenvalues of the particular problem. They were derived by a modification of Godunov's method to staggered grids [105]. In what follows we restrict ourselves to uniform finite volume meshes.

A well known example of a flux function related to central schemes is the *Lax-Friedrich* numerical flux

$$\mathcal{H}^{LxF}(u_i, u_{i+1}) = \frac{1}{2}\left(f(u_i) + f(u_{i+1})\right) - \frac{h}{\tau}(u_{i+1} - u_i). \tag{5.11}$$

The corresponding scheme is commonly used in many applications. It is more dissipative than Godunov's method but does not need an entropy fix to approximate the physically relevant solution of (5.1).

After the derivation of the scheme (5.5), (5.11) in [53, 109], higher order central schemes were developed, e.g., in [105, 127]. Many of these schemes are related to the *Monotonic Upstream-Centered Scheme for Conservation Laws* (MUSCL) from [112] which enhances Godunov's method with a piecewise linear reconstruction in each computational cell. To explain the underlying idea, let s_i denote an approximated slope of $u(\cdot, t^n)$ in the cell C_i on a uniform grid. An example is the central difference

$$s_i = \frac{u_{i+1} - u_{i-1}}{2h}.$$

Using the approximate slopes, we can define the interface reconstructions from the left and from the right as

$$u^L_{i+1/2} = u_i + \frac{h}{2}s_i, \quad u^R_{i+1/2} = u_{i+1} - \frac{h}{2}s_{i+1},$$

see also Figure 5.1. Higher accuracy of the scheme (5.5) can then be obtained by evaluating the numerical flux function at the interface reconstructions instead of at the cell averages, i.e. by replacing (5.4) by

$$\mathcal{H}_{i+1/2} = \mathcal{H}(u^L_{i+1/2}, u^R_{i+1/2}). \tag{5.12}$$

A consistent reconstruction by central (or forward/backward) differences in s_i for higher resolution introduces further problems. It can lead, for example, to over- and undershooting interface reconstruction at local extrema and discontinuities of the solution. These in turn result in numerical instabilities.

To overcome the stability issues the classes of *total variation bounded* (TVB) and *total variation diminishing* (TVD) schemes were constructed in literature.

Definition 5.2 (Total variation) Consider a function $u \in L^1((a,b))$ and a numerical solution on a finite volume mesh at a fixed time instance denoted by $u_h(t^n)$.

1. The *total variation* of u is given by

$$TV(u) = \limsup_{\varepsilon \to 0} \frac{1}{\varepsilon} \int_a^b |u(x) - u(x-\varepsilon)|\, dx.$$

2. For numerical data we define

$$TV(u_h(t^n)) = \sum_{i=2}^{N} |u_i^n - u_{i-1}^n|.$$

3. A numerical method is TVD, if it satisfies

$$TV(u_h(t^{n+1})) \leqslant TV(u_h(t^n)).$$

For given discrete slopes we can define piecewise linear reconstructions of finite volume solutions as

$$\tilde{u}(x, t^n) = \sum_{i=1}^{N} \chi_{C_i}(x) \left(u_i^n + s_i \left(x - x_i\right)\right), \tag{5.13}$$

where χ_{C_i} refers to the characteristic function over grid cell C_i. The idea for the derivation of TVD schemes is to choose the discrete slopes in such a way that the linear reconstruction satisfies $TV(\tilde{u}(\cdot, t^n)) \leqslant TV(u_h(t^n))$. To achieve this property slope limiters have been proposed, e.g., in [112]. We will consider, in particular, the *minimized central* (MC) limiter derived in [111] for the slope computation. On uniform meshes it reads

$$s_i = \text{minmod}\left(2\frac{u_i - u_{i-1}}{h},\ \frac{u_{i+1} - u_{i-1}}{2h},\ 2\frac{u_{i+1} - u_i}{h}\right). \tag{5.14}$$

Here the *minmod operator* is given by

$$\text{minmod}(v_1, \ldots, v_n) = \begin{cases} \max\{v_1, \ldots, v_n\}, & \text{if } v_k < 0,\ k = 1, \ldots, n, \\ \min\{v_1, \ldots, v_n\}, & \text{if } v_k > 0,\ k = 1, \ldots, n, \\ 0, & \text{otherwise.} \end{cases} \tag{5.15}$$

The limiter (5.14) preserves the monotonicity of the discrete solution, yields steep and sharp resolutions near discontinuities by considering twice the forward or backward difference, but does not distort the solution by admitting the central difference in smooth regions [110]. We will generalize the limiter to nonuniform grids in Section 5.3 and prove that the corresponding upwind scheme (5.5), (5.12), (5.10) is TVD. In this way, we justify that the nonoscillatory property of the reconstruction, i.e. $TV(\tilde{u}(\cdot, t^n)) \leqslant TV(u_h(t^n))$, also holds in the uniform case.

Based on the MUSCL approach the *central upwind scheme* was introduced in [104]. It was build on the central scheme from [105]. The corresponding flux function reads

$$\begin{aligned} \mathcal{H}_{i+1/2}^{CU} = &\frac{a_{i+1/2}^+ f(u_{i+1/2}^L) - a_{i+1/2}^- f(u_{i+1/2}^R)}{a_{i+1/2}^+ - a_{i+1/2}^-} \\ &+ \frac{a_{i+1/2}^+ a_{i+1/2}^-}{a_{i+1/2}^+ - a_{i+1/2}^-} \left(u_{i+1/2}^R - u_{i+1/2}^L\right), \end{aligned} \tag{5.16}$$

where $u_{i+1/2}^{L/R}$ are determined by a nonoscillatory slope reconstruction such as (5.14). The *local propagation speeds* needed for the computation of the numerical flux (5.16) are given by

$$a_{i+1/2}^+ = \max\left(f'(u_{i+1/2}^L),\ f'(u_{i+1/2}^R),\ 0\right), \tag{5.17a}$$

$$a_{i+1/2}^- = \min\left(f'(u_{i+1/2}^L),\ f'(u_{i+1/2}^R),\ 0\right). \tag{5.17b}$$

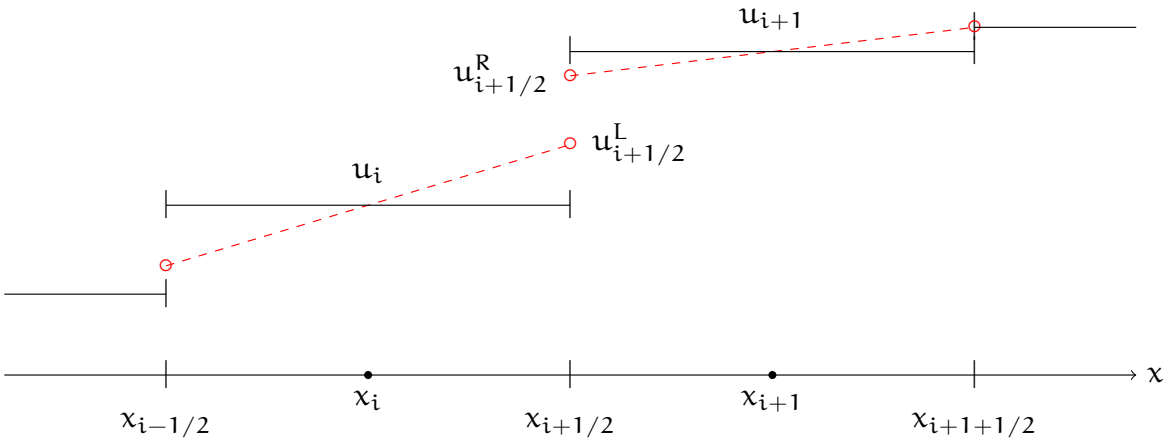

Figure 5.1: Interface reconstructions between the computational cells C_i and C_{i+1} from the left and from the right by the MC-limiter (5.14).

We refer to the original paper [104] for a more general formulation for hyperbolic systems. Flux (5.16) is related to the upwind flux since in the case of the linear transport equation and piecewise constants ($s_i = 0$) it reduces to (5.10). Moreover, the scheme (5.5), (5.16) remains simple and efficient because the flux computation requires, except for the reconstruction, only the propagation speeds that are needed anyway for the determination of the time increment τ, see Section 5.6.

The central-upwind scheme (5.5), (5.16) allows for a straightforward extension to *advection-diffusion-reaction* (ADR) equations of the form

$$\partial_t u + \partial_x f(u) = D\,\partial_x^2 u + S(u), \quad x \in \Omega = (a, b), \quad t > 0, \tag{5.18}$$

where S is an arbitrary Lipschitz continuous source term that satisfies $S(0) = 0$. Hence, it implies positive analytical solutions of (5.18). For these types of problems we consider an approximation of the second derivative by central differences. The source terms are simply approximated by an evaluation at the cell average u_i^n corresponding to the current mesh cell. We will follow this approach in the discretization of the cancer invasion system.

5.2 The central upwind scheme for chemo- and haptotaxis problems

In this section we introduce the finite volume/finite difference scheme for chemo and haptotaxis systems. To this end we will accordingly adapt the central upwind scheme introduced in the previous section.

We consider in this section the (parabolic-parabolic) 1D Keller-Segel model (2.25). As the spatial derivative of the chemo-attractant density a appears in the divergence term in the equation for the cell density, this system cannot be treated directly in the usual context of hyperbolic systems. In [31] the evolution equation for the concentration of the chemo-attractant was replaced by its gradient in order to follow a discretization approach for hyperbolic systems. In this way, an accurate positivity preserving scheme could be constructed. However, the modified system turned out not to be hyperbolic for certain relevant states. Consequently, the method had to be adjusted in these cases. Moreover, treating the gradient of the chemo-attractant instead of the chemo-attractant itself by a numerical scheme, increased the number

of equations to discretize in higher space dimensions. This elevated in turn the complexity of the numerical method.

In the subsequent works [32, 103] a simpler *finite volume/finite difference* (FVFD) scheme was proposed. The authors considered a decoupling of the cell equation from the chemo-attractant equation. They treated the attracting species with a finite difference scheme and the migrating species with the central upwind scheme introduced above. The local propagation speeds were obtained by using central difference approximations of the gradients of the chemo-attractant density.

In more detail, consider a uniform finite volume grid in 1D, the discrete cell averages for the cell densities $c_i^n \approx |C_i|^{-1} \int_{C_i} c(x, t^n)\,dx$ and point values for the chemo-attractant densities $a_i^n \approx a(x_i, t^n)$. Then the scheme is given by

$$c_i^{n+1} = c_i^n - \tau \left[\frac{\mathcal{H}_{i+1/2} - \mathcal{H}_{i-1/2}}{h} - D_c \, \frac{c_{i-1}^n - 2c_i^n + c_{i+1}^n}{h^2} \right], \tag{5.19a}$$

$$a_i^{n+1} = a_i^n + \tau \left[D_a \, \frac{a_{i-1}^n - 2a_i^n + a_{i+1}^n}{h^2} + \alpha c_i^n - \beta c_i^n \right] \tag{5.19b}$$

for $1 \leqslant i \leqslant N$ and a time increment $\tau = t^{n+1} - t^n$. Recall that D_c, D_a, α and β refer to constant and positive model variables. We prescribe the local propagation speeds for the central upwind flux by

$$a_{i+1/2}^{\pm} = \chi \left(\frac{a_{i+1} - a_i}{h} \right)^{\pm},$$

where we use the positive and negative part defined by $x^+ = \max\{0, x\}$ and $x^- = -\min\{0, x\}$. In this way, the numerical fluxes (5.16) reduce to

$$\mathcal{H}_{i+1/2}^{CU} = \chi \left(\frac{a_{i+1} - a_i}{h} \right)^{+} c_{i+1/2}^{L} - \chi \left(\frac{a_{i+1} - a_i}{h} \right)^{-} c_{i+1/2}^{R} \tag{5.19c}$$

with interface reconstructions $c_{i+1/2}^{L/R}$ computed by the MC limiter (5.14). We note that the flux (5.19c) can also be understood as the Godunov flux $\mathcal{H}^G(c_{i+1/2}^L c_{i+1/2}^R)$ solving the Riemann problem for the transport equation $\partial_t c - \chi \partial_x (\frac{a_{i+1} - a_i}{h} c) = 0$.

One can show that the numerical fluxes that we use yield local second order approximations of the advection terms in most computational cells.

Theorem 5.3 *Consider a uniform finite volume grid in 1D at a fixed time instance and let the concentrations* c *and* a *be sufficiently smooth in* $\Omega = (a, b)$. *Let* $c_i = |C_i|^{-1} \int_{C_i} c(x)\,dx$ *denote the exact cell averages of the cell concentrations and let* $a_i = a(x_i)$ *denote the point values of the chemo-attractant densities. Moreover, consider the numerical fluxes and local propagation speeds given by scheme* (5.19).

If a) C_i *is sufficiently far away from the boundary, b) the local propagation speeds* $a_{i\pm1/2}$ *do not change signs in a neighborhood of* C_i *and c) there is no discrete local extrema of* c_i *in a neighborhood of* C_i, *then the local truncation error is of second order, i.e.*

$$E_i^{CU} = \left| \frac{\mathcal{H}_{i+1/2}^{CU} - \mathcal{H}_{i-1/2}^{CU}}{h} - \frac{\chi}{|C_i|} \int_{C_i} \partial_x (c \partial_x a)\,dx \right| = \mathcal{O}(h^2). \tag{5.20}$$

If a), b) and c) are not all satisfied, then we still have $E_i^{CU} = \mathcal{O}(h)$.

Proof. Taylor expansion, see [97] for technical details. □

We also mention here the numerical schemes for KS-type systems considered in [55, 56, 80]. Here the authors followed a similar second order upwind approach on uniform grids but employed different slope reconstructions. The schemes have been proved successful in the context of cancer invasion systems, see, e.g., [7, 44].

Another implicit finite volume scheme for the parabolic-elliptic Keller-Segel model was developed in [50]. It is only of first order, but its convergence to the analytical solution in the case of a subcritical initial mass could be shown rigorously.

5.3 Reconstruction and diffusion on nonuniform grids

In the previous section we introduced the central upwind scheme (5.19) for the Keller-Segel model for uniform finite volume meshes. A generalization to nonuniform grids will be discussed in this section. To this end we elaborate on the suitable discretization of the diffusion term on nonuniform grids as well as on a generalization of the MC limiter (5.14).

We need the nonuniform version of the scheme especially for the construction of the adaptive mesh refinement method. We will address the mesh adaptation in Chapter 6 and consider in this section only a static nonuniform finite volume mesh. This section is based on a part of our paper [96].

The generalized MC limiter

In the case of a nonuniform one-dimensional grid, the slope definition in (5.14) does not yield an approximation of the gradient in smooth regions. It also leads to a significant influence of the grid structure on the reconstruction.

For a consistent approximation of the first derivative, we firstly consider the following central difference

$$(u_x^c)_i = \frac{-2\kappa_i u_{i-1}}{\kappa_{i-1}(\kappa_{i-1}+\kappa_i)} + \frac{2(\kappa_i^2-\kappa_{i-1}^2)u_i}{\kappa_{i-1}\kappa_i(\kappa_{i-1}+\kappa_i)} + \frac{2\kappa_{i-1}u_{i+1}}{\kappa_i(\kappa_{i-1}+\kappa_i)},$$

where $\kappa_i = h_i + h_{i+1}$. This is a second order approximation of the first derivative of u at the center of the cell C_i as can be seen by Taylor expansion. We indeed have $(u_x^c)_i = \partial_x u(x_i) + \mathcal{O}(h^2)$. We have dropped here the dependence on the time instance for brevity and we will do the same in the rest of this section.

By using the new central difference formula we define now the *generalized minimized central* (GMC) limiter by

$$s_i = \operatorname{minmod}\left(2\theta_i\frac{u_i-u_{i-1}}{\kappa_{i-1}},\ (u_x^c)_i,\ 2\theta_i\frac{u_{i+1}-u_i}{\kappa_i}\right), \tag{5.21a}$$

where

$$\theta_i = 1 + \frac{\min\{h_{i-1}, h_{i+1}\}}{h_i}. \tag{5.21b}$$

We note that in the locally uniform case $h_{i-1} = h_i = h_{i+1}$ (5.21) reduces to the uniform MC limiter (5.14). The local dependence on θ that replaces the constant two in the uniform case is needed to obtain a non over- or undershooting reconstruction. In what follows we prove this nonoscillatory property of the proposed GMC limiter (5.21).

Proposition 5.4 *We consider the linear reconstructions*

$$u^L_{i+1/2} = u_i + \frac{h_i}{2}s_i, \quad u^R_{i+1/2} = u_{i+1} - \frac{h_{i+1}}{2}s_{i+1}, \tag{5.22}$$

with slopes given by the GMC limiter (5.21).

The interface reconstructions $u^{L/R}_{i+1/2}$ *satisfy the maximum principle* $u_i \leqslant u^L_{i+1/2}, u^R_{i+1/2} \leqslant u_{i+1}$ *for increasing data* $u_i \leqslant u_{i+1}$ *and conversely,* $u_i \geqslant u^L_{i+1/2}, u^R_{i+1/2} \geqslant u_{i+1}$ *for decreasing data* $u_i \geqslant u_{i+1}$.

Proof. Equation (5.21) yields

$$0 \leqslant s_i \leqslant \operatorname{minmod}\left(2k^L_i\frac{u_{i+1}-u_i}{h_i},\ 2k^R_i\frac{u_i-u_{i-1}}{h_i}\right), \tag{5.23a}$$

if either $u_i \leqslant u_{i+1}$ or $u_{i-1} \leqslant u_i$. Moreover, we have

$$0 \geqslant s_i \geqslant \operatorname{minmod}\left(2k^L_i\frac{u_{i+1}-u_i}{h_i},\ 2k^R_i\frac{u_i-u_{i-1}}{h_i}\right), \tag{5.23b}$$

if either $u_i \geqslant u_{i+1}$ or $u_{i-1} \geqslant u_i$. Here we have used the notations

$$k^L_i = \frac{h_i + \min\{h_{i-1}, h_{i+1}\}}{h_i + h_{i+1}}, \quad k^R_i = \frac{h_i + \min\{h_{i-1}, h_{i+1}\}}{h_{i-1} + h_i},$$

and therefore $0 \leqslant k^L_i, k^R_i \leqslant 1$. Thus, for $u_i \leqslant u_{i+1}$, where $s_i, s_{i+1} \geqslant 0$, we get

$$\begin{aligned} u_i \leqslant & u^L_{i+1/2} \leqslant u_i + k^L_i(u_{i+1}-u_i) \leqslant u_{i+1}, \\ u_{i+1} \geqslant & u^R_{i+1/2} \geqslant u_{i+1} - k^R_{i+1}(u_{i+1}-u_i) \geqslant u_i. \end{aligned}$$

Similarly, for $u_i \geqslant u_{i+1}$, where $s_i, s_{i+1} \leqslant 0$, we obtain

$$\begin{aligned} u_i \geqslant & u^L_{i+1/2} \geqslant u_i + k^L_i(u_{i+1}-u_i) \geqslant u_{i+1}, \\ u_{i+1} \leqslant & u^R_{i+1/2} \leqslant u_{i+1} - k^R_{i+1}(u_{i+1}-u_i) \leqslant u_i, \end{aligned}$$

implying hence the nonoscillatory property of the GMC limiter. □

Following [15] we can see that the above maximum principle and the properties (5.23a) and (5.23b) are sufficient to obtain a nonuniform TVD scheme in the case of the linear transport equation.

Proposition 5.5 *We consider for the constant velocity* $a > 0$ *the linear transport equation*

$$\partial_t u + a\partial_x u = 0,$$

being resolved by the following upwind scheme

$$u^{n+1}_i = u^n_i - \frac{\tau a}{h_i}(u^L_{i+1/2} - u^L_{i-1/2}).$$

The interface reconstructions above are computed by the GMC limiter (5.21)*. This scheme is TVD, if we abide by the condition*

$$\min_{1\leqslant i\leqslant N}\frac{a\tau}{h_i} \leqslant \frac{1}{2}.$$

Proof. We proceed in two steps. Firstly, we show that local maxima decrease. Secondly, we prove that monotonically increasing solutions remain monotone. It can be shown analogously that monotonically decreasing solutions remain monotonically decreasing and that local minima increase. These properties are sufficient to obtain a TVD scheme.

We first consider the local maximum case $u_{i-1}^n < u_i^n$ and $u_i^n > u_{i+1}^n$. Here the slope is limited by (5.21) resulting in $s_i = 0$ and $s_{i-1} \geqslant 0$. The updated cell average can be estimated using (5.23a), (5.23b) as

$$\begin{aligned} u_i^{n+1} &= u_i^n - \lambda_i \left(u_i^n - u_{i-1}^n - \frac{s_{i-1}^n h_i}{2} \right) \\ &\leqslant u_i^n - \lambda_i (u_i^n - u_{i-1}^n - k_{i-1}^L (u_i^n - u_{i-1}^n)) \leqslant u_i^n, \end{aligned}$$

where $\lambda_i = \tau a / h_i$. Next, we consider the monotonically increasing data $u_{i-1}^n \leqslant u_i^n \leqslant u_{i+1}^n$. Using Proposition 5.4 and $s_i \geqslant 0$ we get $u_i^{n+1} \leqslant u_i^n - \lambda_i (u_i^n - u_i^n) = u_i^n$ and similarly $u_{i-1}^{n+1} \leqslant u_{i-1}^n$, $u_{i+1}^{n+1} \leqslant u_{i+1}^n$. We also use the restriction $\lambda_i \leqslant 1/2$ and derive a lower bound

$$\begin{aligned} u_i^{n+1} &= u_i^n - \lambda_i \left(u_i^n + \frac{h_i s_i}{2} - \left(u_{i-1}^n + \frac{h_{i-1} s_{i-1}}{2} \right) \right) \\ &\geqslant u_i^n - \lambda_i \left(u_i^n + k_i^L \left(u_i^n - u_{i-1}^n \right) \right) + \lambda_i u_{i-1}^n \\ &\geqslant (1 - 2\lambda_i) u_i^n + 2\lambda_i u_{i-1}^n \geqslant u_{i-1}^n. \end{aligned}$$

In the same way we can estimate $u_{i+1}^{n+1} \geqslant u_i^n$. Combining the inequalities we conclude that $u_{i-1}^{n+1} \leqslant u_{i-1}^n \leqslant u_i^{n+1} \leqslant u_i^n \leqslant u_{i+1}^{n+1} \leqslant u_{i+1}^n$. Thus, the solution remains monotone. □

Nonuniform discretization of diffusion terms

The numerical schemes for ADR systems such as (5.18) employ central differences to approximate the diffusion terms. On uniform meshes one usually uses the three point central difference

$$\frac{-u_{i-1}^n + 2\,u_i^n - u_{i+1}^n}{h^2} = \partial_x^2 u(x_i, t^n) + \mathcal{O}(h^2).$$

We aim for a finite difference formula on nonuniform grids that has a second order truncation error, too. For general grids it is not possible to obtain such a resolution with only three points. Hence, we consider symmetrical five point stencils and define the discrete difference operator

$$\mathcal{D}_i(u_h(t^n)) = \alpha_i^{(-2)} u_{i-2}^n + \alpha_i^{(-1)} u_{i-1}^n + \alpha_i^{(0)} u_i^n + \alpha_i^{(+1)} u_{i+1}^n + \alpha_i^{(+2)} u_{i+2}^n. \tag{5.24}$$

The mesh dependent coefficients α_i are chosen such, that they satisfy the four conditions that are necessary for the second order truncation error as well as $\alpha_i^{(+2)} = -\alpha_i^{(-2)}$. The latter condition results in the property that the difference formula generalizes the common three point central difference. Indeed, if the grid is locally uniform, i.e. $h_{i-2} = h_{i-1} = h_i = h_{i+1} = h_{i+2}$, formula (5.24) reduces to the usual central difference. Another beneficial property of formula (5.24) is the fact that the dependence on u_{i-2}^n and u_{i+2}^n vanishes in the

case $h_{i-1} = h_{i+1}$. The coefficients read in closed form

$$\begin{aligned}
\alpha_i^{(-2)} &= -\alpha_i^{(+2)} = -\frac{8\,(h_{i-1} - h_{i+1})}{(h_{i-2} + 2h_{i-1} + 2h_i + 2h_{i+1} + h_{i+2})\sigma_i},\\
\alpha_i^{(-1)}\omega_i &= h_{i-1}(4h_{i-1} + 4h_{i-2} + 2h_i - 4h_{i+1} - 2h_{i+2}) + 3h_{i+1}^2\\
&\quad + h_{i+2}^2 + 4h_{i+1}h_{i+2} + h_i h_{i+2} + h_{i-2}(h_{i-2} - 2h_{i+1} - h_{i+2} + h_i),\\
\alpha_i^{(0)} &= -(\alpha_i^{(-1)} + \alpha_i^{(+1)}),\\
\alpha_i^{(+1)}\omega_i &= h_{i+1}(4h_{i+1} + 4h_{i+2} + 2h_i - 4h_{i-1} - 2h_{i-2}) + 3h_{i-1}^2\\
&\quad + h_{i-2}^2 + 4h_{i-1}h_{i-2} + h_i h_{i-2} + h_{i+2}(h_{i+2} - 2h_{i-1} - h_{i-2} + h_i),
\end{aligned}$$

where we used the auxiliary variables

$$\begin{aligned}
\omega_i &= (h_i + h_{i-1})(h_{i-1} + 2h_i + h_{i+1})\,\frac{\sigma_i}{8},\\
\sigma_i &= h_{i-2}^2 + h_{i+2}^2 + 2(h_{i-1}^2 + h_{i+1}^2) + 3(h_{i-1}h_{i-2} + h_{i+1}h_{i+2})\\
&\quad + h_i(h_{i+1} + h_{i-1} + h_{i+2} + h_{i-2}) - (h_{i+1} + h_{i+2})(h_{i+1} + h_{i+2}).
\end{aligned}$$

Positivity of the quotient σ_i can be guaranteed, if the grid satisfies the regularity conditions

$$h_{i-2} + h_{i-1} + h_i \geqslant h_{i+1} + h_{i+2}, \quad \text{if } h_{i-2} = h_i^{\max}, \tag{5.25a}$$
$$h_{i+2} + h_{i+1} + h_i \geqslant h_{i-1} + h_{i-2}, \quad \text{if } h_{i+2} = h_i^{\max} \tag{5.25b}$$

for all $i = 3, \dots, N-2$ where $h_i^{\max} = \max\{h_{i-2}, h_{i-1}, h_i, h_{i+1}, h_{i+2}\}$. We will only consider grids that satisfy this condition and thus the computation of the coefficients in (5.24) is numerically stable.

Another nonuniform central difference formula

The full FVFD scheme for the cancer invasion systems requires a numerical approximation of the first derivative of the attracting species in the mesh cell interfaces. These are needed to compute the local propagation speeds. In the uniform case, the usual central difference

$$\frac{u_{i+1}^n - u_i^n}{h} = \partial_x u(x_{i+1/2}, t^n) + \mathcal{O}(h^2)$$

yields a sufficiently accurate approximation. Similar as for the diffusion terms, we cannot obtain an analog two-point formula of second order accuracy in the general nonuniform case. Instead, we propose the symmetrical four-point difference formula

$$L_{i+1/2}(u_h) = \beta_{i+1/2}^{(-1.5)} u_{i-1} + \beta_{i+1/2}^{(-0.5)} u_i + \beta_{i+1/2}^{(+0.5)} u_{i+1} + \beta_{i+1/2}^{(+1.5)} u_{i+2}, \tag{5.26}$$

where the coefficients are chosen such that (5.26) yields a third order accurate approximation of the first derivative. In closed form the coefficients are given by

$$\begin{aligned}
\beta_{i+1/2}^{(-1.5)} &= \frac{h_{i+1}(6h_i - 4h_{i+1} - 2h_{i+2}) + 2h_i h_{i+2}}{(h_i + h_{i-1})(h_{i-1} + 2h_i + h_{i+1})\tilde{\sigma}_i},\\
\beta_{i+1/2}^{(-0.5)} &= -\frac{h_{i+1}(12h_i + 6h_{i-1} - 2h_{i+2} - 4h_{i+1}) + h_{i+2}(2h_{i-1} + 4h_i)}{(h_{i-1} + h_i)(h_i + h_{i+1})(h_i + 2h_{i+1} + h_{i+2})},\\
\beta_{i+1/2}^{(+0.5)} &= \frac{h_i(12h_{i+1} + 6h_{i+2} - 2h_{i-1} - 4h_i) + h_{i-1}(2h_{i+2} + 4h_{i+1})}{(h_{i+1} + h_{i+2})(h_i + h_{i+1})(h_{i-1} + 2h_i + h_{i+1})},\\
\beta_{i+1/2}^{(+1.5)} &= \frac{-h_i(6h_{i+1} - 4h_i - 2h_{i-1}) - 2h_{i+1}h_{i-1}}{(h_{i+1} + h_{i+2})(h_i + 2h_{i+1} + h_{i+2})\tilde{\sigma}_i},\\
\tilde{\sigma}_i &= h_{i-1} + 2h_i + 2h_{i+1} + h_{i+2}.
\end{aligned}$$

Remark 5.6 The formula (5.26) implies a further central difference for diffusion terms. Indeed,

$$\tilde{\mathcal{D}}_i(u_h(t^n)) = \frac{L_{i+1/2}(u_h(t^n)) - L_{i-1/2}(u_h(t^n))}{h_i} \tag{5.27}$$

is another five point central difference of second order for the second derivative. Unlike difference formula (5.24), the new approximation (5.27) yields a conservative scheme for diffusion problems. However, we promote the difference formula (5.24) to approximate the diffusion terms in our applications. This is because we do not need the mass conservation of the full scheme as the invasion systems we consider are not mass conservative. Moreover, (5.24) results in a more efficient scheme by employing smaller stencils in uniform regions of the computational grid.

5.4 Finite volume schemes in 2D

In this section we discuss the extension of finite volume methods to two-dimensional meshes. In this respect, we consider, in particular, scalar conservation laws and the MUSCL approach. This information will allow us to adjust the FVFD scheme (5.19) to the 2D case and thus to construct 2D schemes for the discussed cancer invasion systems. We will only treat quadrilateral meshes that allow for a straightforward adaptation.

Definition 5.7 Consider the rectangular domain $\Omega = (a_1, b_1) \times (a_2, b_2) \subset \mathbb{R}^2$. The corresponding *quadrilateral finite volume mesh* is given by *grid cells* of size $(h^{[x]}, h^{[y]})$ where $h^{[x]} = (b_1 - a_1)/L$ and $h^{[y]} = (b_2 - a_2)/M$ for some $L, M \in \mathbb{N}$. These cells can be defined using their midpoints as follows

$$\begin{aligned}
x_{i,j} &= \left(a_1 + \left(i - \tfrac{1}{2}\right) h^{[x]}, a_2 + \left(j - \tfrac{1}{2}\right) h^{[y]}\right),\\
C_{i,j} &= \left\{x_{i,j} + \left(\lambda_1 h^{[x]}, \lambda_2 h^{[y]}\right), \quad \lambda_1, \lambda_2 \in (-1/2, 1/2)\right\}
\end{aligned}$$

for $i = 1, \dots, L$ and $j = 1, \dots, M$. The cell diameter corresponding to the mesh is given by $h = \sqrt{(h^{[x]})^2 + (h^{[y]})^2}$.

Given a conservation law of type (5.1) in 2D and a quadrilateral finite volume mesh, integration over a cell $C_{i,j}$ and a time interval (t^n, t^{n+1}) analog to (5.2) yields

$$0 = u_i^{n+1} - u_i^n + \frac{1}{|C_{i,j}|}\int_{t^n}^{t^{n+1}} \left[\int_{C_{i+1/2,j}} f(u(x,t))\,dx - \int_{C_{i-1/2,j}} f(u(x,t))\,dx \right.$$
$$\left. + \int_{C_{i,j+1/2}} f(u(x,t))\,dx - \int_{C_{i,j-1/2}} f(u(x,t))\,dx\right] dt. \tag{5.28}$$

Here we have denoted the vertical cell interfaces by $C_{i\pm1/2,j} = \bar{C}_{i,j} \cap \bar{C}_{i\pm1,j}$ and the horizontal cell interfaces by $C_{i,j\pm1/2} = \bar{C}_{i,j} \cap \bar{C}_{i,j\pm1}$. The numerical fluxes that are used in the corresponding finite volume scheme approximate the integrals

$$\mathcal{H}_{i\pm1/2,j} \approx \frac{1}{(t^{n+1}-t^n)h^{[y]}}\int_{t^n}^{t^{n+1}}\int_{C_{i\pm1/2,j}} f(u(x,t))\,dx\,dt,$$

$$\mathcal{H}_{i,j\pm1/2} \approx \frac{1}{(t^{n+1}-t^n)h^{[x]}}\int_{t^n}^{t^{n+1}}\int_{C_{i,j\pm1/2}} f(u(x,t))\,dx\,dt.$$

To adjust the MUSCL approach to the quadrilateral meshes we need linear reconstructions on four cell interfaces. Therefore, we consider the piecewise linear function

$$\tilde{u}(x,t^n) = \sum_{i=1}^{N} \chi_{C_i}(x)\left(u_i^n + \left(s_{i,j}^{[x]}, s_{i,j}^{[y]}\right)\cdot(x - x_{i,j})\right)$$

and the corresponding interface reconstructions from the west and the east $u_{i\pm1/2,j}^{W/E}$ and from the south and the north $u_{i,j\pm1/2}^{S/N}$. The slopes that we need in the reconstruction are obtained by a limiter such as (5.14) applied in the corresponding space direction. In more detail, we apply the limiter to $u_{i-1,j}, u_{i,j}$ and $u_{i+1,j}$ to obtain $s_{i,j}^{[x]}$ and to $u_{i,j-1}, u_{i,j}$ and $u_{i,j+1}$ to obtain $s_{i,j}^{[y]}$. For the detailed formulas we refer to the full semi-discrete schemes in the next section. We eventually compute the numerical fluxes by taking

$$\mathcal{H}(u_{i+1/2,j}^W, u_{i+1/2,j}^E) = \mathcal{H}_{i+1/2,j},$$
$$\mathcal{H}(u_{i,j+1/2}^S, u_{i,j+1/2}^N) = \mathcal{H}_{i,j+1/2}$$

for a numerical flux function $\mathcal{H}$ such as those introduced in Section 5.1.

5.5 The semi-discrete schemes

In this section we formulate the semi-discrete schemes for the numerical approximation of cancer invasion systems (I), (II) and (III). Therefore, we will build on the central upwind scheme introduced in Sections 5.1 and 5.2 and the generalization to 2D domains from Section 5.4. We provide the schemes for the 2D case but also discuss the adaptation to the nonuniform 1D case making use of the reconstruction and difference formulas introduced in Section 5.3.

In the case of ADR systems such as the cancer invasion models under discussion, forward Euler time integration used in (5.19) is often inefficient. This is due to the facts that the

forward Euler scheme is only of first order of accuracy in time and small time steps in $\mathcal{O}(h^2)$ are needed for the stability of the scheme. See also Section 5.6 for more detail.

The central upwind scheme (5.19) allows for a more general *semi-discrete* form. It can easily be derived by taking the limit as $\tau \to 0$. In this way, (5.19) becomes a system of ODEs for which a plethora of accurate and stable numerical methods is available. The approach of discretizing a time dependent PDE by an ODE system is called *method of lines*.

In the following subsections we provide the semi-discrete schemes for the considered invasion systems. We will also refer to them indistinguishably as FVFD schemes. We consider for the spatial discretization a quadrilateral finite volume mesh on the rectangular domain $\Omega = (a_1, b_1) \times (a_2, b_2)$. For any given discrete cell concentration $c_{i,j}$ for $1 \leqslant i \leqslant L$ and $1 \leqslant j \leqslant M$ we will use the interface reconstructions

$$
\begin{aligned}
c^{W}_{i+1/2,j} &= c_{i,j} + \frac{h^{[x]}}{2} s^{[x]}_{i,j}, & c^{E}_{i+1/2,j} &= c_{i+1,j} - \frac{h^{[x]}}{2} s^{[x]}_{i+1,j}, \\
c^{S}_{i,j+1/2} &= c_{i,j} + \frac{h^{[y]}}{2} s^{[y]}_{i,j}, & c^{N}_{i,j+1/2} &= c_{i,j+1} - \frac{h^{[y]}}{2} s^{[y]}_{i,j+1}.
\end{aligned} \tag{5.29a}
$$

Here the slopes are given by the MC limiter and read

$$
\begin{aligned}
s^{[x]}_{i,j} &= \operatorname{minmod}\left(2\frac{c_{i,j} - c_{i-1,j}}{h^{[x]}},\ \frac{c_{i+1,j} - c_{i-1,j}}{2h^{[x]}},\ 2\frac{c_{i+1,j} - c_{i,j}}{h^{[x]}}\right), \\
s^{[y]}_{i,j} &= \operatorname{minmod}\left(2\frac{c_{i,j} - c_{i,j-1}}{h^{[y]}},\ \frac{c_{i,j+1} - c_{i,j-1}}{2h^{[y]}},\ 2\frac{c_{i,j+1} - c_{i,j}}{h^{[y]}}\right).
\end{aligned} \tag{5.29b}
$$

We have dropped the dependence on the time instance t^n in the above definition for clarity.

Discretization of the uPA system

We denote the approximate time dependent cell averages of the tumor cell concentration by $c_{i,j}(t) \approx |C_{i,j}|^{-1} \int_{C_{i,j}} c(x,t)\,dx$ and the approximate point values of the densities of vitronectin, uPA, PAI-1 and plasmin by $v_{i,j}(t) \approx v(x_{i,j},t)$, $u_{i,j}(t) \approx u(x_{i,j},t)$, $p_{i,j}(t) \approx p(x_{i,j},t)$ and $m_{i,j}(t) \approx m(x_i,t)$. Then we define the numerical fluxes as

$$
\mathcal{H}_{i+1/2,j}(t) = \begin{cases} a_{i+1/2,j}(t)\, c^{W}_{i+1/2,j}(t), & a_{i+1/2,j}(t) \geqslant 0, \\ a_{i+1/2,j}(t)\, c^{E}_{i+1/2,j}(t), & a_{i+1/2,j}(t) < 0, \end{cases} \tag{5.30a}
$$

$$
\mathcal{H}_{i,j+1/2}(t) = \begin{cases} a_{i,j+1/2}(t)\, c^{S}_{i,j+1/2}(t), & a_{i,j+1/2}(t) \geqslant 0, \\ a_{i,j+1/2}(t)\, c^{N}_{i,j+1/2}(t), & a_{i,j+1/2}(t) < 0. \end{cases} \tag{5.30b}
$$

The corresponding local propagation speeds are determined by finite differences in the following way

$$
\begin{aligned}
a_{i+1/2,j}(t) &= \chi_v \frac{v_{i+1,j}(t) - v_{i,j}(t)}{h^{[x]}} + \chi_u \frac{u_{i+1,j}(t) - u_{i,j}(t)}{h^{[x]}} + \chi_p \frac{p_{i+1,j}(t) - p_{i,j}(t)}{h^{[x]}}, \\
a_{i,j+1/2}(t) &= \chi_v \frac{v_{i,j+1}(t) - v_{i,j}(t)}{h^{[y]}} + \chi_u \frac{u_{i,j+1}(t) - u_{i,j}(t)}{h^{[y]}} + \chi_p \frac{p_{i,j+1}(t) - p_{i,j}(t)}{h^{[y]}}.
\end{aligned}
$$

Using the defined numerical fluxes the semi-discrete scheme for system (I) reads

$$
\begin{cases}
\partial_t c_{i,j} = D_c \left[\dfrac{c_{i-1,j} - 2c_{i,j} + c_{i+1,j}}{(h^{[x]})^2} + \dfrac{c_{i,j-1} - 2c_{i,j} + c_{i,j+1}}{(h^{[y]})^2} \right] \\
\qquad\qquad - \dfrac{\mathcal{H}_{i+1/2,j}(t) - \mathcal{H}_{i-1/2,j}(t)}{h^{[x]}} - \dfrac{\mathcal{H}_{i,j+1/2}(t) - \mathcal{H}_{i,j-1/2}(t)}{h^{[y]}} \\
\qquad\qquad + \mu_1 c_{i,j}(1 - c_{i,j}), \\
\partial_t v_{i,j} = -\delta v_{i,j}\, m_{i,j} + \phi_{21} u_{i,j}\, p_{i,j} - \phi_{22} v_{i,j}\, p_{i,j} + \mu_2 v_{i,j}\,(1 - v_{i,j}), \\
\partial_t u_{i,j} = D_u \left[\dfrac{u_{i-1,j} - 2u_{i,j} + u_{i+1,j}}{(h^{[x]})^2} + \dfrac{u_{i,j-1} - 2u_{i,j} + u_{i,j+1}}{(h^{[y]})^2} \right] \\
\qquad\qquad - \phi_{31} u_{i,j} p_{i,j} - \phi_{33} c_{i,j} u_{i,j} + \alpha_3 c_{i,j}, \\
\partial_t p_{i,j} = D_p \left[\dfrac{p_{i-1,j} - 2p_{i,j} + p_{i+1,j}}{(h^{[x]})^2} + \dfrac{p_{i,j-1} - 2p_{i,j} + p_{i,j+1}}{(h^{[y]})^2} \right] \\
\qquad\qquad - \phi_{41} u_{i,j} p_{i,j} - \phi_{42} v_{i,j} p_{i,j} + \alpha_4 m_{i,j}, \\
\partial_t m_{i,j} = D_m \left[\dfrac{m_{i-1,j} - 2m_{i,j} + m_{i+1,j}}{(h^{[x]})^2} + \dfrac{m_{i,j-1} - 2m_{i,j} + m_{i,j+1}}{(h^{[y]})^2} \right] \\
\qquad\qquad + \phi_{52} v_{i,j} p_{i,j} + \phi_{53} c_{i,j} u_{i,j} - \alpha_5 m_{i,j}
\end{cases}
\tag{5.30c}
$$

for $1 \leqslant i \leqslant L$ and $1 \leqslant j \leqslant M$.

The haptotaxis EMT/invasion system

In the same way, we formulate the semi-discrete scheme for the two cancer species model (II). Let the approximate time dependent cell averages of the concentrations of DCCs, CSCs and fibroblasts be given by

$$
c^D_{i,j}(t) \approx |C_{i,j}|^{-1} \int_{C_{i,j}} c^D(x,t)\,dx, \quad c^S_{i,j}(t) \approx |C_{i,j}|^{-1} \int_{C_{i,j}} c^S(x,t)\,dx,
$$

$$
c^F_{i,j}(t) \approx |C_{i,j}|^{-1} \int_{C_{i,j}} c^F(x,t)\,dx.
$$

Moreover, we consider approximate point values of the densities of the ECM and the MMPs on the midpoint of each computational cell by $v_{i,j}(t) \approx v(x_{i,j},t)$ and $m_{i,j}(t) \approx m(x_{i,j},t)$.

To formulate the FVFD scheme for model (II) we firstly define the space dependent and nonlocal approximation of the EMT coefficient

$$
[\mathrm{EGFR}]_0(t) = \frac{h^{[x]}h^{[y]}}{(b-a)(d-c)} \sum_{i,j=1}^{L,M} \left[\lambda^S c^S_{i,j}(t) + \lambda^D c^D_{i,j}(t) \right], \tag{5.31a}
$$

$$
g_f(t) = \frac{1}{2}\left(\Gamma + \sqrt{(k_D - \Gamma + [\mathrm{EGFR}]_0(t))^2 + 4k_D\Gamma} - k_D \right) - \frac{1}{2}[\mathrm{EGFR}]_0(t), \tag{5.31b}
$$

$$
\mu_{\mathrm{EMT},i,j}(t) = \mu_0 \frac{\lambda^D c^D_{i,j}(t)}{\mu_{1/2}(k_D g_f(t)^{-1} + 1) + \lambda^D c^D_{i,j}(t),} \tag{5.31c}
$$

which constitutes a discrete version of the EMT coefficient from Section 2.7. Next, we prescribe the evolution of the cell averages and point values by the scheme

$$
\begin{cases}
\partial_t c^D_{i,j} = D_D \left[\dfrac{c^D_{i-1,j} - 2c^D_{i,j} + c^D_{i+1,j}}{(h^{[x]})^2} + \dfrac{c^D_{i,j-1} - 2c^D_{i,j} + c^D_{i,j+1}}{(h^{[y]})^2} \right] \\
\qquad - \dfrac{\mathcal{H}^D_{i+1/2,j}(t) - \mathcal{H}^D_{i-1/2,j}(t)}{h^{[x]}} - \dfrac{\mathcal{H}^D_{i,j+1/2}(t) - \mathcal{H}^D_{i,j-1/2}(t)}{h^{[y]}} \\
\qquad - \mu_{EMT,i,j}\, c^D_{i,j} + \mu_D\, c^D_{i,j}\, R^+_{i,j}(t)\,, \\
\partial_t c^S_{i,j} = D_S \left[\dfrac{c^S_{i-1,j} - 2c^S_{i,j} + c^S_{i+1,j}}{(h^{[x]})^2} + \dfrac{c^S_{i,j-1} - 2c^S_{i,j} + c^S_{i,j+1}}{(h^{[y]})^2} \right] \\
\qquad - \dfrac{\mathcal{H}^S_{i+1/2,j}(t) - \mathcal{H}^S_{i-1/2,j}(t)}{h^{[x]}} - \dfrac{\mathcal{H}^S_{i,j+1/2}(t) - \mathcal{H}^S_{i,j-1/2}(t)}{h^{[y]}} \\
\qquad - \mu_T\, c^S_{i,j} + \mu_{EMT,i,j}\, c^D_{i,j} + \mu_S\, c^S_{i,j}\, R^+_{i,j}(t)\,, \\
\partial_t c^F_{i,j} = D_F \left[\dfrac{c^F_{i-1,j} - 2c^F_{i,j} + c^F_{i+1,j}}{(h^{[x]})^2} + \dfrac{c^F_{i,j-1} - 2c^F_{i,j} + c^F_{i,j+1}}{(h^{[y]})^2} \right] \\
\qquad - \dfrac{\mathcal{H}^F_{i+1/2,j}(t) - \mathcal{H}^F_{i-1/2,j}(t)}{h^{[x]}} - \dfrac{\mathcal{H}^F_{i,j+1/2}(t) - \mathcal{H}^F_{i,j-1/2}(t)}{h^{[y]}} \\
\qquad + \mu_T\, c^S_{i,j} - \beta_F\, c^F_{i,j} + \mu_F\, c^F_{i,j}\, R^+_{i,j}(t)\,, \\
\partial_t \nu_{i,j} = -\delta_\nu\, m_{i,j} \nu_{i,j} + \mu_\nu\, c^F_{i,j}\, R^+_{i,j}(t)\,, \\
\partial_t m_{i,j} = D_m \left[\dfrac{m_{i-1,j} - 2m_{i,j} + m_{i+1,j}}{(h^{[x]})^2} + \dfrac{m_{i,j-1} - 2m_{i,j} + m_{i,j+1}}{(h^{[y]})^2} \right] \\
\qquad + \alpha_D\, c^D_{i,j} + \alpha_S\, c^S_{i,j} - \beta_m\, m_{i,j}\,.
\end{cases}
\tag{5.31d}
$$

The amount of resources necessary for reproduction, which appears in the equations for the cells and the ECM, is given by

$$
R^+_{i,j}(t) = \max\{0, 1 - c^D_{i,j}(t) - c^S_{i,j}(t) - c^F_{i,j}(t) - \nu_{i,j}(t)\}. \tag{5.31e}
$$

The numerical fluxes of the scheme read for the DCCs and the CSCs (i.e. for $I \in \{D, S\}$)

$$
\mathcal{H}^I_{i+1/2,j}(t) = \begin{cases} \frac{\nu_{i+1,j}(t) - \nu_{i,j}(t)}{h^{[x]}}\, \chi_I\, c^{I,W}_{i+1/2,j}(t), & \frac{\nu_{i+1,j}(t) - \nu_{i,j}(t)}{h^{[x]}} \geqslant 0, \\ \frac{\nu_{i,j+1}(t) - \nu_{i,j}(t)}{h^{[y]}}\, \chi_I\, c^{I,E}_{i+1/2,j}(t), & \frac{\nu_{i+1,j}(t) - \nu_{i,j}(t)}{h^{[x]}} < 0, \end{cases} \tag{5.31f}
$$

$$
\mathcal{H}^I_{i,j+1/2}(t) = \begin{cases} \frac{\nu_{i,j+1}(t) - \nu_{i,j}(t)}{h^{[y]}}\, \chi_I\, c^{I,S}_{i,j+1/2}(t), & \frac{\nu_{i,j+1}(t) - \nu_{i,j}(t)}{h^{[y]}} \geqslant 0, \\ \frac{\nu_{i,j+1}(t) - \nu_{i,j}(t)}{h^{[y]}}\, \chi_I\, c^{I,N}_{i,j+1/2}(t), & \frac{\nu_{i,j+1}(t) - \nu_{i,j}(t)}{h^{[y]}} < 0. \end{cases} \tag{5.31g}
$$

In the case of the fibroblasts the numerical fluxes predict a movement in the opposite direction

and read

$$\mathcal{H}^{F}_{i+1/2,j}(t) = \begin{cases} -\frac{\nu_{i+1,j}(t)-\nu_{i,j}(t)}{h^{[x]}}\,\chi_F\,c^{F,W}_{i+1/2,j}(t), & \frac{\nu_{i+1,j}(t)-\nu_{i,j}(t)}{h^{[x]}} \leqslant 0, \\ -\frac{\nu_{i,j+1}(t)-\nu_{i,j}(t)}{h^{[y]}}\,\chi_F\,c^{F,E}_{i+1/2,j}(t), & \frac{\nu_{i+1,j}(t)-\nu_{i,j}(t)}{h^{[x]}} > 0, \end{cases} \tag{5.31h}$$

$$\mathcal{H}^{F}_{i,j+1/2}(t) = \begin{cases} -\frac{\nu_{i,j+1}(t)-\nu_{i,j}(t)}{h^{[y]}}\,\chi_F\,c^{F,S}_{i,j+1/2}(t), & \frac{\nu_{i,j+1}(t)-\nu_{i,j}(t)}{h^{[y]}} \leqslant 0, \\ -\frac{\nu_{i,j+1}(t)-\nu_{i,j}(t)}{h^{[y]}}\,\chi_F\,c^{F,N}_{i,j+1/2}(t), & \frac{\nu_{i,j+1}(t)-\nu_{i,j}(t)}{h^{[y]}} > 0. \end{cases} \tag{5.31i}$$

The local propagation speeds needed for the determination of the time step size, see Section 5.6, are obtained according to

$$a_{i+1/2,j}(t) = \max\{\chi_D, \chi_S, \chi_F\}\,\frac{\nu_{i+1,j}(t)-\nu_{i,j}(t)}{h^{[x]}},$$

$$a_{i,j+1/2}(t) = \max\{\chi_D, \chi_S, \chi_F\}\,\frac{\nu_{i,j+1}(t)-\nu_{i,j}(t)}{h^{[y]}}.$$

All definitions in the scheme (5.31) are provided for $1 \leqslant i \leqslant L$ and $1 \leqslant j \leqslant M$.

The contractivity model (III)

Finally, we construct a semi-discrete scheme for system (III). We name the approximate cell averages of migrating tumor cell concentrations $c^m_{i,j}(t) \approx |C_{i,j}|^{-1}\int_{C_{i,j}} c^m(x,t)\,dx$. Further, we denote the approximate point values of the contractivity, of the proliferating cancer cell density, of the ECM density and of the integrins density by $\kappa_{i,j} \approx \kappa(x_{i,j},t)$, $c^p_{i,j}(t) \approx c^p(x_{i,j},t)$, $\nu_{i,j}(t) \approx \nu(x_{i,j},t)$ and $y_{i,j} \approx y(x_{i,j},t)$, respectively.

Contrary to systems (I) and (II), model (III) features space dependent diffusion and haptotaxis coefficients in conservative form. In the case of the diffusion, we approximate the coefficient at the cell interfaces. To this end we compute the mean value of adjacent cells. In this way, we obtain the semi-discrete scheme

$$\begin{cases} \partial_t c^p_{i,j} = \mu_p c^p_{i,j}(1-(c^p_{i,j}+c^m_{i,j})-\eta_p\,\nu_{i,j}) + \gamma c^m_{i,j} - \lambda c^p_{i,j}, \\ \partial_t c^m_{i,j} = \dfrac{D_{i+1,j}(t)+D_{i,j}(t)}{2}\,\dfrac{c^m_{i+1,j}-c^m_{i,j}}{(h^{[x]})^2} - \dfrac{D_{i,j}(t)+D_{i-1,j}(t)}{2}\,\dfrac{c^m_{i,j}-c^m_{i-1,j}}{(h^{[x]})^2} \\ \qquad + \dfrac{D_{i,j+1}(t)+D_{i,j}(t)}{2}\,\dfrac{c^m_{i,j+1}-c^m_{i,j}}{(h^{[y]})^2} - \dfrac{D_{i,j}(t)+D_{i,j-1}(t)}{2}\,\dfrac{c^m_{i,j}-c^m_{i,j-1}}{(h^{[y]})^2} \\ \qquad - \dfrac{\mathcal{H}^M_{i+1/2,j}(t)-\mathcal{H}^M_{i-1/2,j}(t)}{h^{[x]}} - \dfrac{\mathcal{H}^M_{i,j+1/2}(t)-\mathcal{H}^M_{i,j-1/2}(t)}{h^{[y]}} \\ \qquad + \lambda c^p_{i,j} - \gamma c^m_{i,j}, \\ \partial_t \nu_{i,j} = -\delta_\nu(c^p_{i,j}+c^m_{i,j})\,\nu_{i,j} + \mu_\nu \nu_{i,j}(1-\eta_\nu\,(c^p_{i,j}+c^m_{i,j})-\nu_{i,j}), \\ \partial_t y_{i,j} = \varepsilon^{-1}\,k_+\,\nu_{i,j}(1-y_{i,j}) - \varepsilon^{-1}\,k_-\,y_{i,j}, \\ \partial_t \kappa_{i,j} = -\varepsilon^{-1}\,q\kappa_{i,j} + \varepsilon^{-1}\,M\,y_{i,j}(t-\varepsilon\tau) \end{cases} \tag{5.32a}$$

for $1 \leqslant i \leqslant L$ and $1 \leqslant j \leqslant M$. The nonconstant diffusion coefficient of the migratory cells that we have used in the scheme reads

$$D_{i,j}(t) = \frac{D_d\,\kappa_{i,j}(t)}{1+(c^p_{i,j}(t)+c^m_{i,j}(t))\,\nu_{i,j}(t)}. \tag{5.32b}$$

Similarly as for the diffusion term, we define the local propagation speeds by incorporating mean values of adjacent cells

$$a_{i+1/2,j}(t) = \frac{D_h}{2}\left(\frac{\kappa_{i,j}(t)\,v_{i,j}(t)}{1+v_{i,j}(t)} + \frac{\kappa_{i+1,j}(t)\,v_{i+1,j}(t)}{1+v_{i+1,j}(t)}\right)\frac{v_{i+1,j}(t)-v_{i,j}(t)}{h^{[x]}},$$

$$a_{i,j+1/2}(t) = \frac{D_h}{2}\left(\frac{\kappa_{i,j}(t)\,v_{i,j}(t)}{1+v_{i,j}(t)} + \frac{\kappa_{i,j+1}(t)\,v_{i,j+1}(t)}{1+v_{i,j+1}(t)}\right)\frac{v_{i,j+1}(t)-v_{i,j}(t)}{h^{[y]}}.$$

Given the local propagation speeds, we can define the numerical fluxes that occur in (5.32a) as

$$\mathcal{H}^M_{i+1/2,j}(t) = \begin{cases} a_{i+1/2,j}(t)\,c^{M,W}_{i+1/2,j}(t), & a_{i+1/2,j}(t) \geqslant 0, \\ a_{i+1/2,j}(t)\,c^{M,E}_{i+1/2,j}(t), & a_{i+1/2,j}(t) < 0, \end{cases} \tag{5.32c}$$

$$\mathcal{H}^M_{i,j+1/2}(t) = \begin{cases} a_{i,j+1/2}(t)\,c^{M,S}_{i,j+1/2}(t), & a_{i,j+1/2}(t) \geqslant 0, \\ a_{i,j+1/2}(t)\,c^{M,S}_{i,j+1/2}(t), & a_{i,j+1/2}(t) < 0. \end{cases} \tag{5.32d}$$

Remarks

We close this section with some remarks on suitable boundary values and technical details on the adaptation to 1D simulations. We further introduce a shorter vector form of the FVFD schemes and discuss their consistency in space.

Initial data and boundary conditions For each species u occurring in the model of interest we derive discrete initial data from the given continuous data u_0. While the point values can be extracted directly, we use the midpoint rule to obtain approximate initial cell averages.

For consistency with the homogeneous Neumann boundary conditions that we consider we moreover prescribe concentrations on *ghost cells* by

$$\begin{cases} u_{-1,j}(t) = u_{2,j}(t), & u_{0,j}(t) = u_{1,j}(t), \\ u_{L+1,j}(t) = u_{L,j}(t), & u_{L+2,j}(t) = u_{L-1,j}(t), \\ u_{i,-1}(t) = u_{i,2}(t), & u_{i,0}(t) = u_{i,1}(t), \\ u_{i,M+1}(t) = u_{i,M}(t), & u_{i,M+2}(t) = u_{i,M-1}(t) \end{cases} \tag{5.33}$$

for indexes $1 \leqslant i \leqslant L$ and $1 \leqslant j \leqslant M$ and any occurring species u. In this way, all presented semi-discrete schemes are well defined at the boundary.

1D schemes The adjustment of the schemes to one-dimensional space dimensions and corresponding one-dimensional finite volume grids is straightforward. In the uniform case one simply drops the numerical fluxes and the discrete diffusion terms in y-direction of the form $(\mathcal{H}_{i,j+1/2}(t) - \mathcal{H}_{i,j-1/2}(t))/h^{[y]}$ and $(u_{i,j-1} - 2u_{i,j} + u_{i,j+1})/(h^{[y]})^2$. The interface reconstructions from the west and from the north are then understood as their 1D counterpart from the left and from the right.

In the case of nonuniform one-dimensional finite volume grids we employ the GMC limiter (5.21) for the slope computation instead of the common MC limiter. Further we replace the interface reconstructions (5.29a) with the nonuniform formula (5.22). In addition, we replace the discrete advection terms $(\mathcal{H}_{i+1/2,j}(t) - \mathcal{H}_{i-1/2,j}(t))/h^{[x]}$ by $(\mathcal{H}_{i+1/2}(t) - \mathcal{H}_{i-1/2}(t))/h_i$, the discrete diffusion terms $(u_{i-1,j} - 2u_{i,j} + u_{i+1,j})/(h^{[x]})^2$ by the nonuniform

central difference (5.24) and the two point differences used to compute the local propagation speeds $a_{i+1/2,j}(t)$ by the four point nonuniform central difference (5.26). Lastly, we make the assumption that the ghost cells have the sizes

$$h_{-1} = h_2, \quad h_0 = h_1, \quad h_{L+1} = h_L, \quad h_{L+2} = h_{L-1},$$

such that the numerical fluxes and diffusion terms are well defined at the boundary of the domain.

Vector form For a convenient discussion of the time discretisation method that follows in the next section, we introduce here the vector form of the semi-discrete schemes. We derive this formulation in the 2D case and note that the same form can be derived in the 1D case analogously.

Let $w_{i,j}^{[k]}(t)$ denote the discrete concentration in cell $C_{i,j}$ of the k-th component of the model under discussion at time t. The time dependent vector

$$\mathbf{w}_h(t) = \left(w_{i,j}^{[k]}(t)\right)_{i,j,k=1}^{L,M,5} \tag{5.34}$$

comprises all of these discrete densities at the time t. Note that by coincidence all the three systems that we treat numerically have five components. Time evolution of each vector entry by the corresponding semi-discrete scheme can be written as

$$\partial_t w_{i,j}^{[k]}(t) = \mathcal{A}_{i,j}^{[k]}(\mathbf{w}_h(t)) + \mathcal{D}_{i,j}^{[k]}(\mathbf{w}_h(t)) + \mathcal{R}_{i,j}^{[k]}(\mathbf{w}_h(t)),$$

where $\mathcal{A}_{i,j}^{[k]}(\mathbf{w}_h(t))$, $\mathcal{D}_{i,j}^{[k]}(\mathbf{w}_h(t))$ and $\mathcal{R}_{i,j}^{[k]}(\mathbf{w}_h(t))$ include the corresponding discretization of the advection, the diffusion and the reaction terms. We group these terms using the following expressions

$$\mathcal{A}(\mathbf{w}_h(t)) = \left(\mathcal{A}_{i,j}^{[k]}(\mathbf{w}_h(t))\right)_{i,j,k=1}^{L,M,5}, \quad \mathcal{D}(\mathbf{w}_h(t)) = \left(\mathcal{D}_{i,j}^{[k]}(\mathbf{w}_h(t))\right)_{i,j,k=1}^{L,M,5},$$
$$\mathcal{R}(\mathbf{w}_h(t)) = \left(\mathcal{R}_{i,j}^{[k]}(\mathbf{w}_h(t))\right)_{i,j,k=1}^{L,M,5}$$

to which we will refer to as *advecion*, *diffusion*, and *reaction operator*, respectively. By adapting the former notations the semi-discrete scheme can be written as the ODE system

$$\partial_t \mathbf{w}_h = \mathcal{A}(\mathbf{w}_h) + \mathcal{R}(\mathbf{w}_h) + \mathcal{D}(\mathbf{w}_h) \tag{5.35}$$

for each of the three models (I), (II) and (III).

Remark 5.8 (Consistency of the semi-discrete schemes) If $\mathbf{w}_h(t)$ is the exact solution of ODE system (5.35) and the vector valued function $\mathbf{w}(x,t) = (w_1(x,t), \ldots, w_5(x,t))$ is the exact solution of the PDE system, then we obtain for the error depending only on the space discretization that

$$E^{[k]}(t) = h^{[x]}h^{[y]} \sum_{i,j=1}^{L,M} \left| w_{i,j}^{[k]}(t) - |C_{i,j}|^{-1} \int_{C_{i,j}} w_k(x,t)\, dx \right| = \mathcal{O}(h) \tag{5.36}$$

for $1 \leqslant k \leqslant 5$ at any point in time. This can be shown by an application of the Gronwall Lemma when we use that a) the approximations of advection, diffusion and reaction terms

that we use in the schemes yield at least a local truncation error of first order when compared to their continuous form and that b) the right hand side of the ODE system (5.35) is Lipschitz continuous in $\mathbf{w}_h$. For technical details on the proof we refer to [55].

In fact, we can replace $\mathcal{O}(h)$ in (5.36) by $\mathcal{O}(h^p)$, if all local truncation errors are of p-th order. Since we have mostly local truncation error of second order, except in regions where the numerical fluxes reduces to a first order approximation (see Theorem 5.3), we expect that the above spatial error (5.36) is rather of second order in practice. We will confirm this in our numerical experiments in Sections 5.11 and 8.1.

5.6 Fundamentals of time discretization

In the following sections we will construct appropriate time integration methods for the semi-discrete schemes introduced in the previous Section 5.5. The present section discusses some prerequisites and motivates the derivation of these methods.

Firstly, we discretize the time axis by $t^n,\ n = 0, 1, 2, \dots$ and introduce the corresponding time step sizes $\tau_n = t^{n+1} - t^n$. We consider the semi-discrete schemes in the vector form (5.35). The numerical solution at discrete points in time t^n will be denoted as $\mathbf{w}_h^n \approx \mathbf{w}_h(t^n)$.

Definition 5.9 As in Remark 5.8 let $\mathbf{w}_h(t)$ denote the exact solution of scheme (5.35) at the time t. Assume that $\mathbf{w}_h^0 = \mathbf{w}_h(t^0)$ and let $\mathbf{w}_h^1$ denote a numerical solution of (5.35) after a single time step of length $\tau = \tau_n$. We say that the method is consistent of order q in time, if

$$\|\mathbf{w}_h^1 - \mathbf{w}_h(\tau)\|_1 = \mathcal{O}\left(\tau^{q+1}\right).$$

Assume now that a) the semi-discrete scheme (5.35) is consistent of order p, i.e. $E^{[k]}(t) = \mathcal{O}(h^p)$, see Remark 5.8, b) we use a space discretization that is consistent of order q in time and c) the method is stable, i.e. numerical errors only propagate in a controlled manner. Then we would expect that the *discrete* L^1 *error*

$$E_{h,\tau}^{[k]}(t) = \begin{cases} \sum_{i=1}^{N} |h_i| \left| w_i^{[k]}(t) - |h_i|^{-1} \int_{x_{i-1/2}}^{x_{i+1/2}} w_k(x,t)\,dx \right|, & d = 1, \\ \sum_{i,j=1}^{L,M} |C_{i,j}| \left| w_{i,j}^{[k]}(t) - |C_{i,j}|^{-1} \int_{C_{i,j}} w_k(x,t)\,dx \right|, & d = 2, \end{cases} \tag{5.37}$$

where $\tau = \max_n \tau_n$, behaves in the following way

$$E_{h,\tau}^{[k]}(t) \leqslant C_1 h^p + C_2 \tau^q. \tag{5.38}$$

Our space discretization was constructed such that we expect the order $p = 2$. The aim of the following sections is to choose a time discretization that is efficient and that yields an appropriately high q for our application.

Time step restriction by the CFL condition For the stability of the fully discrete method we take the Courant, Friedrichs and Lewy (CFL) condition [38], into account. It states roughly that a numerical method can only converge to the solution of a PDE, if the numerical domain of dependence contains the analytical domain of dependence of the PDE under discussion as $\tau, h \to 0$. By analytical *domain of dependence* we refer to the subset $D_y \subset \Omega$, such that the PDE solution $u(y, t+\tau)$ depends only on $u(x,t)$ for $x \in D_y$ in time t. Its numerical counterpart considers the stencil around a mesh point x_i in time t on which a discrete solution in $(x_i, t+\tau)$ depends.

If we consider a scalar conservation law, where the PDE solution follows characteristic lines, and an explicit finite volume method, this leads to a condition of the kind $a\tau = \mathcal{O}(h)$. Here we have denoted the absolute maximal propagation speed by a. We will also treat the advection terms in system (5.35) explicitly. Neglecting the remaining terms, we obtain in the uniform 2D case the CFL condition

$$\tau_n \leqslant \mathrm{CFL}\ \min\left\{\frac{h^{[x]}}{a^{[x]}(t)},\ \frac{h^{[y]}}{a^{[y]}(t)}\right\} \tag{5.39a}$$

with maximal absolute propagation speeds

$$a^{[x]}(t) = \max_{i,j} |a_{i+1/2,j}(t)|, \quad a^{[y]}(t) = \max_{i,j} |a_{i,j+1/2}(t)|.$$

Similarly, we get for the nonuniform 1D method the local condition

$$\tau_n \leqslant \mathrm{CFL}\ \min_i \frac{h_i + h_{i+1}}{2\,|a_{i+1/2}(t)|}. \tag{5.39b}$$

In both conditions (5.39a) and (5.39b) CFL denotes a fixed number $0 \leqslant \mathrm{CFL} \leqslant 1$ depending on the problem and on the method.

The condition (5.39) couples the time step size and the spatial discretization parameter h. The global error (5.38) in this case can be considered being only dependent on the computational grid via

$$E_h^{[k]}(t) \leqslant C_3 h^{\min\{p,q\}}. \tag{5.40}$$

To take the full profit out of the second order FVFD schemes we aim thus for $q \geqslant 2$.

Restrictions by the diffusion terms In parabolic problems the analytical domain of dependence covers the full domain on which the problem is considered. Thus, a condition of the form (5.39) is not sufficient to obtain an explicit and stable method. One can indeed show by means of the von Neumann analysis [83] that an explicit central difference method for the diffusion equation requires $\tau = \mathcal{O}(h^2)$ in order to be stable. The same is not true for implicit methods for which the numerical domain of dependence in an arbitrary grid point covers the whole computational grid. We mention here in addition the class of *L-stable* time discretization methods. These are implicit and induce a beneficial damping effect of solution components occurring in the discretization of the Laplacian [68]. Therefore, they are particularly well suited to resolve diffusion problems. This suggests a treatment by an implicit, and possibly L-stable, method of the diffusion terms in (5.35).

Due to the nonlinearity of the numerical fluxes, a treatment of the full ODE system with an implicit method would require costly computational methods. Conversely, a fully explicit treatment of system (5.35) would need small time steps $\tau_n \in \mathcal{O}(h^2)$ to ensure stability. To overcome this conflict we consider an *implicit-explicit splitting* of the system. In the following sections we study two general approaches to this splitting and use them to construct suitable time discretizations for system (5.35).

5.7 The Strang splitting method

In this section we introduce the second order Strang splitting method for time discretization of the semi-discrete scheme (5.35).

The *operator splitting* is a simple approach that allows for the use of various time discretisation methods in a single ODE system. Let $\Xi_{\mathcal{F}}(\tau)y$ be a numerical solution of the initial value problem

$$\partial_t w_h = \mathcal{F}(w_h), \quad w_h(0) = y \tag{5.41}$$

at the time $t = \tau$. We allow $\mathcal{F}$ to be any of the operators $\{\mathcal{A}, \mathcal{D}, \mathcal{R}\}$ or a linear combination of those. The *Godunov-splitting* method of the form

$$\mathbf{w}_h^{n+1} = \Xi_{\mathcal{A}+\mathcal{R}}(\tau_n)\Xi_{\mathcal{D}}(\tau_n)\mathbf{w}_h^n \tag{5.42}$$

would first solve the diffusion system and afterwards the advection-reaction system. In this way, we can treat the diffusion with an implicit method. The scheme (5.42) is of first order consistency, if both methods used to integrate the subsystems are at least of first order consistency, too [110].

In what follows we construct a method using the *Strang splitting* that extends the above idea to second order consistency in time. To this end we define three operators to solve system (5.41) numerically for any $\mathcal{F} \in \{\mathcal{A}, \mathcal{D}, \mathcal{R}\}$.

The advection step We solve the advection problem $\partial_t \mathbf{w}_h = \mathcal{A}(\mathbf{w}_h)$ explicitly using the classical fourth order Runge-Kutta method [66]. It requires four successive computations of the numerical fluxes and reads

$$\begin{aligned}
&K^{[1]} = \mathcal{A}(\mathbf{w}_h), && K^{[2]} = \mathcal{A}(\mathbf{w}_h + \frac{\tau}{2} K^{[1]}),\\
&K^{[3]} = \mathcal{A}(\mathbf{w}_h + \frac{\tau}{2} K^{[2]}), && K^{[4]} = \mathcal{A}(\mathbf{w}_h + \tau K^{[3]}),\\
&\Xi_{\mathcal{A}}(\tau)\mathbf{w}_h = \mathbf{w}_h + \frac{\tau}{6}\left(K^{[1]} + 2K^{[2]} + 2K^{[3]} + K^{[4]}\right).
\end{aligned} \tag{5.43}$$

We will apply this operator to the initial data $\mathbf{w}_h$, which are either given from the previous time step ($\mathbf{w}_h = \mathbf{w}_h^n$) or obtained after applying a series of numerical operators to $\mathbf{w}_h^n$.

The diffusion step To solve the stiff diffusion system $\partial_t \mathbf{w}_h = \mathcal{D}(\mathbf{w}_h)$ we consider the combined *trapezoidal-rule/backward-differential-formula* (TR-BDF2) method. It is applied by solving the following two linear system consecutively

$$(I - \frac{\tau}{4}\mathcal{D})W^{[1/2]} = \mathbf{w}_h^* + \frac{\tau}{4}\mathcal{D}\mathbf{w}_h^*, \tag{5.44a}$$

$$(I - \frac{\tau}{3}\mathcal{D})\Xi_{\mathcal{D}}(\tau)\mathbf{w}_h^* = \frac{4}{3}W^{[1/2]} - \frac{1}{3}\mathbf{w}_h^*. \tag{5.44b}$$

We obtain the intermediate stage $W^{[1/2]}$ by the trapezoidal rule with step size $\tau/2$. The final stage $\Xi_{\mathcal{D}}(\tau)\mathbf{w}_h^*$ follows after an application of the second order backward-differential-formula (BDF2) to $\mathbf{w}_h^*$ and $W^{[1/2]}$ [13]. The overall method can be understood as an implicit Runge-Kutta method. It is not only second order consistent in time but also L-stable and thus well suited for solving parabolic problems. The application of this method in an operator splitting scheme in the context of KS-type systems was proposed in [168] after instabilites were observed when using the more common Crank-Nicolson method in the diffusion step.

The data $\mathbf{w}_h^*$ to which we apply this operator were obtained after the application of the advection operator to $\mathbf{w}_h^n$.

The reaction step As in the advection problem we use the explicit classical Runge Kutta method to solve the reaction system $\partial_t \mathbf{w}_h = \mathcal{R}(\mathbf{w}_h)$. The corresponding numerical operator reads

$$\begin{aligned}
&K^{[1]} = \mathcal{R}(\mathbf{w}_h^{**}), && K^{[2]} = \mathcal{R}(\mathbf{w}_h^{**} + \frac{\tau}{2} K^{[1]}),\\
&K^{[3]} = \mathcal{R}(\mathbf{w}_h^{**} + \frac{\tau}{2} K^{[2]}), && K^{[4]} = \mathcal{R}(\mathbf{w}_h^{**} + \tau K^{[3]}),\\
&\Xi_{\mathcal{R}}(\tau)\mathbf{w}_h^{**} = \mathbf{w}_h^{**} + \frac{\tau}{6}\left(K^{[1]} + 2K^{[2]} + 2K^{[3]} + K^{[4]}\right).
\end{aligned} \tag{5.45}$$

The initial state $\mathbf{w}_h^{**}$ originates from $\mathbf{w}_h^n$ after the application of the advection and diffusion operator.

The full Strang splitting method In a similar way as the Godunov-splitting (5.42) we define our *Strang-splitting* method by a successive application of the numerical operators

$$\mathbf{w}_h^{n+1} = \Xi_{\mathcal{A}}\left(\frac{\tau_n}{2}\right)\Xi_{\mathcal{D}}\left(\frac{\tau_n}{2}\right)\Xi_{\mathcal{R}}(\tau_n)\Xi_{\mathcal{D}}\left(\frac{\tau_n}{2}\right)\Xi_{\mathcal{A}}\left(\frac{\tau_n}{2}\right)\mathbf{w}_h^n, \tag{5.46}$$

where the operators are defined above. Throughout this work we will refer to this method as *STRANG*. By the use of numerical operators of at least second order in time and the symmetrical structure, we expect an overall second order of consistence of this method.

The particular order in which the operators are applied was chosen such, that the results that we obtained in the numerical experiments were optimal concerning order of convergence and positivity, see Section 5.11. Since we start with the advection step in (5.46), we can compute the time increment according to the CFL condition (5.39) based on the initially computed propagation speeds without any additional computational effort.

5.8 Implicit-explicit Runge-Kutta methods

In this section we consider further splitting methods for time discretization of system (5.35) which can reach higher orders of consistency in time. We will discuss examples of first up to third order.

In particular, we examine the class of *Implicit-explicit Runge-Kutta* (IMEX RK) methods. They couple a diagonally implicit Runge-Kutta scheme for the diffusion terms with an explicit Runge-Kutta scheme for the remaining terms. A general s-stage IMEX RK method reads

$$\begin{aligned}
W^{[i]} = \mathbf{w}_h^n &+ \tau_n \sum_{j=1}^{i-1} a_{i,j}^E\,(\mathcal{A}+\mathcal{R})(W^{[j]})\\
&+ \tau_n \sum_{j=1}^{i} a_{i,j}^I\,\mathcal{D}(W^{[j]}), \qquad i = 1,\dots,s,
\end{aligned} \tag{5.47a}$$

$$\mathbf{w}_h^{n+1} = \mathbf{w}_h^n + \tau_n \sum_{i=1}^{s} b_i^E\,(\mathcal{A}+\mathcal{R})(W^{[i]}) + \tau_n \sum_{i=1}^{s} b_i^I\,\mathcal{D}(W^{[i]}), \tag{5.47b}$$

where $(b_i^E)_{i=1}^s = \mathbf{b}^E \in \mathbb{R}^s$, $(a_{i,j}^E)_{i,j=1}^s = A^E \in \mathbb{R}^{s\times s}$ denote the coefficients of the explicit embedded scheme on the one hand, and $(b_i^I)_{i=1}^s = \mathbf{b}^I, (a_{i,j}^I)_{i,j=1}^s = A^I \in \mathbb{R}^{s\times s}$ denote the coefficients of the implicit embedded scheme on the other hand.

0	0	0
1	1	0
	1	0

0	0	0
1	θ	$1-\theta$
	θ	$1-\theta$

Table 5.1: Tableaux for the explicit part (left) and the implicit part (right) of the IMEX-θ scheme (5.49), $\theta \in [0,1]$.

For simplicity we have formulated the scheme (5.47) for autonomous systems. Note though that system (III) is not autonomous due to the delay term in the reaction part. One obtains the form of (5.47) for time dependent reaction terms by replacing $(\mathcal{A}+\mathcal{R})(W^{[j]})$ in the scheme by $(\mathcal{A}+\mathcal{R})(t^n + c_j^E \tau_n, W^{[j]})$, where $(c_i^E)_{i=1}^s = c^E$ are given coefficients of the scheme.

For the computation of a single time step with an s-stage IMEX RK method we need to solve s linear systems and to conduct s numerical flux computations. As with the usual Runge-Kutta schemes, a larger number of stages allows for higher orders of consistency in time. To obtain an IMEX RK scheme of a particular order not only the usual order conditions have to hold for the coefficients of both embedded schemes, but also further coupling conditions must be satisfied. For methods of order $p \in \{2,3\}$ it is sufficient to have $b^E = b^I$ such as $c^E = c^I$ for all coupling conditions to hold [134]. We restrict ourselves in this work to methods that satisfy this condition in the context of higher order methods.

In the rest of this section we consider particular schemes of first, second and third order in more detail.

The IMEX-θ scheme A simple family of IMEX RK schemes is given by the *IMEX-θ scheme*

$$\mathbf{w}_h^{n+1} = \mathbf{w}_h^n + \tau_n \left(\mathcal{A}(\mathbf{w}_h^n) + \mathcal{R}(\mathbf{w}_h^n) + (1-\theta)\mathcal{D}(\mathbf{w}_h^n) + \theta \mathcal{D}(\mathbf{w}_h^{n+1}) \right) \tag{5.48}$$

for $\theta \in [0,1]$. In Table 5.1 we provide the Butcher tableaux of both embedded schemes [66]. In the case $\theta = 0$, scheme (5.48) reduces to the common *forward Euler scheme* (EXPLICIT) which is fully explicit and not an actual IMEX method. The choice $\theta = 1/2$ leads to the *IMEX-Crank-Nicolson scheme* (IMEX-CN). We mention moreover the *IMEX-Euler scheme*, which we obtain for $\theta = 1$, and which reads

$$\mathbf{w}_h^{n+1} = \mathbf{w}_h^n + \tau_n \left(\mathcal{A}(\mathbf{w}_h^n) + \mathcal{R}(\mathbf{w}_h^n) + \mathcal{D}(\mathbf{w}_h^{n+1}) \right). \tag{5.49}$$

This method treats advection and reaction with the forward Euler method and diffusion with the backward Euler method. We will use it to study the positivity of our FVFD scheme in the case of system (II). Note that independent of the choice of θ, the scheme is only first order consistent in time. This is even the case for the IMEX-CN method for which the embedded implicit scheme is of second order in time.

The IMEX midpoint scheme The *implicit-explicit midpoint scheme* (IMEX-MP) [134] is an efficient IMEX RK method of second order consistency in time. It employs two explicit but only one implicit stage and can be written as

$$W^{[1/2]} = \mathbf{w}_h^n + \frac{\tau_n}{2} \left(\mathcal{A}(\mathbf{w}_h^n) + \mathcal{R}(\mathbf{w}_h^n) + \mathcal{D}(W^{[1/2]}) \right), \tag{5.50a}$$

$$\mathbf{w}_h^{n+1} = \mathbf{w}_h^n + \tau_n \left(\mathcal{A}(W^{[1/2]}) + \mathcal{D}(W^{[1/2]}) + \mathcal{R}(W^{[1/2]}) \right). \tag{5.50b}$$

The corresponding Butcher tableaux are shown in Table 5.2. The embedded implicit scheme concurs with the usual A-stable midpoint rule [80].

0	0	0
$\frac{1}{2}$	$\frac{1}{2}$	0
	0	1

0	0	0
$\frac{1}{2}$	0	$\frac{1}{2}$
	0	1

Table 5.2: Tableaux for the explicit part (left) and the implicit part (right) of the IMEX-MP scheme (5.50).

0				
$\frac{1767732205903}{2027836641118}$	$\frac{1767732205903}{2027836641118}$			
$\frac{3}{5}$	$\frac{5535828885825}{10492691773637}$	$\frac{788022342437}{10882634858940}$		
1	$\frac{6485989280629}{16251701735622}$	$-\frac{4246266847089}{9704473918619}$	$\frac{10755448449292}{10357097424841}$	
	$\frac{1471266399579}{7840856788654}$	$-\frac{4482444167858}{7529755066697}$	$\frac{11266239266428}{11593286722821}$	$\frac{1767732205903}{4055673282236}$

0	0			
$\frac{1767732205903}{2027836641118}$	$\frac{1767732205903}{4055673282236}$	$\frac{1767732205903}{4055673282236}$		
$\frac{3}{5}$	$\frac{2746238789719}{10658868560708}$	$-\frac{640167445237}{6845629431997}$	$\frac{1767732205903}{4055673282236}$	
1	$\frac{1471266399579}{7840856788654}$	$-\frac{4482444167858}{7529755066697}$	$\frac{11266239266428}{11593286722821}$	$\frac{1767732205903}{4055673282236}$
	$\frac{1471266399579}{7840856788654}$	$-\frac{4482444167858}{7529755066697}$	$\frac{11266239266428}{11593286722821}$	$\frac{1767732205903}{4055673282236}$

Table 5.3: Tableaux for the explicit (top) and the implicit (bottom) embedded scheme of the IMEX3 (originally ARK3(2)4L[2]SA) method [91].

A third order IMEX RK method From the class of higher order IMEX RK schemes we consider the ARK3(2)4L[2]SA scheme from [91]. The name encodes its third order of consistency in time, an embedded control method of second order, four stages, L-stability, a stage order of 2 and stiffly accuracy.

With an embedded implicit scheme which is both L-stable and *stiffly accurate*, implying $a^I_{4,j} = b^I_j$ for $1 \leqslant j \leqslant 4$, the method is particularly well suited for ADR problems such as the invasion models we consider. The embedded implicit scheme can moreover be classified as an explicit singly diagonally implicit Runge-Kutta method. It starts with an explicit first stage and possess a stage order of two [3]. In addition, the coefficients of the scheme were adjusted to minimize the terms of leading order in the error computation [91].

For brevity, we will refer to this method as IMEX3 throughout this thesis. The corresponding Butcher tableaux are provided in Table 5.3 and we refer to the general formulation (5.47) for its implementation. Note that we neither use the embedded second order method for adaptive time step control, nor we provide it in Table 5.3.

5.9 Model (II): positivity preserving property

In this section we prove that the semi-discrete scheme (5.31) for model (II) endowed with either the IMEX-Euler or the EXPLICIT scheme preserves the positivity of numerical solutions under suitable CFL conditions.

As discussed already in Section 4.3 we expect for positive initial data in model (II) that the PDE solution does not become negative. A numerical method with the same property on the

discrete level would be favorable not only to obtain biologically relevant numerical solutions but also to prevent instabilities. In fact, in [31] the instability of a finite volume scheme for the Keller-Segel model was reported due to negative numerical solutions.

We consider the fully discrete scheme that combines the IMEX-Euler time discretization (5.49), ($\theta = 1$) with the FVFD scheme (5.31). It reads for the approximate cell concentrations

$$\begin{aligned} c_{i,j}^{I,n+1} = c_{i,j}^{I,n} &+ \tau_n D_D \left[\frac{c_{i-1,j}^{I,n+1} - 2c_{i,j}^{I,n+1} + c_{i+1,j}^{I,n+1}}{(h^{[x]})^2} + \frac{c_{i,j-1}^{I,n+1} - 2c_{i,j}^{I,n+1} + c_{i,j+1}^{I,n+1}}{(h^{[y]})^2} \right] \\ &- \tau_n \left[\frac{\mathcal{H}_{i+1/2,j}^{I}(t^n) - \mathcal{H}_{i-1/2,j}^{I}(t^n)}{h^{[x]}} + \frac{\mathcal{H}_{i,j+1/2}^{I}(t^n) - \mathcal{H}_{i,j-1/2}^{I}(t^n)}{h^{[y]}} \right] \\ &+ \tau_n \mathcal{R}_{i,j}^{I} \end{aligned} \tag{5.51a}$$

for $I \in \{D, S, F\}$. The reaction terms depend on the cell type via

$$\mathcal{R}_{i,j}^{I} = \begin{cases} \mu_D \, c_{i,j}^{D,n} \; R_{i,j}^{+}(t^n) - \mu_{EMT,i,j}(t^n) c_{i,j}^{D,n}, & I = D, \\ \mu_S \, c^{S,n} \, R_{i,j}^{+}(t^n) + \mu_{EMT,i,j}(t^n) c_{i,j}^{D,n} - \mu_T \, c_{i,j}^{S,n}, & I = S, \\ \mu_F \, c_{i,j}^{F,n} \, R_{i,j}^{+}(t^n) + \mu_T \, c_{i,j}^{S,n} - \beta_F c_{i,j}^{F,n}, & I = F. \end{cases}$$

Moreover, the scheme reads for the ECM and the MMPs

$$v_{i,j}^{n+1} = v_{i,j}^{n} - \tau_n \delta_v \, m_{i,j}^{n} v_{i,j}^{n} + \tau_n \mu_v \, c_{i,j}^{F,n} \, R_{i,j}^{+}(t^n), \tag{5.51b}$$

$$\begin{aligned} m_{i,j}^{n+1} = m_{i,j}^{n} &+ \tau_n \alpha_D \, c_{i,j}^{D,n} + \tau_n \alpha_S \, c_{i,j}^{S,n} - \tau_n \beta_m \, m_{i,j}^{n} \\ &+ \tau_n \, D_m \left[\frac{m_{i-1,j}^{n+1} - 2m_{i,j}^{n+1} + m_{i+1,j}^{n+1}}{(h^{[x]})^2} + \frac{m_{i,j-1}^{n+1} - 2m_{i,j}^{n+1} + m_{i,j+1}^{n+1}}{(h^{[y]})^2} \right]. \end{aligned} \tag{5.51c}$$

For the definition of the fluxes and the discrete EMT coefficient we refer to the semi-discrete formulation (5.31).

Theorem 5.10 *Consider the IMEX-Euler FVFD scheme* (5.51) *for system* (II). *Then the numerical cell concentrations* $c_{i,j}^{I,n}$ *remain nonnegative for any* $I \in \{D, S, F\}$, *if the initial data is nonnegative and the CFL condition*

$$\tau_n < \min \left\{ \frac{h^{[x]}}{8 \, a^{[x]}(t)}, \; \frac{h^{[y]}}{8 \, a^{[y]}(t)}, \; \frac{1}{2 \, \max\{\mu_0, \mu_T, \beta_F\}} \right\} \tag{5.52}$$

is satisfied at every time step.

Proof. We follow the strategy from the positivity proofs in [31, 32]. Firstly, we fix $I \in \{D, S, F\}$ and note that

$$\mathcal{R}_{i,j}^{I} \geqslant -\max\{\mu_0, \mu_T, \beta_F\} \, c_{i,j}^{I,n}. \tag{5.53}$$

Secondly, we obtain by Proposition 5.4 and $c_{i,j}^{I,n} \geqslant 0$ that the interface reconstruction by the MC limiter satisfy $c_{i+1/2,j}^{I,E/W}, c_{i,j+1/2}^{I,S/N} \geqslant 0$. They allow moreover for the decomposition

$$c_{i,j}^{I,n} = \frac{1}{2} c_{i,j}^{I,n} + \frac{1}{8} \left(c_{i-1/2,j}^{I,E} + c_{i+1/2,j}^{I,W} + c_{i,j-1/2}^{I,N} + c_{i,j+1/2}^{I,S} \right).$$

We have dropped the time index in the reconstructions for clarity. Next, we define the interface derivatives of the ECM by

$$v^{[x]}_{i+1/2,j} = \frac{v^n_{i+1,j} - v^n_{i,j}}{h^{[x]}}, \quad v^{[y]}_{i,j+1/2} = \frac{v^n_{i,j+1} - v^n_{i,j}}{h^{[y]}}.$$

Now we are in the position to rewrite the scheme

$$\begin{aligned}
c^{I,n+1}_{i,j} = &\left[\frac{1}{8} - \frac{\chi_I \tau_n}{h^{[x]}}(v^{[x]}_{i-1/2,j})^+\right] c^{I,E}_{i-1/2,j} + \frac{\chi_I \tau_n}{h^{[x]}}(v^{[x]}_{i-1/2,j})^- c^{I,W}_{i-1/2,j} \\
&+ \left[\frac{1}{8} - \frac{\chi_I \tau_n}{h^{[x]}}(v^{[x]}_{i+1/2,j})^-\right] c^{I,W}_{i+1/2,j} + \frac{\chi_I \tau_n}{h^{[x]}}(v^{[x]}_{i+1/2,j})^+ c^{I,E}_{i-1/2,j} \\
&+ \left[\frac{1}{8} - \frac{\chi_I \tau_n}{h^{[y]}}(v^{[y]}_{i,j-1/2})^+\right] c^{I,N}_{i,j-1/2} + \frac{\chi_I \tau_n}{h^{[x]}}(v^{[y]}_{i,j-1/2})^- c^{I,S}_{i,j-1/2} \\
&+ \left[\frac{1}{8} - \frac{\chi_I \tau_n}{h^{[y]}}(v^{[y]}_{i,j+1/2})^-\right] c^{I,S}_{i,j+1/2} + \frac{\chi_I \tau_n}{h^{[y]}}(v^{[y]}_{i,j+1/2})^+ c^{I,N}_{i,j+1/2} \\
&+ \tau_n D_I \left[\frac{c^{I,n+1}_{i-1,j} - 2c^{I,n+1}_{i,j} + c^{I,n+1}_{i+1,j}}{(h^{[x]})^2} + \frac{c^{I,n+1}_{i,j-1} - 2c^{I,n+1}_{i,j} + c^{I,n+1}_{i,j+1}}{(h^{[y]})^2}\right] \\
&+ \frac{c^{I,n}_{i,j}}{2} + \tau_n \mathcal{R}^I_{i,j}.
\end{aligned} \tag{5.54}$$

Equation (5.54) considered for all $1 \leqslant i \leqslant L$ and $1 \leqslant j \leqslant M$ leads to the system of linear equations

$$(I - \tau_n D) c^{I,n+1} = R(\mathbf{w}^n_h), \tag{5.55}$$

where $c^{I,n+1}$ includes all cell averages $c^{I,n+1}_{i,j}$. By the CFL condition (5.52), the estimate (5.53) and (5.54), the right hand side of this system is nonnegative. The matrix $I - \tau_n D$ is diagonally dominant, has only negative nondiagonal entries and is therefore an *M-matrix* [80]. Every M-matrix M is regular and satisfies the monotonicity property $M^{-1}x \geqslant 0$ for any $x \geqslant 0$. Thus, the statement of the theorem follows from (5.55). □

Remark 5.11 The CFL condition (5.52) in Theorem 5.10 is not optimal and can be further adjusted to

$$\tau_n < \min\left\{\frac{(1-\varepsilon)h^{[x]}}{4\,a^{[x]}(t)}, \frac{(1-\varepsilon)h^{[y]}}{4\,a^{[y]}(t)}, \frac{\varepsilon}{\max\{\mu_0, \mu_T, \beta_F\}}\right\} \tag{5.56}$$

for any $0 < \varepsilon < 1$. To obtain condition (5.56) we have altered the decomposition in the proof to

$$c^{I,n}_{i,j} = \varepsilon c^{I,n}_{i,j} + \frac{1-\varepsilon}{4}(c^{I,E}_{i-1/2,j} + c^{I,W}_{i+1/2,j} + c^{I,N}_{i,j-1/2} + c^{I,S}_{i,j+1/2}).$$

An optimal value of ε can be balanced out with respect to a given mesh resolution and parameters μ_0, μ_T, β_F.

The IMEX-Euler scheme is only first order accurate in time. For efficiency, we use thus the higher order IMEX3 method for time discretization of (5.31) in our numerical simulations. We guarantee the nonnegativity of the cell densities in the method by the following strategy.

Whenever negative numerical cell concentrations occur in the approximate solution obtained by time integration with IMEX3, we repeat the current time step with the IMEX-Euler time discretization (5.51) and CFL condition (5.52). In practice only very few time steps (less than one in a thousand) had to be recomputed with the IMEX-Euler scheme. This strategy moreover did not affect the experimental order of convergence, as we will demonstrate in Chapter 8.

One can obtain similar but possibly more restrictive results with higher order methods when using particular positivity preserving IMEX schemes proposed in the literature [72]. The derivation of a CFL condition that is sufficient for the nonnegativity in these methods and that depends only on the propagation speeds is an open problem.

For completeness, we note that the above theorem can be adjusted to the fully explicit forward Euler scheme (5.49), ($\theta = 0$) under a more restrictive condition.

Corollary 5.12 *Consider the FVFD scheme* (5.31) *discretized in time by the forward Euler scheme* (5.49), *($\theta = 0$) to resolve system* (II) *numerically. Then the numerical solution for the densities of DCCs, CSCs and fibroblasts remain nonnegative, provided we have positive initial data and the following CFL condition holds*

$$\tau_n < \min\left\{ \frac{h^{[x]}}{8\,a^{[x]}(t)}, \frac{h^{[y]}}{8\,a^{[y]}(t)}, \frac{1}{4\max\{\mu_0, \mu_T, \beta_F\}}, \frac{h^{[x]}\,h^{[y]}}{8C_D} \right\}, \tag{5.57}$$

where $C_D = \max\{D_D, D_S, D_F\}(h^{[x]}/h^{[y]} + h^{[y]}/h^{[x]})$.

Proof. This result follows by a modification of the proof of Theorem 5.10 analog to [32]. Instead of using the M-matrix argument, we estimate in the explicit scheme

$$\begin{aligned}
&\frac{c_{i,j}^{I,n}}{4} + \tau_n D_I \left[\frac{c_{i-1,j}^{I,n} - 2c_{i,j}^{I,n} + c_{i+1,j}^{I,n}}{(h^{[x]})^2} + \frac{c_{i,j-1}^{I,n} - 2c_{i,j}^{I,n} + c_{i,j+1}^{I,n}}{(h^{[y]})^2} \right] \\
&\geqslant \left[\frac{1}{4} - \tau_n \frac{2\,C_D}{h^{[x]}h^{[y]}} \right] c_{i,j}^{I,n} + \tau_n \left[\frac{c_{i-1,j}^{I,n} + c_{i+1,j}^{I,n}}{(h^{[x]})^2} + \frac{c_{i,j-1}^{I,n} + c_{i,j+1}^{I,n}}{(h^{[y]})^2} \right] \geqslant 0.
\end{aligned}$$

Here we have used the CFL condition (5.57) and $c^{I,n} \geqslant 0$. The tightened time step restriction (5.57) implies moreover $c_{i,j}^{I,n}/4 + \tau_n \mathcal{R}_{i,j}^{I} \geqslant 0$. By rewriting the remaining advection related terms in the computation of $c_{i,j}^{I,n+1}$ as in (5.54) we deduce the nonnegativity in the next time step. □

The above result can be directly extended to higher order *strong stability preserving* (SSP) Runge-Kutta schemes [64]. These are explicit schemes that can be written as convex combinations of forward Euler steps. Their positivity preserving property follows thus with Corollary 5.12.

5.10 Model (III): treatment of the delay and the fast integrin dynamics

For simulations with the contractivity model (III), we promote the IMEX3 method (Table 5.3) for the time discretization of the semi-discrete scheme (5.32). This is because of its high accuracy and efficiency which we will present along with experimental convergence rates in Chapter 8. In this section we discuss three adaptations of this scheme that account for peculiarities of system (III). In particular, we discuss the treatment of the nonlinear diffusion

terms, an interpolation technique to deal with the delay term and a time step adaptation that avoids problems due to the fast dynamics of the contractivity. The paragraphs on the delay term and the time step adaptations are based on a part of our paper [98].

Stiff reaction terms and nonlinear diffusion In the case of large coefficients in the reaction terms, the evolution equation for the integrin densities in the semi-discrete scheme (5.32) is stiff. To overcome possible problems with instabilities we treat these terms implicitly in the IMEX RK method.

In more detail, we formally modify the discrete diffusion and reaction operators in the case of system (III) by

$$\mathcal{D}_{i,j}^{[4]}(\mathbf{w}_h(t)) = \varepsilon^{-1}\, k_+\, \nu_{i,j}(1-y_{i,j}) - \varepsilon^{-1}\, k_-\, y_{i,j}, \quad \mathcal{R}_{i,j}^{[4]}(\mathbf{w}_h(t)) = 0, \tag{5.58}$$

for all $1 \leqslant i \leqslant L$ and $1 \leqslant j \leqslant M$. In this way, the discrete operator $\mathcal{D}_{i,j}^{[4]}(\mathbf{w}_h(t))$ does not include only diffusion terms, but with the definition (5.47) the implicit treatment of the stiff reaction is clearly defined. Note that we treat the evolution equation for the integrin concentration y fully explicitly and thus (5.58) does not result in a nonlinear equation system.

The discrete diffusion terms $\mathcal{D}_{i,j}^{[2]}(\mathbf{w}_h(t))$ include state dependent coefficients $D_{i,j}(t)$ and are therefore nonlinear. For a full implicit treatment in the IMEX3 method we would need to solve four nonlinear systems in each time step. To reduce the computational complexity, we consider a linearization of $\mathcal{D}_{i,j}^{[2]}(\mathbf{w}_h(t))$. More precisely, we compute the coefficients only once in the beginning of each time update $t^n \to t^{n+1}$ based on the current state, i.e. we compute the coefficients $D_{i,j}(t^n)$. They remain constant for the rest of the time step. In this way, it suffices to solve four linear systems in the time integration by the IMEX3 scheme. This modification has hampered neither the stability of the method nor the experimental order of convergence in our numerical experiments, as we will demonstrate in Section 8.1.

Treatment of the delay term An important component of system (III) is the time delay term $y(t-\chi\tau)$ that appears in the contractivity equation of the component κ. Its discrete counterpart is a reaction term in the semi-discrete scheme (5.32). In the vector formulation (5.35) it is included in the operator $\mathcal{R}(\mathbf{w}_h^n)$. We evaluate this delay term consequently in the explicit part of the IMEX RK method.

Assume that we compute the stage j of an IMEX RK method. In this process we evaluate the operator $\mathcal{R}$ at the time instance $\hat{t} = t^n + c_j^E \tau$ and thus need an approximation for $y(\hat{t}-\chi\tau)$. We have dropped the subindex of the time step size for clarity. To find a suitable approximation we identify the position of $\hat{t}-\chi\tau$ and interpolate between the known values of y_h. In more detail, we consider the time instances $t_{d,1} \leqslant t_{d,2} \leqslant t^n \leqslant \hat{t}$, where $t_{d,1} \leqslant \hat{t}-\chi\tau$, and corresponding densities of the integrins $y_h(t_{d,1})$, $y_h(t_{d,2})$, $y_h(t^n)$, $y_h(\hat{t})$. Then we interpolate as follows

$$y_D = y_h(\hat{t}-\chi\tau) = y_h(t_a) + \frac{\hat{t}-\chi\tau-t_a}{t_b-t_a}\left(y_h(t_b)-y_h(t_a)\right), \tag{5.59}$$

where $(t_a, t_b) \in \{(t_{d,1}, t_{d,2}), (t_{d,2}, t^n), (t^n, \hat{t})\}$ is such that $t_a \leqslant \hat{t}-\chi\tau < t_b$. As numerical integrin densities at these time instances we use the current numerical solution $y_h(t^n) = (y_{i,j}(t^n))_{i,j=1}^{L,M}$ and previously computed densities $y_h(t_{d,1}), y_h(t_{d,2})$. Moreover, we make the assumption that $W^{[j]} \approx w_h(\hat{t})$ and employ the current stage restricted to the integrin component as approximation of the integrin density at the time instance $\hat{t}$, i.e. we employ $y_h(\hat{t}) = W^{[j],y}$.

After the computation of the full time update w_h^{n+1}, we verify whether the delay time at the next time integration step will overshoot $t_{d,2}$. More precisely, if $t^{n+1} - \chi\tau \geqslant t_{d,2}$, we update the delay time instances $t_{d,1}, t_{d,2}$ and the corresponding numerical densities used for the interpolation by

$$t_{d,1} \leftarrow t_{d,2}, \quad t_{d,2} \leftarrow t_n, \quad y_h(t_{d,1}) \leftarrow y_h(t_{d,2}), \quad y_h(t_{d,2}) \leftarrow y_h(t_n).$$

Time step adaptation The ODE subsystem consisting of the last two equations of (III) is stiff due to the large parameter ε^{-1}. Since we aim to treat the delay explicitly, we can only treat a part of the ODE subsystem by the implicit scheme embedded in the IMEX RK method. As a result, we observed instabilities and inaccuracies when using an IMEX RK method, if the time steps were not further regulated. To address this problem we adapt τ_n such that the relative change of κ remains bounded in each time step, i.e.

$$\frac{\|\kappa_h(t_n) - \tilde{\kappa}_h(t_n + \tau_n)\|_\infty}{\|\kappa_h(t_n)\|_\infty} \leqslant \Theta_\kappa \,, \tag{5.60}$$

where $\kappa_h(t_n) = (\kappa_{i,j}(t^n))_{i,j=1}^{L,M}$. The time increment τ_n is needed in the method to compute the actual approximate contractivity $\kappa_h(t_n + \tau_n) = (\kappa_{i,j}(t^n + \tau_n))_{i,j=1}^{L,M}$. Thus, we apply an estimator $\tilde{\kappa}_h(t_n + \tau_n) \approx \kappa_h(t_n + \tau_n)$ in (5.60) instead of the complete approximation $\kappa_h(t_n + \tau_n)$.

One can see in the unscaled model (2.61) that the component κ evolves quickly to a quasi-steady-state. We refer to [175] for more details in this regard. After the quasi-equilibrium is reached, the contractivity κ evolves very slowly. Consequently, the condition (5.60) affects the time step size only in the beginning of the computation.

The practical computation of τ_n based on the CFL condition (5.39) and (5.60) works as follows. We start the IMEX RK method by computing $\mathcal{A}(\mathbf{w}_h^n)$ and $\mathcal{R}(t_n, \mathbf{w}_h^n)$ which are needed for the first stage of the IMEX RK updates. All the terms in the evolution equation for the contractivity are discretized in the reaction operator $\mathcal{R}(t^n, \mathbf{w}_h^n)$. We can thus define the forward Euler estimator

$$\tilde{\kappa}_h(t_n + \tau_n) = \kappa_h(t_n) + \tau_n \mathcal{R}^\kappa(t^n, \mathbf{w}_h^n),$$

where $\mathcal{R}^\kappa(t^n, \mathbf{w}_h^n)$ denotes the discrete reaction operator restricted to the component κ. By substituting into (5.60) we obtain the time step restriction

$$\tau_n < \frac{\|\Theta_\kappa\, \kappa_h(t_n)\|_\infty}{\|\mathcal{R}^\kappa(t^n, \mathbf{w}_h^n)\|_\infty} \tag{5.61}$$

that we employ in combination with the CFL condition (5.39). In this way, we adjust the time increment τ_n without any additional computational effort. In our computations we employ a threshold value of $\Theta_\kappa = 0.01$ in (5.60) that followed from numerical experimentation.

When we use this technique, we resolve the microscopic dynamics of the model efficiently instead of choosing small time steps throughout the full computation. In this way, we ensure the stability of the explicit method in the stiff contractivity subsystem.

5.11 Model (I): numerical experiments and comparison of time integration methods

This section is devoted to the experimental study of the proposed numerical method. We compare, in particular, the discussed time discretization schemes. To this end we consult

	EOC	rel. CPU time	L^1 error $E(1/400)$
IMEX-CN	1.162	0.32	5.544×10^{-1}
STRANG	1.925	1.00	3.472×10^{-2}
EXPLICIT	2.067	3.24	2.425×10^{-2}
IMEX3	1.940	0.64	1.775×10^{-2}

Table 5.4: Experiment 1: Comparison of the time integration methods in terms of EOC, error and CPU time. The EOCs were computed using formula (5.65) for $h_1 = 1/600$ and $h_2 = 1/800$. The relative CPU times (with STRANG as the reference method) and the L^1 error refer to a computation on $N = 2000$ uniform mesh cells.

the well established invasion model (I), which provides the typical dynamics of KS-type cancer-invasion models. Thus, the results will also serve as a reference when we deal with the models (II) and (III). All numerical computations were conducted using MATLAB[1]. This section is based on a part of our publication [96].

Experiment 1: setting and dynamics In our first numerical experiment we considered system (I) on the 1D domain $\Omega = (0, 10)$. The parameters that we used are provided in Appendix A. As initial data we employed for $x \in (0, 10)$ the functions

$$c_0(x) = e^{-x^2/\varepsilon}, \qquad v_0(x) = 1 - \frac{1}{2}e^{-x^2/\varepsilon}, \qquad u_0(x) = \frac{1}{2}e^{-x^2/\varepsilon},$$
$$p_0(x) = \frac{1}{20}e^{-x^2/\varepsilon}, \qquad m_0(x) = 0, \qquad \varepsilon = 5 \times 10^{-3}. \tag{5.62}$$

The initial conditions model a single tumor that starts the ECM invasion from the left boundary of the 1D domain. Except for the location of the cancer cell accumulation the tissue is intact. While no plasmin was activated, small amounts of the chemicals uPA and PAI-1 were already produced by the tumor at the initial time instance $t = 0$.

We present the time evolution of the system components in Figure 5.2 for $t \leqslant 150$. The main tumor propagates to the right side of the domain and degrades at the same time the ECM. In the invaded area, where proteolysis already diminished the tissue density to a small amount, new tumor cell clusters emerge. They take the form of peaks in the cancer cell concentrations. The number of these peaks as well as their maximal concentration vary in time. They evolve in time by moving and merging with each other. At the time instance $t = 75$ almost half of the domain is invaded by cancer cells. The interaction of the peaks continues as the invaded area becomes larger. No steady state is attained even in later time instances $300 \leqslant t \leqslant 500$ when the full domain has been invaded. The remaining components of the system behave differently: we observe only small spikes in the uPA and plasmin densities while the more diffusive inhibitor PAI-1 exhibits a smooth density over space. The densities of the enzymes have not overshot a concentration of one throughout the simulation.

These results were computed by the FVFD scheme (5.30) with IMEX3 time discretization on a uniform computational grid of $N = 5000$ cells .

Experiment 1: study of numerical methods For a numerical test of the methods, we considered the previous experiment on the shorter domain $\Omega = (0, 5)$ and fixed the final

[1]MATLAB is a registered trademark by The MathWorks, Inc., Natick, Massachusetts, United States.

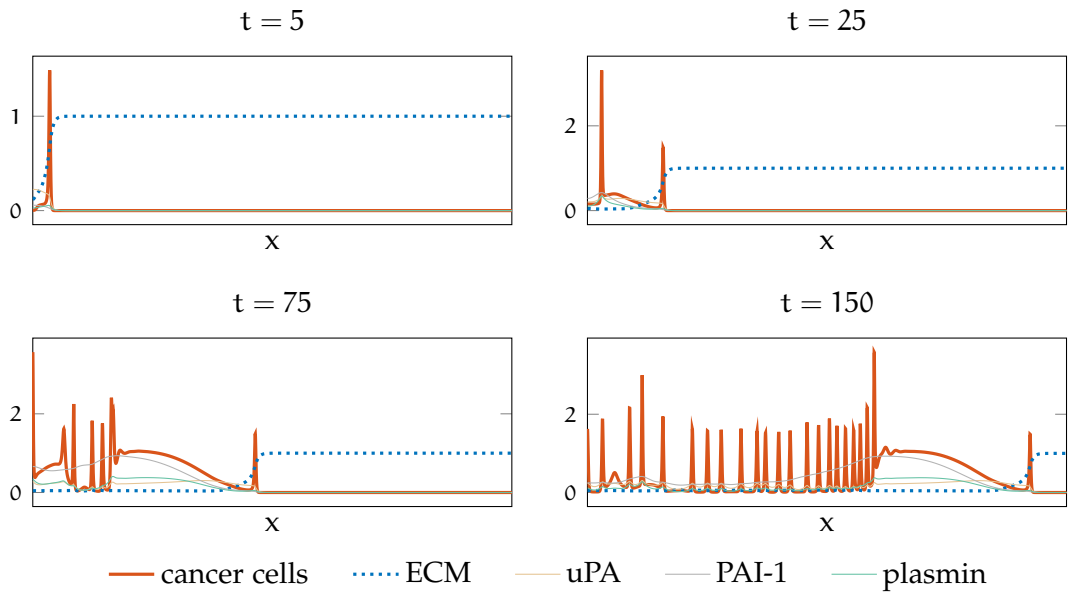

Figure 5.2: Experiment 1: Spatio-temporal dynamics of cancer invasion system (I). We present the spatial concentrations of the system components in four subsequent time instances. Computed with the FVFD scheme (5.30) on a uniform mesh (N = 5000) and IMEX3 time discretization.

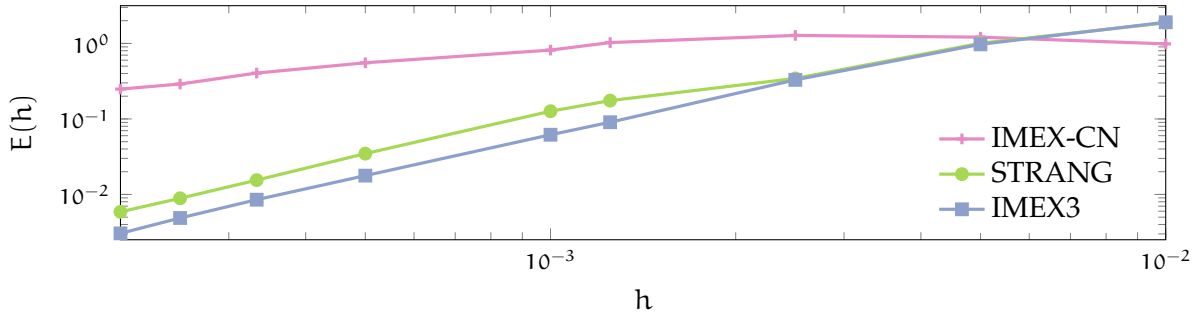

Figure 5.3: Experiment 1: Experimental convergence plot for three tested splitting methods. STRANG and IMEX3 converge with order two and IMEX-CN converges with order one. IMEX3 achieves the most accurate numerical solutions

time $T = 60$. We integrated the FVFD scheme (5.30) with various methods introduced in Sections 5.7 and 5.8. In particular, we compared the performance of the methods STRANG, EXPLICIT, IMEX-CN, IMEX-MP and IMEX3. In the case of EXPLICIT we employed time steps in $\mathcal{O}(h^2)$ as in condition (5.57). For all other methods we used the less restrictive CFL condition (5.39) with Courant number CFL$= 0.49$.

An exact solution of PDE system (I) in the setting of Experiment 1 has not been available. For this reason we computed a reference solution $\mathbf{w}^{\text{ref}}$ on a very fine grid with $N_{\text{ref}} = 30\,000$ uniform cells. We used our consistent FVFD space discretization (5.30) integrated by the explicit fifth order method of Dormand and Prince [45] and a strict positivity preserving time step restriction[2] for its computation.

To explain the error computation let us denote the cancer cell component of the reference

[2]We employed adaptive time step control using the common fourth order control method within the Dormand and Prince scheme with a relative and absolute error tolerance of 10^{-12} [68]. Moreover, we checked in each time step for negative values. If these occurred, we repeated the corresponding time step using the adapted time increment $\tau^{\text{new}} = 0.8\,\tau^{\text{old}}$.

solution on the cell C_i^{ref} by c_i^{ref}. We consider only the final time $T = 60$ and thus drop the time index for clarity. Assume a numerical solution computed on $N = 1/h$ uniform cells $C_1^h, \dots, C_N^h$ and let c_i^h denote the corresponding approximation of the cancer cell concentration on the computational cell C_i^h. To measure the accuracy of a given method we project the reference solution to the computational cells $C_1^h, \dots, C_N^h$ and introduce

$$c_i^{ref(h)} = \sum_{\{j : C_j^{ref} \cap C_i^h \neq \emptyset\}} \frac{|C_j^{ref} \cap C_i^h|}{|C_i^h|} c_j^{ref} \tag{5.63}$$

for $i = 1, \dots, N$. Then we can define the discrete L^1 error

$$E(h) = \sum_{i=1}^{N} \left|C_i^h\right| \, |c_i^h - c_i^{ref(h)}|. \tag{5.64}$$

Note that (5.63) and (5.64) also describe our error computation for nonuniform finite volume meshes and the 2D case.

Except for the method EXPLICIT we expect the error (5.64) to behave as in (5.40) and to convergence thus with order $\min\{q, 2\}$ as $h \to 0$. The integer q denotes here the order of consistency in time. As a result the error $E(h)$ should converge with order two in all tested methods except for IMEX-CN, which is only first order accurate in time. In the case of EXPLICIT we expect an error convergence of order two due to $\tau \in \mathcal{O}(h^2)$.

To verify our expectations we computed the numerical solutions on N cells for any

$$N \in \{100, 200, 400, 800, 1000, 2000, 3000, 4000, 5000\}$$

and for each considered time integration scheme. Due to the limited accuracy of our reference solution we did not consider numerical solutions on grids with more than $N = 5000$ computational cells.

Figure 5.3 presents the error $E(h)$ plotted against the discretization parameter h in log-log scale for three tested methods in Experiment 1. We can see a first order convergence of the method IMEX-CN. However, its error $E(h)$ is larger than 10^{-1} even for high grid resolution using 5000 mesh cells. Thus, IMEX-CN is not a useful method for this problem. STRANG and IMEX3 on the other hand seem to converge with order two. In particular, IMEX3 achieves slightly lower errors than STRANG. The IMEX-MP scheme suffered from instabilities on finer grids and no convergence could be observed.

In Table 5.4 we summarize the *experimental order of convergence* (EOC), the discrete L^1 error of a generic solution with cell size $h = 1/400$ and the corresponding computation times relative to the computation time of the STRANG method. To compute the EOCs we used the discrete L^1 errors for cell sizes $h_1 = 1/600$ and $h_2 = 1/800$ and the formula

$$EOC = \frac{\log(E(h_1)) - \log(E(h_2))}{\log(h_1) - \log(h_2)}. \tag{5.65}$$

Our expected orders of convergence are verified by the EOC numbers. We can also confirm the second order convergence of EXPLICIT. Concerning the computational costs though, EXPLICIT can not compete with the splitting methods that were more than three times faster. Overall, considering the EOC close to two the fast computation time and also the small L^1 errors, IMEX3 has delivered the best performance in Experiment 1.

We note that all tested methods computed nonnegative results at the final time. The method STRANG however, is the only tested methods for which the solution stayed nonnegative in all

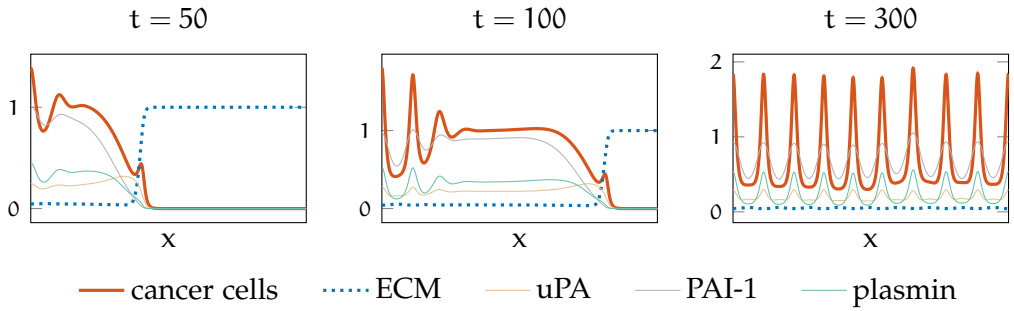

Figure 5.4: Experiment 2: Spatio-temporal dynamics of system (I) with modified $D_c = 5.3 \times 10^{-3}$. We present the spatial concentrations of the system components in three subsequent time instances. Computed with the FVFD scheme (5.30) on a uniform finite volume mesh ($N = 5000$) and IMEX3 time discretization.

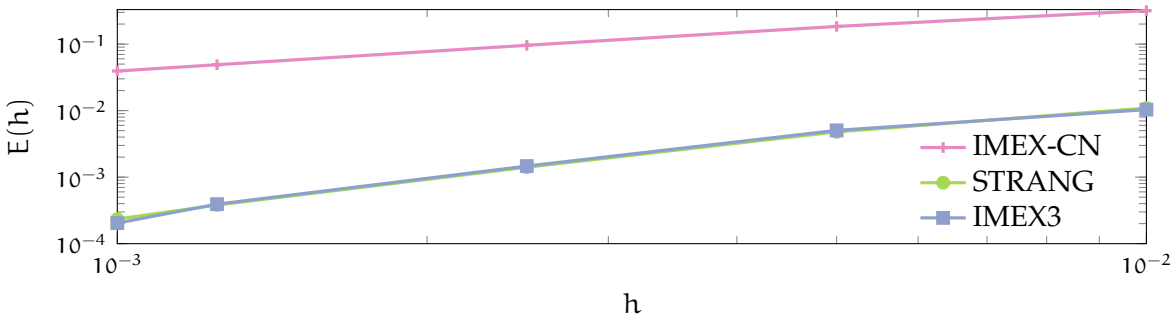

Figure 5.5: Experiment 2: Experimental convergence plot for three tested splitting methods. STRANG and IMEX3 converge with order two and IMEX-CN converges with order one. STRANG achieves similarly accurate numerical solutions as IMEX3.

time steps between 0 and T. By its EOC, accuracy and relatively low computational costs the STRANG method is thus another good choice for problems of this kind.

In the original study we also included *Rosenbrock type methods* and schemes endowed with *adaptive time step control*. With these strategies however, we did not gain any considerable advantages over STRANG and IMEX3 in the numerical experiments [96].

Experiment 2 In our second experiment we considered again system (I) on the interval $\Omega = (0, 10)$. We employed the initial conditions (5.62) and the same parameters as before but opposed to Experiment 1, we chose an increased diffusion coefficient of the cancer cells, i.e.

$$D_c = 5.3 \times 10^{-3}.$$

In Figure 5.4 we show the dynamics of the solution. As in Experiment 1, a tumor propagates

	EOC	L^1 error $E(1/200)$
IMEX-CN	0.973	3.933×10^{-2}
STRANG	1.958	2.341×10^{-4}
IMEX3	2.154	2.037×10^{-4}

Table 5.5: Experiment 2: Comparison of the splitting methods in terms of EOC, error and CPU time. The EOCs were computed using formula (5.65) for $h_1 = 1/80$ and $h_2 = 1/200$. The L^1 error refers to a computation on $N = 1000$ uniform mesh cells.

to the right side of the domain and degrades the ECM. Opposed to the simulation results shown in Figure 5.2, we do not observe a dynamic interaction of clusters, instead a spatial pattern forms in the invaded areas. The solution reaches a steady state at $t = 300$. The visualized numerical solution was computed with the semi-discrete scheme (5.30) and IMEX3 time discretization (see Section 5.8) on a uniform computational grid using $N = 5000$ cells.

To investigate how the numerical methods perform in this "smoother" setting, we did a similar numerical study as done in Experiment 1. We considered the shortened interval $\Omega = (0, 5)$ and the final time $T = 50$ and then computed a reference solution using the Dormand and Prince method on $N = 30\,000$ cells. Again, we fixed $CFL = 0.49$ and computed errors at the final time according to (5.63) and (5.64). We computed on N uniform cells for any $N \in \{100,\ 200,\ 400,\ 800,\ 1000\}$.

We restricted our experimental study to the splitting methods. The convergence of the error $E(h)$ is shown in Figure 5.5. We can clearly observe a second order convergence of STRANG and IMEX3 and a first order convergence of IMEX-CN. In this test the errors of STRANG and IMEX3 are almost indistinguishable. Even in this second experiment the IMEX-MP scheme was unstable and did not converge. This indicates that L-stability of the implicit scheme that IMEX-MP does not possess is a crucial property of splitting methods when dealing with system (I). Once again, the STRANG method delivered only nonnegative numerical solutions in all time steps.

The EOCs computed by (5.65) using $h_1 = 1/80$ and $h_2 = 1/200$ are shown in Table 5.5. Along we present the discrete L^1 error for a generic computation with cell size $h = 1/200$. Compared to the analogous results from Experiment 1 in Table 5.4, we see similar EOCs but lower absolute errors due to the smooth solution profile in this experiment.

Experiment 3 To demonstrate the 2D dynamics in system (I) and the reliability of the IMEX3 method in higher dimensions, we present a third experiment. It was computed on the domain $\Omega = [-15, 15]^2$ and it employed the same parameters as Experiment 1. In the numerical simulation we used a quadrilateral finite volume mesh with $h^{[x]} = h^{[y]} = 0.05$ and IMEX3 time discretization.

To describe the used initial data, let us consider the function

$$y(x_1) = \begin{cases} 4 + 0.7\sin(0.9x_1), & x_1 < 0, \\ 7\sin(0.9x_1) + 0.008x_1^3 + 4, & 0 \leqslant x_1 \leqslant 5, \\ 5 + 0.7\sin(4.5) + 0.7\sin(0.9(x_1 - 5)), & x_1 > 5 \end{cases}$$

and the set $U = \{(x_1, x_2) \in \mathbb{R}^2 : x_2 \geqslant y(x_1)\}$. Then we define the initial condition by

$$c_0(x) = \chi_U(x), \qquad v_0(x) = 1 - \chi_U(x), \qquad u_0(x) = 0.5\,\chi_U(x),$$
$$p_0(x) = 0.05\,\chi_U(x), \qquad m_0(x) = 0$$

for all $x \in \Omega$ with $\chi_U(x)$ denoting the characteristic function over U. To omit boundary effects by the homogeneous Neumann condition we show the results only in $\bar{\Omega} = [0, 5]^2$, which includes 100×100 computational mesh cells.

We present the initial conditions and the numerical results in Figure 5.6. Analogously to the dynamics in 1D in Experiment 1, the cancer cells disseminate and break down the extracellular tissue. In this way, the cells migrate in negative x_2 direction. Heterogeneous structures of cancer cells form in the invaded areas. These areas feature high concentration of tumor cells. But no spatial steady state has occurred until $T = 200$.

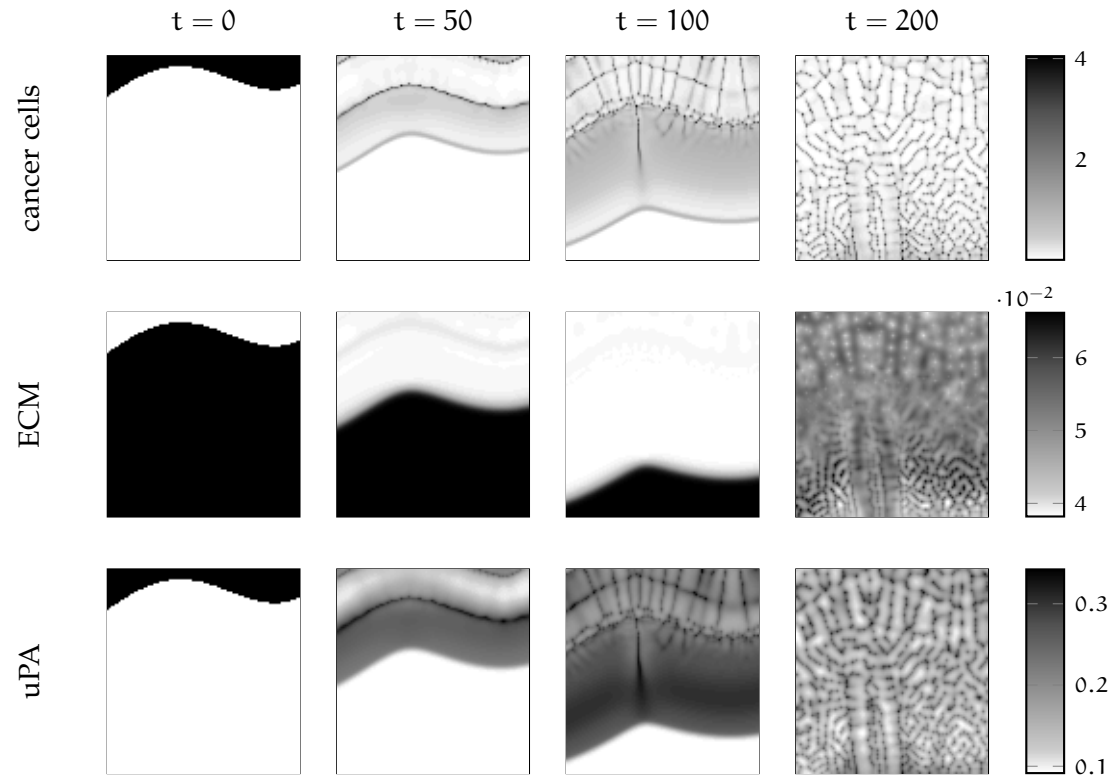

Figure 5.6: Experiment 3: Time evolution of the concentrations of cancer cells, ECM and uPA on the square $\bar{\Omega} = [0, 5]^2$. Computed with the FVFD scheme (5.30) on a 2D finite volume mesh ($h^{[x]} = h^{[y]} = 0.05$) and IMEX3 time integration. The colorbar ticks refer only to the densities at the time instance $t = 200$.

For a study of the performance of the numerical method in 2D, we refer to our experiments with models (II) and (III) in Chapter 8.

Remark 5.13 All three conducted experiments demonstrated the robustness and the reliability of the constructed FVFD scheme (5.30). In Experiments 1 and 2 in 1D we verified the accuracy of the scheme when used with either the STRANG or the IMEX3 time discretization method. For both methods the overall scheme yielded an EOC of two. The IMEX3 method on the one hand delivered the most accurate results in the comparison of time integration methods. The STRANG scheme on the other hand always preserved the nonnegativity of the solutions and also delivered accurate results. For these reasons we promote both time discretization methods for the application in cancer invasion systems.

6 Adaptive mesh refinement for cancer invasion models

In the present chapter we construct adaptive mesh refinement methods for cancer invasion models in space dimensions one and two. We will begin in Section 6.1 by motivating their benefit in the particular case of the KS-type cancer invasion models under discussion. Subsequently, we introduce our grid structure in Section 6.2, discuss the practical implementation in Section 6.3 and the adaptation of the mesh to the numerical solution in Section 6.4. The assembly of the adaptive scheme is described afterwards in Section 6.5 with numerical experiments following in Sections 6.6 and 6.7.

The parts of this chapter concerned with the construction of the 1D scheme and the numerical experiments in Section 6.6 are based on [96]. The parts discussing the mesh administration and the numerical experiments in 2D are further based on [99].

6.1 Motivation

In the first numerical experiments that we presented in Section 5.11 we saw typical dynamics of KS-type cancer invasion models that feature the emerging, merging and movement of concentrations. In Figure 6.1 we demonstrate this behavior more clearly by focusing on the evolution of individual concentrations in the case of Experiment 1.

The presence and the dynamics of peaks in the concentrations provide a challenge for our numerical methods. While we could compute accurate numerical solutions in Experiment 1, this could only be achieved by our scheme using a large number of mesh cells in the range of 10^3. Thus, a significant computational effort is needed to obtain acceptable results. Since we saw similar phenomena in 2D in Experiment 3, we expect that a mesh with the same fine resolution in both space directions is needed to get qualitatively accurate numerical solutions for space dimension $d = 2$. A simulation for these needs would be unfeasible due to its immense computational costs.

Figure 6.2 shows what happens when lower mesh resolutions are used. Albeit the numerical method applied is second order accurate, the propagation speed of the invading tumor deviates from the propagation speed in the reference solution when using a coarse mesh. In the case of Experiment 1 the speed was overestimated using the IMEX3 method; in other settings we saw that the speed was underestimated on coarse grids [97]. This situation is particularly unfavorable when modeling and simulations are applied to estimate the progress of cancer invasion. The error propagation due to incorrect propagation speeds leads to an erroneous resolution of the emerging/merging phenomenon and thus to numerical solutions that are qualitatively incorrect in the invaded part of the computational domain.

We can moreover see in Figure 6.2 that problems due to coarse meshes emerge only locally in the neighborhood of high concentrations of cancer cells; at the largest part of the domain

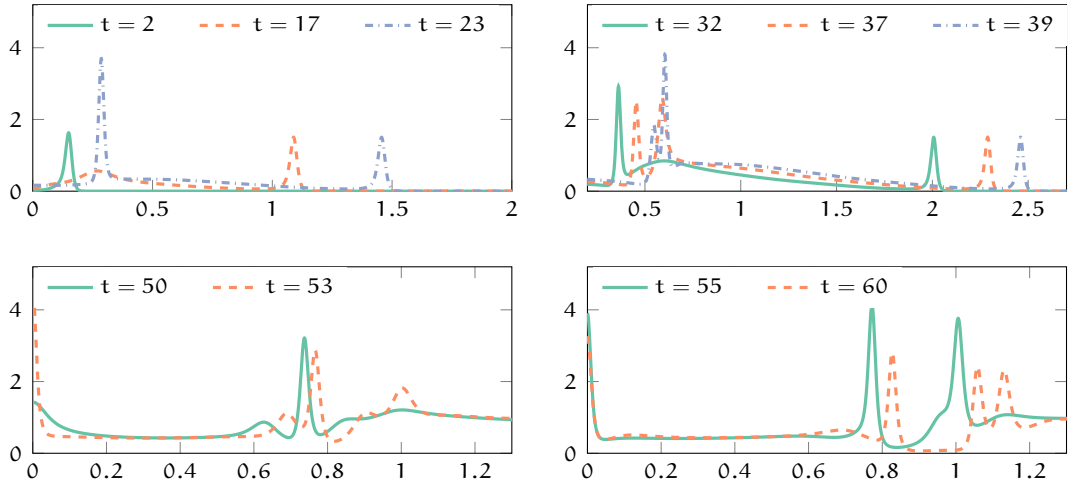

Figure 6.1: The spatio-temporal dynamics for $t \in [0, 60]$ in Experiment 1. We show closeups of the spatial cancer cell density in various time instances computed on a fine grid of $N = 5000$ mesh cells with the FVFD method (5.30) and IMEX3 time discretization. A second concentration emerges around $t = 23$ (top left). While $t \in [30, 40]$ a third concentration emerges and merges with an existing one (top right). Merging and emerging of concentrations continues while $t \in [50, 60]$ (bottom) [96].

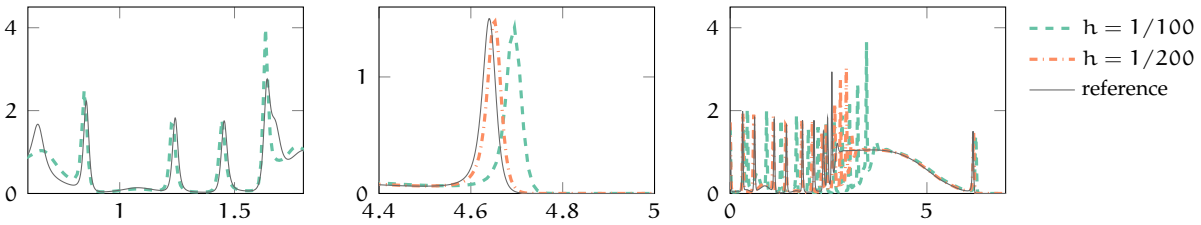

Figure 6.2: The cancer cell density in Experiment 1 computed with the FVFD-IMEX3 scheme on uniform finite volume meshes compared to a reference solution at time instances $t = 75$ (left, center) and $t = 100$ (right). Although many mesh cells were used in the simulations, there are significant deviations from the reference solution. These concern the propagation speed of the invading cluster of cancer cells (center) and the quality of the solution in the invaded area (left). The deviations increase as time evolves (right).

the solutions that we consider here are "smooth", cf. Figure 6.1, and a good numerical approximation is obtained when using only a small number of mesh cells. In this situation the application of an *adaptive mesh refinement* (AMR) method is a reasonable way to decrease the computational complexity while maintaining a high accuracy of the approximate solution. The AMR methods adapt the computational mesh to the numerical solution during the time evolution. This is done either by local refinement and coarsening of the mesh cells or by a complete mesh reconstruction that involves the shifting and deformation of mesh cells.

In the rest of this chapter we will develop a method that takes the approach of local refinement and coarsening by mesh cell bisection. This technique is sometimes referred to as *h-refinement*. Methods of this kind were successfully applied and analytically studied in the numerical approximation of several classes of PDEs [102, 140, 150]. To our knowledge though, the particular application to cancer invasion problems has not been considered prior to our work [96]. Note that we will also discuss a numerical method that shares some similarities with the second mentioned AMR approach of mesh reconstruction in Chapter 7.

6.2 Regularly structured meshes and other basic definitions

In this section we set the foundation for the description of our AMR method. Therefore, we introduce common relations between mesh cells and the class of meshes on which we will operate. For this purpose we rely on the definitions of finite volume meshes in 1D and 2D from Sections 5.1 and 5.4.

For simplicity, we introduce our concepts on either the unit interval or the unit square, $[0,1]^d$ for $d = 1, 2$. The adaptation to an arbitrary interval $[a, b]$ or rectangle $[a, b] \times [c, d]$ is a matter of basic affine mapping. We will apply our AMR method on particular structured meshes that are subsets of nested dyadic meshes. For their definition we assume a fixed integer $N_0 \in \mathbb{N}$.

Definition 6.1 (Dyadic meshes) For any $l \in \mathbb{N}_0$ we denote the uniform one-dimensional finite volume mesh (see Definition 5.1) on $\Omega = [0,1]$ with cell size $h = 1/[N_0\, 2^l]$ by $\mathbb{D}_l^1$. Analogously, we denote by $\mathbb{D}_l^2$ the quadrilateral finite volume mesh (see Definition 5.7) over the domain $\Omega = [0,1]^2$ with cell sizes $h^{[x]} = 1/[N_0\, 2^l]$, $h^{[y]} = 1/[N_0\, 2^l]$. We call $\mathbb{D}_l^d$ for $d = 1, 2$ the *dyadic mesh* of *refinement level* l.

In what follows we define particular relations between mesh cells that are included in dyadic meshes.

Definition 6.2 (Ancestors, descendants and neighbors) Let $l, \tilde{l} \in \mathbb{N}_0$ and $d \in \{1, 2\}$.

a) For every mesh cell $C \in \mathbb{D}_l^d$ we denote its *refinement level* by $L(C) = l$ and its *center* by $M(C) \in \Omega$.

b) A mesh cell $\tilde{C} \in \mathbb{D}_{l+1}^d$ is called *daughter cell* of mesh cell $C \in \mathbb{D}_l^d$ if $M(\tilde{C}) \in C$. Equivalently, the mesh cell C is called the *mother cell* of $\tilde{C}$. Daughter cells of the same mother cell are called *siblings*.

c) The mesh cell $\tilde{C} \in \mathbb{D}_{\tilde{l}}^d$ is a *descendant* of the mesh cell $C \in \mathbb{D}_l^d$ if there is a series of mesh cells in mother-daughter relation between C and $\tilde{C}$. In the same situation we say that C is an *ancestor* of $\tilde{C}$.

d) Two mesh cells $C_1 \in \mathbb{D}_l^d$ and $C_2 \in \mathbb{D}_{\tilde{l}}^d$, for which the intersection $\bar{C}_1 \cap \bar{C}_2$ is of co-dimension 1, are called *neighbors*. In the 2D case, this definition excludes cells that share a single point of their boundary. The common part of the boundaries between two neighbor cells is their *interface*.

We are now in the position to define the mesh objects on which we construct our AMR method.

Definition 6.3 (Regularly structured meshes) The set $M \subset \bigcup_{l=l_{min}}^{l_{max}} \mathbb{D}_l^d$ is called *Regularly structured mesh* (RSM) of dimension $d \in \{1, 2\}$ with *minimum and maximum refinement levels* $l_{min}, l_{max} \in \mathbb{N}_0$ satisfying $l_{min} < l_{max}$ and of *mesh regularity* $m_r \in \mathbb{N}$ if the following conditions are satisfied

a) For all $x \in [0,1]^d$ one of the two following conditions holds. Either
   i) $\exists!\, C \in M$ with $x \in C$ or
   ii) $\exists C \in M$ with $x \in \partial C$.

b) For all neighbor cells $C_1, C_2 \in M$ the *mesh regularity condition* holds

$$|L(C_1) - L(C_2)| \leqslant m_r. \tag{6.1}$$

The AMR method that we propose computes numerical solutions on such RSMs. After each time step the mesh is adapted in a suitable way to the current numerical solution and the current cell averages/point values are projected accordingly to the updated mesh. The mesh adaptation is conducted such that the adjusted RSM is still an RSM that has the same minimum and maximum refinement levels and mesh regularity as the original RSM before the mesh update.

For the update of a mesh M we will employ on the one hand *refinement*, which is the process of replacing C in M by all of its 2^d daughters from the level $L(C) + 1$. On the other hand we will use *coarsening*, which refers to the process of replacing C and all of its $2^d - 1$ siblings in M by their mother cell from the level $L(C) - 1$.

To abide by the minimum and maximum refinement levels and condition (6.1) the cells in M cannot be arbitrarily refined and coarsened. We will propose in Section 6.4 refinement and coarsening procedures that do not violate these restrictions.

We apply the mesh regularity condition (6.1) for reasons of efficiency and computational robustness. In more detail, it reduces the complexity of the mesh update procedures that we use and it results in better robustness of the overall AMR method as we will see in our numerical experiments. We use $m_r = 1$ throughout all our computations. We note that (6.1) together with $m_r = 1$ ensures the property (5.25) resulting hence in a computationally stable approximation of the diffusion terms on nonuniform 1D meshes according to (5.24). We will experimentally verify the benefit of using $m_r = 1$ in Section 6.6.

6.3 Navigation through the mesh

When dealing with finite volume methods on adaptive meshes, many technical issues arise. A prominent one is the organization of the mesh cells in suitable data structures. These structures should allow for a fast identification of mother, daughter, sibling and neighbor cells which is necessary for both manipulations in the mesh and flux computations. The complexity of the mesh organization increases significantly with the space dimension.

For the purpose of mesh organization *pointer based mesh data structures* are employed most commonly in the literature [18, 94]. In this approach the physical coordinates of the mesh vertices, i.e. interfaces in 1D and corners in 2D, are stored in the memory. Then the mesh cells are represented by arrays of pointers to these vertice objects. For our purpose however, we propose a simple technique that has less memory requirements. It is easy to implement and use, and it can handle mesh resolutions that are reasonable for our application to cancer invasion systems.

In more detail, we precompute a matrix containing all necessary information of the full cascade of dyadic meshes. Along with an identifier of the spatial position we store references to the daughter and mother cells for each mesh cell. In this section we provide technical details on the data structure in the 1D and 2D case. We will moreover explain how the structure is used to identify neighbors, ancestors and descendants. Throughout this section we assume $N_0 = 1$ for simplicity.

Mesh organization

When considering all the mesh cells $C \in \bigcup_{l=l_{min}}^{l_{max}} \mathbb{D}_l^1$, we note that every cell C can be uniquely identified by its center $M(C)$. This follows from the observation that each point in Ω that resides either on a cell center or an cell interface in $\mathbb{D}_l^d$ resides on a cell interface in $\mathbb{D}_{l+1}^d$. The center $M(C)$ of an arbitrary mesh cell in turn can be uniquely characterized by the level of refinement of the corresponding dyadic mesh together with an *intra-level index* k enumerating the cells in the current level.

Cell representation in 1D Due to the correspondence between mesh cells and cell centers, we can include the full cascade of one-dimensional dyadic discretization grids $\bigcup_{l=l_{min}}^{l_{max}} \mathbb{D}_l$ in the matrix

$$\mathcal{C} = \begin{pmatrix} | & | & | & | & | \\ k & l & m & d_l & d_r \\ | & | & | & | & | \end{pmatrix}, \tag{6.2}$$

where the lines represent the mesh cells. In each line we store the level of refinement l and the intra-level index k. The further entries m, d_l and d_r refer to the lines of the matrix in which the mother of the current cell and its left and right daughter cells are stored.

For example, the cascade of dyadic meshes $\bigcup_{l=0}^{3} \mathbb{D}_l^1$ would be encoded in the matrix

$$\mathcal{C} = \left(\begin{array}{c|cc|cccc|cccccccc} 1 & 1 & 2 & 1 & 2 & 3 & 4 & 1 & 2 & 3 & 4 & 5 & 6 & 7 & 8 \\ 0 & 1 & 1 & 2 & 2 & 2 & 2 & 3 & 3 & 3 & 3 & 3 & 3 & 3 & 3 \\ - & 1 & 1 & 2 & 2 & 3 & 3 & 4 & 4 & 5 & 5 & 6 & 6 & 7 & 7 \\ 2 & 4 & 6 & 8 & 10 & 12 & 14 & - & - & - & - & - & - & - & - \\ 3 & 5 & 7 & 9 & 11 & 13 & 15 & - & - & - & - & - & - & - & - \end{array}\right)^T \tag{6.3}$$

with the vertical lines separating the refinement levels of the mesh cells. The empty components imply that $\bigcup_{l=l_0^3} \mathbb{D}_l^1$ does neither include the mother cell of the single mesh cell in $\mathbb{D}_0^1$ nor the daughter cells of the mesh cells in $\mathbb{D}_3^1$.

Remark 6.4 (Memory usage in 1D) We consider a reasonable situation in the numerical simulation of cancer invasion systems and start on a coarse mesh $\mathbb{D}_{l_{min}=6}^1$ of 64 cells and assume that the resolution is coarser or equal to the resolution of the dyadic mesh $\mathbb{D}_{l_{max}=12}^1$ having 4096 cells. The matrix $\mathcal{C}$ in its formulation (6.2) would have $(2^6 + \cdots + 2^{12}) = 8128$ lines, accounting for all included levels $l = 6, \ldots, 12$ and 40640 (unsigned) integer valued entries. The memory needed to store $\mathcal{C}$ is (for 4 bytes per integer entry) approximately 163 KB.

Cell representation in 2D For computations in two space dimension we use four columns in the matrix $\mathcal{C}$ to account for all four children of a particular mesh cell, instead of two in the 1D case. Consequently, we obtain a matrix of the form

$$\mathcal{C} = \begin{pmatrix} | & | & | & | & | & | & | \\ k & l & m & d_{NW} & d_{NE} & d_{SW} & d_{SE} \\ | & | & | & | & | & | & | \end{pmatrix} \tag{6.4}$$

to represent all the mesh cells in $\bigcup_{l=l_{min}}^{l_{max}} \mathbb{D}_l^1$. As in (6.2) each line of $\mathcal{C}$ represents a particular mesh cell. Let us consider an arbitrary line corresponding to a particular mesh cell. The

intra-level index k identifies the position of this mesh cell with respect to a lexicographic order of the dyadic mesh in which the mesh cell is included. The entries d_{NW}, d_{NE}, d_{SW}, d_{SE} refer to the lines of $\mathcal{C}$ corresponding to the four daughters cells of the considered mesh cell. These daughter cells are located northwest (NW), northeast (NE), southwest (SW) and southeast (SE) relative to the center of the mesh cell. As in one dimension, l and m denote the refinement level and the line associated with the mother cell of our mesh cell.

Remark 6.5 (Memory usage in 2D) We assume a numerical computation that incorporates a cascade of grids where $l_{min} = 4$ and $l_{max} = 10$, i.e. the dyadic meshes ranges from 16×16 cells to 1024×1024 cells. In this case, the total number of inputs of the matrix $\mathcal{C}$ is 9786112 and with 4 bytes per input the memory needed is approximately 39 MB. This is not a strong constraint considering the high 2D resolution.

We note that we can significantly reduce the memory usage by eliminating the empty entries for a) the mother cells of the grid cells on the coarsest level l_{min} and b) the daughter cells of the mesh cells on the finest level l_{max}. In the above example 4194560 entries in $\mathcal{C}$ are empty and the actual needed memory used reduces to approximately 22 MB.

An even further reduction of the memory consumption can be achieved by removing the k- and l-column out of the matrix $\mathcal{C}$. The refinement level and the intra-level index can be easily recomputed on the fly in the following way. If i is the matrix line corresponding to a mesh cell, its level is given by the largest integer $l \geqslant l_{min}$ such that

$$k = i - \sum_{j=l_{min}}^{l-1} 2^{jd}$$

is positive. In this situation, the intra-level index is also given by k. For the example the needed memory reduces to approximately 11 MB when we use this technique.

Storing an RSM We assume fixed parameters l_{min}, l_{max} and d, which allow for a single computation of the matrix $\mathcal{C}$ in the beginning of a numerical computation. An RSM M is stored as an array of line indices of the matrix lines corresponding to the mesh cells included in M. To save most of the expenses of array truncations and prolongation when the mesh is updated, we use an array that starts with more entries than mesh cells, i.e. we use zero-entries that account for "empty mesh cells". In our numerical experiments we start with an array of $2^{d\, l_{max}/3}$ entries.

To store the numerical solution obtained by our FVFD scheme (5.35) we use a 2D array. The entry with indices i, j includes the approximate solution of the j-th system component in the mesh cell that is stored in the i-th entry of the mesh array.

Identification of relatives and neighbors

We consider a mesh cell C that is represented in the line i of the matrix $\mathcal{C}$. Then the information on its mother cell can be found in the line $m = \mathcal{C}_{i,3}$ and on its siblings in the entries $\mathcal{C}_{m,4}$ and $\mathcal{C}_{m,5}$ in 1D and in $\mathcal{C}_{m,4}, \ldots, \mathcal{C}_{m,7}$ in 2D.

Relative position To identify the relative position of a cell among its siblings, i.e. to find out whether it is a NW, NE, SE or SW daughter of the mother, we use the ordering with respect to the intra-level index k. In particular, in 2D a mesh cell is a south (S), north (N), west (W) or

east (E) *daughter* according to the rules

$$\begin{cases} \text{N daughter}, & \text{if } \lfloor \frac{k}{2^l} \rfloor \text{ is odd}, \\ \text{S daughter}, & \text{if } \lfloor \frac{k}{2^l} \rfloor \text{ is even} \end{cases} \quad \text{and} \quad \begin{cases} \text{W daughter}, & \text{if } k \text{ is odd}, \\ \text{E daughter}, & \text{if } k \text{ is even}, \end{cases} \tag{6.5}$$

where the floor operator $\lfloor \cdot \rfloor$ denotes the closest integer that is less or equal. We obtain the relative position among the siblings by combining both rules in (6.5).

Neighbors To efficiently identify the neighbors of a cell we make extensive use of the regularity of the mesh. We assume an RSM M of smoothness m_r and a cell $C \in G$ represented in the line i of the matrix $\mathcal{C}$ with refinement level $L(C) = l$ and intra-level index k. We can identify the neighbors by distinguishing between the following cases.

Neighbors of the same level The neighbors of C on the uniform mesh $\mathbb{D}_l^d$ can be easily identified by using the intra-level index k. Neighbors to the left and right in dimension one and to the W and E in dimension two, have intra-level indices $k \mp 1$. Neighbors to the S and N in dimension two have intra-level indices $k \mp 2^{l-1}$. Thus, neighbors of this kind are represented in the corresponding lines $i \mp 1$ and $i \mp 2^{l-1}$ of the matrix $\mathcal{C}$.

The *same level neighbors* are not necessarily included in the mesh M. Nevertheless the identification of these 2 cells in 1D or 4 cells in 2D is crucial in the neighbor finding process that we propose.

Neighbors of lower levels If N is a same level neighbor of C, but not part of the actual mesh, i.e. $N \notin M$, then an ancestor A of N could be included in the current mesh M. If there is such an ancestor $A \in M$, then A is also a neighbor of C due to the structure of the dyadic meshes. In order to find all possible neighbors, we check m_r generations of ancestors if they are included in the current mesh. These ancestors can be identified by iteratively using the mother cell entries m in the matrix C and by jumping to the corresponding line.

Neighbors of higher levels Again, let N be a same-level neighbor of the cell C. If neither N nor any of its ancestors is included in G, we look for neighbors of C among the descendants of N. Once again, m_r generations have to be screened.

In the algorithm that we propose for the identification of neighbors on higher levels, we exploit the relative position of N. Let us exemplary assume in the 2D case that N is a neighbor of C to the east, then we proceed as follows.

> We start with a queue containing only N. Then we iterate through the queue by checking each entry for being included or not in M. If it is included, we have found a neighbor, otherwise we add the NE and SE daughter of the entry to the cue for the next iteration step.

In this way the neighbors of C that are among the descendants of N can be found in at most $m_r + 1$ iteration steps.

For an efficient computation of all neighbors of a cell $C \in M$ we propose to compute all same level neighbors first and afterwards check the same level neighbors themselves, then their ancestors and last their descendants for being included in the grid M.

6.4 Mesh manipulation and data projection

In this section we discuss the mesh update steps in the proposed AMR method for cancer invasion systems. The mesh update consists of a sequence of refinement, coarsening and projection procedures which are used to adjust the mesh to the numerical solution.

Marking of mesh cells For the mesh update we employ a *monitor function* θ which depends on the current numerical solution and assigns values to the mesh cells. Two *thresholds* $\theta_{coars} < \theta_{refin}$ determine if a cell will be refined or coarsened. More precisely, a mesh cell C_c with $L(C_c) > l_{min}$ where the monitor function is below the coarsening threshold, i.e. $\theta(C_c) < \theta_{coars}$, is marked for coarsening. A cell C_r with $L(C_r) < l_{max}$, where the monitor function is above the refinement threshold, i.e. $\theta(C_r) > \theta_{refin}$, is marked for refinement. For the monitor functions, which we will use in the numerical experiments, we refer to Sections 6.5 and 6.7.

As pointed out in Section 6.2, the updated mesh should preserve the RSM properties of the former mesh, i.e. its minimum and maximum level of refinement and the regularity condition (6.1). To this end the set of cells in M that are marked for refinement and coarsening has to be further modified before the actual mesh adaptation takes place. For this purpose we develop the *strong refinement* and *weak coarsening* procedures discussed in the following paragraphs.

Strong refinement The primary aim of the AMR method is to increase accuracy of the numerical solution. Thus, the refinement of mesh cells has a high priority. For this reason we strictly refine all the cells that are marked for refinement and possibly even more to preserve the RSM properties. For efficiency though we do not refine more cells than needed.

In more detail, let $S_r \subset M$ denote the set of cells that are marked for refinement by the monitor function. Moreover, let $M_{ref(S_r)}$ denote the mesh M where all cells $C \in S_r$ have been refined, i.e. replaced by their daughter cells. In general $M_{ref(S_r)}$ is an RSM with the same maximum and minimum refinement levels as M, however the mesh regularity condition (6.1) might be violated. We define for each cell $C \in S_r$ the *dependency set* $D_R(C)$ to be the set of minimal cardinality such that $M_{ref(D_R(C))}$ satisfies (6.1). Then the *strong refinement set* that includes the cells that are actually refined is formally given by

$$S_R = \bigcup_{C_r \in S_r} D_r(C_r) \supset S_r.$$

In practice we conduct the strong refinement by iterating through the cells that are marked for refinement. We iterate from the maximal to the minimal refinement level and mark additional neighbor cells for refinement that would otherwise violate (6.1). For more details we refer to Algorithm 1.

Weak coarsening The coarsening in the AMR method increases the efficiency by locally reducing the resolution wherever only a minor impact of lower accuracy is expected. The first priority of the mesh update though remains the refinement to locally increase the mesh resolution. In order to prevent conflicts with the strong refinement we allow for the coarsening of fewer cells than initially marked. We will see in the numerical experiments in Sections 6.6 and 6.7 that the proposed strategy leads to a reasonable coarsening in practice.

We denote the set of mesh cells that are marked for coarsening by $S_c \subset M$. Further, by $M_{coar(S_r)}$ we refer to the modified mesh M where all cells $C \subset S_r$ have been coarsened,

Algorithm 1: Strong refinement. The mesh cells that are marked for refinement are sorted by their refinement level in $S_{l_{min}}, \dots, S_{l_{max}}$ making a fast iteration from high level cells to lower level cells possible. The sorted iteration identifies conflicts due to the mesh regularity conditions and efficiently adds involved neighbor cells to the refinement set.

Input: the current mesh M^{old}, the current numerical solution $\mathbf{w}_h^{old}$
initialize the new mesh, $M^{new} \leftarrow M^{old}$;
initialize $S_{l_{min}}, \dots, S_{l_{max}} \leftarrow \emptyset$;
for $C \in M^{old}$ **do**
  if $\theta(C) > \theta_{refin}$ *and* $L(C) < l_{max}$ **then** $S_{L(C)} \leftarrow S_{L(C)} \cup \{C\}$;
end
for $l = l_{max} - 1, \dots, l_{min} + m_r$ **do**
  for $C \in S_l$ **do**
    compute the set of neighbors of C, $N(C)$;
    for $C_N \in N(C)$ **do**
      if $l - L(C_N) = m_r$ *and* $C_N \notin S_{l-m_r}$ **then** $S_{l-m_r} \leftarrow S_{l-m_r} \cup \{C_N\}$;
    end
  end
end
for $C \in S$ **do**
  identify the daughters of C, $D(C)$;
  $M^{new} \leftarrow M^{new} \backslash \{C\}$;
  $M^{new} \leftarrow M^{new} \cup D(C)$;
  project the numerical solution from $\mathbf{w}_h^{old}|_C$ to $\mathbf{w}_h^{new}|_{D(C)}$;
end
Output: the refined mesh M^{new}, the updated numerical solution $\mathbf{w}_h^{new}$

i.e. replaced by their mother cell. We note that $M_{coar(S_r)}$ does only include mesh cells of refinement levels between l_{min} and l_{max} with regard to M. However, $M_{coar(S_r)}$ might not be an RSM. An obvious reason for that is a possible violation of (6.1), which can occur in the refinement. One further obtains a problem when a mesh cell is marked for coarsening but there is at least one sibling cell that is not. In fact there might be even sibling cells of marked mesh cells that are not even included in the mesh M which lead to a similar problem.

As done in the case of strong refinement we can set forth a formal description of the coarsening set M_C that we employ in the weak coarsening. To this end let the dependency set $D_c(C)$ for each mesh cell $C \in S_c$ denote the set of minimal cardinality such that $M_{ref(D_R(C))}$ is an RSM that satisfies especially (6.1). Then we define the *weak coarsening set* as

$$S_C = \{C_c \in M_c : \quad D_c(C_c) \subseteq M_c\}.$$

We refer to Algorithm 2 for our implementation of the weak coarsening in practice. The procedure features an iteration through the set of marked cells from the maximal to the minimal levels of refinement as it was used in Algorithm 1. Neighbors that cause conflicts of the mesh regularity in the process provoke a removal of mesh cells from the coarsening set.

Mesh update The mesh update consists of a sequence of strong refinement and weak coarsening procedures. In more detail, we initially fix the parameters $n_{ref}, n_{coars} \in \mathbb{N}$. In the mesh update, which takes place after each time evolution of the numerical solution, we first

Algorithm 2: Weak coarsening. The marked mesh cells are sorted by their refinement levels in $S_{l_{min}}, \dots, S_{l_{max}}$. The iteration from higher to lower level cells prevents conflicts due to changes in the refinement sets.

Input: the current mesh M^{old}, the current numerical solution $\mathbf{w}_h^{old}$

1 initialize the new mesh $M^{new} \leftarrow M^{old}$;
2 initialize the new numerical solution $\mathbf{w}_h^{new} \leftarrow \mathbf{w}_h^{old}$;
3 initialize $S_{l_{min}}, \dots, S_{l_{max}} \leftarrow \emptyset$;
4 **for** $C \in M$ **do**
5 | **if** $\theta(C) < \theta_{coars}$ *and* $L(C) > l_{min}$ **then** $S_{L(C)} \leftarrow S_{L(C)} \cup \{C\}$;
6 **end**
7 **for** $l = l_{max}, \dots, l_{min} + 1$ **do**
8 | **for** $C \in S_l$ **do**
9 | | identify the set of siblings of C, $Sib(C)$;
10 | | **if** $Sib(C) \not\subset S_l$ **then**
11 | | | $S_l \leftarrow S_l \backslash \{Sib(C)\}$;
12 | | | **continue** for loop in line 8;
13 | | **end**
14 | | **if** $l < l_{max} - m_r$ **then**
15 | | | compute the set of neighbors of C, $N(C)$;
16 | | | **for** $C_N \in N(C)$ **do**
17 | | | | **if** $L(C_N) - l = m_r$ *and* $C_N \notin S_{l+m_r}$ **then**
18 | | | | | $S_l \leftarrow S_l \backslash \{Sib(C)\}$;
19 | | | | | **continue** for loop in line 8 ;
20 | | | | **end**
21 | | | **end**
22 | | **end**
23 | | identify the mother cell of C, C_M;
24 | | $M^{new} \leftarrow M^{new} \backslash Sib(C)$;
25 | | $M^{new} \leftarrow M^{new} \cup \{C_M\}$;
26 | | project the numerical solution from $\mathbf{w}_h^{old}|_{Sib(C)}$ to $\mathbf{w}_h^{new}|_{C_M}$;
27 | **end**
28 **end**

Output: the coarsened mesh M^{new}, the updated numerical solution $\mathbf{w}_h^{new}$

conduct n_{ref} successive strong refinement procedures and n_{coars} successive weak coarsening procedures afterwards. In practice we obtained good results using mostly $n_{ref} = n_{coars} = 1$. To improve the efficiency we store the values of the monitor function in memory and recompute them only in cells that are affected by previous changes in the mesh.

Projection of the numerical solution

Each change in the mesh structure necessitates a suitable projection of the numerical solution between the old and the modified mesh. In what follows we discuss this step within the proposed refinement and coarsening procedures in more detail.

We assume to this end a given numerical solution $\mathbf{w}_h^{old}$ on the mesh M^{old}. After either

strong refinement or weak coarsening has delivered a modified mesh M^{new} we refer to the numerical solution projected to this mesh as $\mathbf{w}_h^{new}$. We consider the solution in a fixed time instance and have thus dropped the time dependence in the notation. For clarity of the presentation we denote the vector including the cell averages and midpoint values of the old and new numerical solution at the cell C by $\mathbf{w}_h^{old}(C)$ and $\mathbf{w}_h^{new}(C)$, respectively.

Projection to lower levels In the weak coarsening procedure, see Algorithm 2, we are confronted with the following situation: there are 2^d sibling cells gathered in the set $Sib \subset M^{old}$ which are replaced by their mother cell $C_M \in M^{new}$. We project the corresponding numerical solution by averaging via

$$\mathbf{w}_h^{new}(C_M) = \frac{1}{2^d} \sum_{C_S \in Sib} \mathbf{w}_h^{old}(C_S). \tag{6.6}$$

This step corresponds to line 28 in Algorithm 2. We note that projection (6.6) does not introduce an additional error to the AMR method.

Projection to higher levels The projection step in the strong refinement procedure is more delicate and subject to a loss of accuracy. Assume the situation of line 22 of Algorithm 1, i.e. there is a given mother cell $C_M \in M^{old}$ that is to be replaced by its daughter cells collected in the set $D(C_M) \subset M^{new}$.

In the case $d = 2$ we will consider only the *trivial projection*

$$\mathbf{w}_h^{new}(C_D) = \mathbf{w}_h^{old}(C_M), \quad C_D \in D(C_M) \tag{6.7}$$

that maps the numerical solution on the mother cell C_M to the numerical solution on its daughter cells $C_D \in D(C_M)$ without any further modification.

For $d = 1$ we will study an AMR method of higher order which requires a more elaborate projection method. In more detail, we employ a second order mass conservative polynomial reconstruction: consider on the mesh M^{old} the mother cell $C_i = C_M$ and its neighbor cells to the left and to the right C_{i-1} and C_{i+1}. We consider the reconstruction polynomial $\mathbf{r}_i(x) = \mathbf{a}_i + \mathbf{b}_i x + \mathbf{c}_i x^2$ that satisfies

$$\int_{C_{i-1}} \mathbf{r}_i(x)\,dx = \mathbf{w}_h^{old}(C_{i-1}), \quad \int_{C_i} \mathbf{r}_i(x)\,dx = \mathbf{w}_h^{old}(C_i), \quad \int_{C_{i+1}} \mathbf{r}_i(x)\,dx = \mathbf{w}_h^{old}(C_{i+1}).$$

For the left and the right daughter cells $C_l, C_r \in D(C_i) \subset M^{new}$ we project the numerical solution via

$$\mathbf{w}_h^{new}(C_l) = \int_{x_{i-1/2}}^{x_i} \mathbf{r}_i(x)\,dx, \quad \mathbf{w}_h^{new}(C_r) = \int_{x_i}^{x_{i+1/2}} \mathbf{r}_i(x)\,dx. \tag{6.8}$$

We note that a closed form of (6.8) can be easily derived by basic algebra and polynomial integration, which leads to negligible computational costs in practice. The benefit of such a data reconstruction by a second order polynomial is that discrete differential operators of first and second order such as those employed in the FVFD scheme yield consistent approximations in refined areas. Therefore, we expect no instabilities due to the refinement when using (6.8).

Note that care has to be taken when using a reconstruction such as (6.8) in line 22 of Algorithm 1. It is advisable to keep a copy of the previous numerical solution $\mathbf{w}_h^{old}$ throughout the algorithm in order to be able to reconstruct with respect to the numerical solution of the neighbor cells on the old mesh M^{old}. If one reconstructs instead with respect to the temporary representation $\mathbf{w}_h^{new}$ on M^{new}, inaccuracies may arise due to stored densities of the neighbor cells that originate from a previous reconstruction.

6.5 The AMR method

In this section we present the full AMR method for a cancer invasion problem. We consider here the 1D case where we can employ the nonuniform FVFD scheme equipped with an appropriate time integration method for the time update part of the method. To adapt the mesh to the numerical solution we use the algorithms introduced in the previous section. We will also comment on an adaptation to 2D.

Model and numerical method We apply the AMR method in space dimension $d = 1$ to model (I). The uPA model is well established in the literature and we already constructed the corresponding numerical scheme in Chapter 5. In the case of a uniform mesh its accuracy and efficiency were verified in Section 5.11. The derived scheme is also capable of handling RSMs in 1D; for this setting we formulated the elements of the method on nonuniform meshes in Section 5.3, see also the remarks in Section 5.5. The nonuniform version of (5.30) in 1D is the semi-discrete scheme that we apply in the AMR method. For the time integration we choose the STRANG scheme (5.46) that delivered accurate and nonnegative results in our numerical experiments in Section 5.11.

Monitor functions We test three different criteria that drive the refinement and coarsening of the mesh cells. More precisely, we will apply three monitor functions that we define in this paragraph. We employ only one monitor function in each simulation. Let $\mathbf{w}_h$ denote a numerical solution at a fixed time instance with dropped time index, given with all of its components on a finite volume mesh $M = \{C_1, \dots, C_N\}$. We consider especially the cancer cell density that is given by the discrete cell averages $c_1, \dots, c_N$.

The first monitor functions that we employ takes the discrete gradient of the cancer cell concentration into account and reads

$$\theta(C_i) = \max\left\{\left|2\frac{c_{i+1} - c_i}{h_{i+1} + h_i}\right|, \left|2\frac{c_i - c_{i-1}}{h_i + h_{i-1}}\right|\right\}. \tag{6.9a}$$

The second monitor function considers another geometrical attribute of the numerical solution, namely its discrete local variation

$$\theta(C_i) = \max\{|c_{i+1} - c_i|, |c_i - c_{i-1}|\}, \tag{6.9b}$$

and the third monitor function is based on a hierarchical error estimator of the discretized propagation speeds

$$\theta(C_i) = \max\left\{\left|a_{i-1/2} - a^{\text{low}}_{i-1/2}\right|, \left|a_{i+1/2} - a^{\text{low}}_{i+1/2}\right|\right\}, \tag{6.9c}$$

where $a_{i\pm1/2}$ is computed using the nonuniform central differences (5.26), see the remarks in Section 5.5. We estimate the corresponding discretization error by comparing with the first order approximation

$$a^{\text{low}}_{i+1/2} = 2\chi_v \frac{v_{i+1} - v_i}{h_i + h_{i+1}} + 2\chi_u \frac{u_{i+1} - u_i}{h_i + h_{i+1}} + 2\chi_p \frac{p_{i+1} - p_i}{h_i + h_{i+1}}.$$

Our numerical experiments indicated that geometric estimators as (6.9a) and (6.9b) are more robust and problem independent than the model-driven estimator (6.9c), see also [12, 102, 140, 150].

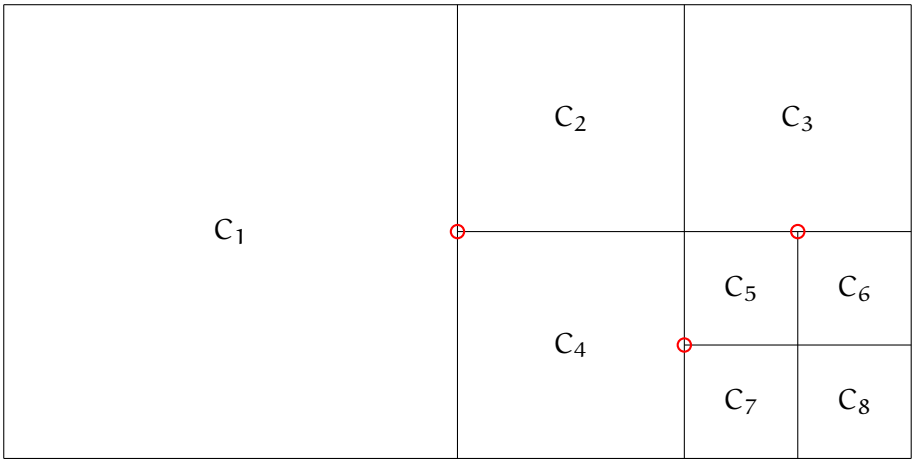

Figure 6.3: Excerpt of an RSM in 2D with $m_r = 1$. Mesh cells of three different refinement levels are included. The red circles indicate the hanging nodes.

Mesh initialization At the beginning of the AMR scheme we prescribe a uniform computational grid equal to the dyadic mesh on the prescribed minimal refinement level, i.e. $M \leftarrow \mathbb{D}^1_{l_{min}}$. We assume analytically given initial conditions that we evaluate over this mesh. Before we start the time evolution we adjust the mesh to the initial data using the chosen monitor function and a series of strong refinement steps defined in Algorithm 1. In this initial refinement we do not project the numerical solution as discussed in Section 6.4. Instead, we reevaluate the analytical initial function with respect to the updated mesh M^{new} to obtain the suitable representation of the initial data $\mathbf{w}_h^{new}$. We apply $n_{ref,0}$ strong refinement operations in the initial refinement, where the parameter $n_{ref,0}$ is chosen larger than the corresponding parameter n_{ref} in the usual mesh updates.

Time evolution by the AMR scheme Our proposed AMR scheme alternates between the manipulation of the grid and the time evolution of the numerical solution. Thus, after the computation of each time step by the FVFD-STRANG scheme (5.30), (5.46) a mesh update is conducted starting with a strong refinement step. In this way, we iterate until the final time of computation is reached. In the projection step we employ the polynomial reconstruction (6.8). We refer to Algorithm 3 for a description of the complete AMR method.

Adaptation to 2D An adaptation of the 2D FVFD scheme to nonuniform RSMs requires more elaborate techniques. Most prominently, the scheme must be able to deal with *hanging nodes* shown in Figure 6.3. We do not consider the full implicit-explict FVFD scheme in the AMR method but propose instead a simple explicit scheme of first order in space for $d = 2$ that we will describe in Section 6.7 . Except for the time evolution step the 2D AMR method will be structured as its 1D counterpart in Algorithm 3.

6.6 Numerical experiments in 1D

In this section we investigate the AMR method introduced in the previous section experimentally. All numerical computations were conducted using MATLAB.

For our numerical study we used again Experiment 1 from Section 5.11. In more detail, we considered the domain $\Omega = (0, 5)$ and set the mesh update parameters $n_{ref} = 1$, $n_{coars} = 1$,

Algorithm 3: The AMR method in 1D for system (I). We alternate between time integration by the numerical scheme (5.30), (5.46) and mesh adaptation. Refer to Algorithms 1 and 2 for the strong refinement and weak coarsening procedures.

initialize uniform grid $M \leftarrow \mathbb{D}^d_{l_{min}}$;
extract initial data $\mathbf{w}_h(0)$ from given analytical initial condition;
for $k = 1, \dots, n_{ref,0}$ **do** strong refinement update of $(M, \mathbf{w}_h(0))$ using the analytical initial condition ;
$t \leftarrow 0$;
while $t < T$ **do**
    Conduct one time step by the FVFD-STRANG scheme (5.30), (5.46) using the numerical data $\mathbf{w}_h(t)$ on the mesh M to obtain τ and $\mathbf{w}_h(t+\tau)$;
    $t \leftarrow t + \tau$;
    for $k = 1, \dots, n_{ref}$ **do** strong refinement update of $(M, \mathbf{w}_h(t))$;
    for $k = 1, \dots, n_{coars}$ **do** weak coarsening update of $(M, \mathbf{w}_h(t))$;
end

$n_{ref,0} = 3$ such as the refinement levels of the AMR method $l_{min} = 0$, $l_{max} = 3$. Instead of varying the limits of the refinement levels l_{min} and l_{max} we altered the number of mesh cells on level 0, N_0 to study the performance of the AMR method. Wherever not otherwise stated we used mesh regularity $m_r = 1$.

We consulted again the reference solution computed by the method of Dormand and Prince [45] on a uniform mesh with 30 000 cells, see Section 5.11. To explain the error computation we assume that the AMR method with fixed $N_0 \in \mathbb{N}$ delivered the RSM $M(N_0, t^n) = \{C_1, \dots, C_N\}$ with cell sizes $h_1, \dots, h_N$ and approximate cancer cell densities $c_1^n, \dots, c_N^n$ as part of the numerical solution $\mathbf{w}_h(t^n)$ at the time instance t^n. Then we define $c_i^{n,\mathrm{ref}(M(N_0,t^n))}$ to be the approximate cancer cell density of the reference solution at time instance t^n projected to the cell C_i as in projection (5.63). We can now define the discrete L^1 error

$$E(N_0, t^n) = \sum_{i=1}^{N} h_i |c_i^n - c_i^{n,\mathrm{ref}(M(N_0,t^n))}| \tag{6.10}$$

that depends on the initial number of mesh cells N_0 and the time instance t^n.

We conducted Experiment 1 using three variations of the AMR method that employed one of the monitor functions (6.9a), (6.9b), (6.9c) each. In the case of the gradient monitor (6.9a) we applied the thresholds $\theta_{ref} = 10$ and $\theta_{coars} = 2.5$. For the estimated discretization error of the propagation speeds (6.9c), henceforth referred to as error based monitor, we used the thresholds $\theta_{ref} = 2 \times 10^{-5}$ and $\theta_{coars} = 1.25 \times 10^{-7}$, whereas $\theta_{ref} = 1.25\, N_0$ and $\theta_{coars} = 0.25\, \theta_{ref}$ were chosen for the variation monitor (6.9b). We emphasize the dependence on the initial count of cells in the thresholds for the variation monitor.

In Figure 6.4 we show the numerical solution of system (I) in Experiment 1 over an adaptive grid. We used the AMR method and the gradient of c as monitor function for the computation. The adjustment of the mesh to the geometry of the solution can be seen by the sizes of the computational cells that vary over the spatial domain.

To compare the performance of the three tested AMR methods among each other and also with the uniform FVFD-STRANG method (5.30), (5.46) we analyzed the relation between the average number of cells and the L^1 errors given by (6.10) at the fixed time instance $t = 50$.

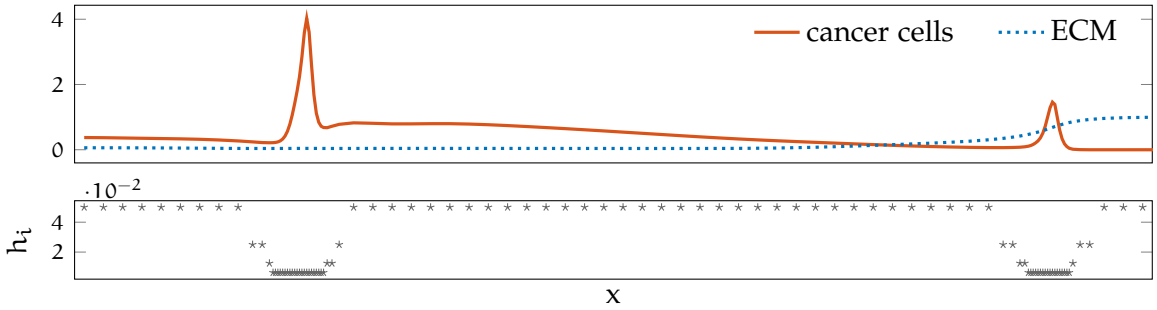

Figure 6.4: The spatial distribution of cancer cells and ECM density at time instance $t = 41$ in Experiment 1 computed by the AMR method with monitor function (6.9a) (top) and the sizes of the computational cells at the corresponding positions in space (bottom). The mesh is locally refined at areas of large gradients of the cancer cell density c [96].

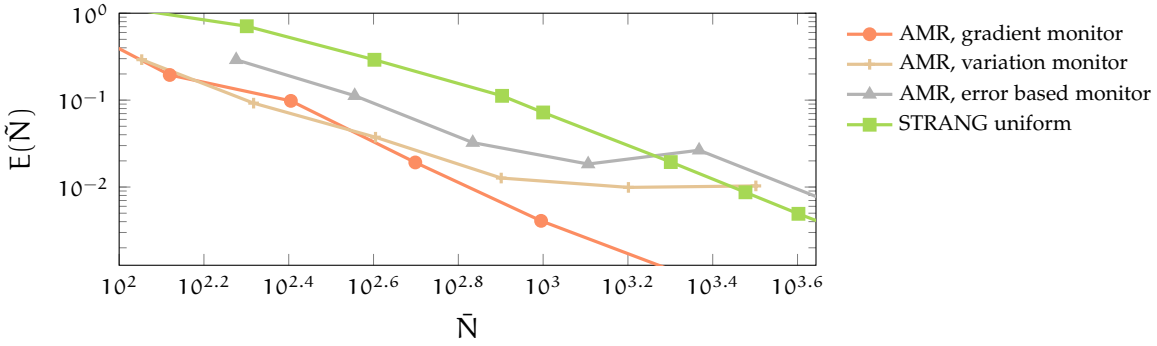

Figure 6.5: Experimental convergence with respect to the average number of cells of three AMR methods and the uniform scheme in Experiment 1 at the time instance $t = 50$. We computed the error $E(\bar{N})$ according to (6.10) for various N_0. The gradient monitor based AMR method is the most efficient of the four methods [96].

When performing the time step $t^k \to t^{k+1}$ with an AMR method, let the number of mesh cells included in the mesh $M(t^k)$ be given by $N_k = |M(t^k)|$. Then we define the *average number of mesh cells* by $\bar{N}(t^n) = \frac{1}{t^n}\sum_{k=0}^{n} N_k \tau_k$. The average number of cells in the uniform method is obviously equal to $N = 1/h$.

In Figure 6.5 we present the resulted experimental convergence of the discrete L^1 errors (6.10) for $t = 50$ with respect to the average number of cells. We computed the errors for $N_0 \in \{50, 100, 200, 400, 800, 1600\}$ in the AMR methods and for $N \in \{100, 200, 400, 800, 1000, 2000, 3000, 4000\}$ in the uniform method. As the average cell-number raises (up to $\bar{N} = 2000$) all three AMR methods outperform the uniform method, with the gradient based one being most efficient. Even on very fine grids, the gradient based AMR scheme yields lower errors than the uniform method. Both the gradient and the error based refinement methods converge.

It is interesting to study the error evolution with respect to the dynamics that the numerical solution resolves. In Figure 6.6 we display the time evolution of the error (6.10) for the three AMR methods starting with an initial mesh of $N_0 = 400$ cells on level 0. Along we present the same error evolution for the uniform FVFD STRANG method on 2000 and 3000 mesh cells. When the second peak in the solution around $t = 20$ is formed, see Figure 6.1, the error of the uniform method with $N = 2000$ mesh cells becomes larger than the error of all three tested AMR methods albeit the AMR methods employed significantly less mesh cells, as can be seen in the legend of Figure 6.6. Employing the discretization errors in monitor functions seems to be beneficial since the error of the corresponding AMR method is for all times $t \leqslant 35$ less

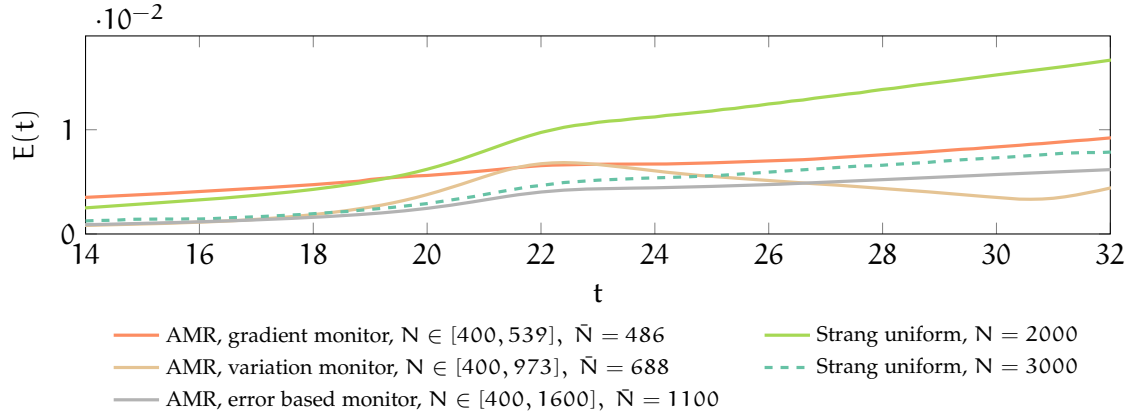

Figure 6.6: Time evolution of the error (6.10) for three AMR methods compared with two uniform solutions in Experiment 1 for $t \leqslant 32$. The legend shows the number of computational cells (range and average) that the methods employed. The AMR methods exhibit smaller errors than the uniform ones while employing fewer mesh cells [96].

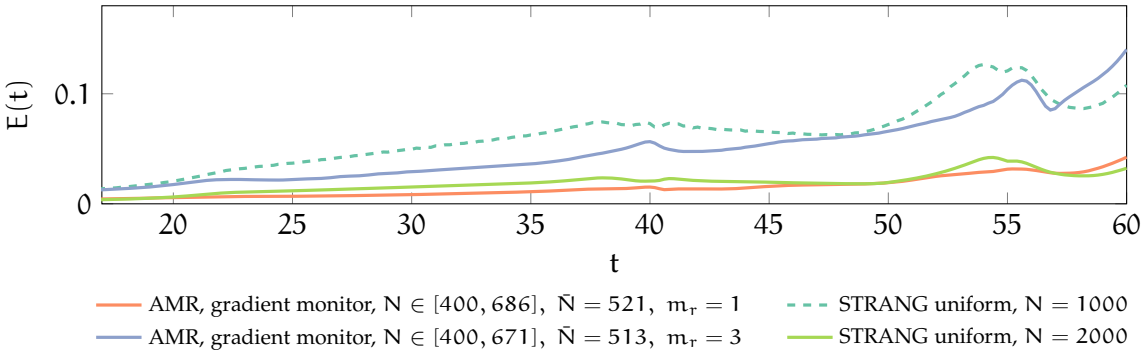

Figure 6.7: Time evolution of the error (6.10) of two gradient based AMR methods and two uniform solutions in Experiment 1 for $t \in [0, 60]$. The legend shows the number of computational cells (range and average) that the methods employed. The AMR method that uses a very regular mesh ($m_r = 1$) is more efficient than the less restrictive AMR method ($m_r = 3$) while both use approximately the same number of mesh cells [96].

than the error of the uniform solution on 3000 cells. Note that this method used only 1100 cells in average. The variation based AMR method also outperforms the uniform method on 3000 cells except in the time of emergence of the second peak. The error of the gradient based AMR method follows a straight linear increase in time that does not seem to be affected by sudden dynamics of the cancer cell density in the solution. In this way, its temporal error approaches the error curve of the uniform method on 3000 cells for increasing t while the method did not employ more than 540 mesh cells.

The gradient monitor based AMR method performed very well in both error comparisons. In a final test we demonstrate the advantage of restricting this method to an RMS with the mesh regularity condition (6.1) with $m_r = 1$. To this end we present the error evolution of the gradient based AMR method using $N_0 = 400$ with $m_r = 1$ and $m_r = 3$ during $t \in [0, 60]$ in Figure 6.7. The choice $m_r = 3$ can be understood as a restriction in the refinement level which is only due to the minimum and maximum refinement level l_{min} and l_{max}. Similarly as in Figure 6.6, we compare the solutions of the AMR schemes with uniform solutions for $N \in \{1000, 2000\}$. The AMR method that employed a more regular RSM ($m_r = 1$) approaches the accuracy of the uniform method using 2000 mesh cells even for large t. On the contrary,

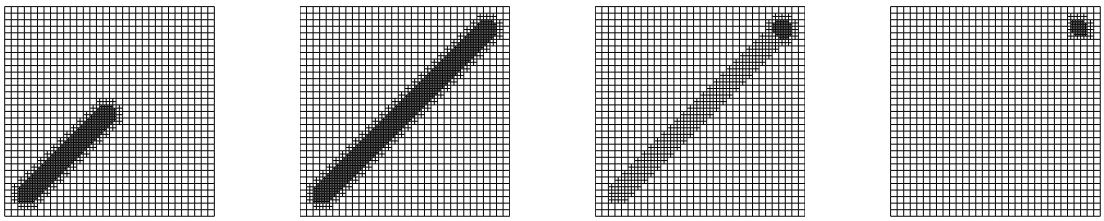

Figure 6.8: Diagonal movement of the monitor function (6.11a) driving the refinement of an RSM. We present an intermediate time instance (first), the final time instance (second), the final time instance plus one step of weak coarsening (third) and the final time instance plus two steps of weak coarsening (forth) [99].

the less restrictive AMR method ($m_r = 3$) is closer to the uniform solution on 1000 mesh cells. One can further see that the mesh regularity condition (6.1) in combination with $m_r = 1$ increases the average number of cells only slightly by 12 compared to the less restrictive AMR method. Thus, the condition (6.1) does not increase the computational costs significantly. Moreover, the dynamics of the solution, as, e.g., the first process of merging concentrations around $t = 40$, see Figure 6.1, have a smaller impact on the error of the AMR method when using the more regular mesh.

6.7 Numerical experiments in 2D

Two-dimensional AMR methods are significantly more complex than their one-dimensional counterparts. The hanging nodes or equivalently the presence of multiple neighbor cells of a given mesh cell in a single space direction, as shown in Figure 6.3, require a mesh administration technique like the one we introduced in Section 6.3. To test the proposed algorithms in 2D we start this section with generic proofs of concept for the mesh administration technique, the strong refinement and the weak coarsening. Afterwards we study an application to a cancer invasion problem for which we construct a simple explicit method of first order. All numerical computations were conducted using the programming language Fortran 2008.

Proof of concept

For a first test we used a 2D RSM determined by the parameters $l_{min} = 5,\ l_{max} = 7,\ N_0 = 1$ and mesh regularity $m_r = 1$. As in the 1D AMR Algorithm 3 we started on a uniform mesh on the lowest level, i.e. $M \leftarrow \mathbb{D}_5^2$. To enforce a dynamical mesh evolution we considered the time dependent monitor function

$$\theta_1(t) = \exp(-100\,|x - (0.1 + t)(1,\ 1)|^2). \tag{6.11a}$$

We set the small time step $\tau = 0.005$ and, starting by $t = 0$, we alternated between performing the strong refinement and updating the current time by $t \leftarrow t + \tau$ until $t = 0.8$ was reached. We employed the refinement threshold $\theta_{ref} = 0.8$.

The adapted mesh that we obtained in this process is shown in Figure 6.8 at the time instances $t = 0.4$ and $t = 0.8$. Temporal movement of the Gaussian monitor function leaves a trace on the grid. On the diagonal of the square domain where the Gaussian moves, the cells are refined to the maximal refinement level $l = 7$. Mesh cells of level 6 occur only in the transition to the coarser grid and are a result of the mesh regularity condition (6.1).

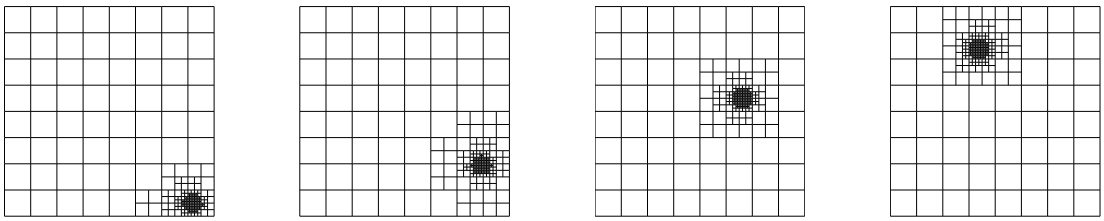

Figure 6.9: Circular movement of the monitor function (6.11b) in time drives the mesh updates. The equal refinement and coarsening thresholds employed lead to an instantaneous adjustment of the mesh to the monitor function [99].

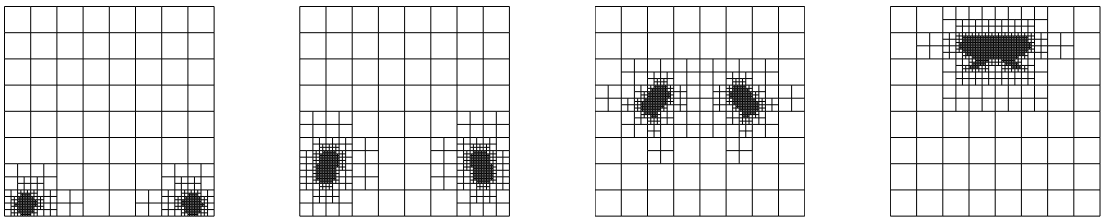

Figure 6.10: The mesh updates are driven by two concentrations in the moving monitor functions. The tails are caused by distinct refinement and coarsening thresholds [99].

After the time evolution and refinement iteration, we coarsened the mesh again two times using $\theta_{\text{coars}} = 0.8$ but kept the time constant at $t = 0.8$. In Figure 6.8 we show the mesh after each weak coarsening procedure. The trace of the movement is completely coarsened having performed the second coarsening. Thus, we see that few weak coarsening procedures are sufficient to obtain a good adjustment of the mesh to the monitor function.

In a second test we considered coarsening in every time step analog to Algorithm 3. To this end we assumed 2D RSM with $l_{\min} = 3$ and $l_{\max} = 7$ and mesh regularity $m_r = 1$. We started again with a uniform mesh on the lowest level, $M \leftarrow \mathbb{D}_3^2$, and considered two time dependent monitor functions

$$\theta_2(t) = \exp(-100\,|x - 0.9(\cos(0.5\,\pi t),\, \sin(0.5\,\pi t))|^2), \tag{6.11b}$$

$$\theta_3(t) = \exp(-100\,|x - 0.9(\cos(\pi(1 - 0.5\,t)),\, \sin(\pi(1 - 0.5\,t)))|^2) + M_2(t). \tag{6.11c}$$

We conducted a similar procedure as in the first test using the time step size $\tau = 0.005$: we started with $t = 0$ and conducted strong refinement first, weak coarsening second, a time update $t \leftarrow t + \tau$ third and iterated this process.

In Figure 6.9 we present snapshots of the mesh obtained in this process for monitor function θ_2 and $\theta_{\text{ref}} = \theta_{\text{coars}} = 0.8$. Opposed to the results of the first test in Figure 6.8 we can see that the circular movement of the Gaussian monitor is not memorized by the mesh. At each time instance the mesh structure allows to draw conclusions about the monitor function. Moreover, the mesh regularity (6.1) leads to a stepwise decrease of the cell levels when moving away from the center of the Gaussian of the monitor function. The center itself is refined to the maximal refinement level.

When considering the monitor function θ_3 together with the thresholds $\theta_{\text{ref}} = 0.8$, $\theta_{\text{coars}} = 0.3$ we obtained a certain memory effect of the mesh structure in the form of tails which followed the two traveling Gaussians of the monitor function. This can be seen in the corresponding adapted meshes shown in Figure 6.10. The appearance of the tails in this

experiment is caused by the distinct choices of the refinement and coarsening thresholds as can be seen when comparing with Figure 6.9. The tails represent a delay of the mesh adaptation which might be beneficial in the numerical simulations of fast dynamics.

2D AMR method in a cancer invasion system

In what follows we present an adaptation of the AMR scheme to the two-dimensional cancer invasion model (2.28) that we have augmented with cancer cell proliferation represented by a logistic growth term. The model reads

$$\begin{cases} \partial_t c = \nabla \cdot (D_c \nabla c - \chi c \nabla a) + \mu c(1-c), \\ \partial_t v = -\delta v m, \\ \partial_t m = D_m \Delta m + \alpha c - \beta m. \end{cases} \tag{6.12}$$

We refer to Section 2.5 for further details on the modeling. For the needs of the following numerical simulations we consider the parameters

$$\chi = 2 \times 10^{-2},\ D_c = 2 \times 10^{-4},\ D_m = 10^{-3},\ \mu = 0.5,\ \delta = 4,\ \alpha = 0.5,\ \beta = 0.3. \tag{6.13}$$

Numerical scheme We use a simple first order finite volume scheme for the numerical approximation of model (6.12). The scheme is provided for a fixed RSM $M = \{C_1, \dots, C_N\}$ in space dimension $d = 2$. The corresponding AMR method alternates between mesh update and time evolution as Algorithm 3. Note that in contrary to the case of uniform quadrilateral meshes, we have enumerated the mesh cells in M by a single index. By $N(C_i)$ we denote for any $1 \leqslant i \leqslant N$ the set of neighbors of the mesh cell C_i. If further $C_j \in N(C_i)$, we denote by $\partial C_{i,j} = \partial C_i \cap \partial C_j$ the interface between the mesh cells C_i and C_j. By $\mathbf{n}_{i,j}$ we then denote the unit vector perpendicular to $\partial C_{i,j}$ pointing from the mesh cell C_i to its neighbor cell C_j.

We note that the derivation of a finite volume method on a 2D RSM for a scalar conservation law analogously to (5.2) and (5.28) yields

$$u_i^{n+1} = u_i^n - |C_i^n|^{-1} \sum_{C_j^n \in N(C_i^n)} \int_{t^n}^{t^{n+1}} \int_{\partial C_{i,j}} f(u(x,t)) \mathbf{n}_{i,j} \, dx \, dt \tag{6.14}$$

for $i = 1, \dots, N$ and cell averages $u_i^n = |C_i|^{-1} \int_{C_i} u(x, t^n) \, dx$. The numerical fluxes in this setting are sought for the approximation

$$H_{i,j}(t^n, \mathbf{n}_{i,j}) \approx \frac{1}{(t^{n+1} - t^n)\,|\partial C_{i,j}|} \int_{t^n}^{t^{n+1}} \int_{\partial C_{i,j}} f(u(x,t)) \mathbf{n}_{i,j} \, dx \, dt. \tag{6.15}$$

To design a scheme for cancer invasion system (6.12) we consider now the discrete cell averages of the cancer cells $c_i^n = |C_i|^{-1} \int_{C_i} c(x, t^n) \, dx$ and the point values of the concentrations of the ECM and the MMPs $v_i^n \approx v(M(C_i), t^n)$ and $m_i^n \approx m(M(C_i), t^n)$. An application of the above approach to system (6.12) leads to the scheme

$$\begin{cases} c_i^{n+1} = c_i^n + \tau_n \mu \, c_i^n \, (1 - c_i^n) - \tau_n \displaystyle\sum_{C_j \in N(C_i)} \frac{|\partial C_{i,j}|}{|C_i|} \, H_{i,j}^C(t^n, \mathbf{n}_{i,j}), \\ v_i^{n+1} = v_i^n - \tau_n \, \delta \, v_i^n \, m_i^n, \\ m_i^{n+1} = m_i^n + \tau_n \alpha \, c_i^n - \tau_n \beta \, m_i^n - \tau_n \displaystyle\sum_{C_j \in N(C_i)} \frac{|\partial C_{i,j}|}{|C_i|} \, H_{i,j}^M(t^n, \mathbf{n}_{i,j}), \end{cases} \tag{6.16a}$$

where the numerical fluxes $H^C_{i,j}(\mathbf{n}_{i,j})$ and $H^M_{i,j}(\mathbf{n}_{i,j})$ include both approximations of advection and diffusion fluxes. We take a piecewise constant approach and use central differences to obtain the diffusion flux which thus reads for the MMP density

$$H^M_{i,j}(t^n, \mathbf{e}_k) = -D_m \frac{m_j^n - m_i^n}{|\partial C_{i,j}|}. \tag{6.16b}$$

Here $\mathbf{e}_k$ denotes a unit versor in $\mathbb{R}^2$ and we use this notation for the rest of this section. To discretize the advection term we take the central upwind approach from Section 5.2 applied to piecewise constant solutions and thus get the following numerical fluxes for the cancer cell concentration

$$H^C_{i,j}(t^n, \mathbf{e}_k) = -D_c \frac{c_j^n - c_i^n}{|\partial C_{i,j}|} + \chi \left(\frac{v_j^n - v_i^n}{|\partial C_{i,j}|} \right)^+ c_i^n - \chi \left(\frac{v_j^n - v_i^n}{|\partial C_{i,j}|} \right)^- c_j^n. \tag{6.16c}$$

For consistency, both numerical flux functions shall satisfy the symmetry condition

$$H^C_{i,j}(t^n, -\mathbf{e}_k) = -H^C_{i,j}(t^n, \mathbf{e}_k), \quad H^M_{i,j}(t^n, -\mathbf{e}_k) = -H^M_{i,j}(t^n, \mathbf{e}_k). \tag{6.16d}$$

For the well posednes of the scheme at the boundary we employ the ghost values (5.33). The forward Euler time integration in (6.16) in combination with the discrete diffusion terms that we use requires small time step sizes. We choose these according to the CFL condition

$$\tau_n \leqslant \mathrm{CFL} \min \left\{ \frac{h}{a^n}, \frac{h^2}{D_m} \right\}, \tag{6.17}$$

where we have used the mesh parameter $h = \min_{C_i \in M} \operatorname{diam}(C_i)$ and the maximal absolute propagation speed

$$a^n = \max_{C_i \in M,\ C_j \in N(C_i)} \frac{|v_j^n - v_i^n|}{|\partial C_{i,j}|}.$$

Due to restrictions by the explicit diffusion terms we have not considered a localized CFL condition like (5.39b) in (6.17). In the experiments we use $\mathrm{CFL} = 0.49$.

The scheme (6.16) will serve us to exhibit first numerical experiments with 2D AMR methods in the cancer invasion model. Development of a more efficient scheme of higher order will be subject of future work.

Monitor function The application of a monitor function that takes the gradient of the numerical solution into account resulted in an efficient 1D AMR method for model (I), as demonstrated in Section 6.6. In the 2D case we take a similar approach that follows [49]. For RSM $M = \{C_1, \dots, C_N\}$, the notations used in scheme (6.16) and corresponding cancer cell densities at a fixed time instance denoted by $c_1, \dots, c_N$ we define the monitor function

$$\theta(C_i) = \frac{g(C_i)}{\max_{1 \leqslant i \leqslant N} g(C_i)}, \quad g(C_i) = \max_{C_j \in N(C_i)} \frac{|c_j - c_i|}{|\partial C_{i,j}|}. \tag{6.18}$$

It is applied together with refinement and coarsening thresholds $\theta_{\mathrm{ref}} = 0.2$ and $\theta_{\mathrm{coars}} = 0.1$.

AMR method The full method follows the lines of Algorithm 3. We use scheme (6.16) together with the CFL condition (6.17) for the time evolution step and monitor function (6.18) in the mesh update together with the trivial projection (6.7). Again we employ the mesh update parameters $n_{\mathrm{ref}} = 1,\ n_{\mathrm{coars}} = 1,\ n_{\mathrm{ref},0} = 3$. The simulations are performed on an RSM with parameters $l_{\min} = 5,\ l_{\max} = 7$ and $N_0 = 1$.

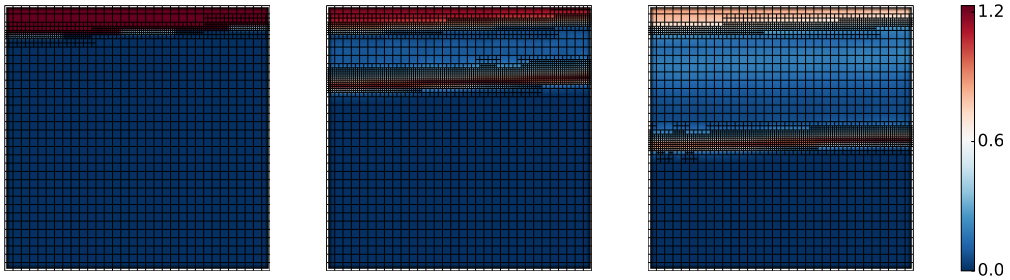

Figure 6.11: Three time instances ($t = 0,\ 2.5,\ 5$) in the evolution of the cancer cell density over nonuniform meshes in Experiment 4a computed with the 2D AMR method. The colorbar refers to the time instance $t = 5$. The cancer cells invade the ECM in the form of a wave, the mesh is adapted to the regions of interest [99].

numerical method	number of mesh cells	L^1 error
FVFD scheme (6.16), uniform mesh, $l = 5$	1024	3.989×10^{-2}
FVFD scheme (6.16), uniform mesh, $l = 6$	4096	1.451×10^{-2}
FVFD-AMR method, $l \in \{5, 6, 7\}$	3391	1.002×10^{-2}

Table 6.1: The L^1 errors (5.63), (5.64) of the uniform and the AMR method with respect to the numerical solution on a uniform RSM of refinement level 7 in Experiment 4a at $t = 2.5$. The AMR methods improves the accuracy when compared to the uniform method on refinement level $l = 6$.

Numerical experiments We split the unit square Ω into two parts to define discontinuous initial data for our numerical experiments. Consider to this end the domain

$$U = \left\{ (x_1, x_2) \in \Omega,\ x_2 \geqslant \sin\left(\frac{x_1^3}{125} + \frac{2x_1 + 26}{25} + \frac{1}{20} \right) \right\}$$

and the initial data

$$c_0(x) = \chi_U(x), \quad v_0(x) = v^* \chi_{\Omega \setminus U}(x), \quad m_0(x) = 0.3\, \chi_U(x) \tag{6.19}$$

with χ denoting the characteristic function.

In our first 2D AMR simulation (Experiment 4a) we considered the initial condition (6.19) for $v^* = 1$. In Figure 6.11 we present three time instances of the cancer cell concentration computed by the AMR method. Similarly as in Experiment 3 shown in Figure 5.6, a wave of cancer cells emanates from the bulk of the tumor and invades the ECM. Between the main body of the tumor and the invading wave of cancer cells a smoother part of the solution with lower cell density develops and grows as time evolves. The mesh resolution is increased in the area of the first cancer wave, as well as at the front of the main body of the tumor.

We noticed a gain of accuracy of the AMR method compared to the uniform method even when using our first order scheme. To show the advantage of the adaptive scheme we chose method (6.16) on the uniform RSM on level $l = 7$ as reference solution. We considered the finale time $t = 2.5$ and computed the L^1 error according to (5.63), (5.64) for the uniform method on the RSMs of levels 5 and 6 and for the AMR method. The computed errors presented in Table 6.1 point out that the AMR method operating on the refinement levels $l = 5, 6, 7$ outperforms the uniform method on refinement level $l = 6$ regarding the L^1 error, albeit the uniform method employs significantly more mesh cells.

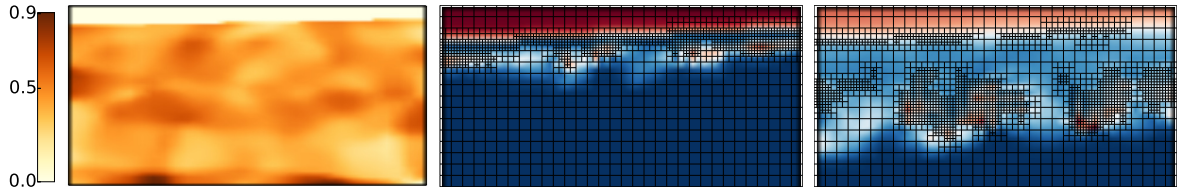

Figure 6.12: Initial ECM density (left, precomputed by Nikolaos Sfakianakis) and two time instances ($t = 1,\ 4$) in the evolution of the cancer cell density over nonuniform meshes in Experiment 4a computed with the 2D AMR method (middle and right). The cancer cell density at $t = 4$ ranges between 0 and 1.4. The migration of the cancer cells is controlled by the nonuniform structure of the ECM. The mesh adaptation follows the dynamics of the cancer cells [99].

We consider the second test case (Experiment 4b), where we included a nonuniform ECM in the invasion of the cancer cells. We used the same parameters (6.13) and initial data (6.19) as in Experiment 4b except for the choice of v^*. In this experiment we used a precomputed nonuniform density v^*. We show this initial ECM concentration in Figure 6.12 and refer to Appendix A for more details on its computation.

The obtained dynamics of the numerical solution shown in Figure 6.12 are significantly more complex when compared to the dynamics of Experiment 4a. Again a wave of propagating cancer cells is formed. In this experiment though the cancer cells concentrate in isolated clusters as they move through the matrix. This is induced by the heterogeneous tissue structure. The invading clusters separate from the main body of the tumor; a behavior that is consistent with the biomedical understanding of cancer invasion. The mesh follows the dynamics of the solution by increasing the resolution at the invading clusters and at the front of the main body of the tumor. The employed distinct refinement and coarsening thresholds θ_{ref} and θ_{coars} cause a memory effect in the mesh evolution. The effect results in a higher density of mesh cells at previous locations of the invading clusters. This improves the numerical resolution of the interactions of the proteolytic enzymes and the ECM close to the invading front of cancer cells and might be particularly useful when considering more complex models of cancer invasion.

7 A mass-transport finite element method for Keller-Segel type systems

In this chapter we propose yet another approach to the numerical approximation of cancer invasion systems in 1D. We formulate the idea of the method for a general two equation KS-type systems with reaction terms. In the method derivation we propose a splitting of the system and separate a mass conservative part of the system from the rest. The corresponding subsystem allows for a particular transformation of variables that we discuss in Section 7.1. The numerical scheme that is described in Section 7.2 couples both subsystems by an operator splitting approach and employs finite differences and finite elements in different coordinates. We elaborate on the stability of the scheme in Section 7.3 and present numerical experiments in various biological models in Section 7.4. The numerical results exhibit the mesh adaptation to the solution that is included in the scheme by its design. This motivates a comparison to the AMR method derived in Chapter 6, which we consider in the same section.

The chapter is based on a joint work with José Antonio Carrillo and Mária Lukáčová-Medviďová. A modified version of the following was recently submitted for publication, see [28]. The computations in this chapter were conducted using both the Python programming language and MATLAB.

7.1 Splitting and coordinate transformation

In the present chapter we focus on the numerical study of one-dimensional ADR systems of the following type

$$\begin{cases} \partial_t c = \partial_x \left(D_c \partial_x c - \chi c \partial_x a \right) + R_c(c) & \text{in } I \times \mathbb{R}^+, \\ \varepsilon \partial_t a = D_a \partial_x^2 a + R_a(c, a) & \text{in } I \times \mathbb{R}^+, \\ \partial_x c = \partial_x a = 0 & \text{in } \partial I \times \mathbb{R}^+, \\ c(\cdot, 0) = c_0, \quad a(\cdot, 0) = a_0. \end{cases} \tag{7.1}$$

We consider nonnegative initial data $c_0, a_0 \geqslant 0$ and reaction terms R_c, R_a that are taken in such a way that the solution stays nonnegative for all $t > 0$, e.g., Lipschitz continuous with $R_c(0), R_a(c, 0) \geqslant 0$. We set $\Omega = I = (a_I, b_I)$. System (7.1) can be understood as an augmentation of system (KS) in 1D. We refer to Section 2.4 for the corresponding modeling and to Section 4.1 for analytical properties of the system without reaction terms. Recall that c denotes the concentration of a particular cell species and a the concentration of a chemo-attractant.

The scheme that we are going to derive is motivated by [17]. In this work a new *mass-*

transport steepest descent scheme was proposed to resolve numerically a modified 1D Keller-Segel model for the log interaction kernel introduced in [25]. The method satisfies a discrete free energy dissipation principle and by considering the problem in transformed variables the method can resolve areas of high concentrations accurately without any mesh refinement. In this chapter we extend the mass-transport approach to the general class of systems (7.1). We will test different scenarios that feature particularly the splitting, traveling and emerging of concentrations, which occur in cancer invasion models and which constitute a challenge for classical numerical methods, see Section 6.1.

In our adaptation of the method we will employ the technique from [17] to the part of the system being similar to the Keller-Segel model (i.e. the first equation of (7.1) with $R_c = 0$). The remaining system of an ODE and a diffusion-reaction equation will be decoupled and solved by a suitable finite element method.

More precisely, we consider the splitting of (7.1) into two subsystems. Then the solution of the full system, i.e. system (7.1), will be approximated by an appropriate combination of short time solution of the subsystems. We firstly introduce the diffusion-advection subsystem given as

$$\begin{cases} \partial_t c = \partial_x \left(D_c \partial_x c - \chi c \partial_x a \right) & \text{in } I \times \mathbb{R}^+, \\ \partial_t a = 0 & \text{in } I \times \mathbb{R}^+, \\ \partial_x c = 0 & \text{in } \partial I \times \mathbb{R}^+, \\ c(\cdot, 0) = c_0^A, \quad a(\cdot, 0) = a_0^A. \end{cases} \tag{A}$$

This system assumes a steady chemo-attractant density a and transport in the cell density c due to advection and diffusion. Note that the mass of the cells is conserved in this system. Secondly, we consider the reaction-diffusion subsystem

$$\begin{cases} \partial_t c = R_c(c) & \text{in } I \times \mathbb{R}^+, \\ \partial_t a = D_a \partial_x^2 a + R_a(c, a) & \text{in } I \times \mathbb{R}^+, \\ \partial_x a = 0 & \text{in } \partial I \times \mathbb{R}^+, \\ c(0, \cdot) = c_0^B, \quad c(0, \cdot) = c_0^B \end{cases} \tag{B}$$

that contains the remaining terms of system (7.1).

In the next step we derive another formulation of diffusion-advection subsystem (A). To this end we consider the *cumulative distribution function* of the cell density

$$F(y, t) = \int_{a_I}^{y} c(x, t)\, dx, \quad y \in I, \tag{7.2}$$

which is monotonically increasing in the variable y by the nonnegativity of the density c. The pseudo inverse function of F to which we will henceforth refer to as the *inverse cumulative distribution* is given by

$$V(w, t) = \inf \left\{ y : \int_{a_I}^{y} c(x, t)\, dx > w \right\}, \quad w \in (0, m). \tag{7.3}$$

It is defined for positive values of w that do not exceed the total mass of cells

$$m = \int_I c_0^A\, dx. \tag{7.4}$$

The mass (7.4) remains constant in time when considering only subsystem (A) isolated. The function V is, in particular, a right inverse of F, i.e. $F(V(w,t),t) = w$. Thus, we have

$$0 = \frac{d}{dt}F(V(w,t),t) = \partial_t V(w,t)\, c(V(w,t),t) + \partial_t F(V(w,t),t),$$

which implies

$$c(V,t)\,\partial_t V = -\partial_t F(V,t) = -\frac{d}{dt}\int_{a_I}^{V} c(x,t)\,dx = -\int_{a_I}^{V} \partial_t c(x,t)\,dx. \tag{7.5}$$

Here we have assumed the continuity of the density function c and its time derivative to derive the latter equation. Substituting system (A) into (7.5) and applying the homogeneous Neumann boundary conditions yield

$$\begin{aligned} c(V,t)\,\partial_t V &= -\int_{a_I}^{V} \partial_x \left(D_c \partial_x c - \chi c \partial_x a\right)\,dx = -\left[D_c \partial_x c - \chi c \partial_x a\right]_{a_I}^{V} \\ &= -D_c \partial_x c(V,t) + \chi c(V,t)\partial_x a(V,t). \end{aligned} \tag{7.6}$$

Since it holds $\frac{d}{dw}c(V(w,t),t) = \partial_w V \partial_x c(V,t)$ by the chain rule and $\partial_w V = \frac{1}{c(V,t)}$ by the inverse function theorem, we obtain the evolution equation for the inverse distribution

$$\partial_t V = -D_c \partial_w \left([\partial_w V]^{-1}\right) + \chi \partial_x a(V,t). \tag{7.7}$$

Diffusion-advection system (A) can consequently be rewritten as

$$\begin{cases} \partial_t V = -D_c \partial_w \left([\partial_w V]^{-1}\right) + \chi \partial_x a(V,t) & \text{in } (0,m)\times\mathbb{R}^+, \\ \partial_t a = 0 & \text{in } I\times\mathbb{R}^+, \\ V(0,\cdot) = a_I, \quad V(m,\cdot) = b_I, \\ V(\cdot,0) = V_A, \quad a(\cdot,0) = a_A, \end{cases} \tag{A'}$$

where m is given by (7.4) and V_A is the pseudo inverse distribution (7.3) corresponding to density c_A in system (A).

7.2 Numerical method

In this section we describe a numerical treatment for system (7.1) that makes use of the splitting into subsystems (A') and (B). We consider the inverse distribution function V for the cells on the *mass space* $(0,m)$, whereas the chemo-attractant a is considered in the Eulerian coordinates in Ω. This leads to two meshes that the proposed numerical method employs.

To start with we discretize the normalized mass space $(0,1)$ on which the inverse distribution V resides uniformly by

$$0 = w_0 < w_1 < \cdots < w_M = 1, \quad w_j = j\Delta w, \quad j = 0,\dots,M \tag{7.8}$$

with a mesh length $M \in \mathbb{N}$ and point distance $\Delta w = 1/M$. Since the mass of the cells m changes throughout the computation, it is more convenient to consider here the unit interval instead of $(0,m)$.

The second mesh partitions the physical space interval I for the chemo-attractants concentration a into

$$a_I = x_0 < x_1 < \cdots < x_N = b_I, \quad x_k = a_I + k\Delta x, \quad k = 0, \ldots, N, \tag{7.9}$$

which results in N mesh cells of size $\Delta x = (b_I - a_I)/N$.

We denote the point values of V by $V_j(t) = V(m_h(t)\, w_j, t)$ for $j = 0, \ldots, M$ and introduce the linear spline in w, connecting the discrete values, that we denote by $V_h(t, m_h(t)\, w)$. Here we have used the discrete mass of the cells

$$m_h(t) = \int_I c_h(x, t)\, dx, \tag{7.10}$$

where c_h is a discrete representation of the cell density to be defined later on.

For the chemo-attractant density a we employ a linear finite element representation. Let $\{\phi_k,\ k = 1, \ldots, N-1\}$ be the basis of piecewise linear hat functions on the grid (7.9), which satisfy the homogeneous Neumann boundary conditions in (B). In particular, we have

$$\phi_k(x) = \begin{cases} (x - x_{k-1})/\Delta x & \text{if } x_{k-1} \leqslant x \leqslant x_k, \\ (x_{k+1} - x)/\Delta x & \text{if } x_k \leqslant x \leqslant x_{k+1}, , \\ 0 & \text{otherwise} \end{cases} \qquad k = 2, \ldots, N-2$$

in the center of the domain and

$$\phi_1(x) = \begin{cases} 1 & \text{if } a \leqslant x \leqslant x_1, \\ (x_2 - x)/\Delta x & \text{if } x_1 \leqslant x \leqslant x_2, \\ 0 & \text{otherwise,} \end{cases}$$

$$\phi_{N-1}(x) = \begin{cases} (x - x_{N-2})/\Delta x & \text{if } x_{N-2} \leqslant x \leqslant x_{N-1}, \\ 1 & \text{if } x_{N-1} \leqslant x \leqslant b, \\ 0 & \text{otherwise} \end{cases}$$

near the boundary. By using the basis functions we can define the approximate chemo-attractant density as

$$a_h(x, t) = \sum_{k=1}^{N} a_i(t)\phi_i(x). \tag{7.11}$$

For the construction of the splitting method we define solution operators for both systems (A′) and (B). This is done similarly as in the formulation of the STRANG method in Section 5.7. We first construct T to be a numerical solution operator of system (A′). In particular, if $(V_h(\tilde{t}), a_h(\tilde{t}), m_h(\tilde{t}))$ is a numerical solution at $t = \tilde{t}$ then $T_\tau(V_h(\tilde{t}), a_h(\tilde{t}), m_h(\tilde{t}))$ will be a numerical solution of system (A′) at time $t = \tilde{t} + \tau$. In the same manner, we will define a solution operator S for system (B) afterwards.

The advection-diffusion operator T for system (A′)

For a discretization of the system (A′) we need to evaluate the derivative of the chemo-attractant concentration in the state variable V. To this end we consider a cubic spline interpolation of the discrete density of the attracting species.

Let $(V_h(t), a_h(t), m_h(t))$ be given initial data. By $\hat{a}_h$ we denote the cubic spline over the data points $(x_k, a_h(x_k, t))$ for $k = 1, \dots, N$ that satisfies the boundary conditions $\partial_x \hat{a}_h(a) = \partial_x \hat{a}_h(b) = 0$. We use this spline for the approximation of the advection term. Concerning the time integration we split again the advection and the diffusion terms, as motivated in Section 5.6. In this way we allow for both large time steps and stability of the scheme. For this purpose we apply the IMEX midpoint scheme, see Section 5.8. It reads here

$$-2\frac{\tilde{V}_j(t) - V_j(t)}{\tau} = \frac{D_c}{\tilde{V}_{j+1}(t) - \tilde{V}_j(t)} - \frac{D_c}{\tilde{V}_j(t) - \tilde{V}_{j-1}(t)} - \chi \partial_x \hat{a}_h(V_j(t)), \tag{7.12a}$$

$$-\frac{T_\tau V_j(t) - V_j(t)}{\tau} = \frac{D_c}{\tilde{V}_{j+1}(t) - \tilde{V}_j(t)} - \frac{D_c}{\tilde{V}_j(t) - \tilde{V}_{j-1}(t)} - \chi \partial_x \hat{a}_h(\tilde{V}_j(t)) \tag{7.12b}$$

for $j = 1, \dots, M-1$. We have used the central difference formula for the diffusion terms analogously to [17]. The intermediate stage $\tilde{V}_j(t)$ is given by the nonlinear implicit equation (7.12a) and we use Newton's method for its computation. For computation of the taxis terms in (7.12a) and (7.12b) we evaluate the afore determined spline $\hat{a}_h$. At the boundaries we keep V_h fixed, i.e. we set $T_\tau V_0(t) = a_I$ and $T_\tau V_M(t) = b_I$.

The chemo-attractant density and the mass of the cells do not change when we prescribe their evolution according to subsystem (A'). Thus, we define the numerical operator accordingly by

$$T_\tau a_h(t) = a_h(t), \quad T_\tau m_h(t) = m_h(t).$$

The special attribute that distinguishes this scheme from the methods discussed in Chapters 5 and 6 is that it discretizes system (A') obtained after the coordinate transformation. We will henceforth refer to methods like (7.12) that operate on inverse distributions as *mass-transport methods*.

The reaction-diffusion operator S for system (B)

In the overall splitting method we apply the reaction-diffusion operator S starting with the data $(T_\tau V_h(t), T_\tau a_h(t), T_\tau m_h(t))$ obtained from a previous evaluation of the advection-diffusion operator T. For simplicity though we describe here the numerical operator S for general initial data $(V_h(t), a_h(t), m_h(t))$.

PDE system (B) is formulated for physical densities of cells. To provide adequate initial data using the given approximations $(V_h(t), c_h(t), m_h(t))$ we transform the discrete pseudo inverse distribution $V_h(t)$ on $(0, 1)$ to a finite volume representation of $c(\cdot, t)$ on (a, b). Since we assume that the approximate density c_h satisfies

$$\int_{V_{j-1}(t)}^{V_j(t)} c_h(x, t)\, dx = m_h(t) \Delta w \tag{7.13}$$

for all $j = 1, \dots, M$, we can define the cell averages and the piecewise constant function c_h as

$$c_j(t) = \frac{m_h(t)\, \Delta w}{V_j(t) - V_{j-1}(t)}, \quad j = 1, \dots, M,$$

$$c_h(x, t) = \sum_{j=1}^{M} c_j(t)\, \chi_{(V_{j-1}(t), V_j(t))}(x) \tag{7.14}$$

with χ denoting the characteristic function. This approximation of the cell densities resides on the physical space Ω. Note though that the cell averages are given on a nonuniform mesh, which differs from the mesh of the chemo-attractant a given in (7.9).

After the discrete variable transformation we are in the position to write down the scheme for system (B). Again we split diffusion from reaction and apply the IMEX midpoint scheme, which reads for the intermediate stage

$$\tilde{c}_j(t) = c_j(t) + \frac{\tau}{2} R_c(c_j(t)), \tag{7.15a}$$

$$2\varepsilon \frac{\tilde{a}_k(t) - a_k(t)}{\tau} \int_{a_I}^{b_I} \phi_k \phi_l \, dx = -\tilde{a}_k(t) D_c \int_{a_I}^{b_I} \frac{\partial \phi_k}{\partial x} \frac{\partial \phi_l}{\partial x} \, dx + \int_{a_I}^{b_I} R_a(c_h(t), a_h(t)) \phi_l \, dx \tag{7.15b}$$

for $j = 1, \dots, M$ and $k, l = 1, \dots, N-1$. The full update is then obtained by

$$S_\tau c_j(t) = c_j(t) + \frac{\tau}{2} R_c(\tilde{c}_j(t)), \tag{7.15c}$$

$$\varepsilon \frac{S_\tau a_k(t) - a_k(t)}{\tau} \int_{a_I}^{b_I} \phi_k \phi_l \, dx = -\tilde{a}_k(t) D_a \int_{a_I}^{b_I} \frac{\partial \phi_k}{\partial x} \frac{\partial \phi_l}{\partial x} \, dx + \int_{a_I}^{b_I} R_a(\tilde{c}_h(t), \tilde{a}_h(t)) \phi_l \, dx \tag{7.15d}$$

for $j = 1, \dots, M$ and $k, l = 1, \dots, N-1$. As usual, we employ precomputed integrals of the basis functions $\int_{a_I}^{b_I} \phi_k \phi_l \, dx$ and $\int_{a_I}^{b_I} \frac{\partial \phi_k}{\partial x} \frac{\partial \phi_l}{\partial x} \, dx$ in the computation of linear systems (7.15b) and (7.15d). The integrals of the form $\int_a^b R_c(c_h(t), a_h(t)) \phi_l \, dx$ are dependent on $V_h(t)$. For their computation we use suitable quadratures together with an indicator function to identify the position of a particular point $x \in \Omega$ on the grid corresponding to the cell density c_h. The reaction update in the cell density c_h alters the mass of the cells over the interval I. To take that into account we update $m_h(t)$ by

$$S_\tau m_h(t) = \sum_{j=1}^{M} S_\tau c_j(t) (V_j(t) - V_{j-1}(t)). \tag{7.16}$$

In order to be able to apply the advection-diffusion operator after the reaction diffusion update we transform $S_\tau c_h(t)$ to its inverse distribution representation $S_\tau V_j(t)$. Therefore, we use the formula

$$\int_{S_\tau V_{j-1}(t)}^{S_\tau V_j(t)} \sum_{j=1}^{M} S_\tau c_j(t) \, \chi_{(V_{j-1}(t), V_j(t))}(x) \, dx = S_\tau m_h(t) \Delta w, \quad j = 1, \dots, M. \tag{7.17}$$

Since we assume $S_\tau V_j(t)$ to be monotonically increasing in j, formula (7.17) allows for an efficient update of the inverse distribution V_h.

The splitting method

To resolve system (7.1) numerically we propose the Strang operator splitting method using both numerical operators defined above. Initially, we assume given nonnegative and

sufficiently smooth initial data c_0 and a_0 for system (7.1) and deduce discrete initial data $(V_h(0), a_h(0), m_h(0))$. To compute the discrete representation $V_h(0)$ of the normalized concentration $c_0/m_h(0)$ we employ successive integration as in (7.17).

We define the fully discrete Strang splitting scheme for system (7.1) iteratively by

$$(V_h(t^{n+1}), a_h(t^{n+1}), m_h(t^{n+1})) = T_{\tau_n/2} S_{\tau_n} T_{\tau_n/2}(V_h(t^n), a_h(t^n), m_h(t^n)) \tag{7.18}$$

for $n = 0, 1, 2, \dots$ and for a discretization of the time axis by $0 = t^0 < t^n = \sum_{i=1}^{n} \tau_i$. Scheme (7.18) alternates between applying the diffusion-advection and the diffusion-reaction operator. The symmetrical structure leads to the second order splitting error and thus to an expected consistency order of two in time for the overall scheme [110]. We will henceforth refer to the full method (7.18) as *mass-transport finite element* (MTFE) scheme.

To optimize the efficiency we adapt the time increment τ in each time step. Since the discretization of system (A) is more sensitive to instabilities that are caused by large time increments τ compared to the discretization of the diffusion-reaction system, we start the method in each time step with the numerical operator T in which we determine τ_n. We will elaborate on the choice of τ and the stability of the scheme in Section 7.3. We note moreover that the spline interpolations in the scheme (7.18) needs to be computed only once per time step after the update by the reaction-diffusion operator S.

The scheme (7.18) is not limited to the case of a single pair of a cell and a chemo-attractant. An extension to multiple chemo-attractants as in model (I) is straightforward. The case of multiple cells such as in model (II) can be treated as well. Note though that each additional cell species in the PDE system brings along another nonuniform mesh for the space domain Ω which requires in turn further projections in the numerical operator S.

In addition, a more general reaction term in the cell concentration that also depends on the chemo-attractants can be handled by projecting c_h to the finite volume grid before applying the updates (7.15a) and (7.15c).

Concerning an adaptation to higher space dimensions, we note that the adopted mass-transport scheme in [17] was derived by considering the Keller-Segel model as a *gradient flow* of the free energy [6] and by applying the general steepest descent scheme from [88] to the 1D case. An adaptation of this method to the Keller-Segel model in 2D that involves evolving diffeomorphisms was proposed in [26]. However, the effort is delicate and associated with high computational costs [17]. For these reasons an adaptation of the MTFE scheme to $d > 1$ is out of the scope of this thesis.

7.3 Monotonicity preservation of the diffusion-taxis operator

In this section we consider a stability issue that arises in numerical schemes for the approximation of inverse distribution functions. The concept confers the idea of positivity preserving schemes to mass-transport methods.

We already discussed the importance of preserving the positivity of a numerical solution when dealing with densities. To this end we developed a scheme that preserves the nonnegativity in the computed cell averages, see Section 5.9. A nonnegative density c implies a monotonically increasing inverse distribution V by its definition (7.3). Thus, mass-transport methods should preserve the discrete monotonicity of V.

In particular, we call a method *monotonicity preserving* if from $V_j(t) - V_{j-1}(t) > 0$ for all $0 \leqslant j \leqslant M$ follows that $V_j(t+\tau) - V_{j-1}(t+\tau) > 0$ also holds for all $1 \leqslant j \leqslant M$. Here τ denotes the time increment of the method.

The analysis of the full scheme (7.18) regarding the monotonicity preserving property is challenging due to the nonlinearity in (7.12) introduced by the diffusion terms. In the rest of this section we will instead consider a simplified problem that motivates a way to adapt the time increment τ in such a way, that the instabilities due to nonmonotone solutions are avoided. We consider, in particular, the system

$$\begin{cases} \partial_t V = \chi \partial_x a(V,t) & \text{in } (0,1)\times\mathbb{R}^+, \\ V(0,\cdot) = a_I, & V(1,\cdot) = b_I, \\ V(\cdot,0) = V_0, \end{cases} \tag{7.19}$$

where $a \in C^1(a_I, b_I)$. This is a diffusion free version of (A'). To discretize (7.19) we combine our approach for the advection-diffusion operator in Section 7.2 with the forward Euler scheme and obtain

$$V_j(t+\tau) = V_j(t) + \tau\chi\partial_x a(V_j(t)) \tag{7.20}$$

for $j = 1,\dots,M-1$. The approximated point values above are given as defined in Section 7.2. Again, we keep V_0 and V_M fixed. Contrary to the scheme (7.18) we assume that function a does not evolve in time. Thus, we do not consider any spline interpolation in this case. We can easily find a bound on τ that makes the scheme (7.20) monotonicity preserving. Note that a similar result to the one that follows was already derived in [63].

Proposition 7.1 *The scheme* (7.20) *is monotonicity preserving in* V_h*, if the CFL condition*

$$\tau^n < \min_{0\leqslant j<M} \frac{(V_{j+1}(t^n) - V_j(t^n))}{\chi \left|\partial_x a(V_{j+1}(t)) - \partial_x a(V_j(t))\right|} \tag{7.21}$$

is satisfied.

Proof. We consider a single time step τ and drop the superscript n in this proof for clarity. For $2 \leqslant j \leqslant M-2$ we compute

$$\begin{aligned} V_{j+1}(t+\tau) - V_j(t+\tau) &= V_{j+1}(t) - V_j(t) + \tau\chi\left(\partial_x a(V_{j+1}(t)) - \partial_x a(V_j(t))\right) \\ &\geqslant (V_{j+1}(t) - V_j(t))\left(1 - \tau\chi|L_{j+1/2}|\right), \end{aligned} \tag{7.22}$$

where $L_{j+1/2} = (\partial_x a(V_{j+1}(t)) - \partial_x a(V_j(t)))/(V_{j+1}(t) - V_j(t))$. By assuming the condition (7.21) and using the monotonicity at time instance t, the positivity of the right hand side of (7.22) follows. □

The point values of the inverse distribution $V_j(t)$ for $1 \leqslant j \leqslant M-1$ coincide with the mesh cell interfaces of the nonuniform mesh corresponding to the cell densities $c_h(t)$. Hence, the quantity $L_{j+1/2}$ in the proof of Proposition 7.1 can be understood as a finite difference formula for the second derivative of the chemo-attractant density a. Thus, the above CFL condition (7.21) motivates to choose the time increment τ^n according to

$$\tau^n \propto \left(\chi \sup_{\{x\in I\}} |\partial_x^2 a(x)|\right)^{-1}. \tag{7.23}$$

In our numerical experiments with the more elaborated scheme (7.18) we computed the time increments by

$$\tau^n = \mathrm{CFL}\ \min\left\{ \min_{0\leqslant j<M} \frac{(V_{j+1}(t^n) - V_j(t^n))}{\chi \left|\partial_x a(V_{j+1}(t)) - \partial_x a(V_j(t))\right|},\ K\Delta w \right\} \tag{7.24}$$

for constants $\mathrm{CFL}, K > 0$. The choice (7.24) is motivated by Proposition 7.1. The additional bound proportional to Δw balances the temporal and the spatial errors; large values of K can be used in practice. Whenever not otherwise stated we chose $\mathrm{CFL} = 0.49$ and $K = 100$ in our numerical experiments. Using this condition we did not observe any instabilities due to nonmonotonic numerical solutions.

7.4 Numerical experiments

In this section we consider various test cases for the MTFE scheme derived in Section 7.2. We exhibit that the method is capable to resolve accurately the splitting and moving phenomena often observed in KS-type systems and demonstrate the "automatic" mesh adaptation that is included in the method. Further, we study the experimental convergence of the scheme and compare it to the AMR method that we derived in Chapter 6.

The parabolic-elliptic Keller-Segel model with logistic growth

As our first test case we consider an application of our method in the modified Keller-Segel model from [25] with added logistic growth

$$\begin{cases} \partial_t c = \partial_x \left(D_c \partial_x c - \chi c \partial_x a \right) + \mu c(1-c) & \text{in } \mathbb{R} \times \mathbb{R}^+, \\ a(x,\cdot) = -\dfrac{1}{2\pi} \displaystyle\int_{\mathbb{R}} \log(|x-y|) c(y,\cdot)\, dy & \text{in } \mathbb{R} \times \mathbb{R}^+, \\ c(\cdot,0) = c_0 \geqslant 0. \end{cases} \tag{7.25}$$

An adaptation of system (7.28) to two dimensions with $\mu = 0$ is equivalent to the simplified system from [84], where the chemo-attractant density a is determined by the Poisson equation. In the case $d = 1$, which we consider here, system (7.28) is an interesting toy model to study the blowup phenomenon. The logistic term that we have added accounts for cell growth that is locally limited by resources and space modeled according to (2.9).

The chemo-attractant density a in the second equation of (7.25) is determined by the convolution term. Therefore, we did not need to use finite element approximations in our numerical simulations. Instead, we proceeded as in [17] and used a diffusion-taxis operator expanded as follows

$$\begin{aligned} -2\frac{\tilde{V}_j(t) - V_j(t)}{\tau} &= \frac{D_c}{\tilde{V}_{j+1}(t) - \tilde{V}_j(t)} - \frac{D_c}{\tilde{V}_j(t) - \tilde{V}_{j-1}(t)} \\ &\quad + m_h(t)\, \frac{\chi \Delta w}{2\pi} \sum_{i : |\tilde{V}_j(t) - \tilde{V}_i(t)| \geqslant \varepsilon} \frac{1}{\tilde{V}_j(t) - \tilde{V}_i(t)}, \end{aligned} \tag{7.26a}$$

$$\begin{aligned} -\frac{T_\tau V_j(t) - V_j(t)}{\tau} &= \frac{D_c}{\tilde{V}_{j+1}(t) - \tilde{V}_j(t)} - \frac{D_c}{\tilde{V}_j(t) - \tilde{V}_{j-1}(t)} \\ &\quad + m_h(t)\, \frac{\chi \Delta w}{2\pi} \sum_{i : |\tilde{V}_j(t) - \tilde{V}_i(t)| \geqslant \varepsilon} \frac{1}{\tilde{V}_j(t) - \tilde{V}_i(t)}, \end{aligned} \tag{7.26b}$$

where we employed $\varepsilon = 10^{-9}$ in the computations. The intermediate stage of the scheme, given implicitly by (7.26a), was computed by Newton's method. Throughout the corresponding

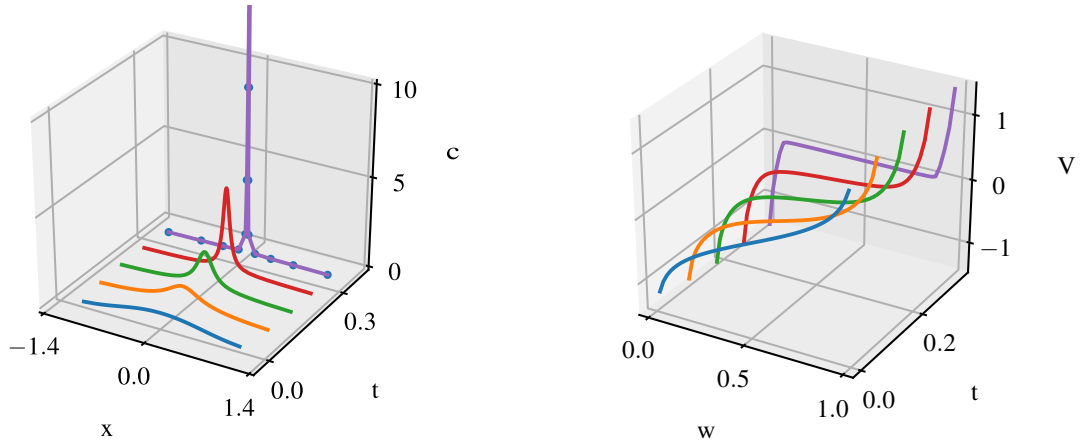

Figure 7.1: Numerical results (cell concentration and inverse cumulative function in space and time) in Experiment 4.3.1 in [17] with model (7.25). The cell concentration blows up.

iteration we controlled the convergence by the comparison of subsequent iterates [68]. In case the Newton iteration failed to converge, we aborted the computation and assumed blowup of the numerical solution. Time increments were adapted in such a way, that the Jacobian of (7.26a), which occurred in the Newton iteration, were strictly diagonally dominant.

The reaction-diffusion operator for system (7.28) approximates only the logistic growth term in the evolution equation for the cell density. Therefore, we only needed to fix initially a single mesh for the discretization of V_h. To account for the infinite domain length we used the Neumann boundary conditions

$$\frac{1}{V_1(t) - V_0(t)} = \frac{1}{V_M(t) - V_{M-1}(t)} = 0.$$

Moreover, the discrete concentrations at the boundary $c_0(t)$ and $c_M(t)$ were omitted in the reaction-diffusion operator. In our numerical simulations we used a mesh with only $M = 50$ points.

We considered the parameters $D_c = 1$, $\chi = 2.5\pi$ and initial data given by the inverse distribution

$$V_0(w) = \frac{w - 0.5}{\sqrt[4]{(w + 0.01)\,(1.01 - w)}}. \tag{7.27}$$

This experiment was studied for $\mu = 0$ in [17] and blowup in finite time around $t = 0.33$ was obtained numerically. We confirmed the same phenomenon using the splitting method, compare Figure 7.1. Blowup occurred and was indicated by our method in the computation.

When we conducted the experiment with altered $\mu = 1$, no blowup occurred, as can be seen in Figure 7.2. In the numerical results, the aggregation stops and reverses and the cell concentration seems to approach a stationary state. The CFL condition given by (7.23) caused an increase of the time increment over the computation time.

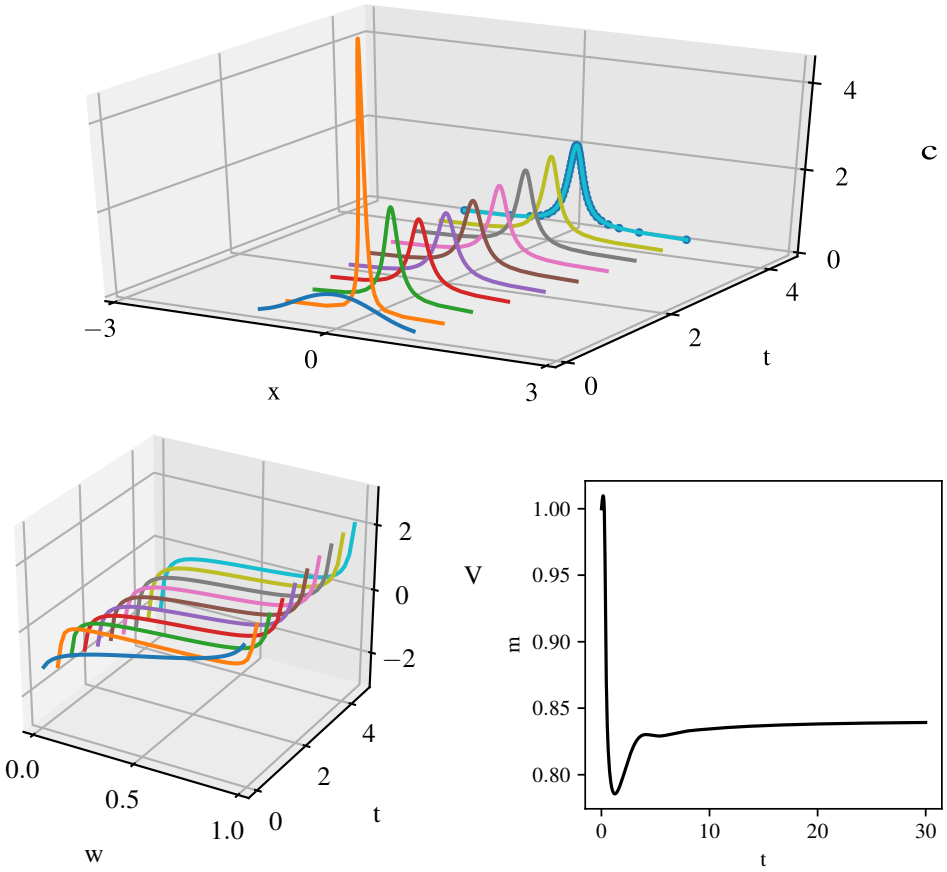

Figure 7.2: Numerical results (cell concentration, inverse cumulative function and mass) for the parabolic elliptic Keller-Segel model with added logistic growth (7.25). The blowup was prevented by the additional reaction term.

The parabolic-parabolic Keller-Segel model

Next, we consider simulations by our scheme for the parabolic-parabolic Keller-Segel model in 1D, which reads

$$\begin{cases} \partial_t c = \partial_x \left(D_c \partial_x c - \chi c \partial_x a \right) & \text{in } I \times \mathbb{R}^+, \\ \partial_t a = D_c \partial_x^2 a + c - a & \text{in } I \times \mathbb{R}^+. \end{cases} \tag{7.28}$$

As assumed in the generic model (7.1), we consider (7.28) with positive initial data and homogeneous boundary conditions. Opposed to the parabolic-elliptic case, this system features an additional parabolic equation that we treated by the splitting method.

In order to exhibit the phenomena that the scheme can resolve we considered two test cases with distinct initial chemo-attractant densities controlling the cell movement. In both tests we assumed initial data for the inverse distribution V given by (7.27).

Peak movement In our first numerical experiment with system (7.28) we used the parameters $D_c = 0.1$, $D_a = 0.01$, $\chi = 2.5$, $\alpha = 0.5$, $\beta = 1$ and the domain $I = (a_I, b_I)$ with boundaries chosen $a_I = V_0(0) \approx -1.58$, $b_I = V_0(1) \approx 1.58$. As initial chemo-attractant

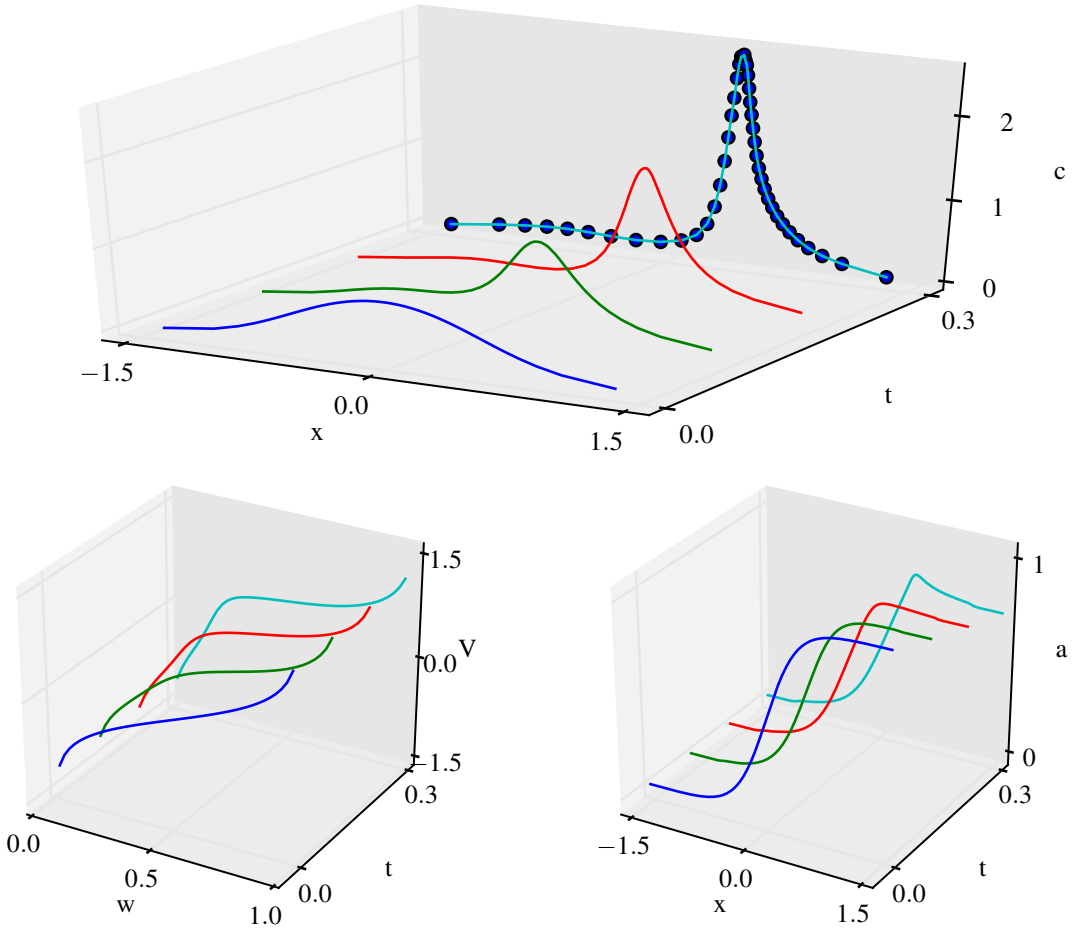

Figure 7.3: Numerical results (cell concentration, inverse cumulative function and chemo-attractant density in space and time) for the parabolic-parabolic Keller-Segel model (7.28) in the "peak movement" experiment. The movement and aggregation that model (7.28) dictates are accurately resolved using only $M = 45$ grid points.

concentration we chose the logistic function

$$c_0(x) = \frac{1}{1 + e^{-5x}}, \quad x \in I.$$

For the simulation we used meshes with $M = 45$ and $N = 230$ points and the CFL condition (7.24).

Figure 7.3 present the cell dynamics, showing their movement to the right side of the domain. As the cells produce the chemical with density a, an additional negative gradient is created. This gradient leads to additive cell aggregation which counteracts the movement. We point out that both the migration and the growth are well resolved by our simulations.

Peak splitting In another test we used the parameters $D_c = D_a = 0.1$, $\chi = 5$, $\alpha = \beta = 1$ and considered the computational domain (a_I, b_I) with boundaries chosen as in the "peak movement" experiment. The initial chemo-attractant density is given by

$$a_0(x) = 1 - e^{-20x^2}, \quad x \in (a_I, b_I).$$

Figure 7.4 shows the computational results for the discretization parameters $M = 90$ and $N = 450$. The cells move out of the center of the domain on which the most part of the

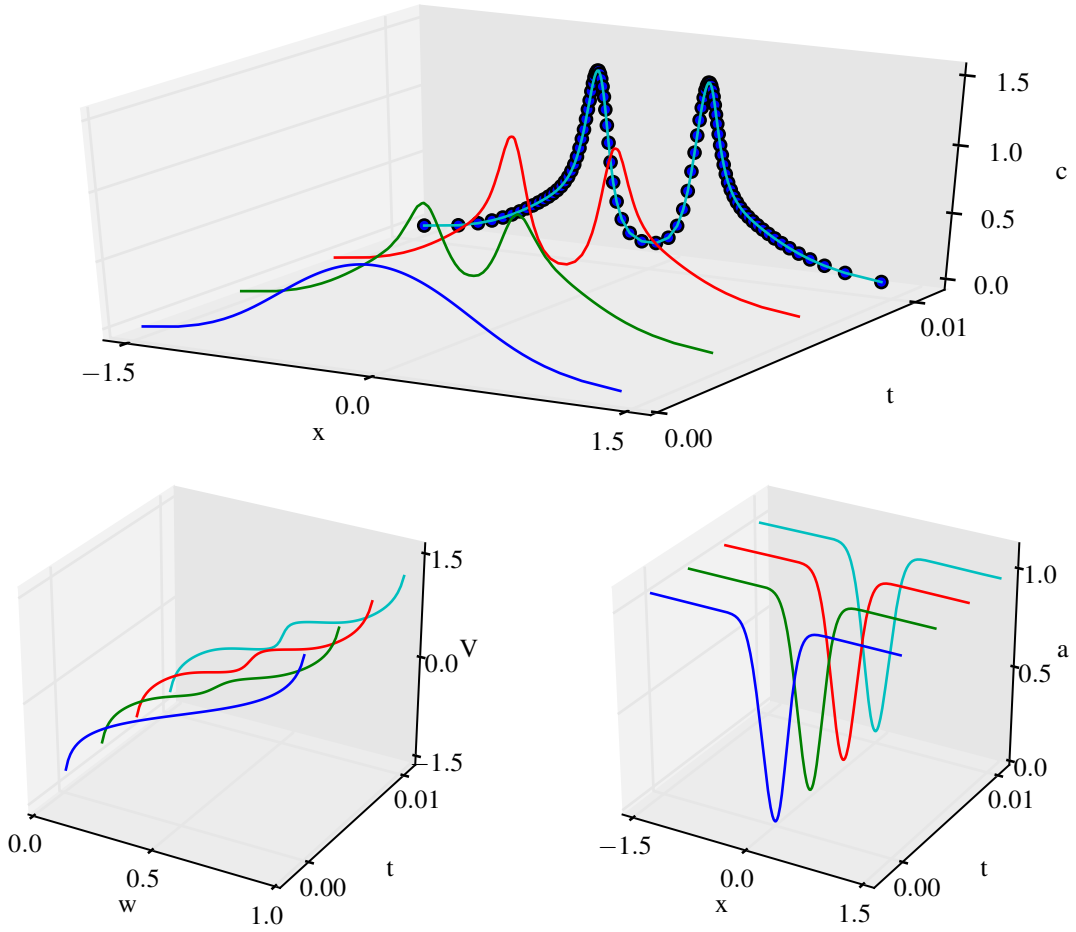

Figure 7.4: Numerical results (cell concentration, inverse cumulative function and chemo-attractant density in space and time) for the parabolic-parabolic Keller-Segel model (7.28) in the "peak splitting" experiment. The grid of the cell densities adapts to the two splitting peaks.

chemo-attractant is already consumed. The symmetrical movement to both sides of the domain leads to a splitting of the initial concentration into two peaks. The mesh points for the approximation of the cells on the density level concentrate at the locations of both peaks and adapt to the solution over time.

In the setting of the above experiment we study the convergence of the introduced splitting scheme experimentally. For a fixed instance in time and M given, let V_i^h for $i = 1, \dots, M-1$ denote a numerical solution corresponding to the mesh discretization parameter M. Then we define the following approximate L^1 finite difference error

$$E_M^V = \frac{1}{M} \sum_{j=1}^{M-1} \left| V_j^h - V_{2j}^{h/2} \right|, \tag{7.29}$$

where we have used a numerical solution on a finer mesh with $2M$ points, $V_j^{h/2}$ for $j = 1, \dots, 2M-1$, as the reference solution. The EOC for the discretization error in V_h can now be defined by

$$EOC^V(M) = \log_2(E_M^V) - \log_2(E_{M/2}^V) \tag{7.30}$$

for any even integer M. Similarly, we define the EOC for the cell densities on their nonuniform

M/M^{ref}	error E_M^V	EOC^V	error E_M^c	EOC^c
20 / 40	7.231e-04		1.360e-02	
40 / 80	7.427e-05	3.283	1.719e-03	2.984
80 / 160	1.416e-05	2.391	2.768e-04	2.635
160 / 320	4.698e-06	1.592	7.085e-05	1.966
320 / 640	1.615e-06	1.541	2.591e-05	1.451
640 / 1280	6.919e-07	1.223	1.554e-05	0.738

Table 7.1: Mesh convergence in the peak splitting experiment up to $T = 0.01$ with respect to the discretization parameter M. We adapted the number of points on the finite element mesh by $N = M$. The EOCs approach two in the inverse distributions as well as in the corresponding densities. Yet, for large M the EOC drops which is probably due to limitations by the finite element mesh.

finite volume mesh. To this end let c_i^h for $i = 1, \dots, M$ denote the finite volume representation corresponding to V_i^h for $i = 1, \dots, M-1$ and consider the error $E^c(M)$ given by (5.63), (5.64) where we employ as reference c_i^{ref} for $i = 1, \dots, 2M$ the finite volume representation of $V_j^{h/2}$ for $j = 1, \dots, 2M-1$. Then we define for even integers M

$$EOC^c(M) = \log_2(E_M^c) - \log_2(E_{M/2}^c).$$

In Table 7.1 we exhibit the errors and EOCs computed at the final time $T = 0.01$ and with constant time increment $\tau = 10^{-4}$ when doubling the mesh resolution on the mass space mesh iteratively. We coupled the resolution of the finite volume mesh to the number of points for the inverse distribution using $N = M$. We can clearly see that the method converges as the mesh size is refined. The EOCs indicate a convergence order of two in both the inverse distributions and the densities. However, we see that the EOC decreases as the grids becomes very fine. We suppose that this is caused by the finite element mesh that is only uniformly but not locally refined. As M increases the number of mesh cells on the nonuniform finite volume mesh for the cell densities aggregates around the positions of the peaks. For the MTFE scheme the finite element solution a_h must thus be interpolated in many points in a small physical area which leads to a loss of accuracy as the number $\max_i |\{j : x_i \leqslant V_j \leqslant x_{i+1}\}|$ increases.

Moreover, Table 7.1 shows that the method delivered accurate numerical results using only a few mesh points. We suppose that even higher accuracy can be obtained if necessary with a higher resolution in the finite element mesh or an adaptation of the finite element mesh to the initial data V_0.

A simple cancer invasion system

In the next step we address the numerical resolution of a cancer invasion model. In more detail, we consider model (6.12) that we used already in Section 6.7 to study our 2D AMR scheme. The system expands the pioneering model in [8] with a logistic growth term. We refer to Section 2.5 for the model derivation. Converse to our numerical study in Experiment 6.7 we take here the 1D case into account, which reads

$$\begin{cases} \partial_t c = \partial_x \left(D_c \partial_x c - \chi c \partial_x v \right) + \mu c(1-c) & \text{in } I \times \mathbb{R}^+, \\ \partial_t v = -\delta v m & \text{in } I \times \mathbb{R}^+, \\ \partial_t m = D_m \partial_x^2 m + \alpha c - \beta m & \text{in } I \times \mathbb{R}^+. \end{cases} \tag{7.31}$$

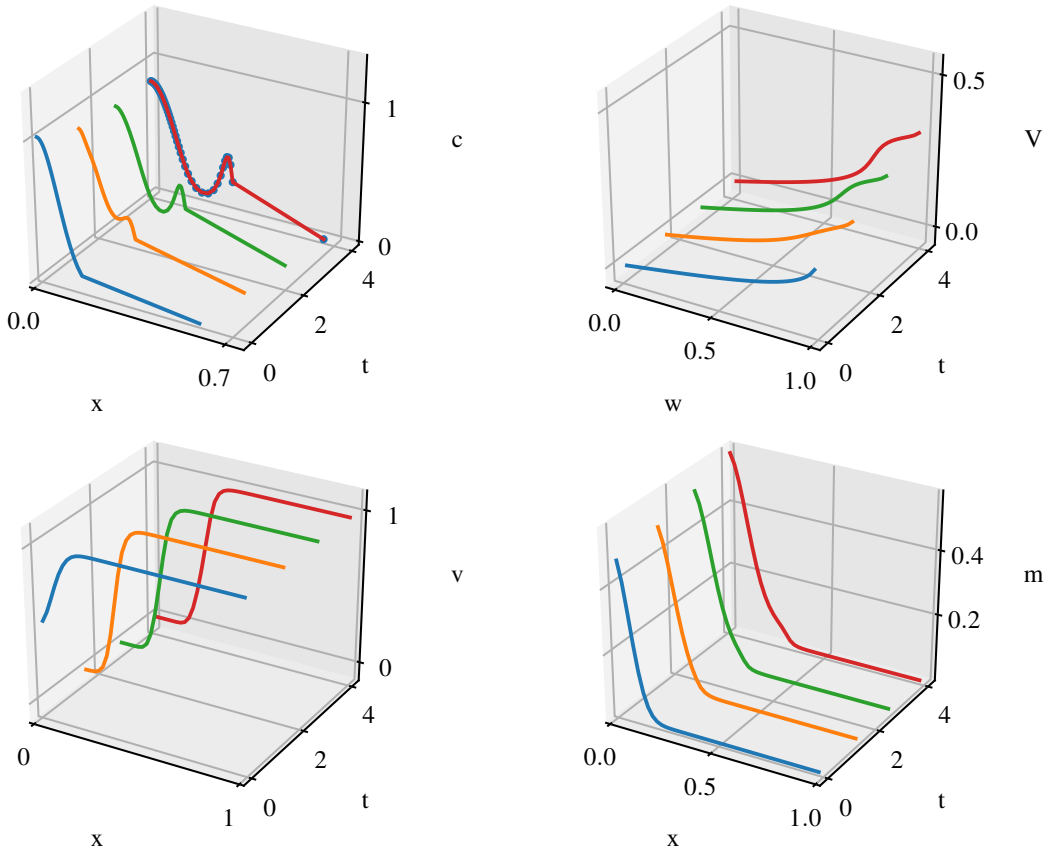

Figure 7.5: Numerical results (cell concentration, inverse cumulative function, tissue and MMP density) in Experiment 4c with model (7.31) using only $N = M = 45$ mesh points. A high concentration of tumor cells emerges and invades the tissue. The grid of the tumor density omits the part of the tissue that is not yet invaded.

We assume positive initial data c_0, v_0, m_0 and homogeneous boundary conditions together with system (7.31).

The adapted MTFE method discretizes both the ECM density v and the MMP concentration m on the same finite element basis. The corresponding approximations are updated in the reaction-diffusion operator of the splitting method. The interpolations are only needed with respect to the ECM density v. We resolve the migration of the cancer cells in transformed variables with the advection-diffusion operator and the cell proliferation with the reaction-diffusion operator.

For our numerical experiment, namely Experiment 4c, we used the computational domain $I = (0, 1)$ and the following initial conditions

$$c_0(x) = e^{-x^2/\varepsilon}, \quad v_0(x) = 1 - 0.5\, e^{-x^2/\varepsilon}, \quad m_0(x) = 0.5\, e^{-x^2/\varepsilon}$$

with $\varepsilon = 10^{-2}$. Moreover, we used the parameter $D_c = 2 \cdot 10^{-4}$, $\chi = 5 \cdot 10^{-3}$, $\mu = 0.2$, $D_a = 10^{-3}$, $\delta = 10$, $\alpha = 0.1$, $\beta = 0$. We applied the splitting scheme (7.18) using meshes of $M = N = 45$ points and the CFL condition (7.23).

This numerical experiment simulates the propagation of cancer cells to the right side. To account for the corresponding temporal expansion of the support of the cancer cell density c we adapted the treatment of the right boundary. In more detail, we ignored the discrete cancer cell density entry adjacent to the right boundary ($c_M(t)$) in the proliferation update

τ/τ^{ref}	error $E^V_{\Delta t}$	EOC^t	M/M^{ref}	error E^V_M	EOC^V
0.1/ 0.05	2.244e-04		10 / 20	7.867e-03	
0.05/ 0.025	4.728e-05	2.247	20 / 40	1.919e-03	2.035
0.025 / 0.0125	1.107e-05	2.094	40 / 80	4.475e-04	2.100
0.0125 / 0.00625	2.766e-06	2.001	80 / 160	1.514e-04	1.563

Table 7.2: Experimental convergence in time (left) and in space (right) in Experiment 4c at $T = 1$. In all computations we set $N = M$. The EOCs suggest a convergence of second order in time and space.

(7.15). However, the corresponding boundary entry in the cumulative function, V_{M-1}, was not excluded from the diffusion and haptotaxis updates of the scheme.

We present the numerical results in Figure 7.5. Apart from the propagation of the cells into the tissue, we observe a build up of cancer cells at the leading front of the tumor. The degradation of the tissue and the MMP production are also visible in the simulation results. Throughout the considered timespan the not invaded part of the tissue is resolved by a single mesh cell in the cancer density.

In the current experiment we also studied the convergence of the scheme experimentally. Along with the errors in space, we computed the errors in time by the formula

$$E^V_{\Delta t} = \frac{1}{M} \sum_{j=1}^{M-1} \left| V_j^{h,\Delta t} - V_j^{h,2\Delta t} \right|, \tag{7.32}$$

where $V_i^{h,\Delta t}$ for $i = 1, \dots, M-1$ denotes a numerical solution computed on M mesh points with constant time increment Δt. For the computation of the temporal errors we considered a fine spatial resolution with $M = N = 600$. The corresponding EOC is given by $EOC^t = \log_2(E^V_{\Delta t}) - \log_2(E^V_{2\Delta t})$. The spatial errors and EOCs were computed according to (7.29) and (7.30) with constant time increment $\Delta t = 2 \times 10^{-4}$ and coupled $N = M$. Both temporal and spatial errors were computed at the final time $T = 1$.

In Table 7.2 we present the computed errors and EOCs in the invasion experiment. We see that the method converges as either the mesh size or the time increment is refined. The EOCs in time and space range around two which confirms our expected second order. As in the "peak splitting" experiment, the EOCs decreases slowly as the mesh is refined. We note that previous numerical tests which did not employ our proposed boundary treatment yielded only a spatial EOC of one.

The uPA model

Lastly, we consider an application of the MTFE scheme to the full uPA model (I). In particular, we apply our method to resolve again Experiment 1 that we studied in Sections 5.11 and 6.6. We refer to Section 2.6 for the model and the parameters and to Section 5.11 for the initial conditions. We conducted the experiment on the domain $I = (0, 10)$.

The corresponding adaptation of the MTFE method uses a single finite element basis to discretize the concentrations of the ECM (v), of uPA (u), of PAI-1 (p) and of plasmin (m). The cubic spline in the advection-diffusion operator interpolates the linear combination $\chi_v v + \chi_u u + \chi_p p$. Similar as in the case of models (7.28) and (7.31) the scheme approximates

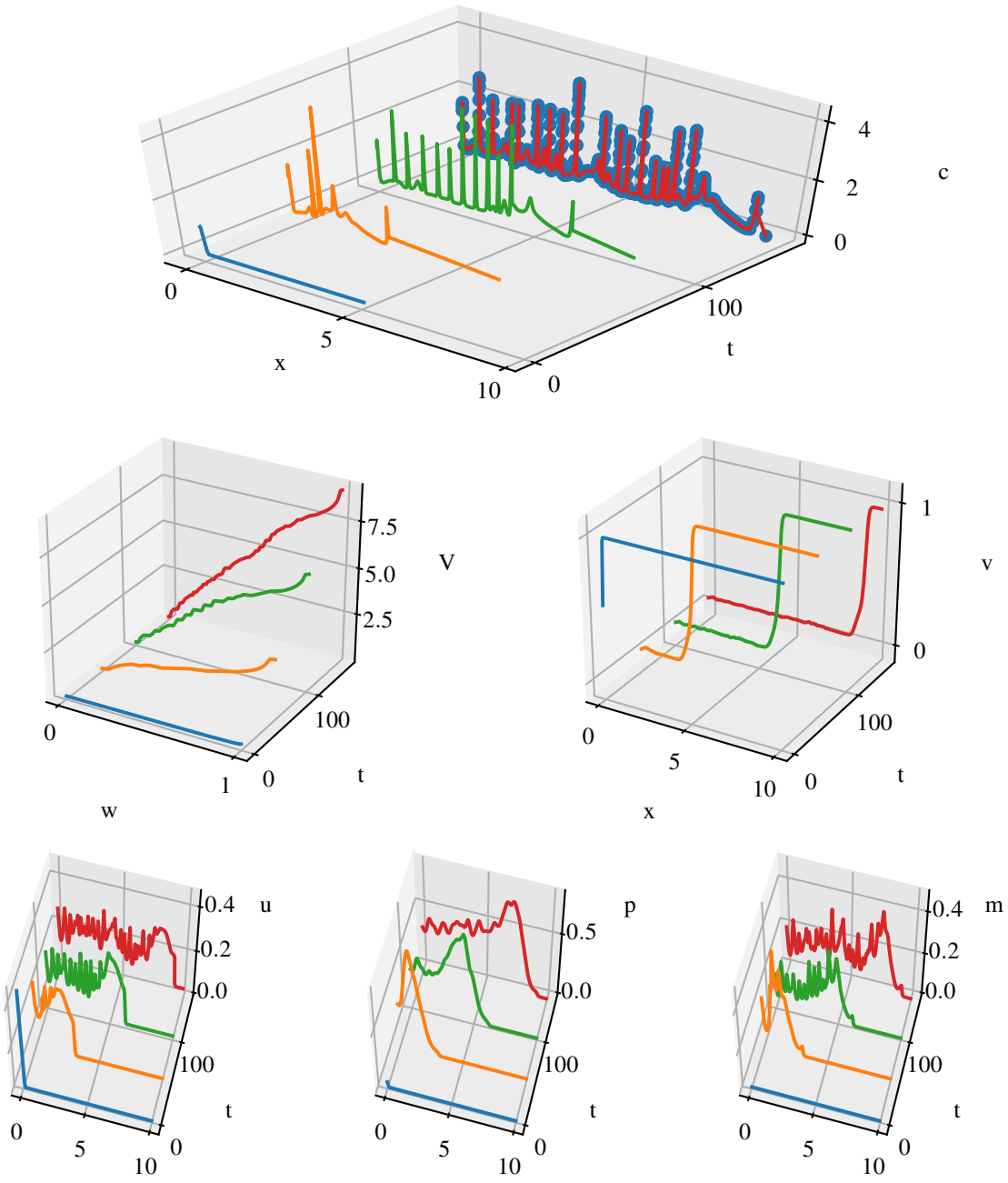

Figure 7.6: Numerical results (cancer cell concentration, inverse cumulative function, ECM, uPA, PAI-1 and plasmin density in space and time) in Experiment 1 computed by the MTFE scheme. The dynamics, particularly the steep peaks in the cancer cell density, are well resolved by the scheme. We used $M = N = 400$ grid points on both meshes.

the cell proliferation in Eulerian coordinates but diffusion and advection in transformed variables. The scheme employs the same boundary treatment as used in Experiment 4c.

In Figure 7.6 we present the simulation results obtained by the MTFE scheme with mesh resolution $M = N = 400$. The method is capable to approximate accurately the dynamics that we saw and discussed in Sections 5.11 and 6.1 including the emergence and movement of multiple steep peeks. The present simulation clearly demonstrates the reliability and robustness of the newly developed MTFE scheme.

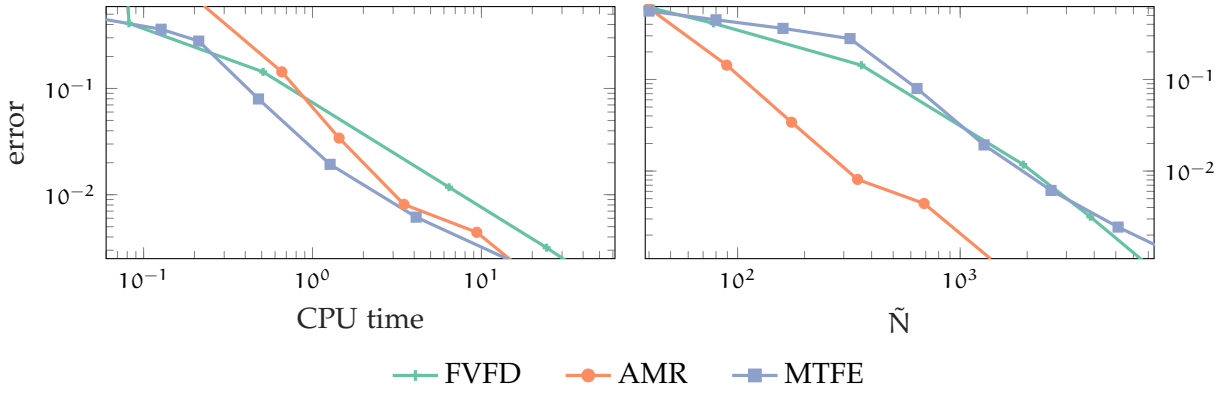

Figure 7.7: Relation between the CPU time and the error (left) and between the average number of cells and the error (right) for the FVFD, the AMR and the MTFE scheme in log-log scale in Experiment 1. The new MTFE method seems to be most efficient in terms of error per CPU time, its relation between the error and the average number of cells is similar as for the FVFD scheme.

In the situation of the current numerical experiment, we further studied how the new method compares in efficiency to the more conventional FVFD scheme introduced in Chapter 5 and to the AMR method developed in Chapter 6. We considered the following two particular methods for the comparison: on the one hand we chose scheme (5.30) for uniform 1D meshes endowed with STRANG time discretization (see Section 5.7). On the other hand we considered its AMR counterpart described in Section 6.5. For the AMR method we chose the gradient monitor function (6.9a) together with the threshold values $\theta_{\text{ref}} = 10$, $\theta_{\text{coars}} = 2.5$, which delivered the best results in our comparison of AMR methods in Section 6.6. Further we chose the AMR parameters $n_{\text{ref}} = n_{\text{coars}} = 1$, $n_{\text{ref},0} = 3$ and $l_{\min} = 0$, $l_{\max} = 2$. For brevity, we will refer to the adaptive method as AMR and to the uniform method as FVFD.

For our comparison we took the set $S = \{40, 80, 160, 320, 640, 1280\}$ and ran the AMR method for $N_0 \in S$, the MTFE method for $M \in S$ and the FVFD method for $N = 6k$ for any $k \in S$. We coupled the two meshes in the MTFE scheme by $N = M$. We did not consider finer resolutions due to restrictions by the uniform reference solution in the error computation of the MTFE scheme. All numerical solutions were computed on the domain $\Omega = (0, 5)$. For comparison reasons we consider the average number of cells $\tilde{N}$ that we defined for the AMR method in Section 6.6. Note that for the FVFD method and the MTFE method it holds that $\tilde{N} = N$.

We used a reference solution that employed a uniform mesh with a cell size of $h = 1.25 \times 10^{-5}$ in the relevant part of the domain[1]. The discrete L^1 error was then computed with respect to the densities using a suitable projection of the reference solution according to (5.63), (5.64). We considered the numerical solutions and the reference solution only at the time instance $t = 23$ that features two steep peaks in the cancer cell concentration, compare Figure 6.1. Note that the results that follow are dependent on our (nonreference) implementation of the numerical methods.

The results of the comparison are shown in Figure 7.7 where we present the relation between the error and the computation time as well as the relation between the error and the average number of cells for all three methods. We see that for all tested methods the error decreases as either the cell number or the CPU time increases. Figure 7.7 (left) exhibits an advantage

[1]We computed a uniform solution in $(0, 2)$ with the STRANG method using $N = 160\,000$ mesh cells. For the rest of the considered domain we used the reference solution considered in Section 5.11 computed by the method of Dormand and Prince.

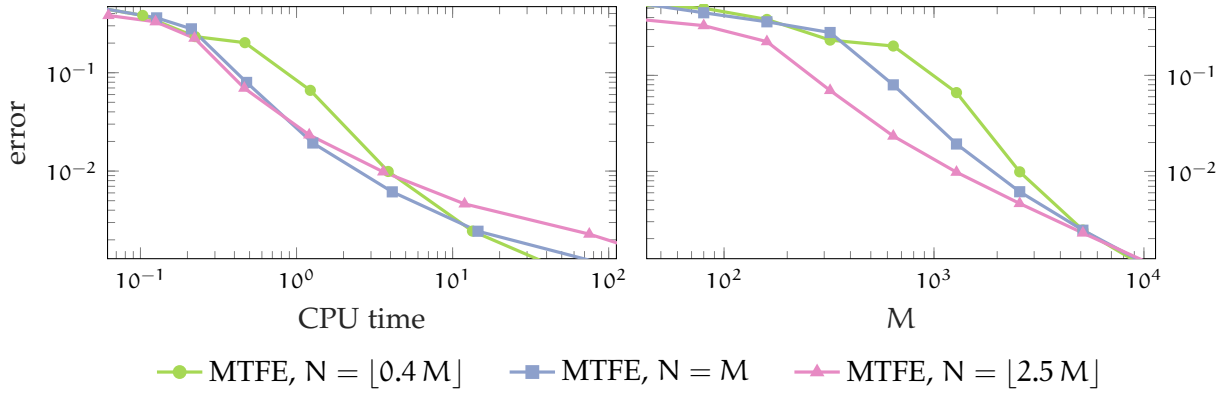

Figure 7.8: Relation between the CPU time and the error (left) and between the number of points in the discretization of V and the error (right) for the MTFE scheme in log-log scale in Experiment 1. Three distinct relations between finite element and mass space mesh are compared.

of the new MTFE method over the other schemes in efficiency for most of the conducted simulations. This is because the MTFE method achieves in most cases lower errors than the FVFD or the AMR scheme using the same CPU time. As the runtime increases the MTFE method approaches the efficiency of the AMR method with the new method being at a slight advantage over the mesh refinement method. Clearly, the AMR and the MTFE scheme both outperform the FVFD method for sufficiently large CPU times.

Figure 7.7 (right) shows that the AMR method achieves the lowest errors when compared with simulations by the FVFD and MTFE scheme employing the same average number of cells. The error of the MTFE scheme has a similar dependence on the number of cells as the error of the FVFD scheme. We thus conjecture that the better efficiency of the MTFE scheme in terms of CPU time, seen in Figure 7.7 (left), is probably caused by the CFL condition in the MTFE scheme allowing for larger time steps compared to the FVFD method.

To address the question, if the finite element mesh should be taken coarser or finer than the mesh over the mass space in the MTFE method, we considered another comparison. Here we computed further numerical solutions by the MTFE scheme choosing the relations $N = \lfloor 0.4\,M \rfloor$ and $N = \lfloor 2.5\,M \rfloor$. We used the same cancer invasion experiment as above.

Figure 7.8 (left) reveals a slightly lower error per CPU time when employing finer finite element meshes but only for low CPU times; for larger CPU times and thus more accurate simulations it seems that coarser finite element meshes are more efficient. However, we see only a small advantage of the $N = \lfloor 2.5\,M \rfloor$ over the $M = N$ strategy for large CPU times. In Figure 7.8 (right) we show the error dependence on the number of points on the mass space M for the three considered strategies. We see that the finer finite element mesh leads to lower, and the coarser finite element mesh lead to larger, errors per M when compared to the strategy $M = N$. However, these benefits and drawbacks over the $M = N$ strategy decrease as M increases and become negligible for large M in the range of 10^4. These results suggest that we can choose coarser finite element meshes for larger M without sacrificing the accuracy of the numerical solution. Also, our initially chosen relation $M = N$ has been a reasonable compromise for the considered test cases.

8 Numerical investigation

The present chapter is devoted to numerical experiments with the contractivity model and with the haptotaxis EMT/invasion model. We study the model dynamics and focus on the characteristic novelties that both models bring along, being the delay term in the contractivity model and the nontrivial EMT coefficient in the haptotaxis EMT/invasion model. To this end we investigate the sensitivity on the model parameters.

To begin with we demonstrate the experimental convergence of our numerical method in Section 8.1. Afterwards we present numerical experiments and parameter studies for model (III) in Section 8.2 and the same for model (II) in Section 8.3. To ease the presentation we have moved the technical details with respect to the parameters used in the numerical experiments to Appendix A. The computations we present were conducted using MATLAB.

8.1 Experimental convergence of the numerical method

All numerical simulations that follow were realized by the FVFD scheme presented in Chapter 5. In more detail, we used the scheme (5.32) for the treatment of model (III) and the scheme (5.31) to resolve the dynamics of model (II). Due to its good performance, as demonstrated in Section 5.11, we chose the IMEX3 scheme for the time integration of both models. In the case of the contractivity model (III) we further employed the modifications discussed in Section 5.10. For the haptotaxis EMT/invasion model (II) we used the positivity preserving IMEX-EULER scheme as fallback in the case of occurring negative solutions with the IMEX3 scheme, see Section 5.9. As in the experiments with system (I), we always used the Courant number $\mathrm{CFL} = 0.49$. All our 1D simulations in the following sections were conducted on a uniform finite volume mesh consisting of $N = 7000$ cells. The 2D simulations employed a quadrilateral Finite Volume mesh consisting of $L = M = 250$ mesh cells in both space directions.

In what follows we present the EOCs of the chosen methods for both models. For that purpose we consecutively refined the full mesh and computed the discrete L^1 error $E(h)$

	c^p		c^m	
mesh cells	L^1-error	EOC	L^1-error	EOC
25×25/50×50	2.399e-02		4.195e-02	
50×50/100×100	6.067e-03	1.983	1.088e-02	1.948
100×100/200×200	1.514e-03	2.003	2.751e-03	1.983
200×200/400×400	3.785e-04	2.000	6.912e-04	1.993

Table 8.1: Experimental convergence of the numerical approximations of the migratory and proliferating cancer cells in Experiment 5a with system (III) at time instance $t = 1$.

	DCCs		CSCs	
mesh cells	L^1 error	EOC	L^1 error	EOC
512/1024	1.953e-05		8.625e-03	
1024/2048	4.430e-06	2.140	3.614e-03	1.255
2048/4096	1.061e-06	2.062	1.193e-03	1.599
4096/8192	2.569e-07	2.046	3.639e-04	1.713

	DCCs	
mesh cells	L^1 error	EOC
16×16/32×32	1.020e-01	
32×32/64×64	3.090e-02	1.723
64×64/128×128	8.453e-03	1.870
128×128/256×256	2.180e-03	1.955

Table 8.2: Experimental convergence in system (II) for the DCC and CSC concentrations in the 1D Experiment 6a (left) and for the DCC densities in the 2D Experiment 6c(right). The errors are computed at the time instance $t = 15$ in the 1D case and at the time instance $t = 10$ in the 2D case [151].

according to (5.64) using a numerical solution with mesh discretization parameter $h/2$ as reference. The EOCs were then computed by $EOC = \log_2(E(h)) - \log_2(E(h/2))$.

In this way, we have studied the experimental convergence in Experiment 5a with system (III) at the fixed final time $T = 1$ with results shown in Table 8.1. The computed EOCs clearly verify our expected second order of convergence in the considered 2D experiment for the computed densities of both cell types, migratory and proliferating cancer cells. Similarly, we computed the EOCs in the case of model (II). We present the results for the 1D Experiment 6a and the 2D Experiment 6c at the final time instances $t = 15$ and $t = 10$ in Table 8.2. Again, the decrease of the errors as the mesh is refined and the EOC of two confirm the suitability of our proposed method for the present models.

The EOCs and the observed drops in the errors in Tables 8.1 and 8.2 along with the fine resolution that we chose for the numerical experiments attest that the simulation results in the following sections are not dominated by numerical artifacts but display the actual dynamics of the cancer invasion models.

8.2 Study of the contractivity model (III)

This section is based on our numerical experiments in [98]. We restrict our study of the contractivity model (III) to a single numerical experiment, namely Experiment 5b, in which we explore the role of the delay parameter τ. The corresponding initial data and parameters were jointly identified with Nikolaos Sfakianakis and Bettina Wiebe. For a deeper study of the dynamics of (III) and related models, we refer to [121, 175].

In our experiment we assumed that the initial density of both proliferating and migratory cancer cells is concentrated at the center of the computational domain, with the migratory cell density being the larger one. As in Experiment 3 the ECM was initially assumed homogeneous and degraded at the position of the cancer cells. Following [121], both integrin density and contractivity were initially only increased in an annular area around the center of the domain. The initial data and numerical results are shown in Figure 8.1. All initial densities, and therefore also the numerical solutions at any time instance, are radially symmetric. Thus, we present only radial cuts of both the numerical solutions and the initial conditions.

As time evolves, a steep front of migratory cancer cells forms and invades the tissue. Further, the integrins located at the bulk of the tumor unbind from the ECM, while almost all the integrins outside of the invaded center of the domain bind to the ECM. The contractivity of the cells in turn develops a similar spatial profile as the density of the ECM bound integrins y. Figure 8.1 exhibits the numerical solution at the time instance $t = 0.5$ for two different

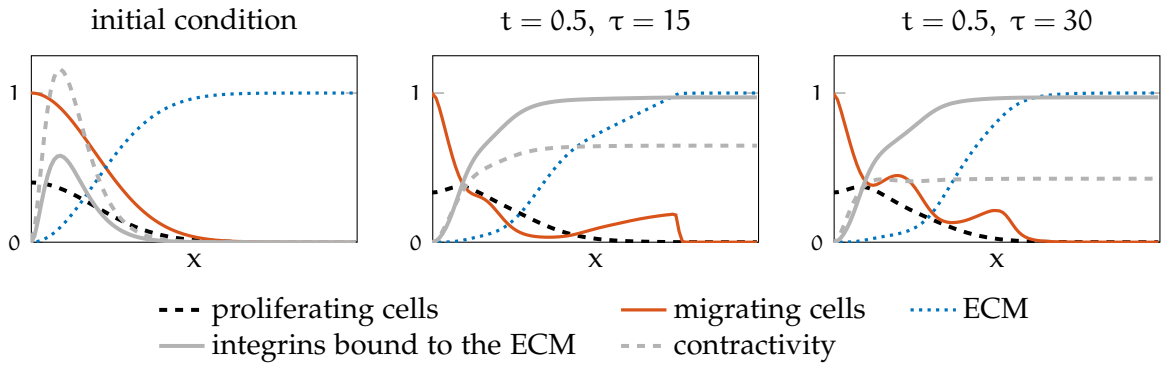

Figure 8.1: Radial cuts of the spatial concentrations in the initial condition and in the numerical solution of Experiment 5b . Time instance $t = 0.5$ is considered for two different delay parameters τ in the contractivity model (III). For both choices of the delay parameter the migratory cells invade the tissue similar as in Experiment 1. The integrins outside of the center of the domain (here on the left border) attach to the ECM [98].

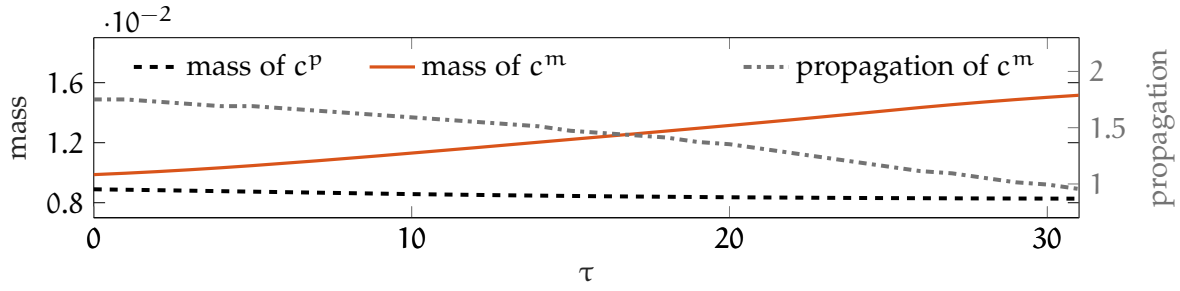

Figure 8.2: Total mass of the proliferating and migratory cancer cells (with densities c^p and c^m) and the propagation of the tumor in Experiment 5b when varying the delay parameter τ in the contractivity model (III). An increase of the delay elevates the mass of the migratory cells but slows down their propagation [98].

choices of the delay parameter. This parameter accounts for the time it takes the integrin bindings to translate into changes with respect to the contractivity. We tested the parameter values $\tau = 15$ and $\tau = 30$. The increase of the delay parameter has a significant impact on the tumor, as the propagation of the migratory cells is apparently slower in the case of a larger delay. In this case we therefore observe the emergence of a pronounced secondary cluster of migratory cancer cells. The longer time that the integrin binding takes to influence the migration capabilities of the tumor in the case of the larger delay ($\tau = 30$) also diminishes the contractivity when compared to the case of the smaller delay ($\tau = 15$).

For a deeper insight in the influence of the delay parameter we ran Experiment 5b multiple times while varying $\tau \in [0, 33]$. In each simulation we computed the total mass of proliferating and migrating cancer cells over the full domain as well as the propagation of the migratory cells[1] at the time instance $t = 0.5$. The results presented in Figure 8.2 show that an increase of the delay τ decreases not only the propagation speed of the migratory cells, but also increases their mass while the mass of the proliferating cells does not seem to be significantly affected by changes in τ. Thus, as expected from the model, the following context is predicted: the longer the ECM/integrin binding triggered pathway needs to affect the contractivity, the more the tumor will stay in place and proliferate rather than propagate into the tissue.

[1]To measure the propagation of the migratory cells into the tissue, we considered a radial cut of the domain, cf. Figure 8.1. Then we computed the location of the discrete local maximum of the migratory cancer cell density that was the closest to the right boundary of the interval.

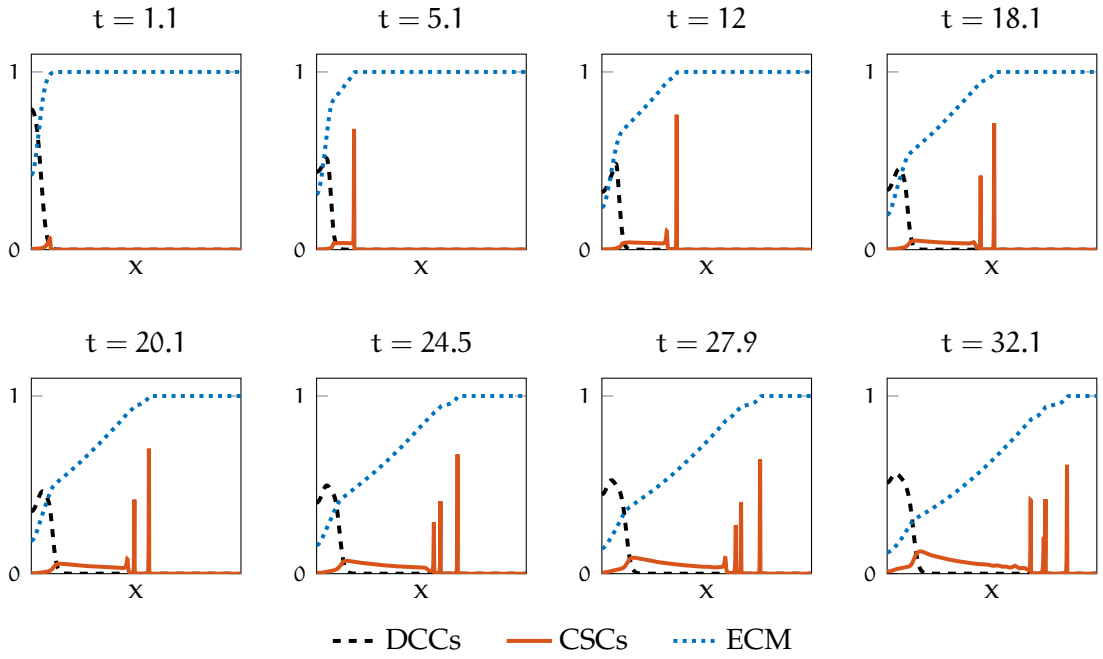

Figure 8.3: Experiment 6a: Dynamics in space and time in model (II) in 1D. We present the spatial concentrations of DCCs, CSCs and the ECM in consecutive time instances. The CSCs evolve from the DCCs via EMT and invade the tissue, exhibiting merging and emerging concentrations and promoting the growth of the main tumor consisting of DCCs [151].

8.3 Study of the haptotaxis EMT/invasion model (II)

The present section is based on a part of [151]. Except for the new Experiments 10a and 10b, the model parameters and the initial conditions of the particular numerical experiments were identified jointly with Nikolaos Sfakianakis.

For a first insight into the model dynamics of system (II) we consider a simulation on a 1D domain (Experiment 6a). Similar as in Experiment 1 we assumed an initial concentration of DCCs along with a small amount of MMPs at the left boundary of the domain and a uniform initial ECM that is degraded at the position of the tumor. We did not assume any present CSCs or fibroblasts at the initial time instance. Figure 8.3 exhibits the dynamics of the numerical solution: the DCCs quickly (i.e. after a few hours) undergo EMT and form a concentration of CSCs that escapes the bulk of the tumor and invades the ECM. The main tumor consisting of DCCs disseminates and slowly invades the tissue following the more motile CSCs. While migrating into the tissue, the CSCs, unlike the DCCs, show the dynamical mergig and emerging behavior that we also saw in Experiment 1.

In Figure 8.4 we present the numerical results of an analog experiment in 2D, namely Experiment 6b. Comparably with Experiment 6a the DCCs break out of the main tumor and invade the ECM in dispersing waves. At the same time the DCCs spread following the CSCs and form a growing tumor while degrading the ECM.

Figure 8.5 contrasts our modeling approach of the EMT with the common trivial model of a constant EMT rate. Therefore, we considered a space independent situation without migration terms and simulated how the number of both cancer cell types DCCs and CSCs evolve in time when we initially assume only a few DCCs and no CSCs. We fitted the EMT rate in the trivial model, such that the dynamics in 1D roughly matched those in a simulation with

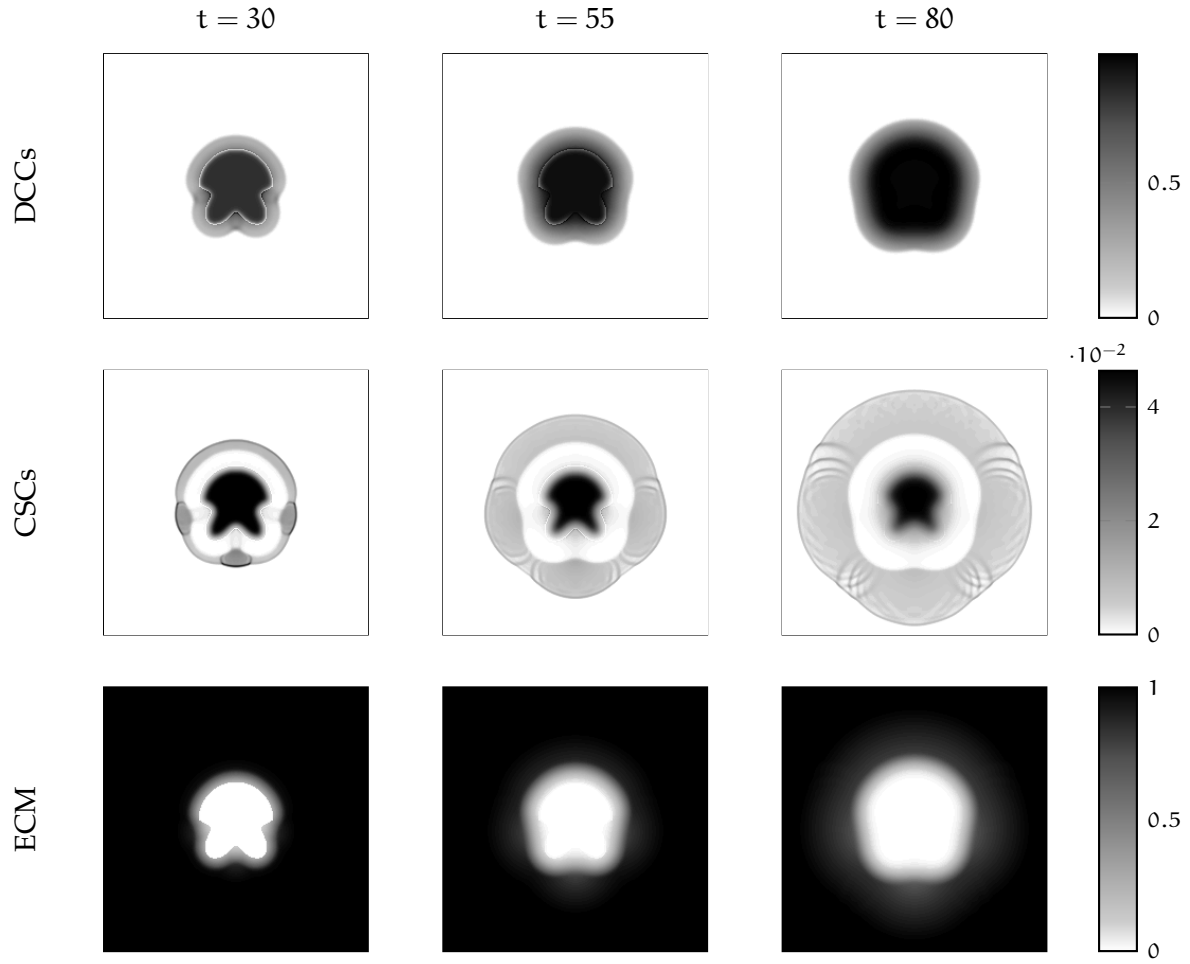

Figure 8.4: Experiment 6b: Numerical solution of the concentrations of DCCs, CSCs and the ECM in consecutive time instances on a square domain. The colorbar ticks refer only to the densities at the time instance t = 80. The CSCs that develop from DCCs via EMT invade the tissue in waves [151].

our EMT model, compare Experiments 7a and 7b. Figure 8.5 shows that in the case of the trivial model the number of CSCs quickly rises over the number of DCCs. Thus, the CSCs reach a detectable quantity even before the DCCs can be detected. The situation is reversed in the case of the proposed EMT model: here the DCCs are the first to grow to a detectable number before the CSCs start to augment. Hence, the prediction of our EMT model assorts well with the observation that the CSCs make up only a small part of the tumor [143], while the prediction of the trivial EMT model does not.

To explore the particular roles of the EMT related model components in the model dynamics, we conducted a parameter study similar as in the previous section. More precisely, we considered Experiment 6a and computed the numerical solution at time instance t = 15 while varying the model parameters one at a time. For each numerical solution we then computed a) the mass of the DCCs over the full domain, b) the mass of the CSCs over the full domain, c) the distance between the propagating fronts of the CSCs and the DCCs[2] and d) the concentration at the invading cluster of CSCs. Figure 8.6 visualizes the effect of varying the

[2]To measure the distance between the propagating fronts we computed the propagation of both the DCCs and the CSCs, as done to obtain the propagation of the migratory cells, c.f. Figure 8.2, and computed the respective difference.

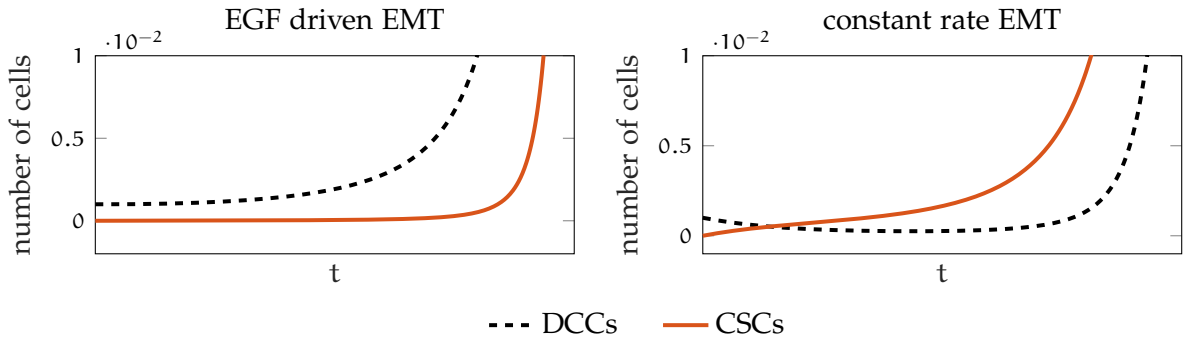

Figure 8.5: Time evolution of the numbers of DCCs and CSCs in the EGF driven EMT model (Experiment 7a, left) and in the trivial EMT model (Experiment 7b, right). Conversely to the trivial model, the EGF model predicts that CSCs are not produced until the DCCs have proliferated to a larger quantity [151].

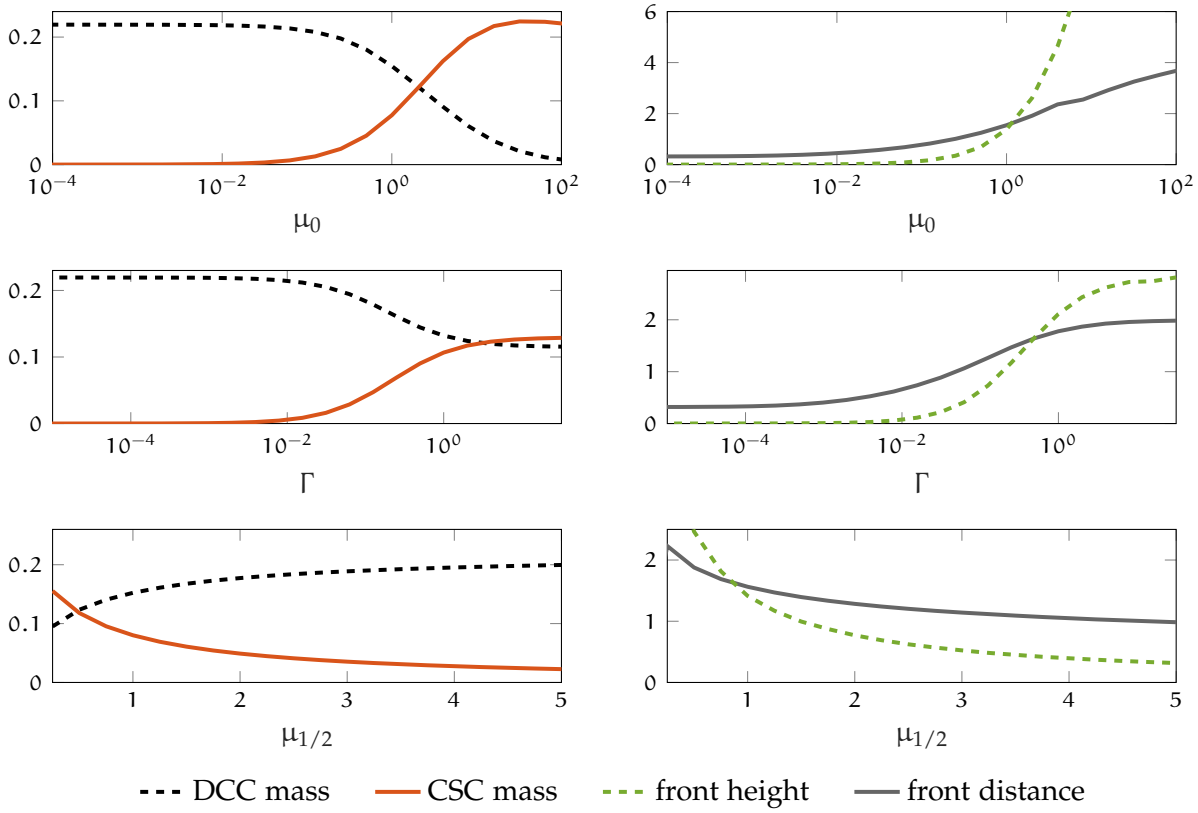

Figure 8.6: Dependence of the mass of cancer cells, of the height of the invading front and of the distance between the DCC and the CSC front on the EMT related parameters in Experiment 6a. An increase of both the EMT factor μ_0 and the number of EGF molecules Γ promotes the tumor aggressiveness by strengthening the EMT. Varying the critical EGF density $\mu_{1/2}$ has the inverse effect [151].

EMT related parameters in model (II). We can clearly see that the model reacts to parameter changes as expected by its construction. An increase of the EMT factor μ_0 promotes the production of CSCs from DCCs as the mass of CSCs raises while the mass of DCCs drops. Thus, also the stem cell invasiveness, quantified by the front peak distance, increases. A raise of the amount of EGFs over the domain, i.e. an increase of the parameter Γ, has a similar effect. However, the influence of Γ on the CSC mass, propagation and front height stagnates once a certain amount of EGF molecules on the domain is reached. This is caused

	parameter	DCC mass	CSC mass	front distance	front height
D_D	diffusion coeff. of DCCs	+1.2342e+01	-8.1722e+00	+1.3714e+02	-7.3024e+01
D_S	diffusion coeff. of CSCs	+9.4182e-02	-3.2915e-01	0	-9.5376e+03
D_F	diffusion coeff. of fibroblasts	-2.2642e-02	+2.1300e-03	0	+3.9125e-01
D_m	diffusion coeff. of MMPs	-2.9334e-01	-9.5195e-02	-2.8800e+01	-1.6365e+02
χ_D	haptotaxis coeff. of DCCs	+8.9096e-01	-3.4507e-01	-1.3500e+01	-3.1985e+00
χ_S	haptotaxis coeff. of CSCs	-9.4425e-03	-3.5106e-03	+1.5600e+00	+4.9956e-01
χ_F	haptotaxis coeff. of fibroblasts	-7.0482e-03	-8.6437e-04	0	-1.6845e-03
λ^D	EGF receptors per DCC	-3.2691e-02	+4.6710e-02	+5.4000e-01	+7.5617e-01
λ^S	EGF receptors per CSC	+5.1239e-04	-6.5509e-04	0	-1.4768e-02
k_D	EGF unbinding/binding	+5.1703e-02	-7.4019e-02	-8.6400e-01	-1.1744e+00
Γ	average of total EGF	-2.1830e-01	+3.1164e-01	+3.6000e+00	+5.0090e+00
μ_0	EMT factor	-6.6859e-02	+9.5767e-02	+1.1345e+00	+1.5432e+00
$\mu_{1/2}$	critical EGF density	+1.7618e-02	-2.5178e-02	-2.8800e-01	-4.0878e-01
μ_D	proliferation rate of DCCs	+2.3304e-01	+3.9116e-02	+1.2000e-01	-6.8597e-04
μ_S	proliferation rate of CSCs	+2.2971e-04	+4.9220e-02	0	+4.6599e-03
μ_F	proliferation rate of fibroblasts	-1.3865e-04	-5.2592e-05	0	+1.1644e-03
μ_v	ECM remodeling rate	+5.2516e-02	+1.0917e-02	+6.6000e-01	+2.4808e-01
β_F	apoptosis of fibroblasts	+1.2117e-03	+4.8903e-04	0	-7.7809e-03
β_m	decay rate of MMPs	-4.7396e-02	-9.1276e-03	-4.9200e-01	-8.6865e-01
α_D	MMP production rate of DCCs	+3.6965e-01	+2.6936e-02	0	+7.9042e-01
α_S	MMP production rate of CSCs	+6.4883e-03	+6.6901e-03	+6.6000e-01	+1.3518e-01
δ_v	ECM degradation rate	-6.8955e-06	-4.4457e-06	0	-4.8110e-05
μ_T	transdifferentiation rate	-2.0113e-01	-6.7081e-01	-1.2000e+01	-3.6641e+01

Table 8.3: Parameter sensitivity in Experiment 6a. Large absolute value in the table indicate a high influence of the parameter (row) on the corresponding attribute (column) [151].

by the limited number of available EGFRs on which the EGF must bind to trigger the EMT. Altering the critical EGF density $\mu_{1/2}$ has an converse effect: an increase diminishes the tumor aggressiveness and promotes the production of DCCs.

For an in-depth look on all the model parameters, we computed the *parameter sensitivities*

$$S_p^{\mathcal{F}} = \frac{\mathcal{F}(\mathbf{w}_h{}^{t=15}(p = p + \delta p)) - \mathcal{F}(\mathbf{w}_h{}^{t=15}(p = p - \delta p))}{2\delta p} \approx \frac{d}{dp}\mathcal{F}(\mathbf{w}_h{}^{t=15}) \tag{8.1}$$

in Experiment 6a, where p denotes an arbitrary model parameter and $\mathbf{w}_h{}^{t=15}(p = p')$ denotes the numerical solution at time instance $t = 15$ with the particular parameter p modified to p'. Moreover, $\mathcal{F}(\mathbf{w}_h)$ denotes either the mass of DCCs or CSCs over the full domain, the distance between the propagating fronts or the density at the invading cluster of CSCs for the numerical solution $\mathbf{w}_h$. We chose δp relative to the considered parameter value by $\delta p = p/100$. We provide an overview on all computed sensitivities in Table 8.3. The sensitivities show that

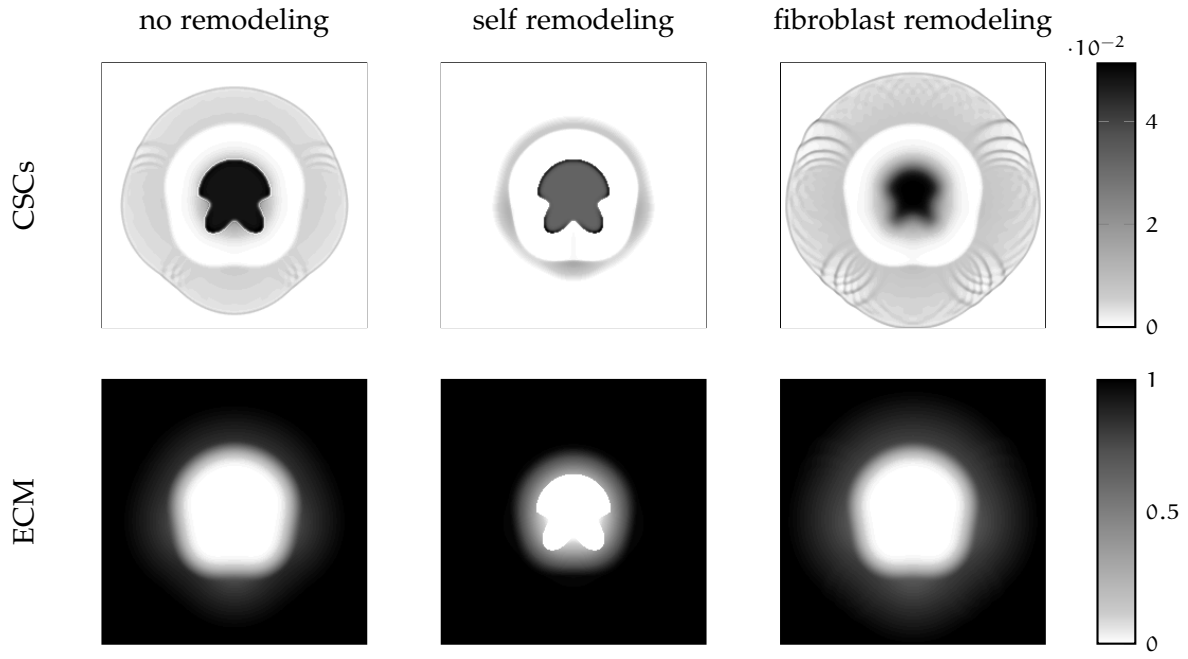

Figure 8.7: Concentrations of the CSCs and the ECM in the cases of no remodeling (Experiment 8a), self remodeling (Experiment 8b) and fibroblast driven remodeling (Experiment 6b) at time instace $t = 90$. Contrary to the other modeling cases, the fibroblast remodeling allows most of the mesenchymal cells to break out of the main tumor [151].

the model exhibits the expected behaviour: the haptotactic sensitivites of both cancer cell types influence the CSC migration significantly and their proliferation rates strongly affect the tumor mass. We can further see that a raise of the transdifferentiation rate from CSCs to fibroblasts decreases the tumor mass, the relative CSCs aggressiveness and the concentration at the invading front.

But the results in Table 8.3 also provide less expected information. In fact, the simulated tumor becomes more malignant as the ECM remodeling rate is increased, since the cancer cell mass and the relative aggressiveness is raised in this case. Moreover, the apoptosis of fibroblast cells affects the tumor mass positively while increasing their proliferation rate diminishes the proliferation of cancer cells. Our model thus predicts a twofold role of the fibroblasts on the tumor: on the one hand their remodeling of the tissue allows for a larger haptotactic motility of the cancer cells but on the other hand the fibroblasts restrict the resources and free space that promote the proliferation of the cancer. By raising the number of EGF receptors on the DCCs the EMT is strengthened as the CSC mass and relative aggresiveness increases in response. On the contrary, altering the EGF receptors on the CSCs weakens the EMT but to a smaller extent.

Following from the results of the parameter study in Figure 8.6 and Table 8.3, our model suggest the following therapy approaches to limit the tumor growth: firstly, according to our model, tumor growth and metastasis can be decelerated by either reducing the amount of EGF in the tissue or by blocking the corresponding EGF receptors on the DCCs in the tumor. A second treatment strategy suggested by the dynamics of (II) would involve a reduction of the number of fibroblasts or a suppression of their remodeling capability.

In Figure 8.7 we take a closer look at the fibroblast driven remodeling of the ECM that we assumed in model (II). To this end, we compared a 2D simulation with our model where

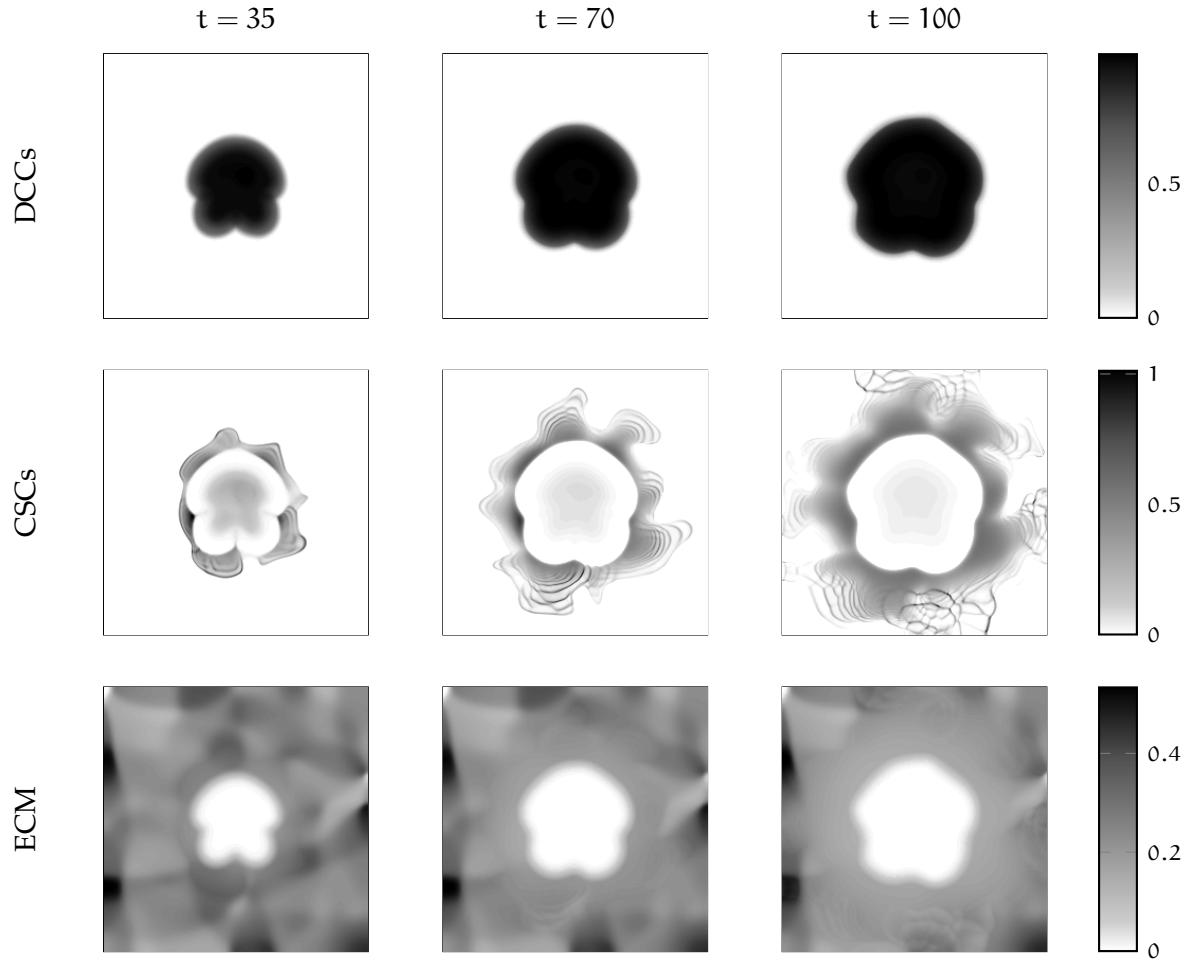

Figure 8.8: Experiment 9: Numerical solutions for the concentrations of DCCs, CSCs and the ECM in consecutive time instances on a square domain in the case of a heterogeneous initial ECM. The tissue concentration was precomputed by Nikolaos Sfakianakis. The colorbar ticks refer only to the densities at the time instance $t = 100$. The maximal CSC density increased from approximately 0.1 in $t = 35$ over 0.45 in $t = 70$ to 1 in $t = 100$. The CSCs break out of the main tumor and invade the tissue along the heterogeneous ECM gradient [151].

we assumed either no remodeling at all, the common self remodeling of the ECM or our proposed fibroblast driven model, compare Experiments 8a, 8b and 6b. Then we visualized the simulated spatial CSC and ECM densities at the same time instance. We can see that the tissue remodeling by fibroblasts allows for a faster migration of the mesenchymal cells into the tissue when compared to the other two cases. Further, only in the fibroblast model the majority of CSCs breaks out of the bulk of the tumor as suggested in [165].

Figure 8.8 shows the simulation results in another numerical experiment in 2D where we assumed a heterogeneous ECM that accounts for the presence of further cells and structures in the tissue (Experiment 9). In this case the invasion of both DCCs and CSCs is significantly affected by the nonuniform ECM. Thus, the growing tumor adapts to the structure of the tissue. In particular, we see the appearance and the interactions of waves in the CSC concentration. These waves propagate along the gradient of the ECM.

Another kind of pattern in the numerical simulations with model (II) can be obtained without assuming a structured ECM but by altering the model parameters. To this end we considered a modified set of parameters that induces an advection-diffusion-driven instability.

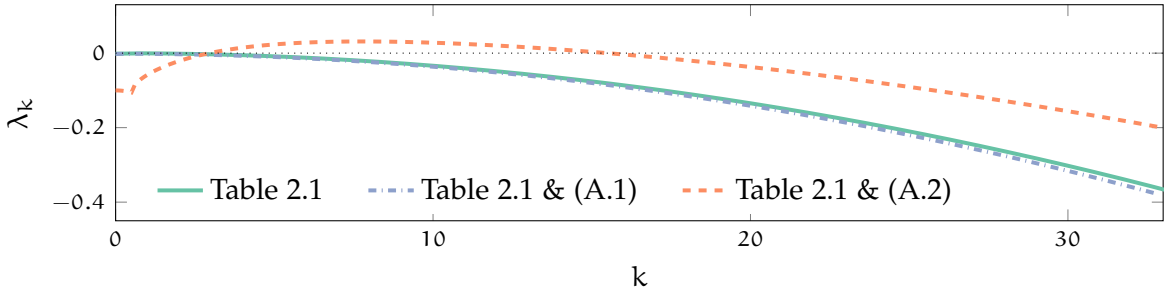

Figure 8.9: Dispersion relations for three parameter sets in the haptotaxis EMT/invasion model (II). The parameter sets correspond to Experiments 6a, 6b and 10a/10b. The positive region in the case that the parameters are given by Table 2.1 and (A.2) indicates an advection-diffusion-driven instability.

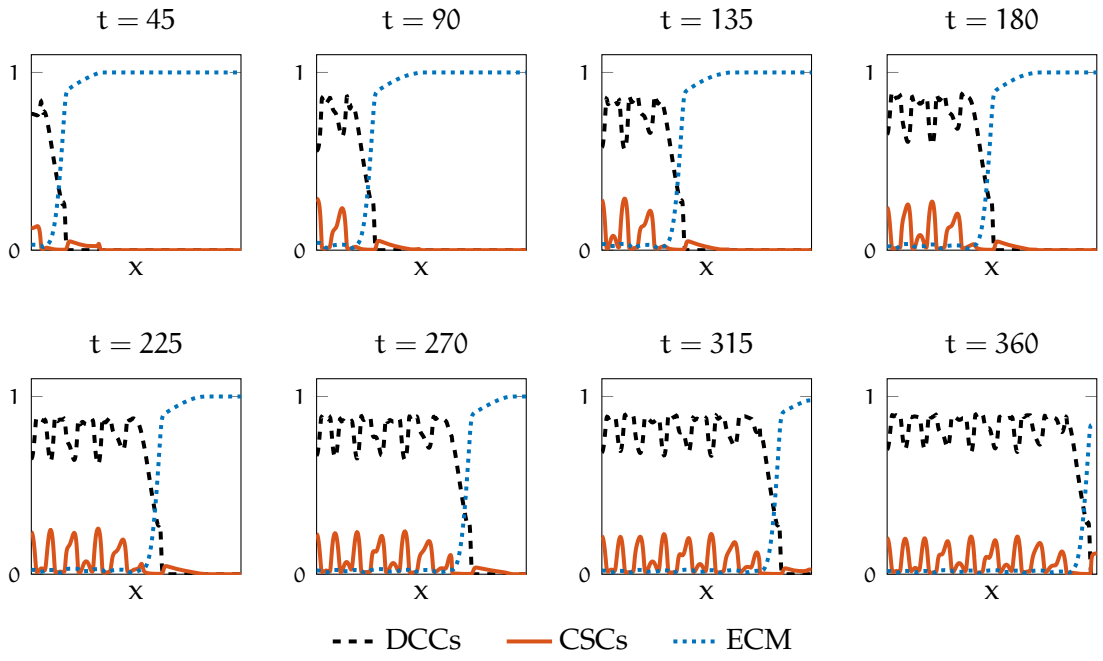

Figure 8.10: Experiment 10a: Space and time dynamics in model (II) in 1D with parameters modified by (A.2). We present the space dependent densities of DCCs, CSCs and the ECM in consecutive time instances. A spatial pattern forms in the invaded area of the tissue that stabilizes in time.

The corresponding parameters are provided in (A.2) in the Appendix. They feature, in particular, reduced diffusion coefficients for the cancer cells that can be understood as the assumption of a stiffer tissue when compared to the previous numerical experiments.

An *advection-diffusion-driven instability* refers to a linearly stable steady state of the reaction terms in an ADR system that is destabilized by small perturbations due to advection and diffusion terms. To identify these instabilities, which are commonly studied in pattern formation, one considers the perturbation of a spatially uniform steady state $\hat{\mathbf{w}}$ by the Fourier mode with wave number k on a periodic domain. The perturbation grows in time, if the *amplification factor* $\lambda_k(\hat{\mathbf{w}})$ is positive, while it is damped otherwise. In more detail, the amplification factor $\lambda_k(\hat{\mathbf{w}})$ refers to the maximal real part of all eigenvalues of the matrix $J_R(\hat{\mathbf{w}}) - k^2 J_{A+T}(\hat{\mathbf{w}})$. Here J_R and J_{A+D} denote the Jacobian of the reaction terms and the Jacobian of the sum of the advection and the diffusion terms. If there is a positive k with $\lambda_k(\hat{\mathbf{w}}) > 0$, one speaks of an advection-diffusion-driven instability. In reaction-diffusion

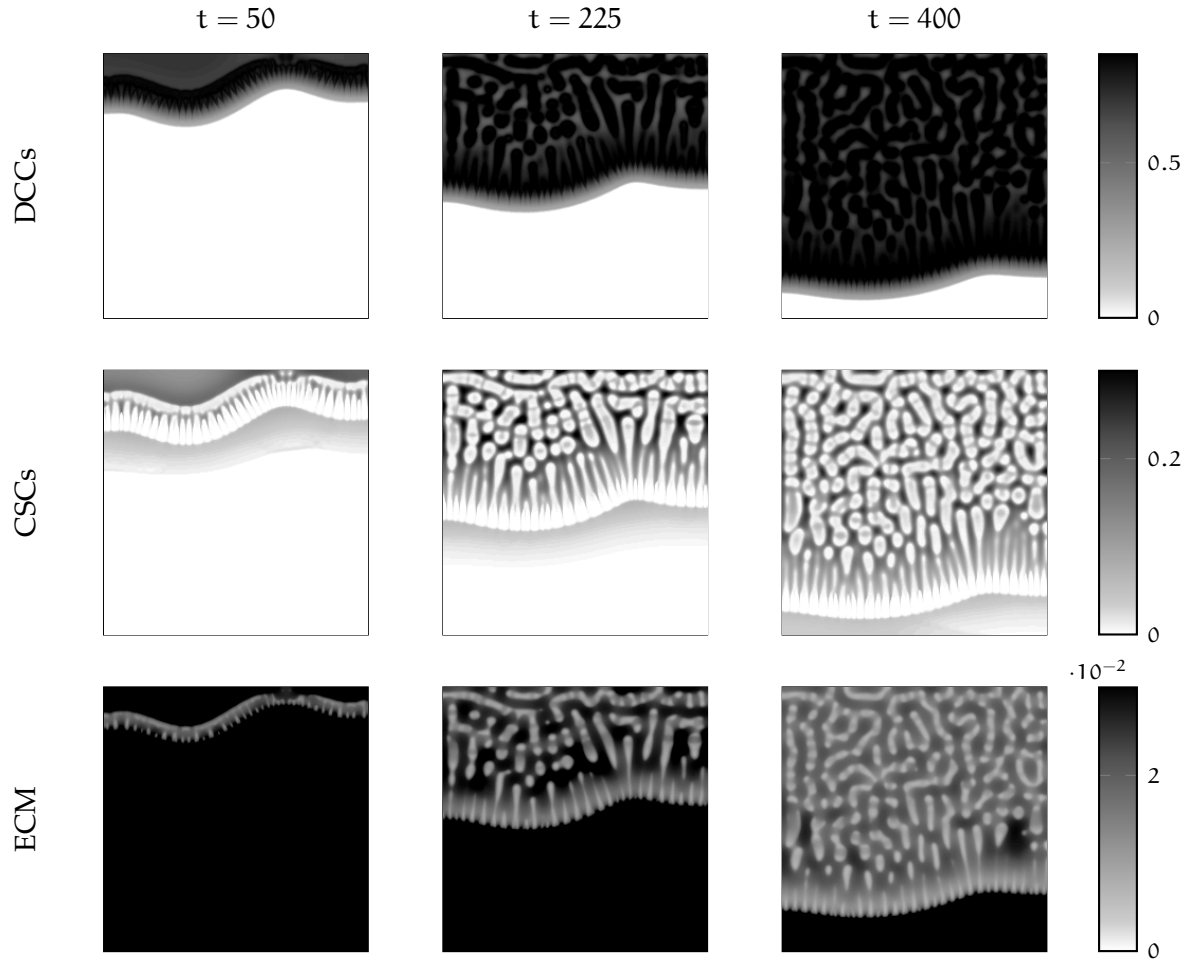

Figure 8.11: Experiment 10b: Numerical solutions for the concentrations of DCCs, CSCs and the ECM in consecutive time instances on a square domain with parameters modified by (A.2). As the ECM is invaded the DCCs and the CSCs develop a spatial pattern.

systems the corresponding counterparts are known as *Turing instabilities*. For more details we refer to [22, 166]. This kind of instabilities triggered pattern formation in various cancer models in 1D and 2D, see, e.g., [7].

Consider the parameters in Table 2.1 used in Experiment 6b, a modification of these parameters by (A.1) used in the 1D Experiment 6a and the new parameters consisting of Table 2.1 and (A.2). In all three cases we identified a single, stable and nonnegative steady state of the reaction terms in system (II). In Figure 8.9 we show the *dispersion relations*, i.e. the relation between the wave number k and the amplification factor $\lambda_k(\hat{\mathbf{w}})$ in the three cases. We can see that there is an advection-diffusion-driven instability when using the new parameters while this does not seem to be the case for both other parameter sets which we considered.

Figure 8.10 shows the numerical results for the new parameters (Table 2.1 and (A.2)) in a 1D simulation (Experiment 10a). In the invasion process a pattern consisting of a series of peaks in both cancer cell concentrations forms in the invaded area and it spreads over the domain as time evolves. Contrary to the results in Experiment 1, the cancer cell concentrations and thus also the pattern stabilize in the invaded area of the tissue. No further dynamic merging/emerging behavior occurs in the regions that were invaded earlier (i.e. several weeks ago). This can be seen, e.g., when comparing the left side of the domain in the time

instances $t \geqslant 270$ in Figure 8.10. Recall that we saw an analogical behavior of the cancer cell concentration in Experiment (2) with model (I).

We observe similar dynamics when employing the same parameters in 2D (Experiment 10b): the DCCs and CSCs leave a structure in the invaded tissue that does not evolve in time any further. The corresponding numerical results are shown in Figure 8.11. Note that the obtained patterns resemble images of *in vitro* examinations of tumor invasion and images from histopathology shown, e.g., in Figures 2.1 and 2.2.

9 Conclusion

In this thesis we have derived and studied a mathematical model of cancer invasion that takes the EMT into account and we have developed and tested several schemes to resolve this and similar models numerically. For the numerical tests we have also considered the uPA model and the contractivity model from the literature.

In the modeling part we have followed the Keller-Segel approach as done in the derivation of the first mathematical model of tumor invasion. This model has then been extended by an additional evolution equation that describes the behavior of the CSCs. The focus has been layed on the coupling term between both cancer cell types that models the transition from DCCs to CSCs via the EMT. We have considered Michaelis-Menten-like binding dynamics between EGFRs on the DCC membrane and EGF in the stroma to model this term. In this process we have scaled the microscopic dynamics on the level of individual cells to the density representation in another time scale. A further novelty of the new model, namely model (II), is the inclusion of fibroblast cells for the remodeling of the ECM. Fibroblasts are both involved in the tissue reconstruction in tumor invasion [16] and related to CSCs [89], which makes their addition to the model particularly interesting.

From an analytical point of view, we have considered a simplification of our model that does not include fibroblasts. For this model we have shown that a unique classical solution exists globally in time. We have proven this result under the assumption of a two-dimensional spatial domain and sufficiently large proliferation rates of both DCCs and CSCs. In the proof we have firstly verified the local existence and afterwards established a series of *a priori* estimates similar as done in the earlier works [161, 162, 164]. We have eventually finalized the proof using a boot-strapping argument.

Concerning the numerical methods we have proceeded in three major steps. In the first step, we have developed a FVFD scheme that uses the central upwind approach from [104]. We have generalized this scheme for nonuniform meshes in 1D and quadrilateral meshes in 2D. Moreover, we have adapted the scheme to all three models under consideration. For the time integration we have proposed different implicit-explicit splitting strategies: a scheme employing the Strang splitting and several IMEX RK methods. All these time integration schemes treat the diffusion terms implicitly but the remaining terms explicitly. We have shown that the first order IMEX RK approach applied to the new model (II) yields a positivity-preserving method. Further, we have conducted several tests with the uPA model: both a third order IMEX RK method (IMEX3) and the Strang splitting scheme (STRANG) have performed very well in accuracy and efficiency. Both have clearly exhibited a spatial EOC of two when the time increments were chosen in $\mathcal{O}(h)$ according to a CFL condition, with h denoting the maximal diameter of the mesh cells. While IMEX3 has delivered slightly more accurate numerical results, STRANG has preserved the nonnegativity of the solution throughout the computations unlike the other tested schemes.

Since in particular situations the implicit-explicit FVFD schemes on their own are not

accurate enough, we have endowed them with an AMR method in the second step. Our proposed technique developed for numerical simulations in 1D and 2D alternates between mesh updates and time integration. For the mesh update we have employed mesh cell bisection. In 1D we have further used the nonuniform formulation of the FVFD-STRANG method for the time integration. We have demonstrated a gain of efficiency of the 1D AMR scheme over its uniform counterpart in applications to the uPA model. The best results have been obtained when the mesh refinement has been driven by the gradient of the cancer cell concentration. The development of AMR methods in 2D is significantly more complex. In this regard, we have proposed a bookkeeping technique that allows for a fast refinement, coarsening and identification of neighbor cells with low memory requirements via a suitable enumeration of all possible mesh cells. Due to complications that arise because of hanging nodes in the mesh, we have considered only a basic numerical scheme of first order for the time integration step in the 2D AMR method. Yet, we have demonstrated that the 2D AMR scheme is more efficient than its uniform counterpart in an application to a simple cancer invasion system.

In the third step concerning the numerical methods we have developed a new 1D scheme for the class of KS-type PDE systems. This method separates a mass conservative part of the PDE system from the rest. In the mass conservative part of the system, the cell density has been transformed to a representation in its pseudo inverse cumulative function, which has led to uncommon finite difference approximations for the diffusion and the chemotaxis terms. For the remaining part of the system we have used a discretization by linear finite elements. Both systems have then been coupled by the Strang splitting. We have demonstrated the automatic mesh refinement that is included in this method in various numerical experiments, among others with the uPA model. Further we have verified temporal and spatial EOCs of two. As a last point, we have tested the efficiency in terms of the relation between computation time and error of the new scheme (MTFE) and compared it to the efficiency of the uniform FVFD-STRANG scheme and its AMR counterpart in an experiment with the uPA model. In our test the MTFE scheme has outperformed both other methods and the AMR method has been more efficient than the uniform method.

Having prepared the new model and suitable numerical methods, we have considered a series of numerical experiments. In these experiments we have qualitatively reproduced the outbreak of the CSCs from the primary tumor after they have developed from the DCCs via the EMT. This process is considered an important first step in metastasis [19, 87, 89, 100]. In our model the CSCs have formed highly dynamic merging and emerging concentrations while propagating into the tissue, similar as in the models [29, 30]. The new transition rate for the EMT that accounts for the binding dynamics of EGF has not only included more biologically relevant details (see, e.g., [120, 171]) to the model, but it has also led to more realistic predictions in the growth of a small tumor when compared to the previous modeling using constant EMT rates. In addition, the inclusion of fibroblast driven remodeling of the ECM has enabled the fast escape of the CSCs from the main tumor, while previous models have resulted in most CSCs staying confined in the main tumor. Through a parameter sensitivity study we have moreover seen that the model predicts that both a suppression of fibroblasts or an inhibition of EGFRs might lead to a reduction of the tumor growth. The latter strategy has been also discussed as a possible cancer therapy in the medical literature [34]. In the numerical experiments, we have further obtained spatial patterns of cancer cells in the tissue that are qualitatively similar to medical images from biopsy. We have generated these either by using a heterogeneous ECM or by employing model parameters that cause a

Turing-like instability.

We must note that macroscopic models of cancer growth, including the new model presented here, have their limitations. Due to the complexity of biochemical systems and also since not all processes in cancer are known and understood, there is at this time no such model to our knowledge that can withstand quantitative comparisons to growing tumors *in vivo*. For this reason the application of mathematical models in the diagnosis of cancer remains a long term goal until the crucial underlying biochemical processes are better understood. The current models, such as model (II), rather aim to contribute in the understanding of these processes. The insights that the models provide might also assist in the development of cancer therapies. We mention here indicatively [138] where the authors used a model similar to those considered here to optimize doses and scheduling of a combined chemo- and radiotherapy for cancer treatment. Model (II) might thus be used to study the impact of a EGFR inhibitor therapy (see [34]) *in silico* in a future work.

Other possible future investigations might involve a comparison to biomedical data of *in vitro* tumor progression in cooperation with experimentalists. This might on the one hand verify the dynamics that the model provides and on the other hand assist in the identification of bio-relevant model parameters. One could moreover augment the model and include further scales that are involved in the invasion and in the EMT. For instance, it would be interesting to study the role of morphological changes in the cytoskeleton during the EMT (see Figure 2.3) in more detail or to consider the fiber orientation of the ECM, as done in [73], in the remodeling by the fibroblasts.

Apart from the modeling, one can study in a future work the existence of solutions for the full model (II). We have discussed the complications involved in this process in Section 4.9. Another issue that is still open is the development of a higher order scheme to be used in the constructed 2D AMR method. To discretize the diffusion terms implicitly on the corresponding meshes one could employ here a wider finite difference stencil as in [49] or a discretization by finite elements. Another promising approach relating to the AMR methods is the derivation of *a posteriori error estimates*. The use of such an error estimator as monitor function for the mesh adaptation could significantly improve the accuracy of the AMR method. These error estimates have been derived in the framework of the relative entropy for other systems, such as hyperbolic conservation laws, in [41, 59, 60]. An application to systems of KS-type remains still open.

A Technical details on the numerical experiments

This appendix contains details on the parameters and on the initial conditions for the numerical experiments considered in this thesis.

Experiment 1: the uPA model in 1D A 1D experiment with model (I). We employ the parameters from [7] that read

$$
\begin{array}{lll}
D_c = 3.5 \times 10^{-4}, & \chi_u = 3.05 \times 10^{-2}, & \mu_1 = 0.25, \\
D_u = 2.5 \times 10^{-3}, & \chi_p = 3.75 \times 10^{-2}, & \mu_2 = 0.15, \\
D_p = 3.5 \times 10^{-3}, & \chi_v = 2.85 \times 10^{-2}, & \delta = 8.15, \\
D_m = 4.91 \times 10^{-3}, & \phi_{21} = 0.75, & \phi_{22} = 0.55, \\
\phi_{31} = 0.75, & \phi_{33} = 0.3, & \phi_{41} = 0.75, \\
\phi_{42} = 0.55, & \phi_{52} = 0.11, & \phi_{53} = 0.75, \\
\alpha_3 = 0.215, & \alpha_4 = 0.5, & \alpha_5 = 0.5
\end{array}
$$

and we refer to [7, 29, 114] for their derivation. The initial condition and the used computational domains are described in Section 5.11 and the dynamics are shown in Figure 5.2. We use this numerical experiment to compare various time discretization methods in Section 5.11, to test the 1D AMR scheme in Section 6.6 and also the MTFE scheme in Section 7.4.

Experiment 2: the uPA model in 1D, less aggressive cancer cells Another 1D experiment with model (I). The parameters and the initial condition are the same as in Experiment 1 except that we assume less random motion of the cancer cells, i.e. we have changed the diffusion coefficient of the cancer cells to $D_c = 5.3 \times 10^{-3}$. In Section 5.11 we compare several splitting schemes with this setting. The dynamics are shown in Figure 5.4.

Experiment 3: the uPA model in 2D A 2D experiment with model (I). The parameters are the same as in Experiment 1. We provide the initial conditions in Section 5.11 where we also show the simulation results in Figure 5.6.

Experiment 4a: the invasion/proliferation model in 2D A 2D experiment with model (6.12). Both model parameters and initial conditions are provided in Section 6.7 in (6.13) and (6.19). We use this experiment to show the capabilities of our 2D AMR scheme. For the corresponding simulation results we refer to Figure 6.11.

Experiment 4b: the invasion/proliferation model in 2D, nonuniform ECM Another 2D experiment with model (6.12). As in Experiment 4a we use the parameters (6.13) and the initial data (6.19). In this experiment we employ a heterogeneous ECM concentration v^* which

was precomputed by Nikolaos Sfakianakis using another ADR system. The simulation results computed by the 2D AMR method are shown in Figure 6.12.

Experiment 4c: the invasion/proliferation model in 1D A 1D experiment with model (7.31) serving as test case for the MTFE method (7.18). We provide the used model parameters along with the initial conditions in Section 7.4 and show the simulation results in Figure 7.5.

Experiment 5a: the contractivity model in 2D, smooth initial data A 2D experiment with the model (III). Both parameters and initial data are inspired by [156]. We employ the computational domain $\Omega = [-2, 2]^2$. The parameters are given by

$$\begin{aligned}
&\mu_p = 1, && \eta_p = 0.05, && \gamma = 0.055, && \lambda = 0.076,\\
&D_d = 0.001, && D_h = 1, &&&&\\
&\delta_v = 10, && \mu_v = 0.3, && \eta_v = 0.9,\\
&k_+ = 2, && k_- = 0.06, &&&&\\
&q = 3, && M = 1, &&&&\\
&\varepsilon = 0.01, && \tau = 0.04 &&&&
\end{aligned}$$

and the initial conditions read

$$\begin{aligned}
&c_0^p(x) = 0.4e^{-3/2\,|x|^2}, && c_0^m(x) = e^{-3/2\,|x|^2}, && v_0(x) = 1 - c_0^m(x),\\
&y_0(x) = 20\left(15^2 \int_0^\infty t\, e^{-t}\, dt\right)^{-1} 5\,|x|^2 e^{-5\,|x|^2/15}, && && \kappa_0 = 2\, y_0,
\end{aligned}$$

for any $x \in \Omega$. This experiment is used in the EOC study in Table 8.1.

Experiment 5b: the contractivity model in 2D, study of the delay parameter Another 2D experiment with model (III). We use the same domain, initial data and parameters as in Experiment 5a except for the modified parameters

$$\lambda = 0.152, \quad D_d = 0.01, \quad D_h = 10, \quad \delta_v = 5$$

and the altered initial concentrations of ECM bound integrins and contractivity

$$y_0(x) = 15\left(7^3 \int_0^\infty t^2\, e^{-t}\, dt\right)^{-1} 80^2 |x|^2 e^{-80\,|x|/7}, \qquad \kappa_0 = 2\, y_0, \qquad x \in \Omega.$$

We present the corresponding numerical simulation results in Figure 8.1.

Experiment 6a: the haptotaxis EMT/invasion model in 1D A 1D experiment with model (II). We use the parameters in Table 2.1 except for

$$\mu_0 = 0.55, \quad k_D = 0.5, \quad \Gamma = 2/15. \tag{A.1}$$

As computational domain we use $\Omega = [0, 7.5]$ and the initial conditions are given by

$$c_0^D(x) = e^{-20x^2}, \quad c_0^S(x) = c_0^F(x) = 0, \quad v_0(x) = 1 - 0.5\, e^{-20x^2}, \quad m_0(x) = 0.2\, e^{-20x^2}$$

for any $x \in \Omega$. We show the results in Figure 8.3. This experiment is also used in the parameter study with sensitivity results in Table 8.3.

Experiment 6b: the haptotaxis EMT/invasion model in 2D A 2D experiment with model (II). We use the parameters from Table 2.1, the computational domain $\Omega = [-5,5]^2$ and the initial data

$$c_0^D(x) = \begin{cases} \sin\left(\arctan(x_2/x_1)\right), & \text{if } |x|^2 < 4,\ x_1 \geqslant 0, x_2 \leqslant 0, \\ \sin\left(\pi + \arctan(x_2/x_1)\right), & \text{if } |x|^2 < 4,\ x_1 < 0, x_2 \leqslant 0, \\ 0, & \text{otherwise,} \end{cases}$$
$$c_0^S(x) = c_0^F(x) = 0, \qquad v_0(x) = 1 - c_0^D(x), \qquad m_0(x) = 0.05\, c_0^D(x)$$

for any $x \in \Omega$. The numerical experiment results are shown in Figure 8.3.

Experiment 6c: the haptotaxis EMT/invasion model in 2D, smooth initial data The same as Experiment 6b, but with smooth initial conditions

$$c_0^D(x) = \mathbf{e} - |x|^2, \quad c_0^S(x) = c_0^F(x) = 0, \quad v_0(x) = 1 - c_0^D(x), \quad m_0(x) = 0.05\, c_0^D(x)$$

for any $x \in \Omega$. This setting is used for the experimental study of convergence in Table 8.2.

Experiment 7a: the haptotaxis EMT/invasion model without translocation The same as Experiment 6a with modified parameters $\mu_0 = 0.034,\ \mu_{1/2} = 0.4,\ k_D = 0.2,\ \lambda^D = 3$. We also neglect advection and diffusion terms and use the initial data $c_0^D = 10^{-3}$, $c_0^S = c_0^F = 0$, $v_0 = 1$, $m_0 = 10^{-6}$. This experiment is used in the comparison of EMT models in Figure 8.5.

Experiment 7b: the haptotaxis EMT/invasion without translocation and with constant rate EMT The same as Experiment 7a, but with the EMT modeled by a constant rate $\mu_{EMT} = 0.017$. The experiment is used in the comparison of EMT models in Figure 8.5.

Experiment 8a: the haptotaxis EMT/invasion model in 2D, no ECM remodeling The same as Experiment 6b, but without ECM remodeling, i.e. $\mu_v = 0$. The experiment is used in the study of the ECM remodeling in Figure 8.7.

Experiment 8b: the haptotaxis EMT/invasion model in 2D, self remodeling of the ECM The same as Experiment 6b, but with self remodeling of the ECM, i.e. we have replaced the fibroblast remodeling term $+\mu_v\, c^F\, R^+$ in (II) by $+\mu_v\, v\, R^+$. The experiment is used in the study of the ECM remodeling in Figure 8.7.

Experiment 9: the haptotaxis EMT/invasion model in 2D, nonuniform ECM The same as Experiment 6b, but with the initial ECM v_0 replaced by a nonuniform ECM. We use the same precomputed ECM as in Experiment 4b scaled to the larger domain $\Omega = [-5,5]^2$. The simulation results are shown in Figure 8.8.

Experiment 10a: the haptotaxis EMT/invasion model in 1D, spatial pattern The same as Experiment 6a with modified parameters

$$\begin{cases} D_D = 2\times 10^{-4}, \quad D_S = 3.8\times 10^{-4}, \quad \chi_S = 0.8, \quad \beta_F = 0.3, \quad \mu_T = 0.1, \\ \quad \mu_v = 5, \quad \alpha_D = 0.3, \quad \alpha_S = 0.1, \quad \mu_0 = 0.25, \quad \Gamma = 1/15, \quad k_D = 0.5. \end{cases} \tag{A.2}$$

We show the corresponding numerical results in Figure 8.10.

Experiment 10b: the haptotaxis EMT/invasion model in 2D, spatial pattern A 2D experiment with model (II) on the computational domain $\Omega = [-5, 5]^2$. We use the parameters from Table 2.1 modified by (A.2) as in Experiment 10a. Moreover, we use the initial conditions from Experiment 3. The numerical results are shown in Figure 8.11.

Bibliography

[1] R. A. Adams and J. J. F. Fournier. *Sobolev spaces*, volume 140 of *Pure and Applied Mathematics (Amsterdam)*. Elsevier/Academic Press, Amsterdam, second edition, 2003, pages xiv+305.

[2] B. Alberts, D. Bray, J. Lewis, M. Raff, K. Roberts and J. D. Watson. *Molecular Biology of the Cell*. Garland, 4th edition, 2002.

[3] R. K. Alexander and J. J. Coyle. Runge-Kutta methods and differential-algebraic systems. *SIAM J. Numer. Anal.*, 27(3):736–752, 1990.

[4] N. D. Alikakos. An application of the invariance principle to reaction-diffusion equations. *J. Differ. Equat.*, 33(2):201–225, 1979.

[5] H. Amann. *Ordinary differential equations*, volume 13 of *De Gruyter Studies in Mathematics*. Walter de Gruyter & Co., Berlin, 1990, pages xiv+458. An introduction to nonlinear analysis, Translated from the German by Gerhard Metzen.

[6] L. Ambrosio, N. Gigli and G. Savaré. *Gradient flows in metric spaces and in the space of probability measures*. Lectures in Mathematics ETH Zürich. Birkhäuser Verlag, Basel, 2005, pages viii+333.

[7] V. Andasari, A. Gerisch, G. Lolas, A. P. South and M. A. J. Chaplain. Mathematical modelling of cancer cell invasion of tissue: biological insight from mathematical analysis and computational simulation. *J. Math. Biol.*, 63(1):141–171, 2011.

[8] A. R. A. Anderson, M. A. J. Chaplain, E. L. Newman, R. J. C. Steele and A. M. Thompson. Mathematical modelling of tumour invasion and metastasis. *Comput. Math. Method. M.*, 2(2):129–154, 2000.

[9] A. R. A. Anderson and M. A. J. Chaplain. Continuous and discrete mathematical models of tumor-induced angiogenesis. *Bull. Math. Biol.*, 60(5):857–899, 1998.

[10] P. A. Andreasen, R. Egelund and H. H. Petersen. The plasminogen activation system in tumor growth, invasion, and metastasis. *Cell. Mol. Life Sci.*, 57(1):25–40, 2000.

[11] P. Armitage and R. Doll. The age distribution of cancer and a multi-stage theory of carcinogenesis. *Br. J. Cancer*, 8(1):1, 1954.

[12] C. Arvanitis, C. Makridakis and N. Sfakianakis. Entropy conservative schemes and adaptive mesh selection for hyperbolic conservation laws. *J. Hyperbol. Differ. Eq.*, 7(03):383–404, 2010.

[13] R. E. Bank, W. M. Coughran, W. Fichtner, E. H. Grosse, D. J. Rose and R. K. Smith. Transient simulation of silicon devices and circuits. *IEEE Trans. Comput. Aided Des. Integr. Circuits Syst.*, 4(4):436–451, 1985.

[14] S. Barr, S. Thomson, E. Buck, S. Russo, F. Petti, I. Sujka-Kwok, A. Eyzaguirre, M. Rosenfeld-Franklin, N. W. Gibson, M. Miglarese, D. Epstein, K. K. Iwata and J. D. Haley. Bypassing cellular egf receptor dependence through epithelial-to-mesenchymal-like transitions. *Clin. Exp. Metastasis*, 25(6):685–693, Oct. 2008.

[15] M. Berger, M. J. Aftosmis and S. M. Murman. Analysis of slope limiters on irregular grids. Technical report 0490, AIAA, 2005.

[16] N. A. Bhowmick, E. G. Neilson and H. L. Moses. Stromal fibroblasts in cancer initiation and progression. *Nature*, 432(7015):332, 2004.

[17] A. Blanchet, V. Calvez and J. A. Carillo. Convergence of the mass-transport steepest descent scheme for the subcritical Patlak-Keller-Segel model. *SIAM J. Numer. Anal.*, 2008.

[18] D. K. Blandford, E. B. Guy, D. E. Cardoze and C. Kadow. Compact representations of simplicial meshes in two and three dimensions. *Int. J. Comput. Geom. AP.*, 15(1):3–24, 2005.

[19] T. Brabletz, A. Jung, S. Spaderna, F. Hlubek and T. Kirchner. Opinion: migrating cancer stem cells - an integrated concept of malignant tumour progression. *Nat. Rev. Cancer*, 5(9):744–749, 2005.

[20] D. Bray. *Cell movements: from molecules to motility*. Garland Science, 2001.

[21] M. P. Brenner, L. S. Levitov and E. O. Budrene. Physical mechanisms for chemotactic pattern formation by bacteria. *Biophys. J.*, 74(4):1677–1693, 1998.

[22] N. Britton. *Essential mathematical biology*. Springer Science & Business Media, 2012.

[23] K. Böttger, H. Hatzikirou, A. Chauviere and A. Deutsch. Investigation of the migration/proliferation dichotomy and its impact on avascular glioma invasion. *Math. Model. Nat. Phenom.*, 7(1):105–135, 2012.

[24] V. Calvez and L. Corrias. The parabolic-parabolic Keller-Segel model in r2. *Comm. Math. Sci.*, 6(2):417–447, 2008.

[25] V. Calvez, B. Perthame and M. Sharifi Tabar. Modified Keller-Segel system and critical mass for the log interaction kernel. In *Stochastic analysis and partial differential equations*. Volume 429, Contemp. Math. Pages 45–62. Amer. Math. Soc., Providence, RI, 2007.

[26] J. A. Carrillo and J. S. Moll. Numerical simulation of diffusive and aggregation phenomena in nonlinear continuity equations by evolving diffeomorphisms. *SIAM J. Sci. Comput.*, 31(6):4305–4329, 2010.

[27] J. A. Carrillo, S. Hittmeir and A. Jüngel. Cross diffusion and nonlinear diffusion preventing blow up in the Keller-Segel model. *Math. Models Methods Appl. Sci.*, 22(12):1250041, 35, 2012.

[28] J. A. Carrillo, N. Kolbe and M. Lukácová-Medviďová. A hybrid mass transport finite element method for Keller-Segel type systems. Preprint, `https://arxiv.org/abs/1709.07394`, submitted, Sept. 2017.

[29] M. A. J. Chaplain and G. Lolas. Mathematical modelling of cancer cell invasion of tissue. the role of the urokinase plasminogen activation system. *Math. Mod. Meth. Appl. S.*, 15(11):1685–1734, 2005.

[30] M. A. J. Chaplain and G. Lolas. Mathematical modelling of cancer invasion of tissue: dynamic heterogeneity. *Netw. Heterog. Media*, 1(3):399–439, 2006.

[31] A. Chertock and A. Kurganov. A second-order positivity preserving central-upwind scheme for chemotaxis and haptotaxis models. *Numer. Math.*, 111(2):169–205, 2008.

[32] A. Chertock, Y. Epshteyn, H. Hu and A. Kurganov. High-order positivity-preserving hybrid finite-volume-finite-difference methods for chemotaxis systems. *Adv. Comput. Math.*, 2017.

[33] A. Chertock, A. Kurganov, X. Wang and Y. Wu. On a chemotaxis model with saturated chemotactic flux. *Kinet. Relat. Models*, 5(1):51–95, 2012.

[34] F. Ciardiello and G. Tortora. EGFR antagonists in cancer treatment. *N. Engl. J. Med.*, 358(11):1160–1174, 2008. PMID: 18337605.

[35] W. A. Coppel. *Dichotomies in stability theory*. Lecture Notes in Mathematics, Vol. 629. Springer-Verlag, Berlin-New York, 1978, pages ii+98.

[36] L. Corrias, B. Perthame and H. Zaag. Global solutions of some chemotaxis and angiogenesis systems in high space dimensions. *Milan J. Math.*, 2004.

[37] L. Corrias and B. Perthame. Critical space for the parabolic-parabolic Keller-Segel model in $\mathbb{R}^d$. *C. R. Math. Acad. Sci. Paris*, 342(10):745–750, 2006.

[38] R Courant, K. Friedrichs and H. Lewy. Über die partiellen Differenzengleichungen der mathematischen Physik. *Math. An..*, 100(1):32–74, 1928.

[39] T. R. Cox and J. T. Erler. Remodeling and homeostasis of the extracellular matrix: implications for fibrotic diseases and cancer. *Dis. Model. Mech.*, 4(2):165–178, 2011.

[40] J. E. Darnell, H. Lodish, D. Baltimore et al. *Molecular cell biology*, volume 2. Scientific American Books New York, 1990.

[41] A. Dedner and J. Giesselmann. A posteriori analysis of fully discrete method of lines discontinuous Galerkin schemes for systems of conservation laws. *SIAM J. Numer. Anal.*, 54(6):3523–3549, 2016.

[42] R. Denk, M. Hieber and J. Prüss. $\mathbb{R}$-boundedness, Fourier multipliers and problems of elliptic and parabolic type. *Mem. Amer. Math. Soc.*, 166(788):viii+114, 2003.

[43] J. Dolbeault and C. Schmeiser. The two-dimensional Keller-Segel model after blow-up. *Discrete Continuous Dyn. Syst. Ser. A*, 25(1):109–121, 2009.

[44] P. Domschke, D. Trucu, A. Gerisch and M. A. J. Chaplain. Mathematical modelling of cancer invasion: implications of cell adhesion variability for tumour infiltrative growth patterns. *J. Theor. Biol.*, 361:41–60, 2014.

[45] J. R. Dormand and P. J. Prince. A family of embedded runge-kutta formulae. *J. Comput. Appl. Math.*, 6(1):19 –26, 1980.

[46] A. Eladdadi and D. Isaacson. A mathematical model for the effects of HER2 overexpression on cell proliferation in breast cancer. *Bull. Math. Biol.*, 70:1707–1729, 2008.

[47] L. C. Evans. *Partial differential equations*, volume 19 of *Graduate Studies in Mathematics*. American Mathematical Society, Providence, RI, second edition, 2010, pages xxii+749.

[48] Y. L. Fan, M. Zheng, Y. L. Tang and X. Liang. A new perspective of vasculogenic mimicry: EMT and cancer stem cells (review). *Oncol. Lett.*, 6(5):1174–1180, 2013.

[49] M. Feistauer, J. Felcman and I. Straškraba. *Mathematical and computational methods for compressible flow*. Numerical Mathematics and Scientific Computation. The Clarendon Press, Oxford University Press, Oxford, 2003, pages xiv+535.

[50] F. Filbet. A finite volume scheme for the Patlak-Keller-Segel chemotaxis model. *Numer. Math.*, 104(4):457–488, 2006.

[51] H. B. Frieboes, X. Zheng, C. H. Sun, B. Tromberg, R. Gatenby and V. Christini. An integrated computational/experimental model of tumor invasion. *Cancer Res.*, 66(3):1597–1604, 2006.

[52] A. Friedman. *Partial differential equations of parabolic type*. Prentice-Hall, Inc., Englewood Cliffs, N.J., 1964, pages xiv+347.

[53] K. O. Friedrichs. Symmetric hyperbolic linear differential equations. *Comm. Pure Appl. Math.*, 7:345–392, 1954.

[54] D. Gao, L. T. Vahdat, S. Wong, J. C. Chang and V. Mittal. Microenvironmental regulation of epithelial-mesenchymal transitions in cancer. *Cancer Res.*, 72(19):4883–4889, 2012.

[55] A. Gerisch. *Numerical Methods for the Simulation of Taxis-Diffusion-Reaction Systems*. PhD thesis, Martin-Luther-Universität Halle-Wittenberg, 2001.

[56] A. Gerisch and M. A. J. Chaplain. Robust numerical methods for taxis–diffusion–reaction systems: Applications to biomedical problems. *Math. Comput. Model.*, 43(1):49–75, 2006.

[57] A. Gerisch and M. A. J. Chaplain. Mathematical modelling of cancer cell invasion of tissue: Local and nonlocal models and the effect of adhesion. *J. Theor. Biol.*, 250(4):684–704, 2008.

[58] J. Giesselmann, N. Kolbe, M. Lukáčová-Medviďová and N. Sfakianakis. Existence and uniqueness of global classical solutions to a two species cancer invasion haptotaxis model. Preprint, `https://arxiv.org/abs/1704.08208`, submitted, Apr. 2017.

[59] J. Giesselmann, C. Makridakis and T. Pryer. A posteriori analysis of discontinuous Galerkin schemes for systems of hyperbolic conservation laws. *SIAM J. Numer. Anal.*, 53(3):1280–1303, 2015.

[60] J. Giesselmann and T. Pryer. Reduced relative entropy techniques for *a* posteriori analysis of multiphase problems in elastodynamics. *IMA J. Numer. Anal.*, 36(4):1685–1714, 2016.

[61] D. Gilbarg and N. S. Trudinger. *Elliptic partial differential equations of second order*. Classics in Mathematics. Springer-Verlag, Berlin, 2001, pages xiv+517. Reprint of the 1998 edition.

[62] G. Giordano. Value of immunohistochemistry in uterine pathology: common and rare diagnostic dilemmas. *Pathol. Res. Pract.*, 205(10):663–676, 2009.

[63] L. Gosse and G. Toscani. Identification of asymptotic decay to self-similarity for one-dimensional filtration equations. *SIAM J. Num. Anal.*, 43(6):2590–2606, 2006.

[64] S. Gottlieb, C.-W. Shu and E. Tadmor. Strong stability-preserving high-order time discretization methods. *SIAM Rev.*, 43(1):89–112, 2001.

[65] P. B. Gupta, C. L. Chaffer and R. A. Weinberg. Cancer stem cells: mirage or reality? *Nat. Med.*, 15(9):1010–1012, 2009.

[66] E. Hairer, S. P. Nørsett and G. Wanner. *Solving ordinary differential equations. I*. Springer Series in Computational Mathematics. Springer-Verlag, Berlin, second edition, 1993.

[67] D. Hanahan and R. A. Weinberg. The hallmarks of cancer. *Cell*, 100(1):57–70, 2000.

[68] M. Hanke-Bourgeois. *Grundlagen der numerischen Mathematik und des wissenschaftlichen Rechnens*. Vieweg + Teubner, Wiesbaden, third edition, 2009, page 840.

[69] J. Haynes, J. Srivastava, N. Madson, T. Wittmann and D. L. Barber. Dynamic actin remodeling during epithelial–mesenchymal transition depends on increased moesin expression. *Mol. Biol. Cell*, 22(24):4750–4764, 2011.

[70] N. Hellmann, N. Kolbe and N. Sfakianakis. A mathematical insight in the epithelial-mesenchymal-like transition in cancer cells and its effect in the invasion of the extracellular matrix. *Bull. Braz. Math. Soc.*, 47(1):397–412, 2016.

[71] M. A. Herrero, E. Medina and J. J. L. Velázquez. Finite-time aggregation into a single point in a reaction-diffusion system. *Nonlinearity*, 10(6):1739–1754, 1997.

[72] I. Higueras and T. Roldán. Positivity-preserving and entropy-decaying IMEX methods. In *Ninth International Conference Zaragoza-Pau on Applied Mathematics and Statistics*. Volume 33, Monogr. Semin. Mat. García Galdeano, pages 129–136. Prensas Univ. Zaragoza, Zaragoza, 2006.

[73] T. Hillen and K. Painter. Transport models for movement in oriented habitats and anisotropic diffusion. In S. P. M.A. Lewis P. M., editor, *Dispersal, individual movement and spatial ecology: A mathematical perspective*. Springer, Heidelberg, 2012.

[74] T. Hillen and K. Painter. Mathematical modelling of glioma growth: the use of diffusion tensor imaging (dti) data to predict the anisotropic pathways of cancer invasion. *J. Theor. Biol.*, 323:25–39, 2013.

[75] T. Hillen, K. Painter and C. Schmeiser. Global existence for chemotaxis with finite sampling radius. *Discrete Continuous Dyn. Syst. Ser. B*, 7(1):125–144, 2007.

[76] S. Hittmeir and A. Jüngel. Cross diffusion preventing blow-up in the two-dimensional Keller-Segel model. *SIAM J. Math. Anal.*, 43(2):997–1022, 2011.

[77] D. Horstmann. From 1970 until present: the Keller-Segel model in chemotaxis and its consequences. I. *Jahresber. Deutsch. Math.-Verein.*, 105(3):103–165, 2003.

[78] D. Horstmann. From 1970 until present: the Keller-Segel model in chemotaxis and its consequences. II. *Jahresber. Deutsch. Math.-Verein.*, 106(2):51–69, 2004.

[79] D. Horstmann and M. Winkler. Boundedness vs. blow-up in a chemotaxis system. *J. Differ. Equat.*, 215(1):52–107, 2005.

[80] W. Hundsdorfer and J. G. Verwer. *Numerical solution of time-dependent advection-diffusion-reaction equations*, volume 33. Springer, 2003.

[81] Y. Imai, C. K. H. Leung, H. G. Friesen and R. P. C. Shiu. Epidermal growth factor receptors and effect of epidermal growth factor on growth of human breast cancer cells in long-term tissue culture. *Cancer Res.*, 42(11):4394–4398, 1982.

[82] International Bureau of Weights and Measures. *The international system of units (SI)*, number 330-331. US Dept. of Commerce, National Bureau of Standards, US Govt. Print. Off., 1977.

[83] E. Isaacson and H. B. Keller. *Analysis of numerical methods*. Courier Dover Publications, 1994.

[84] W. Jäger and S. Luckhaus. On explosions of solutions to a system of partial differential equations modelling chemotaxis. *Trans. Amer. Math. Soc.*, 329(2):819–824, 1992.

[85] C. Jeulin, V. Seltzer, D. Bailbé, K. Andreau and F. Marano. EGF mediates calcium-activated chloride channel activation in the human bronchial epithelial cell line 16hbe14o-: involvement of tyrosine kinase p60c-src. *Am. J. Physiol. Lung. Cell. Mol. Physiol.*, 295(3):489–496, 2008.

[86] M. D. Johnston, P. K. Maini, S. Jonathan-Chapman, C. M. Edwards and W. F. Bodmer. On the proportion of cancer stem cells in a tumour. *J. Theor. Biol.*, 266(4):708–711, 2010.

[87] C. T. Jordan and M. Guzman M. L. N. Cancer stem cells. *N. Engl. J. Med.*, 355:1253–1261, 2006.

[88] R. Jordan, D. Kinderlehrer and F. Otto. The variational formulation of the Fokker-Planck equation. *SIAM J. Math. Anal.*, 29(1):1–17, 1998.

[89] Y. Katsumo, S. Lamouille and R. Derynck. TGF-β signaling and epithelial–mesenchymal transition in cancer progression. *Curr. Opin. Oncol.*, 25(1):76–84, 2013.

[90] E. F. Keller and L. A. Segel. Initiation of slime mold aggregation viewed as an instability. *J. Theor. Biol.*, 26(3):399–415, 1970.

[91] C. A. Kennedy and M. H. Carpenter. Additive Runge-Kutta schemes for convection diffusion reaction equations. *Appl. Numer. Math.*, 1(44):139–181, 2003.

[92] K. Kessenbrock, V. Plaks and Z. Werb. Matrix metalloproteinases: regulators of the tumor microenvironment. *Cell*, 141(1):52–67, 2010.

[93] Y. Kim and A. Friedmann. Interaction of tumor with its micro-environment: a mathematical model. *B. Math. Biol.*, 72(5):1029–1068, 2010.

[94] B. S. Kirk, J. W. Peterson, R. H. Stogner and G. F. Carey. Libmesh: a C++ library for parallel adaptive mesh refinement/coarsening simulations. *Eng. Comput.*, 22(3):237–254, 2006.

[95] P. Klein, D. Mattoon, M. A. Lemmon and J. Schlessinger. A structure-based model for ligand binding and dimerization of EGF receptors. *P. Natl. Acad. Sci. USA*, 101(4):929–934, 2004.

[96] N. Kolbe, J. Kat'uchová, N. Sfakianakis, N. Hellmann and M. Lukáčová-Medviďová. A study on time discretization and adaptive mesh refinement methods for the simulation of cancer invasion : The urokinase model. *Appl. Math. Comput.*, 273:353–376, 2016.

[97] N. Kolbe. *Mathematical Modelling and Numerical Simulations of Cancer Invasion*. Master's thesis, University of Mainz, supervised by M. Lukáčová-Medviďová and N. Sfakianakis, 2013.

[98] N. Kolbe, M. Lukáčová-Medviďová, N. Sfakianakis and B. Wiebe. Numerical simulation of a contractivity based multiscale cancer invasion model. In A. Gerisch, R. Penta and J. Lang, editors, *Multiscale Models in Mechano and Tumor Biology: Modeling, Homogenization, and Applications*. Springer, to appear 2017.

[99] N. Kolbe and N. Sfakianakis. A flexible multidimensional rectangular mesh administration and refinement technique with application in cancer invasion models. Preprint, `https://arxiv.org/abs/1706.06191`, 2016.

[100] D. Kong, Y. Li, Z. Wang and F. H. Sarkar. Cancer stem cells and epithelial-to-mesenchymal transition (emt)-phenotypic cells: are they cousins or twins? *Cancers*, 3:716–729, 2011.

[101] R. Kowalczyk and Z. Szymańska. On the global existence of solutions to an aggregation model. *J. Math. Anal. Appl.*, 343(1):379–398, 2008.

[102] D. Kröner and M. Ohlberger. A posteriori error estimates for upwind finite volume schemes for nonlinear conservation laws in multi dimensions. *Math. Comp.*, 69(229):25–39, 2000.

[103] A. Kurganov and M. Lukáčová-Medviďová. Numerical study of two-species chemotaxis models. *Discrete Continuous Dyn. Syst. Ser. B*, 19(1):131–152, 2014.

[104] A. Kurganov, S. Noelle and G. Petrova. Semidiscrete central-upwind schemes for hyperbolic conservation laws and Hamilton-Jacobi equations. *SIAM J. Sci. Comput.*, 23(3):707–740, 2001.

[105] A. Kurganov and E. Tadmor. New high-resolution central schemes for nonlinear conservation laws and convection-diffusion equations. *J. Comput. Phys.*, 160(1):241–282, 2000.

[106] O. A. Ladyženskaja, V. A. Solonnikov and N. N. Ural'ceva. *Linear and quasilinear equations of parabolic type*. Translated from the Russian by S. Smith. Translations of Mathematical Monographs, Vol. 23. American Mathematical Society, Providence, R. I., 1968, pages xi+648.

[107] S. Lamouille, J. Xu and R. Derynck. Molecular mechanisms of epithelial–mesenchymal transition. *Nat. Rev. Mol. Cell Biol.*, 15(3):178, 2014.

[108] D. A. Lauffenburger and A. F. Horwitz. Cell migration: a physically integrated molecular process. *Cell*, 84(3):359 –369, 1996.

[109] P. D. Lax. Weak solutions of nonlinear hyperbolic equations and their numerical computation. *Comm. Pure Appl. Math.*, 7:159–193, 1954.

[110] R. J. LeVeque. *Finite volume methods for hyperbolic problems*. Cambridge Texts in Applied Mathematics. Cambridge University Press, Cambridge, 2002, pages xx+558.

[111] B. v. Leer. Towards the ultimate conservative difference scheme. IV. A new approach to numerical convection. *J. Comput. Phys.*, 23(3):276–299, 1977.

[112] B. v. Leer. Towards the ultimate conservative difference scheme. V. A second-order sequel to Godunov's method. *J. Comput. Phys.*, 32(1):101 –136, 1979.

[113] E. H. Lieb and M. Loss. *Analysis*, volume 14 of *Graduate Studies in Mathematics*. American Mathematical Society, Providence, RI, second edition, 2001, pages xxii+346.

[114] G. Lolas. *Mathematical modelling of the urokinase plasminogen activation system and its role in cancer invasion of tissue*. PhD thesis, University of Dundee, 2003.

[115] A. J. Lotka. Elements of physical biology, 1925.

[116] T. R. Malthus. *An Essay on the Principle of Population, as it Affects the Future Improvement of Society, with Remarks on the Speculations of Mr. Godwin, M. Condorcet, and Other Writers*. The Lawbook Exchange, Ltd., 1798.

[117] A. Manhart, D. Oelz, C. Schmeiser and N. Sfakianakis. An extended filament based lamellipodium model produces various moving cell shapes in the presence of chemotactic signals. *J. Theor. Biol.*, 382:244–258, 2015.

[118] S. A. Mani, W. Guo, M. J. Liao, E. N. Eaton, A. Ayyanan, A. Y. Zhou, M. Brooks, F. Reinhard, C. C. Zhang, M. Shipitsin, L. L. Campbell, K. Polyak, C. Brisken, J. Yang and R. A. Weinberg. The epithelial-mesenchymal transition generates cells with properties of stem cells. *Cell*, 133(4):704–715, 2008.

[119] A. Marciniak-Czochra and M. Ptashnyk. Boundedness of solutions of a haptotaxis model. *Math. Mod. Meth. Appl. S.*, 2010.

[120] J. Mendelsohn and J. Baselga. The egf receptor family as targets for cancer therapy. *Oncogene*, 19:6550–6555, 2000.

[121] G. Meral, C. Stinner and C. Surulescu. On a multiscale model involving cell contractivity and its effects on tumor invasion, 2013.

[122] J. D. Murray. *Mathematical biology. I*, volume 17 of *Interdisciplinary Applied Mathematics*. Springer-Verlag, New York, third edition, 2002, pages xxiv+551. An introduction.

[123] J. D. Murray. *Mathematical biology. II*, volume 18 of *Interdisciplinary Applied Mathematics*. Springer-Verlag, New York, third edition, 2003, pages xxvi+811. Spatial models and biomedical applications.

[124] T. Nagai. Blow-up of radially symmetric solutions to a chemotaxis system. *Adv. Math. Sci. Appl.*, 5(2):581–601, 1995.

[125] T. Nagai. Behavior of solutions to a parabolic-elliptic system modelling chemotaxis. *J. Korean Math. Soc.*, 37(5):721–733, 2000.

[126] T. Nagai. Blowup of nonradial solutions to parabolic-elliptic systems modeling chemotaxis in two-dimensional domains. *J. Inequal. Appl.*, 6(1):37–55, 2001.

[127] H. Nessyahu and E. Tadmor. Nonoscillatory central differencing for hyperbolic conservation laws. *J. Comput. Phys.*, 87(2):408–463, 1990.

[128] C. O. Nordling. A new theory on the cancer-inducing mechanism. *Br. J. Cancer*, 7(1):68, 1953.

[129] M. L. Nyström, G. J. Thomas, M. Stone, I. C. Mackenzie, I. R. Hart and J. F. Marshall. Development of a quantitative method to analyse tumour cell invasion in organotypic culture. *J. Pathol.*, 205(4):468–475, 2005.

[130] K. Osaki, T. Tsujikawa, A. Yagi and M. Mimura. Exponential attractor for a chemotaxis-growth system of equations. *Nonlinear Anal. Theor. Meth. Appl.*, 51(1):119–144, 2002.

[131] K. Osaki and A. Yagi. Finite dimensional attractor for one-dimensional Keller-Segel equations. *Funkcial. Ekvac.*, 44(3):441–469, 2001.

[132] F. Özcan, P. Klein, M. Lemmon, I. Lax and J. Schlessinger. On the nature of low-and high-affinity EGF receptors on living cells. *P. Natl. Acad. Sci. USA*, 103(15):5735–5740, 2006.

[133] K. J. Painter, N. A. Armstrong and J. A. Sherratt. The impact of adhesion on cellular invasion processes in cancer and development. *J. Theor. Biol.*, 264(3):1057–1067, 2010.

[134] L. Pareschi and G. Russo. Implicit-explicit Runge-Kutta schemes and applications to hyperbolic systems with relaxation. *J. Sci. Comput.*, 25(1-2):129–155, 2005.

[135] B. Perthame. *Transport equations in biology*. Frontiers in Mathematics. Birkhäuser Verlag, Basel, 2007, pages x+198.

[136] A. J. Perumpanani, J. A. Sherratt, J. Norbury and H. M. Byrne. Biological inferences from a mathematical model for malignant invasion. *Invas. Metast.*, 16(4-5):209–221, 1996.

[137] N. J. Poplawski, U. Agero, J. S. Gens, M. Swat, J. A. Glazier and A. R. A. Anderson. Front instabilities and invasiveness of simulated avascular tumors. *Bull. Math. Biol.*, 71(5):1189–1227, 2009.

[138] G. G. Powathil, D. J. A. Adamson and M. A. J. Chaplain. Towards predicting the response of a solid tumour to chemotherapy and radiotherapy treatments: clinical insights from a computational model. *PLoS Comput. Biol.*, 9(7):1–14, July 2013.

[139] L. Preziosi. *Cancer modelling and simulation*. CRC Press, 2003.

[140] G. Puppo and M. Semplice. Numerical entropy and adaptivity for finite volume schemes. *Commun. Comput. Phys.*, 2011.

[141] D. C. Radisky. Epithelial-mesenchymal transition. *J. Cell Sci.*, 118(19):4325–4326, 2005.

[142] D. Reher, B. Klink, A. Deutsch and A. Voss-Böhme. Cell adhesion heterogeneity reinforces tumour cell dissemination: novel insights from a mathematical model. *Biol. Direct*, 12(1):18, 2017.

[143] T. Reya, S. J. Morrison, M. F. Clarke and I. L. Weissman. Stem cells, cancer, and cancer stem cells. *Nature*, 414(6859):105–111, 2001.

[144] K. C. Robbins, L. Summaria, D. Elwyn and G. H. Barlow. Further studies on the purification and characterization of human plasminogen and plasmin. *J. Biol. Chem.*, 240(1):541–550, 1965.

[145] E. T. Roussos, J. S. Condeelis and A. Patsialou. Chemotaxis in cancer. *Nat. Rev. Cancer*, 11(8):573–587, 2011.

[146] R. W. Ruddon. *Cancer biology*. Oxford University Press, 2007.

[147] W. Rudin. *Principles of mathematical analysis*. McGraw-Hill Book Co., New York-Auckland-Düsseldorf, third edition, 1976, pages x+342. International Series in Pure and Applied Mathematics.

[148] T. Sasaki, K. Hiroki and Y. Yamashita. The role of epidermal growth factor receptor in cancer metastasis and microenvironment. *Biomed. Res. Int.*, 2013:546318, 2013.

[149] D. Seiffert, G. Ciambrone, N. V. Wagner, B. R. Binder and D. J. Loskutoff. The somatomedin b domain of vitronectin. structural requirements for the binding and stabilization of active type 1 plasminogen activator inhibitor. *J. Biol. Chem.*, 269(4):2659–2666, 1994.

[150] N. Sfakianakis. Adaptive mesh reconstruction for hyperbolic conservation laws with total variation bound. *Math. Comp.*, 82(281):129–151, 2013.

[151] N. Sfakianakis, N. Kolbe, N. Hellmann and M. Lukáčová-Medviďová. A Multiscale Approach to the Migration of Cancer Stem Cells: Mathematical Modelling and Simulations. *Bull. Math. Biol.*, 79(1):209–235, 2017.

[152] K. Shien et al. Acquired resistance to EGFR inhibitors is associated with a manifestation of stem cell–like properties in cancer cells. *Cancer Res.*, 73(10):3051–3061, 2013.

[153] M. Sporn. The war on cancer. *Lancet*, 347(9012):1377–1381, 1996.

[154] A. Stevens and H. G. Othmer. Aggregation, blowup, and collapse: the abc's of taxis in reinforced random walks. *SIAM J. Appl. Math.*, 57(4):1044–1081, 1997.

[155] T. Stiehl and A. Marciniak-Czochra. Mathematical modeling of leukemogenesis and cancer stem cell dynamics. *Math. Model Nat. Phenom.*, 7(01):166–202, 2012.

[156] C. Stinner, C. Surulescu and A. Uatay. Global existence for a go-or-grow multiscale model for tumor invasion with therapy. *Math. Models Methods Appl. Sci.*, 26(11):2163–2201, 2016.

[157] C. L. Stokes and D. A. Lauffenburger. Analysis of the roles of microvessel endothelial cell random motility and chemotaxis in angiogenesis. *J. Theor. Biol.*, 152(3):377–403, 1991.

[158] C. L. Stokes, D. A. Lauffenburger and S. K. Williams. Migration of individual microvessel endothelial cells: stochastic model and parameter measurement. *J. Cell Sci.*, 99(2):419–430, 1991.

[159] Z. Szymanska, C. M. Rodrigo, M. Lachowicz and M. A. J. Chaplain. Mathematical modelling of cancer invasion of tissue: the role and effect of nonlocal interactions. *Math. Mod. Meth. Appl. S.*, 19(02):257–281, 2009.

[160] M. C. B. Tan, P. S. Goedegebuure and T. J. Eberlein. Tumor biology and tumor markers. In C. M. Townsend, B. R. D. and B. M. Evers, editors, *Sabiston Textbook of Surgery: The Biological Basis of Modern Surgical Practice*. Volume 18. Springer, 18th edition, 2008.

[161] Y. Tao. Global existence of classical solutions to a combined chemotaxis/haptotaxis model with logistic source. *J. Math. Anal. Appl.*, 354(1):60–69, 2009.

[162] Y. Tao. Global existence for a haptotaxis model of cancer invasion with tissue remodeling. *Nonlinear Anal. Real World Appl.*, 12(1):418–435, 2011.

[163] Y. Tao and M. Wang. Global solution for a chemotactic-haptotactic model of cancer invasion. *Nonlinearity*, 21(10):2221–2238, 2008.

[164] Y. Tao and M. Winkler. Energy-type estimates and global solvability in a two-dimensional chemotaxis-haptotaxis model with remodeling of non-diffusible attractant. *J. Differ. Equat.*, 257(3):784–815, 2014.

[165] J. P. Thiery. Epithelial-mesenchymal transitions in tumour progression. *Nat. Rev. Cancer*, 2(6):442–454, 2002.

[166] A. M. Turing. The chemical basis of morphogenesis. *Phil. Trans. Roy. Soc. Lond. B Biol. Sci.*, 237(641):37–72, 1952.

[167] S. Turner and J. A. Sherratt. Intercellular adhesion and cancer invasion: a discrete simulation using the extended potts model. *J. Theor. Biol.*, 216(1):85–100, 2002.

[168] R. Tyson, L. G. Stern and R. J. LeVeque. Fractional step methods applied to a chemotaxis model. *J. Math. Biol.*, 41(5):455–475, 2000.

[169] P. F. Verhulst. Recherches mathématiques sur la loi d'accroissement de la population. *Mem. Acad. Royale Belg.*, 18:14–54, 1845.

[170] V. Volterra. Variations and fluctuations of the number of individuals in animal species living together. *ICES J. Mar. Sci.*, 3(1):3–51, 1928.

[171] D. C. Voon, H. Wang, J. K. W. Koo, J. H. Chai, Y. T. Hor, T. Z. Tan, Y. S. Chu, S. Mori and Y. Ito. EMT-induced stemness and tumorigenicity are fueled by the EGFR/Ras pathway. *PLoS One*, 8(8):e70427, 2013.

[172] C. Walker and G. F. Webb. Global existence of classical solutions for a haptotaxis model. *SIAM J. Math. Anal.*, 38(5):1694–1713, 2007.

[173] Y. Wei, D. A. Waltz, N. Rao, R. J. Drummond, S. Rosenberg and H. A. Chapman. Identification of the urokinase receptor as an adhesion receptor for vitronectin. *J. Biol. Chem.*, 269(51):32380–32388, 1994.

[174] R. Weinberg. *The biology of cancer*. Garland science, 2013.

[175] B. Wiebe. *Numerical Simulations of Multiscale Cancer Invasion Models*. Master's thesis, University of Mainz, supervised by M. Lukáčová-Medviďová and N. Sfakianakis, 2016.

[176] World Health Organisation. Cancer fact sheet. Webpage `http://www.who.int/mediacentre/factsheets/fs297/en/`, Feb. 2017. Accessed 20-August-2017.

[177] X. Zhu, X. Zhou, M. T. Lewis, L. Xia and S. Wong. Cancer stem cell, niche and EGFR decide tumor development and treatment response: a bio-computational simulation study. *J. Theor. Biol.*, 269(1):138–149, 2011.

[178] A. Zlotnik. Chemokines and cancer. *Int. J. Cancer*, 119(9):2026–2029, 2006.

Declaration

I hereby declare that I wrote the dissertation submitted without any unauthorized external assistance and used only sources acknowledged in this work. All textual passages which are appropriated verbatim or paraphrased from published and unpublished texts as well as all information obtained from oral sources are duly indicated and listed in accordance with bibliographical rules. In carrying out this research, I complied with the rules of standard scientific practice as formulated in the statutes of Johannes Gutenberg-University Mainz to insure standard scientific practice.

Mainz, October 2017 Niklas Kolbe